ISSN 1313 - 0927

Space Research and Technology Institute
Bulgarian Academy of Sciences

bl.1, *Acad. G. Bonchev* St.,
1113 Sofia, Bulgaria
tel./fax: (+359 2) 988 35 03,
http://www.space.bas.bg

Aerospace Research in Bulgaria

32

Bulgarian Academy of Sciences

Space Research and Technology Institute

2020

AEROSPACE RESEARCH IN BULGARIA

Founded in 1978

Volume 32, Sofia, 2020
Space Research and Technology Institute
Bulgarian Academy of Sciences

Address
AEROSPACE RESEARCH IN BULGARIA
Space Research and Technology Institute
Acad. Georgi Bonchev St., block 1, 1113 Sofia, Bulgaria

web-site: http://journal.space.bas.bg
e-mail: journal@space.bas.bg

Pre-Publication Processing
Tsveta Srebrova

p-ISSN 1313 – 0927 e-ISSN 2367 – 9522

This issue of *Aerospace Research in Bulgaria* is published with financial support from the Bulgarian National Science Fund – Contract No КП-06-НП1-6 – 28.09.2020

Bulgarian Academy of Sciences **ISSN 1313 – 0927**

Aerospace Research in Bulgaria

32

Sofia, 2020

C o n t e n t s

1. ***Tsvetan Dachev, Jordanka Semkova, Borislav Tomov, Yury Matviichuk, Plamen Dimitrov, Nikolay Bankov, Rositza Koleva, Malina Jordanova, Maxim Litvak, Igor Mitrofanov, Dmitry Golovin Alexander Kozyrev, Alexey Malakhov, Maxim Mokrousov, Anton Sanin, Vladislav Tretyakov, Viacheslav Shurshakov, Victor Benghin, Olga Ivanova***
COMPARISON OF RADIATION MEASUREMENTS BY BTN AND R3DR INSTRUMENTS OUTSIDE INTERNATIONAL SPACE STATION. 5

2. ***Antoaneta Frantzova***
CLASSIFICATIONS AND TYPOLOGY OF THE NATURAL AND TRIGGERED TECHNOLOGICAL RISKS. APPLICABILITY OF REMOTE SENSING TECHNOLOGIES TO THE RISK CLASSIFICATION. 21

3. ***Georgi Jelev***
WATER SURFACE DYNAMIC'S OF THE STUDENA DAM, PERNIK USING SENTINEL 2A AND 2B SATELLITE DATA. 34

4. ***Jordan Tzvetkov***
SPATIAL MODELING OF ARCHAEOLOGICAL LANDSCAPES WITH UAV AND DIGITAL PHOTOGRAMMETRY. 41

5. ***Stefan Kazakov, Valko Biserkov, Luchezar Pehlivanov, Stoyan Nedkov***
TROPHIC STATUS ASSESSMENT OF SMALL TURBID LAKES COMPARING REMOTE SENSING AND *IN SITU* DATA: CASE STUDY AT LOWER DANUBE FLOODPLAIN. 53

6. ***Milen Atanasov***
MATHEMATICAL MODEL AND ALGORITHM OF OPERATION OF SYSTEM FOR RELEASE OF LOAD FROM AIRPLANE. 64

7. ***Hristina Georgieva***
AIRCRAFT NOISE LEVEL CALCULATION DURING TAKE-OFF. 75

8. ***Konstantin Metodiev***
STEADY FLOW ANALYSIS OF A SLENDER WING BY LIFTING SURFACE METHOD. 88

9. ***Dimo Zafirov***
LONG ENDURANCE ELECTRIC MULTIROTOR UNMANNED AERIAL VEHICLE. 99

10. ***Bogdan Gherman, Oana Dumitrescu, Valeriu Dragan***
TRANSONIC FLOW STUDY IN A CENTRIFUGAL COMPRESSOR USING PERFORATED AIRFOILS. 110

11. ***Ion Malael, Ioana Octavia Bucur, Valeriu Dragan***
2.5D LES SIMULATION OF AN AIRFOIL SHOCK WAVE REDUCTION BY USING POROUS MEDIA. 122

12. ***Svetoslav Zabunov***
XZ-SERIES OF UNMANNED AERIAL VEHICLES IN 2020. 134

13. ***Assen Marinov, Georgi Yordanov, Martin Kambushev, Stefan Biliderov, Kiril Kambushev***
QUANTITATIVE ASSESSMENT OF PILOTING TECHNIQUE BY FLIGHT DATA RECORDER. 152

14. ***Nikolay Gueorguiev, Aleksandar Kolarov, Ilian Iliev***
MODULE FOR WIRELESS COMMUNICATION IN AEROSPACE VEHICLES. 160

15. ***Oleksandr Minai, Oleg Ivanov, Ihor Siedykh***
INFLUENCE OF LONG-TERM STAY OF ELEMENTS OF CAPILLARY INTAKE DEVICES IN LIQUID PROPELLANT COMPONENTS ON THEIR PARAMETERS. 175

16. ***Peter Getsov, Tsvetan Tsvetkov, Georgi Sotirov, Iliana Nacheva, Zoya Hubenova, Maria Doneva, Petia Metodieva***
APPLICATION OF CRYOTECHNOLOGY IN THE CREATION OF SPACE FOODS FOR CREWS WORKING IN EXTREME CONDITIONS. 193

17. ***Adelina Miteva, Valeria Stoyanova***
ZEOLITES APPLICATION IN TERRESTRIAL AND SPACE INDUSTRY – A REVIEW. 209

18. ***Lachezar Filchev, Ioannis Manakos, Garo Mardirossian, Dimitar Dimitrov, Rainer Reuter, Tsveta Srebrova, Lubomira Kraleva, Kalliroi Marini, Andreas Rienow***
A REVIEW OF EARTH OBSERVATION RESOURCES FOR SECONDARY SCHOOL EDUCATION – PART 1. 224

New Books

Boyko Ranguelov
A NEW EDITION OF A BOOK ABAUT THE NATURAL HAZARDS, PREVENTION AND PROTECTION. 241

С Ъ Д Ъ Р Ж А Н И Е

1. ***Цветан Дачев, Йорданка Семкова, Борислав Томов, Юрий Матвийчук, Пламен Димитров, Николай Банков, Росица Колева, Малина Йорданова, Максим Литвак, Игор Митрофанов, Дмитрий Головин, Александър Козирев, Алексей Малаков, Максим Мокроусов, Антон Санин, Владислав Третяков, Вячеслав Шуршаков, Виктор Бенгин, Олга Иванова***
СРАВНЯВАНЕ НА ДАННИТЕ ОТ ПРИБОРИТЕ BTN И R3DR ИЗВЪН МЕЖДУНАРОДНАТА КОСМИЧЕСКА СТАНЦИЯ. 5

2. ***Антоанета Францова***
КЛАСИФИКАЦИЯ НА ПРИРОДНИТЕ И ТЕХНОГЕННИ РИСКОВЕ. ПРИЛОЖИМОСТ НА ТЕХНОЛОГИИТЕ ЗА ДИСТАНЦИОННИ ИЗСЛЕДВАНИЯ. 21

3. ***Георги Желев***
ДИНАМИКА НА ВОДНАТА ПОВЪРХНОСТ НА ЯЗОВИР СТУДЕНА, ГР. ПЕРНИК С ИЗПОЛЗВАНЕ НА ИЗОБРАЖЕНИЯ ОТ SENTINEL 2A и 2B. 34

4. ***Йордан Цветков***
ПРОСТРАНСТВЕНО МОДЕЛИРАНЕ НА АРХЕОЛОГИЧЕСКИ ЛАНДШАФТИ ЧРЕЗ БЛА И ЦИФРОВА ФОТОГРАМЕТРИЯ. 41

5. ***Стефан Казаков, Валко Бисерков, Лъчезар Пехливанов, Стоян Недков***
ОЦЕНКА НА ТРОФИЧЕН СТАТУС НА МАЛКИ МЪТНИ ЕЗЕРА ЧРЕЗ СРАВНЕНИЕ НА НАЗЕМНИ И ДИСТАНЦИОННИ МЕТОДИ НА ИЗСЛЕДВАНЕ: ЧАСТЕН СЛУЧАЙ ОТ ЗАЛИВНАТА ТЕРАСА НА ДОЛЕН ДУНАВ. 53

6. ***Милен Атанасов***
МАТЕМАТИЧЕСКИ МОДЕЛ И АЛГОРИТЪМ НА РАБОТА НА СИСТЕМА ЗА ОТДЕЛЯНЕ НА ТЯЛО ОТ ЛЕТАТЕЛЕН АПАРАТ. 64

7. ***Христина Георгиева***
ИЗЧИСЛЯВАНЕ НА НИВОТО НА ШУМА НА САМОЛЕТ ПРИ ИЗЛИТАНЕ. 75

8. ***Константин Методиев***
АНАЛИЗ НА СТАЦИОНАРНО ТЕЧЕНИЕ ОКОЛО ТЪНКО КРИЛО ПО МЕТОДА НА НОСЕЩАТА ПОВЪРХНОСТ. 88

9. ***Димо Зафиров***
МНОГОРОТОРЕН БЕЗПИЛОТЕН ЛЕТАТЕЛЕН АПАРАТ С ГОЛЯМА ПРОДЪЛЖИТЕЛНОСТ НА ПОЛЕТА. 99

10. ***Богдан Герман, Оана Димитреску, Валериу Драган***
ИЗСЛЕДВАНЕ НА ТРАНСЗВУКОВО ТЕЧЕНИЕ
В ЦЕНТРОБЕЖЕН КОМПРЕСОР С ИЗПОЛЗВАНЕ НА ПЕРФОРИРАНИ
КРИЛНИ ПРОФИЛИ. 110

11. ***Йон Малаел, Йоана Октавия Букур, Валериу Драган***
2.5D СИМУЛАЦИЯ ПО МЕТОДА НА ГОЛЕМИТЕ ВИХРИ
НА РЕДУЦИРАНЕ НА УДАРНА ВЪЛНА ОКОЛО КРИЛЕН ПРОФИЛ
С ИЗПОЛЗВАНЕ НА ПОРЬОЗНИ СРЕДИ. 122

12. ***Светослав Забунов***
XZ-СЕРИЯ БЕЗПИЛОТНИ ЛЕТАТЕЛНИ АПАРАТИ ПРЕЗ 2020. 134

13. ***Асен Маринов, Георги Йорданов, Мартин Камбушев,***
Стефан Билидеров, Кирил Камбушев
КОЛИЧЕСТВЕНА ОЦЕНКА НА ТЕХНИКАТА НА ПИЛОТИРАНЕ
ПО ЗАПИСИ ОТ РЕГИСТРАТОР НА ПОЛЕТНИ ДАННИ. 152

14. ***Николай Георгиев, Александър Коларов, Илиан Илиев***
КОМПОЗИТЕН МОДУЛ ЗА БЕЗЖИЧНА КОМУНИКАЦИЯ
В АВИОКОСМИЧЕСКИТЕ СРЕДСТВА. 160

15. ***Александър Минай, Олег Иванов, Игор Седих***
ВЛИЯНИЕ НА ПРОДЪЛЖИТЕЛНОТО ПРЕБИВАВАНЕ
НА ЕЛЕМЕНТИТЕ НА КАПИЛЯРНИ ВСМУКАТЕЛНИ УСТРОЙСТВА
В КОМПОНЕНТИТЕ НА ТЕЧНИТЕ РАКЕТНИ ГОРИВА ВЪРХУ
ПАРАМЕТРИТЕ ИМ. 175

16. ***Петър Гецов, Цветан Цветков, Георги Сотиров, Илиана Начева,***
Зоя Хубенова, Мария Донева, Петя Методиева
ПРИЛОЖЕНИЕ НА КРИОТЕХНОЛОГИЯТА ПРИ СЪЗДАВАНЕ
НА КОСМИЧЕСКИ ХРАНИ ЗА ЕКИПАЖИ, РАБОТЕЩИ
В ЕКСТРЕМНИ УСЛОВИЯ. 193

17. ***Аделина Митева, Валерия Стоянова***
ПРИЛОЖЕНИЕ НА ЗЕОЛИТИТЕ В НАЗЕМНАТА И КОСМИЧЕСКА
ИНДУСТРИЯ – ОБЗОР. 209

18. ***Лъчезар Филчев, Йоанис Манакос, Гаро Мардиросян,***
Димитър Димитров, Райнер Ройтер, Цвета Среброва, Любомира
Кралева, Калирои Марини, Андреас Рийнов
ОБЗОР НА РЕСУРСИТЕ ПО НАБЛЮДЕНИЕ НА ЗЕМЯТА
ЗА СРЕДНОТО ОБРАЗОВАНИЕ – ЧАСТ 1. 224

<u>Нови книги</u>

Бойко Рангелов
НОВО ИЗДАНИЕ НА КНИГА ЗА ПРИРОДНИТЕ БЕДСТВИЯ,
ПРЕВЕНЦИЯ И ЗАЩИТА. 241

Bulgarian Academy of Sciences. Space Research and Technology Institute.
Aerospace Research in Bulgaria. 32, 2020, Sofia

DOI: https://doi.org/10.3897/arb.v32.e01

COMPARISON OF RADIATION MEASUREMENTS BY BTN AND R3DR INSTRUMENTS OUTSIDE INTERNATIONAL SPACE STATION

Tsvetan Dachev[1], Jordanka Semkova[1], Borislav Tomov[1], Yury Matviichuk[1], Plamen Dimitrov[1], Nikolay Bankov[1], Rositza Koleva[1], Malina Jordanova[1], Maxim Litvak[2], Igor Mitrofanov[2], Dmitry Golovin[2] Alexander Kozyrev[2], Alexey Malakhov[2], Maxim Mokrousov[2], Anton Sanin[2], Vladislav Tretyakov[2], Viacheslav Shurshakov[3], Victor Benghin[3], Olga Ivanova[3]

[1]Space Research and Technology Institute – Bulgarian Academy of Sciences
[2]Space Research Institute – Russian Academy of Sciences
[3]Institute of Bio-medical problems, Moscow, Russia

Keywords: *Radiation Measurements, International Space Station*

Abstract

The article presents the first attempt to analyze data obtained simultaneously by the Russian BTN and Bulgarian R3DR instruments, flown in 2010 on the "Zvezda" module of the International space station (ISS). Both instruments have well established sensitivity against gamma radiation. This was verified in space, when the Russian spacecraft Soyuz TMA-16, initially docked to the aft port of the "Zvezda" module, was relocated to the zenith-facing port of the "Poisk" module on January 21, 2010. This maneuver brings a gamma ray source in the angle of view of both the BTN and R3DR instruments. The comparison of the data, after the relocation, for the first channels of the spectrometers reveals that they are elevated. This situation continues till March 18, 2010 when Soyuz TMA-16 spacecraft was undocked from the ISS and landed. The final part of the paper, investigate the decrease of the R3DR instrument dose rates in the region of the South Atlantic anomaly (SAA), generated by the additional mass of the Soyuz TMA-16 spacecraft.

Introduction

Following the European Space Agency announcement of opportunity in 1996 for "Externally mounted payloads for 1st utilization phase" on the ISS, scientists working in the fields of astrobiology proposed experiments, aiming at long-term exposure of a variety of chemical compounds and extremely resistant microorganisms to the hostile space environment [1]. The radiation fields encountered in this environment is of pivotal interest to astrobiology [2]. To provide information about the diurnal variation of this radiation, the EXPOSE-R platform (Fig. 1) accommodated the Radiation Risk Radiometer-Dosimeter (R3D) for the Russian segment (R) R3DR (pls. look at the red oval in Fig. 1). This is a low-mass

and small-dimension automatic device measuring solar UV and visible radiation in four channels and cosmic ionizing radiation during the EXPOSE-R mission in 2009–2010 [3].

The BTN-MD detection block is a spectrometer with four individual neutron detectors. BTN-MD is a spare flight unit of High energy neutron detector (HEND) experiment; installed on-board NASA spacecraft *Mars Odyssey*, intended for the exploration and cartography of neutron radiation of Mars surface in different energy ranges [4]. After several years of successful operation of HEND it was decided to use a spare flight unit for the near Earth measurements on-board the ISS [5]. The Russian *Zvezda* module was chosen for this. Some preparations were made, such as development of the BTN-ME inner control block and the Block-MF (a system for providing temperature conditions) and a special mounting pylon for the BTN-MD outside the station [5].

On Fig. 1 shows the mounting position of the EXPOSE-R facility at the left side of the Russian *Zvezda* module of the ISS (only part of it is seen). The BTN detector unit is seen in the zenith area of the module. Both units are at distance of about 5 m.

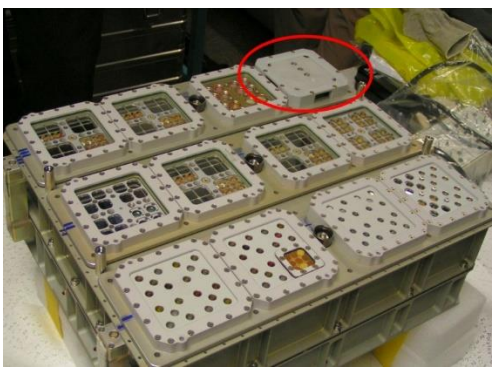

Fig. 1. ESA EXPOSE-R facility

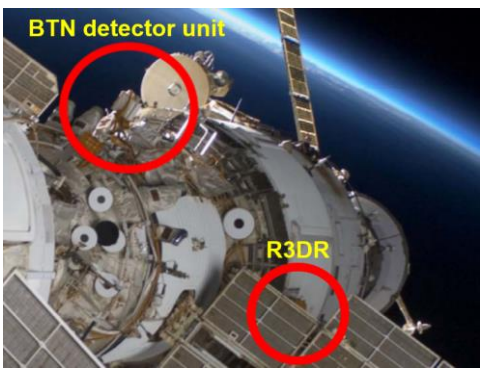

Fig. 2. Position of the BTN detector unit and R3DR instrument outside "Zvezda" module of the ISS

Materials and Methods

R3DR instrument description

The R3DR instrument is a *Liulin*-type miniature spectrometer-dosimeter [6]. Its size is 76 × 76 × 34 mm and weight about 0.12 kg. The alignment of the four photodiodes of the solar irradiance spectrometer is well seen in the centre of the R3DR instrument in Fig. 1. The ionizing radiation PIN diode with a 2 cm^2 area is located beneath the aluminium cover and is therefore not visible.

The ionizing radiation detector of the R3DR instrument (silicon PIN diode of Hamamatsu S2744-08 type) was mounted about 3 mm below the 1 mm thick aluminium cover plate. Additionally, there was a technological shielding of 0.2 mm copper and 0.2 mm plastic material, resulting in less than 0.6 g cm^{-2} total shielding. This allows measuring the direct hits of electrons with energies higher than 1.18 MeV and of protons with energies higher than 27.5 MeV (https://www.nist.gov/pml/stopping-power-range-tables-electrons-protons-and-helium-ions). The surface of the detector (2 cm^2 by 0.3 mm thickness) was oriented to the open space. The detector shielding, being larger from the sides and from behind (Fig. 1), stops the outer radiation belt (ORB) relativistic electrons and attenuates the lower energy inner radiation belt (IRB) protons, but practically does not change the amount of the galactic cosmic rays (GCR) particles.

The instrument obtained one-fixed voltages of +15 V DC from EXPOSE-R facility. The telemetry output from the instrument was arranged as an RS422 serial interface with a maximum rate of 19.2 kbps. The instrument was controlled by a master microprocessor, containing a 12-bit analogue-to-digital converter (ADC) for the UV data channels and the multiplexer. The ionizing radiation dose and the flux measurements were arranged by a charge sensitive preamplifier and another fast 12-bit ADC. The slave microcontroller determined the deposited energy spectrum. Then the spectrum was transferred to the master micro-controller and to the telemetry system. The measurement cycle of the instrument was fixed at 10s. During this time, one energy deposition spectrum from the cosmic ionizing radiation channel was accumulated. A pulse height analysis technique was used for obtaining the deposited energy spectrum, which is further used for the calculation of the absorbed dose and flux in the silicon detector [7].

Data analysis and dose interpretation procedure

The main measurement unit in the ionizing radiation spectrometer was the amplitude of the pulse, after the preamplifier, generated by particles or quanta hitting the detector. It is proportional to the energy loss in the detector by a factor of 240 mV MeV^{-1} and likewise to the dose and the linear energy transfer of the particle. These amplitudes were digitized and organized in a 256-channel spectrum, using only the first 8 bits of the 12 bit fast ADC. The dose D(Si) in Grey [Gy], which by definition in System International is one Joule deposited in 1 kg of material, was calculated by dividing the summarized energy deposition in the spectrum in J by the mass of the detector:

$$D(Gy) = \sum_{i=1}^{255} N_i E_i M D^{-1}, \quad (1)$$

Where *MD* is the mass of the detector in kg, N_i is the number of pulses registered in channel "i", E_i is the deposited energy (in Joules, known through the calibration of the detector) corresponding to channel "i".

The calibration procedures, which were performed with analogical R3DR instruments, are described in [8]. The response curve of the R3DR instrument is expected to be very similar to that published by [9] because all *Liulin* instruments were manufactured using the same electronic parts and the same schematic/scheme. In the specific example of the calibration, performed by Dr. Yukio Uchihori, it was found that the linear coefficient of the response curve, obtained during the calibrations with protons, He^+ and Ne^+ ions was equal to 81.3 keV, whereas the *Liulin* instruments predicted 81.4 keV. During the calibration process of the new *Liulin*-type instruments, we adjusted the position of the first spectrometric channel using a ^{241}Am 60 keV gamma line. Furthermore, the linearity is controlled by electronic methods, as described by AMPTEK INC. in the A225 preamplifier operating notes (http://www.amptek.com/pdf/a225.pdf).

During the calibrations of the Liulin-type instruments it was found that the absolute values of the measured doses were within 2.8% and 8% of the reference value for the ^{137}Cs and ^{60}Co sources, respectively [10]. The response of the LIULIN-4 spectrometer (identical in construction to R3DR2 instrument) was compared in [11] to that of the HAWK TEPC (http://www.fwt.com/detector/fw-ad1ds.htm) on 42 aircraft flights in 2003–2004. On all flights, the absorbed dose measured by both instruments agreed to within 5%. We consider that the flux and dose rate errors of the R3DR measurements on the ISS are within 10% (interval).

The calibrations showed that except for charged energetic particles, the *Liulin* instruments has sensitivity towards gamma rays, which allowed monitoring of the natural background radiation [10]. The detector's neutron effectivity is minimal for neutrons with energy less than 0.5 MeV and has a maximum of a few percent for neutrons with energy of 50 MeV [12]. The Hamamatsu PIN diodes of type S2744-08 "neutron induced nuclear counter effect" was described by [13]. Via this effect, neutrons could be observed in all channels of the spectrum.

Radiation sources selection procedure

The simplest method for source separation is described by Dachev [7], who used the 1971 J. W. Haffner's [14] experimental formulation of the dependence between the incident energy of incoming protons E_p and electrons E_e and the dose to flux ratio (D/F) in nGy cm^2 particle^{-1}:

(2) $$D/F(E_e) = 6x10^{-9} E_e^{-0.9} + 2.5x10^{-8} E_e^{0.15}$$

and

(3) $$D/F(E_p) = 4x10^{-8} E_p^{-0.8} - 6x10^{-10} E_p^{0.85} \quad .$$

The valid ranges for formulae (2) and (3) are 1÷10 MeV, and 1÷1000 MeV, respectively.

Dachev [7] shows that according to formulae (2) and (3) the data can be simply split into two parts by using the dose to flux ratio (D/F). When the D/F is less than 1.12 nGy cm^2 particle^{-1}, the expected predominant type of radiation in a 10-s interval is ORB electrons. When the D/F is greater than 1.12 nGy cm^2 particle^{-1}, the expected type of radiation is IRB or SEP protons [15]. The GCR source spans the two ranges. The GCR source was identified by the requirements that their dose rates are less than 15 μGy h^{-1}.

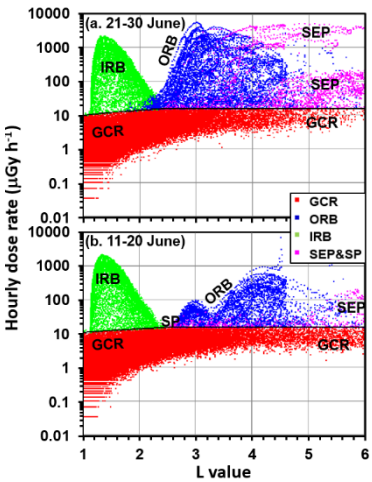

Fig. 3. Latitudinal distribution of the dose rates measured with the R3DR2 instrument

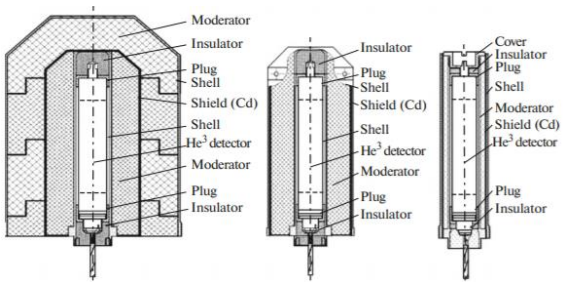

Fig. 4. Design features of BTN-MD instrument

The procedure described by Dachev et al. [15] was upgraded. The result of the separation of the four radiation sources (including SP) is seen in Fig. 3, revealing the latitudinal distribution of the dose rates against McIlwain's L values. The L value is plotted on the x-axis. On the y-axis, the absorbed dose rate measured by the R3DR2 instrument is plotted. Fig. 3a contains data from 21 June to 30 June 2015, whereas the data on Fig. 3b are from 11 June to 20 June 2015. Each section contains 86 400 points at a 10-s resolution (10 days × 360 × 24 h).

Four different primary radiation sources, separated by the heavy black lines, are seen in the data. These sources are plotted in Fig. 3 with different colors for the IRB, ORB, GCR and SEP sources. From one 10-s independent measurement of the dose rate (D) and flux (F), we were able to calculate one dose to flux ratio (D/F).

Using this, we were able to decide only what the predominant radiation sources were, but we were not able to extract the exact doses of each source.

The GCR source contributes for the majority of the measurements in Fig. 3, visualized as the area with many red points in the bottom over the L-value range between 1 and 6. The dose rates vary between 0.03 and 15 $\mu Gy\ h^{-1}$.

The second permanent source of radiation corresponds to the protons in the SAA region of the IRB, presented as a large maximum in the upper left corner of Fig. 3, with a total of 5 876 points in Fig. 3a. They cover L-values between 1.2 and 2.6. The dose rates in the IRB region varied between 10 and 2 748 $\mu Gy\ h^{-1}$.

The GCR and IRB sources in both figures 3a/b look very similar because these two sources have relatively slow time variations. Drastically different are the ORB and SEP sources in the right parts of Figures 3a/b. The reasons for the radically different ORB and SEP distributions are the magnetic storms on 23 and 25 June and the SEP events on 18, 22 and 26 June 2015. The real SEP particles in Fig. 3a/b appear at some smaller L-values. Then they rise and finally maintain some fixed dose rate value at a range of L from 4 to 6. The SEP source in Fig. 3b appears only at $L > 5$, because the SEP event on 18 May was very week.

The boundary seen at $L = 4.7$ in the ORB source in figures 3a/b is generated by the Earth magnetic field hemisphere asymmetries. The ISS orbit in the Southern hemisphere is extended up to $L = 6$, while in the Northern only up to $L = 4.7$.

BTN instrument description

Three detectors (SD, MD, and LD) are based on helium-filled (^3He) proportional neutron counters covered in cadmium shields and polyethylene spheres of different thickness. The design aspects of these detectors are shown in Fig. 4. The proportional ^3He counters are detectors of epithermal neutrons. In this case, having given a good account (also as a part of the HEND experiment flight unit), the LND2517 industrial counters (LND Inc. Company, United States) were used, filled with ^3He and a small addition of CO_2 under an atmosphere pressure of 6. The registration concept in the proportional counter is based on the capture of a thermal or epithermal neutron in a reaction of that type as follows:

(4) $$n + {}^3He \rightarrow {}^3H + p + 764\ keV$$

The total energy output in that reaction is distributed between the proton and the triton in the ratio of 191 keV (triton) and 573 keV (proton) in inverse proportion to their masses.

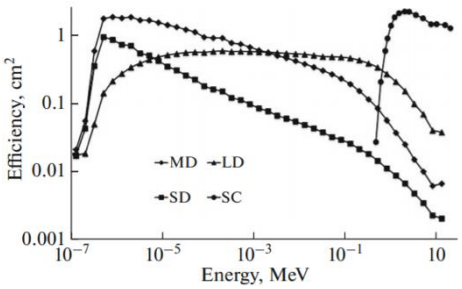

Fig. 5. Sensitivity functions for all BTN-MD instrument detectors

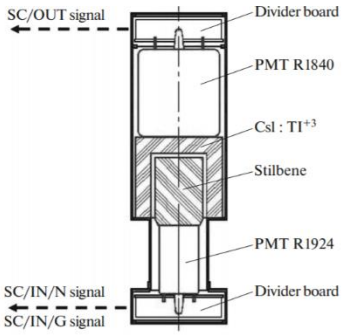

Fig. 6. Scintillation block configuration

The counter itself is a metallic cylinder (cylinder jacket serves as a cathode) with a thin (thickness about the fraction of a millimetre) tungsten wire along the cylinder axis, which serves as the anode. A current of about 1 kV is applied between the cathode and the anode. This allows the counter to work in the so-called proportional mode, when the applied current is high enough for the primary electrons formed during the ionization of gas molecules by a nuclear reaction of $n + {}^3He \rightarrow {}^3H + p$ in order to perform secondary ionization with the generation of a large number of ion pairs. The collected charge on the electrodes of the counter and the corresponding current impulse is proportional to the full energy output in the volume of the counter. The digitalization of the signal received, during one neutron registration act, allows the amplitude spectrum to be obtained.

We used 16 spectral channels to digitalize amplitude. The first 15 spectral channels have approximately equal width and cover energy range up to 1 MeV. The last channel is integral and allows particles that produce energy output greater than 1 MeV to be registered (these particles may be, e.g., high-energy neutrons). The amplitude spectrum form measured in this proportional counter depends on the kinematics of the reaction products and does not depend on the energy of the incoming neutron (except episodes of high-energy neutron registration). The typical form of the amplitude spectrum has a main peak that corresponds to the full energy output (764 keV when both the proton and triton stayed in the volume of the detector) and a wide low-energy plateau that corresponds to the episode when a proton or a triton reached the walls of the detector (wall effects). The cross section of a neutron capture starts in the thermal energy ranges (fractions of eV) and extends to the epithermal energies (units and tens of keV) according to the power law $\sim E^{-1/2}$. If a proportional counter is covered in a layer of a cadmium (effective thermal neutron absorber), its registration efficiency shifts to an epithermal-neutron energy range of 0.4 eV (cadmium threshold) to hundreds of eV.

To increase the energy range of the registered neutrons (suitable for registering neutrons with higher energies), all detectors of the BTN-MD instrument

are covered in polyethylene (CH2) with various thicknesses. The polyethylene is an effective neutron moderator due to the hydrogen in its composition. The various thickness of the polyethylene leads to various moderation rates of incoming neutrons to energies where the registration efficiency in gas-filled counter approaches the maximum.

An SD detector (Fig. 4 to the right), with a polyethylene thickness of 2 mm, has the maximum response to the neutron in the energy range of 0.4 eV to 1 keV. The MD detector (Fig. 4 at the centre), with a thickness of medium polyethylene about 15 mm, has maximum response to neutrons in energy range from 10 eV to 100 keV. LD detector, (Fig. 4 to the left) with a double polyethylene thickness of 30 mm, has the maximum response to neutrons in energy range from 10 eV to 1 MeV. Figure 5 shows the sensitivity functions of all detectors in the BTN-MD instrument. It is clearly seen that, due to various thicknesses of the moderators, in the proportional counters, we managed to succeed in registering neutrons in a wide range of energies of from 0.4 eV up to 1 MeV.

The fourth detector (SC) is intended to register only high-energy neutrons in the energy range of 350 keV to 15 MeV. It was manufactured from a stilbene crystal (C14H12) and covered in the anticoincidence shield from the crystal. The configuration of the scintillation block is shown in Fig. 6. The fast neutron detector is also shown there (in Fig. 6, it is marked as a stilbene). The stilbene is an organic crystal with high hydrogen content. Upon registering a neutron with energy En, a proton with energy Ep < En is dislodged (SC/IN/N signal shown in Fig. 6).

The registration of gamma rays with the formation of a free electron also occurs in the stilbene (SC/IN/G signal). The forms (time profile) of the electric pulses from the protons and the electrons differ very much, so the special electric scheme developed for the BTN-MD allows these two events to be divided with an error of no more than 10^{-3}.

The outer scintillation detector (signal measured in the detector SC/OUT, see Fig. 6) was manufactured from a crystal, which has a high density and an atomic number, which allows the high registration efficiency of gamma rays and charged particles with the energies of more than 50 keV. To distinguish the outer cosmic rays, the protons from the recoil protons formed in stilbene after the interactions with the neutrons, an anticoincidence logic was implemented in the detector block. The proton registration of the cosmic rays act in the outer detector SC/OUT is followed by the VETO signal, which forbids the simultaneous registration of that proton in the inner detector SC/IN.

ISS configuration during the R3DR and BTN simultaneous operation

In November 2006, the BTN MD neutron spectrometer was installed onboard the Russian *Zvezda* module, which is a component of International Space

Station (ISS). The R3DR dosimeter worked in the EXPOSE-R facility outside the Russian Zvezda module of the ISS in the period 11 March 2009–20 August 2010.

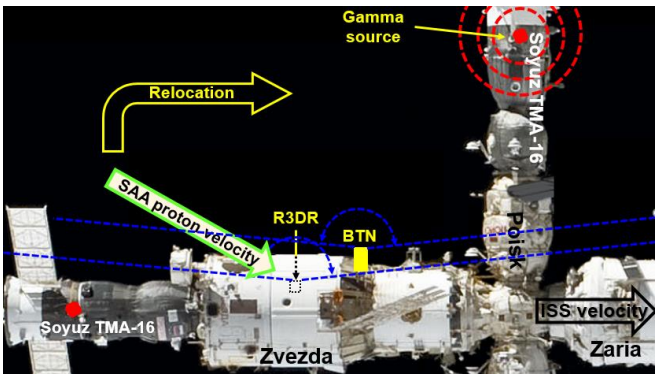

Fig. 7. The configuration of the Russian segment and the positions of both the BTN detector unit and the R3DR instrument

Because of a failure of the computer, connecting the external facility to the ISS and to the ground [16], no data were retrieved in three large time spans: 24 June–28 December 2009, 21 January–18 February 2010 and 12–21 March 2010.

Figure 7 shows the configuration of a part of the Russian segment during the R3DR and BTN simultaneous operation in the period January-March 2010. On the left bottom, part of the figure is the *Zvezda* module. The Zaria module is on the right side. The *Poisk* module is in the middle.

The Soyuz TMA-16 was a crewed flight to and from the ISS. The launch of the Soyuz rocket with the *Soyuz* TMA-16 spacecraft took place on Sept. 30, 2009, at 11:14:42 Moscow Summer Time. It transported two members of the Expedition 21 crew and a Canadian entrepreneur from the Baikonur Cosmodrome in Kazakhstan to the ISS. *Soyuz* TMA-16 was docked to the ISS at the aft port of the *Zvezda* module on Oct. 2, 2009 at 12:35:07 Moscow Time. On January 21, 2010, cosmonaut Suraev and Expedition 22 Commander J. Williams relocated the spacecraft to the zenith-facing port of the *Poisk* module. *Soyuz* TMA-16 landed in Kazakhstan on March 18, 2010.

The gamma ray source (red large circle), part of the KAKTUS-2B gamma altimeter is mounted at the bottom of the descending module of the *Soyuz* TMA-16 spacecraft. It is used to initiate the firing of the boosters during the landing. The position of the BTN detector unit is shown as a yellow rectangle in the figure. Its angle of view is toward up that is why the BTN does not see the gamma source at the *Soyuz* TMA-16 spacecraft until the moment of the relocation on January 21st, 2010.

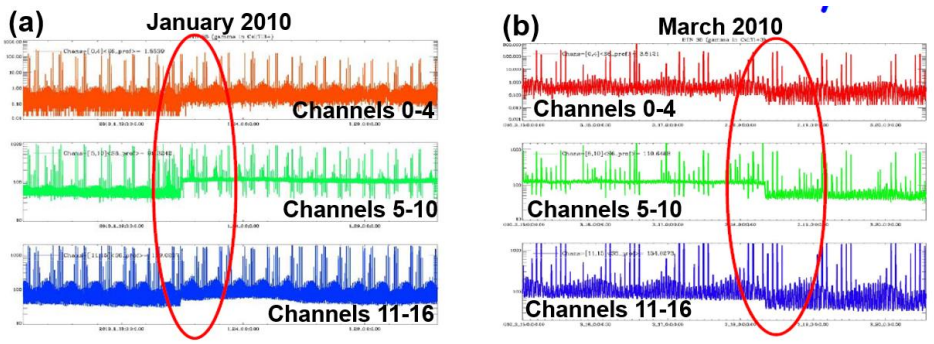

Fig. 8. BTN data obtained in January and March 2010

The R3DR instrument position is shown in Fig. 7 as a black dashed line quadrate. It is mounted on the ESA EXPOSE-R facility and both are behind the body of the *Zvezda* module and are not visible. The R3DR angle of view (blue lines in Fig. 7) is also toward up, analogically to that of the BTN. It does not see the body and the gamma ray source on *Soyuz* TMA-16 spacecraft before the relocation on 21 of January 2010. R3DR and BTN instruments, being gamma ray sensitive, start to show the gamma radiation in the dataflow after the moment of the relocation on January 21st, 2010. On March 18, 2010, when *Soyuz* TMA-16 spacecraft went to landing, both instruments loose the signal of gamma ray.

Data analysis

Gamma ray source analysis

BTN data analysis

Fig. 8a contains the gamma ray background measurements of the BTN detector unit in the period January 14th – February 1st, 2010. Well-seen drop-up in the count rates is observed in all channels, i.e. 1–16, at about 10:30 UT on January 21st, 2010. Since this moment up to about 08:00 UT on March 18 (Fig. 8b), the counts in the mentioned channels were elevated because of the quanta emissions of the ^{60}Co gamma ray source at the *Soyuz* TMA-16 spacecraft. They became visible by the BTN detector unit after the relocation of the *Soyuz* TMA-16 spacecraft.

Fig. 8b contains the gamma ray background measurements by the BTN detector unit in the period 15–21 March 2010. In this case, a well-seen drop-down in the count rates is observed in all channels from 1 to16 at about 08:00 UT on March 18, 2010. The change is associated with the undocking of the *Soyuz* TMA-16 spacecraft from the ISS for further landing. This brings the gamma ray source away from the BTN detector unit, which stop to observe it.

R3DR data analysis

Fig. 9a visualizes the variations of the R3DR instrument first channel count rate in the period 16–25 January 2010, while Fig. 9b – the variations of the periods 6–10 and 22–27 March 2010. With black non-filled points is presented the count rate. The points were selected with the following requirements: a) the total magnetic field strength to be higher than 0.26 Gauss.

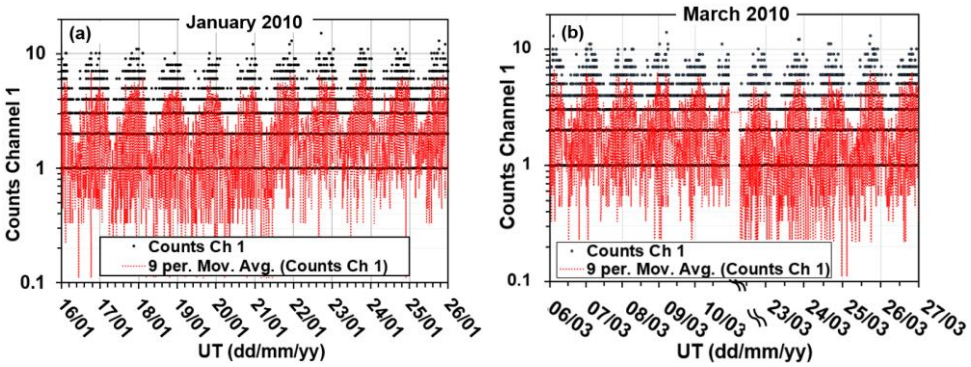

Fig. 9. R3DR data obtained in January and March 2010

This removes from the selection the IRB source protons in the region of the SAA; b) the D/F ratio of the selected data to be higher than 1.5 nGy cm^2 particle^{-1}. This removes from the selection the ORB relativistic electrons. As a result of both requirements, only the GCR radiation was selected. The red dotted line in the figures presents the moving average per 9 points of the count rate.

The first feature seen in the Fig. 9 is the meander of the minima and the maxima in both variables. This is generated by the orbital movement in the longitude of the ISS during 1 day that is why the meander is with about one day frequency. The minima in Fig. 9 correspond to the crossings of the magnetic equatorial region, while the maxima – to the crossings of the high latitudes in both hemispheres. The geomagnetic shielding, measured by the vertical cut-off rigidity [17], is the reason for the reduced GCR fluxes at low L values and for the rising fluxes toward the high L values. The same meander is observed in the BTN data in Fig. 8.

The second main feature is the drop-up of the count rate around 21st of January in Fig. 9a and the drop-down in the interval between 10 and 22 March 2010 in Fig 9b. Those are the same changes as the observed in Fig. 8. That is why we consider that the R3DR count rate data reflect the observation of the gamma ray source at the *Soyuz* TMA-16 spacecraft.

Historically, at first the gamma ray source at *Soyuz* type spacecraft was observed by the R3D-B2 instrument (technologically identical to the R3DR instrument) at the *Foton*-M2 spacecraft. The R3D-B2 instrument was mounted inside the ESA *Biopan*-5 facility in ESTEC, The Nederland (Dachev 2013, look at

Fig. 1 therein) and switched ON in ESTEC on 24 May 2005. It measured the radiation during the whole transportation from ESTEC to Baikonur, Kazakhstan. During the integration of the *Biopan*-5 facility in the *Foton*-M2 spacecraft on 29 May an additional source of radiation was observed by R3D-B2 instrument. It rises up the doses from the normal background level of 0.1 μGy h^{-1} up to about 2 μGy h^{-1}. Having in mind the very small level of the D/F ratio of about 0.2 nGy cm^2 $particle^{-1}$, we identify it as the gamma radiation.

More precisely, the R3DR data analysis gives the following results for the changes of the R3DR parameters on 21 January, connected with the arrival of the *Soyuz* TMA-16 spacecraft, seen in Fig 9a: a) the average count rate in the first channel rises up from 1.87 to 2.46 counts per 10 s; b) the average GCR dose rate rises up from 7.31 to 7.94 μGy h^{-1}. The calculated average ambient dose rate [18] rises from 27.2 to 29.8 μSv h^{-1}. For the changes, connected with the outflow of the *Soyuz* TMA-16 spacecraft, seen in Fig 9b the following results were obtained respectively: a) the average count rate in the first channel falls down from 2.22 to 1.91counts per 10 s; b) the average dose rate fall-down is from 7.59 to 6.53 μGy h^{-1}. The calculated average ambient dose rate [18 falls down from 28.4 to 24.6 μSv h^{-1}.

Analysis of the IRB source decrease

The analysis of the data from the R3DE instrument of the ESA's EXPOSE-E mission, outside the ISS at the European Technological Expose Facility (EuTEF) on the ESA Columbus module, shows that the docking of the Space Shuttle with the ISS decreased the SAA dose rates [19]. The R3DE instrument decreases were from about 1500-μGy h^{-1} down to 600–700 μGy h^{-1} or by a factor of two.

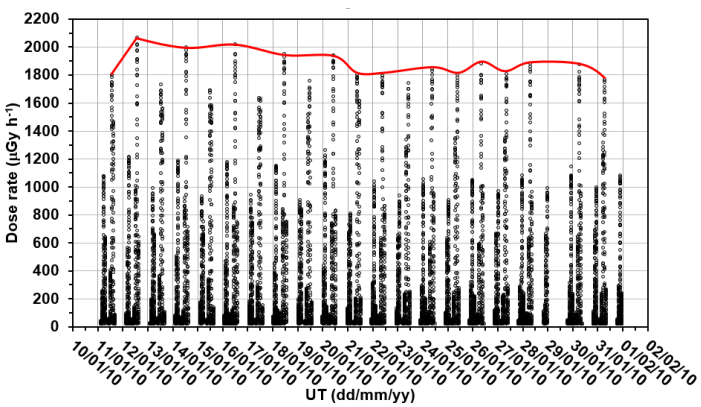

Fig. 10. SAA dose rate variations from 11 to 31 January 2010

The dose rate data from the R3DR instrument showed that: 1) before the Space Shuttle docking, the SAA dose rates, measured with the R3DR, were higher (~2500 μGy h^{-1}) than the R3DE data; 2) The decrease of the SAA dose rates, after the shuttle docking, was only by a factor of 1.25. These differences were explained by the smaller shielding of the R3DR from the body of *Zvezda* module and by the larger distance from the body of the Space Shuttle, docked to the American *Destiny* module.

Having in mind the above, we decided to prove how the relocation of the *Soyuz* TMA-16 spacecraft inside of the view angle (pls. look the blue lines in Fig. 7) changes the SAA energetic protons dose rates.

Fig. 10 shows the SAA dose rate variations from 11 to 31 January 2010. The points were selected with the following requirements: a) the total magnetic field strength to be less than 0.23 Gauss. This specify the selection predominately the IRB source protons in the region of the SAA; b) the D/F ratio of the selected data to be higher than 1.5 nGy cm^2 $particle^{-1}$; c) the dose rate to be higher than 15 μGy h^{-1}.

Because of the large time interval on the X axis in Fig. 10, the 6–8 dose rate data of the ascending and descending crossings of the SAA anomaly per day are presented only by two bars. The first one corresponds to the descending orbits, while the second one to the ascending orbits during one series of 6–8 crossings. The differences in the dose rate amplitudes are produced by the east-west asymmetries of the proton fluxes in the region of the SAA [20], which lead to the existence of a predominant east to west drift velocity of the protons in the SAA.

In Fig. 7 the proton drift velocity is presented with light green arrow. The picture really visualizes the descending orbits situation, when the station is flying in the direction of the ISS velocity to the right. The R3DR instrument, being at the other side of the *Zvezda* module (pls. look also Fig. 2), is shielded from the low energy SAA protons by the body of the Zvezda module. That is why, the dose rate in the descending (first) bars in Fig. 10 are smaller than the ascending bars. During the ascending orbits, the ISS is rotated at 180° and R3DR is directly hit by the SAA protons.

Well seen decrease of the SAA dose rates is observed on 21 January 2010, when *Soyuz* TMA-16 spacecraft was relocated and came in the angle of view of the R3DR instrument. The red curve, which connected the maximal dose rate bars, underlines this change. More precise, the R3DR data analysis gives the following results for the changes of the R3DR parameters on 21 January, connected with arrival of the *Soyuz* TMA-16 spacecraft, as seen in Fig 10: a) the average dose rate in the SAA decreases from 360 to 330 μGy h^{-1}; b) the maximal observed SAA dose rate decreases also from 2063 to 1878 μGy h^{-1}. These changes are statistically verified by 4416 10 sec measurements in the period 11–20 January and 4340 measurements in the period 22–31 January.

The rise of the SAA dose rates, connected with the undocking of the Soyuz TMA-16 spacecraft, on March 18 2010 are not possible to be precisely analysed,

because of rotating of the ISS at 180° on March 3, 2010. The data in the period 6–12 March are not collected in the same way as the data in the period 22–30 March 2010. The result is that both data sets are not possible to be compared.

Conclusions

The simultaneously obtained gamma ray data by the Russian BTN and the Bulgarian R3DR instruments show very similar changes, connected with the appearance of the gamma ray source in the angle of view of both instruments. The undocking of the *Soyuz* TMA-16 spacecraft on March 18 2010 also brings identical changes in both instruments. In conclusion, we are deeply convinced that the first attempt for a mutual data analysis is very successful.

Acknowledgements

This work is supported by: a) Agreement between RAS and BAS on "Fundamental space research"; b) Contract No. 4000117692/16/NL/NDe Funded by the Government of Bulgaria through an ESA Contract under the PECS (Plan for European Cooperating States); c) Contract with National Science Fund – Bulgaria on Project No. 129 FOR BILATERAL PROJECTS – BULGARIA – RUSSIA 2018–2019. In IKI-RAS the work is supported by the Russian Science Foundation under grant 19-52-18009.

Most of the data used in this paper are part of the "Unified web-based database with Liulin-type instruments", which are available online, free of charge at the following URL: http://esa-pro.space.bas.bg/database. The database was created under the ESA contract mentioned above.

References

1. Rabbow, E., Horneck, G., Rettberg, P., Schott, J.-U., Panitz, C., et al., EXPOSE, an astrobiological exposure facility on the International Space Station—from proposal to flight. Orig. Life Evol., Biosphere, 2009, 39, 581–98.
2. Ferrari, F. and Szuszkiewicz, E. Cosmic rays: a review for astrobiologists. Astrobiology 2009, 9, 413–36.
3. Dachev, T. P., G. Horneck, D.-P. Häder, M. Schuster, and M. Lebert, EXPOSE-R cosmic radiation time profile. Journal of Astrobiology, 2015, 14, 17–25.
4. Mitrofanov, I., Anfimov, D., Kozyrev, A., et al., Maps of subsurface hydrogen from the high energy neutron detector, Mars Odyssey, Science, 2002, 297, 5578, 78–81.
5. Tretyakov, V. I., Mitrofanov, I. G., Bobronitskii, Yu. I., et al., The first stage of the "BTN-Neutron" space experiment onboard the Russian segment of the International Space Station. Cosmic Res., 2010, 48, 4, 285–99.
6. Dachev, T. P., B. Tomov, Yu. Matviichuk, Pl. Dimitrov, et al., Calibration Results Obtained With Liulin-4 Type Dosimeters. Adv. Space Res., 2002, 4, 917–25.
7. Dachev, T. P., Characterization of near Earth radiation environment by Liulin type instruments, Adv. Space Res., 2009, 44, 1441–49.

8. Dachev, T. P., J. V. Semkova, B. T. Tomov, Yu. N. Matviichuk, et al., Overview of the Liulin type instruments for space radiation measurement and their scientific results, Life Sciences in Space Research, 2015, 4, 92–114.
9. Uchihori, Y., H. Kitamura, K. Fujitaka, T. P. Dachev, B. T. Tomov, P. G. Dimitrov, and Y. Matviichuk, Analysis of the calibration results obtained with Liulin-4J spectrometer-dosimeter on protons and heavy ions. Radiation Measurements, 2002, 35, 127–34.
10. Spurny, F. and T. P. Dachev, Long-Term Monitoring of the Onboard Aircraft Exposure Level with a Si-Diode Based Spectrometer. Adv. Space Res., 2003, 32, 53–58.
11. Green, A.R., Bennett, L.G.I., Lewis, B.J., Kitching, F., McCall, M.J., Desormeaux, M., Butler, A., An empirical approach to the measurement of the cosmic radiation field at jet aircraft altitudes. Adv. Space Res. 2005, 36, 1618–1626.
12. Spurny, F., Response of a Si-diode-based device to fast neutrons. Radiation Measurements, 2005, 39, 219–23.
13. Zhang, L., Mao, R., and Zhu, R. Fast neutron induced nuclear counter effect in Hamamatsu silicon PIN diodes and APDs. IEEE Transactions on Nuclear Science. 2011, 58, 1249–56.
14. Haffner, J. W., Yadernoe izluchenie i zashchita v kosmose (Nuclear Radiation and Protection in Space), pp 115, Atomizdat, Moscow, 1971. (in Russian), translated from: J. W. Haffner, Radiation and shielding in space. NY: Academic Press, 1967.
15. Dachev, T., Horneck, G., Häder, D.-P., Lebert, M., Richter, P., Schuster, M., and Demets, R. Time profile of cosmic radiation exposure during the EXPOSE-E mission: The R3D instrument. International Journal of Astrobiology, 2012, 12, 403–11.
16. Rabbow, E., Rettberg, P., Barczyk, S., Bohmeier, M., Parpart, A., Panitz, C., … Reitz, G. The astrobiological mission EXPOSE-R on board of the International Space Station. International Journal of Astrobiology, 2015, 14, 3–16.
17. Smart, D. F. and M. A. Shea, A review of geomagnetic cutoff rigidities for Earth-orbiting spacecraft. Advances in Space Research, 2005, 36, 2012–20.
18. Spurny, F., O. Ploc, and I. Jadrnı´kova, Spectrometry of linear energy transfer and dosimetry measurements onboard spacecrafts and aircrafts. Phys. Part. Nuclei Lett., 2009, 70–77. Pleiades Publishing, Ltd. ISSN 1547–4771.
19. Dachev, T P., Semkova, J., Tomov, B., Matviichuk, Y., Dimitrov, P., Koleva, R., … Bankov, N. G., Space shuttle drops down the SAA doses on ISS. Advances in Space Research, 2011, 47, 2030–2038.
20. Wilson, J. W., Nealy, J. E., Dachev, T., Tomov, B. T., Cucinotta, F. A., Badavi, F. F., de Angelis, G., Leutke, N., Atwell, W. Time serial analysis of the induced LEO environment within the ISS 6A. Adv. Space Res. 2007, 40, 1562–70.

СРАВНЯВАНЕ НА ДАННИТЕ ОТ ПРИБОРИТЕ BTN И R3DR ИЗВЪН МЕЖДУНАРОДНАТА КОСМИЧЕСКА СТАНЦИЯ

Ц. Дачев, Й. Семкова, Б. Томов, Ю. Матвийчук, П. Димитров, Н. Банков, Р. Колева, М. Йорданова, М. Литвак, И. Митрофанов, Д. Головин, А. Козирев, А. Малаков, М. Мокроусов, А. Санин, В. Третяков, В. Шуршаков, В. Бенгин, О. Иванова

Резюме

Статията представя първия опит за анализ на данни, получени едновременно от руския прибор BTN и българския прибор R3DR, работили на модула "Звезда" на Международната космическа станция (МКС) през 2010 г. И двата прибора имат добре установена чувствителност към гама-лъчение. Това беше доказано в космоса, когато руският космически кораб "Съюз ТМА-16", който беше скачен към задния порт на модула "Звезда", на 21 януари 2010 г., беше преместен в порта на модула Poisk. В резултат на тази маневра, източник на гама лъчи попада в ъгъла на зрение на двата прибора. Сравнението на скоростите на броене в първите канали на спектрометрите показва, че те са повишени. Това продължава до 18 март 2010 г., когато космическият кораб "Съюз ТМА-16" се отделя от МКС и каца. Последната част от статията изследва намалението на дозата от прибора R3DR в района на Южно-атлантическата аномалия (ЮАА). Последното е генерирано от допълнителната маса на космическия кораб "Съюз ТМА-16", което допълнително екранира прибора R3DR. Намаляването на потока от ниско енергийни протони води до намаляване на регистрираните дози.

Bulgarian Academy of Sciences. Space Research and Technology Institute.
Aerospace Research in Bulgaria. 32, 2020, Sofia

DOI: https://doi.org/10.3897/arb.v32.e02

CLASSIFICATIONS AND TYPOLOGY OF THE NATURAL AND TRIGGERED TECHNOLOGICAL RISKS. APPLICABILITY OF REMOTE SENSING TECHNOLOGIES TO THE RISK CLASSIFICATION

Antoaneta Frantzova

Climate, Atmosphere and Water Research Institute – Bulgarian Academy of Sciences
e-mail: afrantzova@cawri.bas.bg; afrantzova@gmail.com

Keywords: *Acceptable Risk, Natural Disasters, Remote Sensing*

Abstract

New approach to the risk management concept based on the assessment of damages (in % of GDP), probability of occurrence and necessary measures to create resilient society is presented. Several theoretical models are investigated and compared. The "acceptable risk" concept is developed based on the preventive measures and expected results.

"Resilient", "Transition" and "Forbidden" areas related to the damages and probability of occurrence are graphically defined. The classification is based on two main factors (probability of occurrence and potential damage) associated with risk processes and phenomena that develop and run in the "Resilient", "Transition" and "Forbidden" areas. Satellite data and information related to the specific characteristics of the natural hazards and disasters are used.

Introduction

The paper deals with the new approach to the risk management concept of natural hazards on the assessment of damages (in % of GDP), probability of occurrence and necessary measures to create resilient society. Several theoretical models are investigated and compared.

"Normal", "Transition" and "Prohibited" areas related to the damages and the probability of occurrence are graphically defined. Since the consequences of the natural hazards depend not simply on their magnitude, but also on what happened before, a new point of view affording an opportunity for better decisions, reducing the risk and protect the population.

The recent research is based on the studies provided for the last two decades by German Advisory Council of Global Change.

Classifications and typology of the natural hazards and risks according to the GDP, probability of occurrence and expected damages

New approach to the risk management concept based on the assessment of damages (in % of GDP), probability of occurrence and expected damages is presented. Several theoretical models are investigated and compared. The "acceptable risk" concept is developed by author based on the preventive measures and expected results.

Classification is made on the base on German Advisory Council on Global Change. It is change by the author according to our personals purposes and aims. The classification is related to the damages and probability of occurrence. "Normal", "Transition" and "Prohibited" areas related to the damages and probability of occurrence are graphically defined.

Risks in the normal area have the following characteristics [6]:

• Low uncertainties regarding the probability distribution of damage;

• In total, a small catastrophic potential;

• Low to medium uncertainty about both the probability of occurrence and the associated magnitude of damage;

• Low statistical confidence intervals with respect to probability and magnitude of damage;

• Low levels of persistency and ubiquity (scope in time and space);

• High reversibility of potential damage, and

• Low potential for social conflict and mobilization.

The transitional area is reached if one or more of the following conditions are met (WBGU, 1998):

• The damage potential is high;

• The probability of occurrence is high, approaching 1;

• The uncertainty of the probability distribution of adverse effects is high;

• The confidence intervals of probability and magnitude of damage are large;

• Persistency, ubiquity and irreversibility are particularly high, whereby there must be reasonable grounds to assume a causal link between trigger and effects;

• For reasons of perceived distributional injustice or other social and psychological factors, a major potential for conflict or mobilization is to be expected (migration, refusal, protest, resistance).

If one of these conditions is given, then the product of probability and severity will usually be in the transitional area. If the high level of risk is further joined by a low benefit or a low expectation of opportunity, or if the product of the two components of risk assumes extreme levels, then the risk is situated in the *prohibited area*. In the prohibited area, the consequences to be expected from taking a risk are so severe that risk reduction is unconditional. In extreme cases, the proper response here is an immediate ban or moratorium [6].

Table 1. Overview of risk classes according to WBGU and author, P signifies the probability of occurrence and E the extent of damages [3, 6]

Damocles	*P* – low (approaching 0) Reliability of estimation of *P* – high *E* – high Reliability of estimation of *E* – high	Nuclear energy Large-scale chemical facilities Dams
Damocles I (defined by author)	*P* – low (approaching 0) Reliability of estimation of *P* – unknown *E* – high (approaching infinity) Reliability of estimation of *E* – high	Meteorite impacts
Cyclops	*P* – unknown Reliability of estimation of *P* – unknown *E* – high Reliability of estimation of *E* – tends to be high (medium to high)	Earthquakes, Volcanic eruptions AIDS infection; Mass development of anthropogenically influenced species; NBC-weapons systems Collapse of thermohaline circulation, Epidemics
Pythia	*P* – unknown Reliability of estimation of *P* – unknown *E* – unknown (potentially high) Reliability of estimation of *E* – unknown	Self-reinforcing global warming Release and putting into circulation of transgenic plants; BSE/nv-CJD infection; Certain genetic engineering applications; Instability of the West Antarctic ice sheets
Pandora	P – unknown Reliability of estimation of P – unknown E – unknown (only assumptions) Reliability of estimation of E – unknown Persistence is high (several generations)	Persistent organic pollutants (POPs) Endocrine disruptors
Cassandra	P – tends to be high Reliability of estimation of P – tends to be low E – tends to be high Reliability of estimation of E – tends to be high Long delay of consequences	Gradual human-induced climate change Destabilization of terrestrial ecosystems
Medusa	P – tends to be low Reliability of estimation of P – tends to be low E – tends to be low (exposure high) Reliability of estimation of E – tends to be high	Electromagnetic fields (pollution) Nanotechnologies
Achelous (defined by author)	P – high Reliability of estimation of P – tends to be high E – medium to high Reliability of estimation of E – tends to be high	Natural hazard mainly from hydrological and meteorological origin

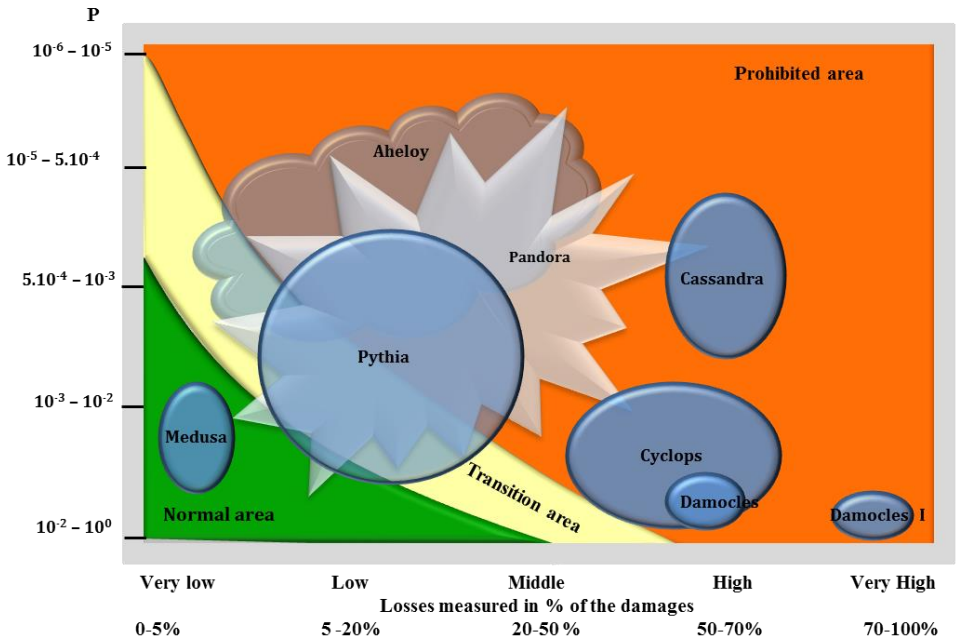

Fig. 1. Classes of risk and their location in the normal (green), transition (yellow) and prohibited (red) areas [3, 6]

Overview of Risk Classes

According to the German Advisory Council on Global Change, the names of risk classes are taken from Greek mythology because of their symbolism. Risk classes are defined in briefly below.

Damocles

Greek mythology reports that Damocles was once invited by his king to a banquet. However, he was obliged to take his meal under a razor-sharp sword hanging above him on a fine thread. For Damocles, opportunity and danger were closely linked, and the Damocles' Sword has become a byword for a happy situation overshadowed by danger.

The threat was expressed as the possibility that, at any point in time, if albeit with low probability, an event deadly to Damocles could occur. This class of risk accordingly comprises sources of risk that have a very high catastrophic potential but where the probability that this potential manifests itself as damage is considered to be conceivably low. Nuclear power plants, large-scale chemical facilities and dams are examples. In addition to large-scale industrial risks, various types of natural disaster also fall within this class.

Damocles I

In a fashion similar to the Damocles class, natural disasters with known damage-probability functions entail major damage potentials in conjunction with usually low probabilities of occurrence, as is for instance the case for meteorite impacts.

Damocles I is created by author to separate anthropogenic risks (Damocles class) from natural threats with very high disastrous and destructive potential.

Cyclops

In the Cyclops class, the probability of occurrence is largely uncertain, while the maximum damage is well defined. A number of natural events such as floods, earthquakes and El Niño fall in this class, as does the occurrence of AIDS, wherever there is no or only contradictory information about the probability of occurrence.

Pythia

When in doubt, the ancient Greeks consulted one of their oracles, among which the most famous was the Delphic Oracle with its blind seeress Pythia. However, Pythia's answers always remained unclear: Pythia's prophecies illustrated that a major danger might be impending, but not how large its probability of occurrence, its severity or its distribution might be. Pythia prophesied to King Croesus that if he were to attack Persia he would destroy a great empire. Belligerent Croesus failed to realize that this meant his own empire. The Pythia class thus involves, for definable damage, a high degree of uncertainty as to possible adverse effects and as to the probability of the risk's occurrence. The potential for damage can be stated, but the scale of damage is still unknown. This class includes risks associated with the possibility of sudden non-linear climatic changes, such as the risk of self-reinforcing global warming or the instability of the West Antarctic ice sheet, with far more disastrous consequences than gradual climate change. It further includes far-reaching technological innovations such as certain applications of genetic engineering, for which neither the precise level of risk nor the probability of certain damaging events occurring can be estimated at the present point in time.

Pandora

This class of risk includes such risks that have persistent, ubiquitous and irreversible effects. Persistent organic pollutants (POPs), which remain stable over long periods in the environment, are a typical example of this. Often the effects of these risks are still unknown, or there are at most reasonable grounds to assume their adverse effect.

Cassandra

Many types of damage occur with high probability, but in such a remote future that for the time being no one is willing to perceive the threat. The Cassandra class of risk thus harbors a paradox: both the probability of occurrence and the damage potential are known, but because the damage will only occur after a long period there is little concern in the present. Risks of the Cassandra class are only then of interest if the damage potential and the probability of occurrence are both relatively high. This class is accordingly located in the prohibited area. The distant time horizon between trigger and consequence easily creates the fallacious impression of security. A typical example of such an effect is gradual anthropogenic climate change, which can trigger severe damage in vulnerable areas such as coastal and mountain zones.

Medusa

Some novel phenomena have an effect on modern people in a way similar to that in which the Gorgons, as purely imaginary figures of fable, aroused fear and terror. Some innovations are rejected even if scientists scarcely view them as dangerous. According to the best knowledge of the risk experts, risks of this type are located within the normal area, but, due to certain characteristics of the risk source, is a particular source of dread that leads to massive rejection.

Achelous is created separately by author to present mainly the meteorological risks (floods, droughts, etc.). This class has a very high probability of occurrence and is very frequent in the everyday practice with very large diapason of power. In relation to the other risks these ones are easy to model and to assess expected damages. This class is one of the examples of assessment, planning and mitigation the negative effects and fighting them with different preventive and protective measures.

Table 2. Probability of occurrence and potential losses estimations [6]

Losses measured	**Very low**	**Low**	**Middle**	**High**	**Very High**
in % of the damages	0 ÷ 5%	5 ÷ 20%	20 ÷ 50%	50 ÷ 70%	70 ÷ 100%
as part of the GDP	0.0001 ÷ 0.05%	0.05 ÷ 0.08%	0.08 ÷ 1.5%	1.5 ÷ 5%	5 ÷ 15%
Probability	**Very low**	**Low**	**Middle**	**High**	**Very High**
High frequency expected	up to 5%	up to 20%	up to 50%	up to 70%	up to 90%
Low frequency expected	$10^{-6} \div 10^{-5}$	$10^{-5} \div 5.10^{-4}$	$10^{-4} \div 10^{-3}$	$10^{-3} \div 10^{-2}$	$10^{-2} \div 10^{0}$

These eight classes of risk call for specific strategies and tools and technologies for action (risk, crisis and emergency management). The goal of the specific strategies for the risk classes is to shift these from the prohibited or transitional area into the normal area. The main aim is thus not to reduce risks down to zero, but to a level that permits routine management. Naturally, more than one strategy and more than one tool will be necessary for the classes in the cases. Strategies and tools for action are out of scope of present report and will not be described here.

The "acceptable risk" concept is developed based on the risk classes and their location in the normal, transition and prohibited areas. Expected damages are measured in % of GDP and "acceptable risk" is graphically defined on Fig. 2.

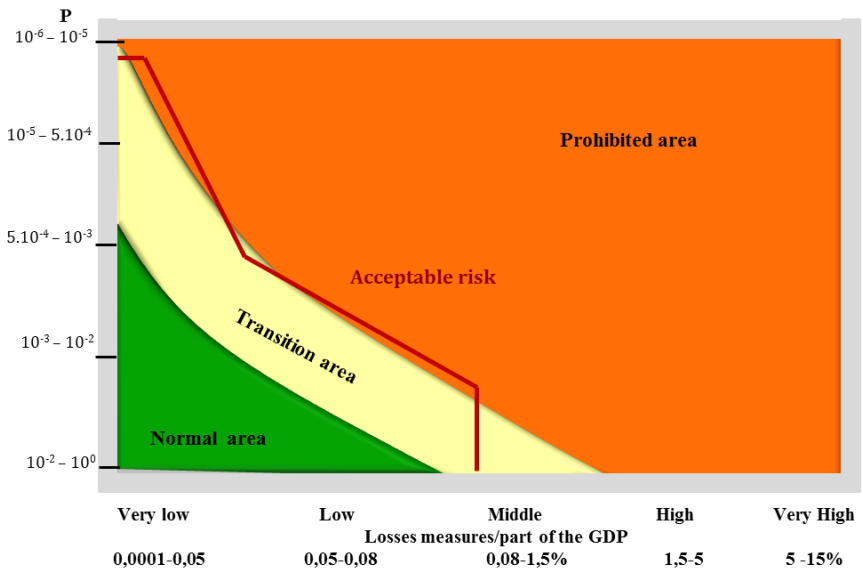

Fig. 2. "Acceptable risk" in % of GDP [6]

According to the UNISDR [7], risk assessment is the core of the risk management process. As shown in the diagram, if the levels of risk are not acceptable, the process of risk management requires different approaches, methods, techniques, tools and strategies to reduce it, depending on the specific characteristics of a particular risk. As stated before, in the prohibited area, the consequences to be expected are so severe that risk reduction is unconditional. In extreme cases, the proper response here is an immediate ban or moratorium.

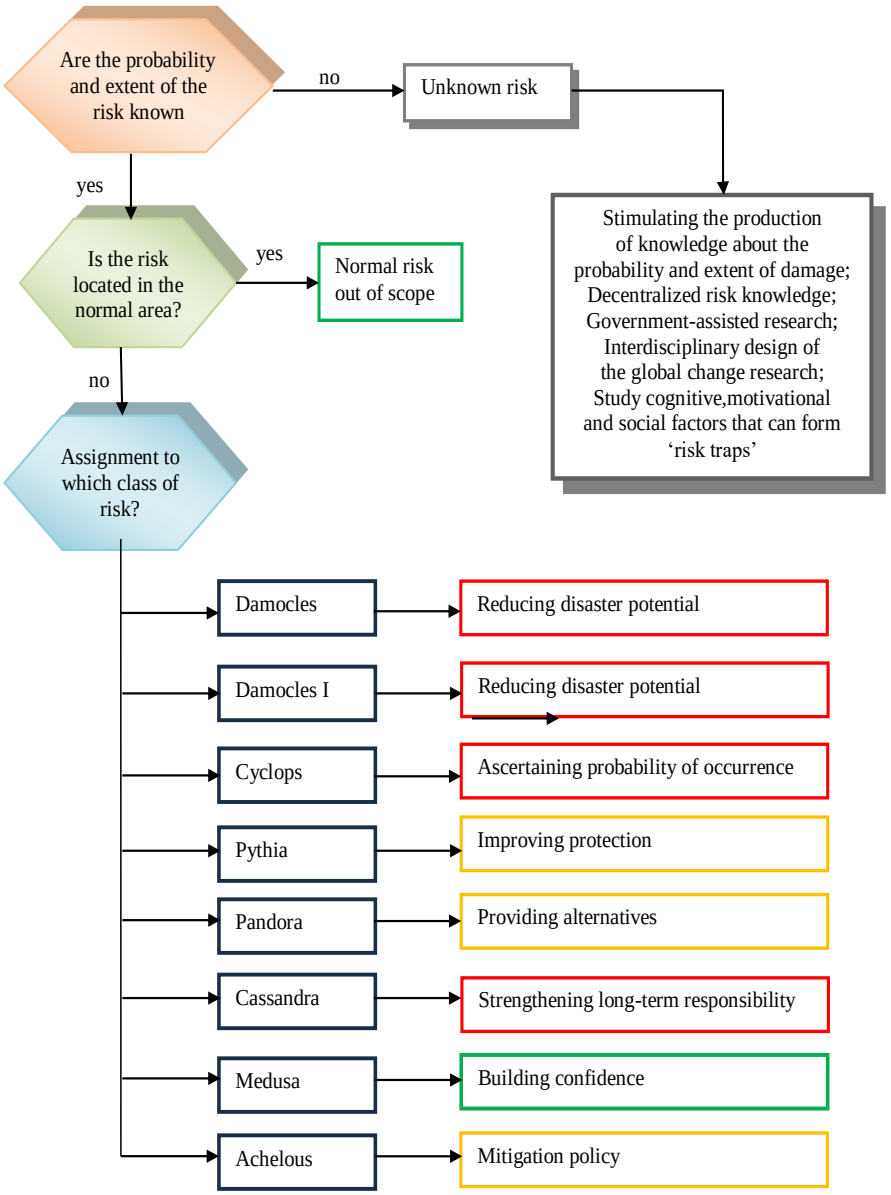

Fig. 3. Decision tree for classifying the risks of global change [3, 6]

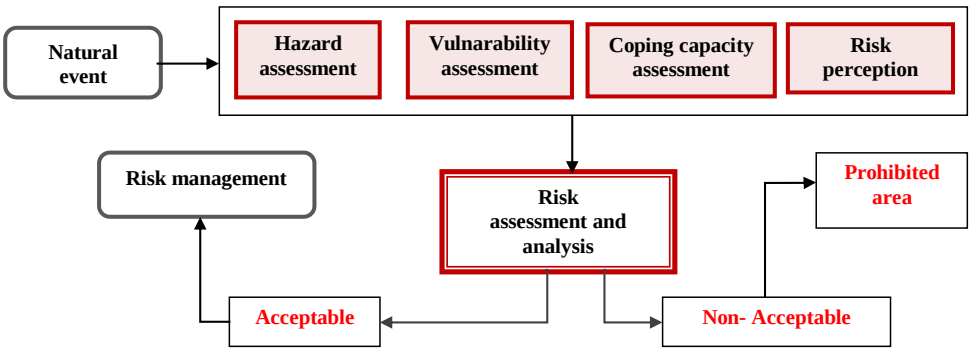

Fig. 4. A Methodological framework for risk assessment [3, 7]

Further Differentiation of Evaluation Criteria According to the German Advisory Council on Global Change

In addition to the two classic components of risk – probability and magnitude – further evaluation elements should be included in risk characterization [1, 4, 5]. These evaluation elements can be derived from risk perception research. They have already been proposed as criteria for risk evaluation procedures in a number of countries (such as Denmark, the Netherlands and Switzerland). The following are particularly important:

Location – Spatial distribution of damage or of damage potential

Persistency – Temporal scope of damage or damage potential

Irreversibility – Non-restorability of the state that prevailed prior to occurrence of damage. In the environmental context, this is primarily a matter of the restorability of processes of dynamic change (such as reforestation or water treatment), not of the individual restoration of an original state (such as preserving an individual tree or extirpating non-native plant and animal species).

Delay effect – The possibility that there is large latency between the cause and its consequential damage. Latency can be of physical (low reaction speed), chemical or biological nature (such as in many forms of cancer or mutagenic changes). It can also result from a long chain of variables (such as cessation of the Gulf Stream due to climatic changes).

Mobilization potential (refusal of acceptance) – The violation of individual, social or cultural interests and values that leads to a corresponding reaction on the part of those affected. Such reactions can include open protest, the withdrawal of trust in decision makers, covert acts of sabotage or other forms of resistance. Psychosomatic consequences can also be included in this category.

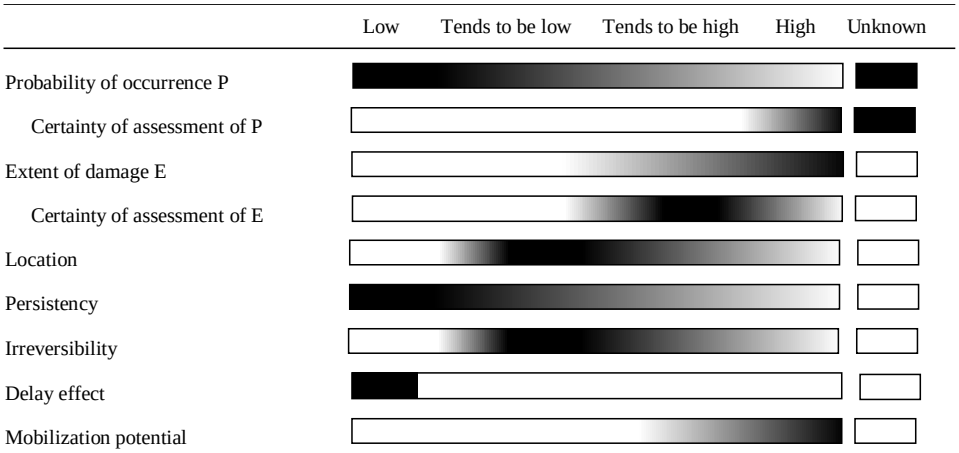

Fig. 5. An example of the application of the hazards evaluation criteria to the risk potential of earthquakes; Cyclops risk class

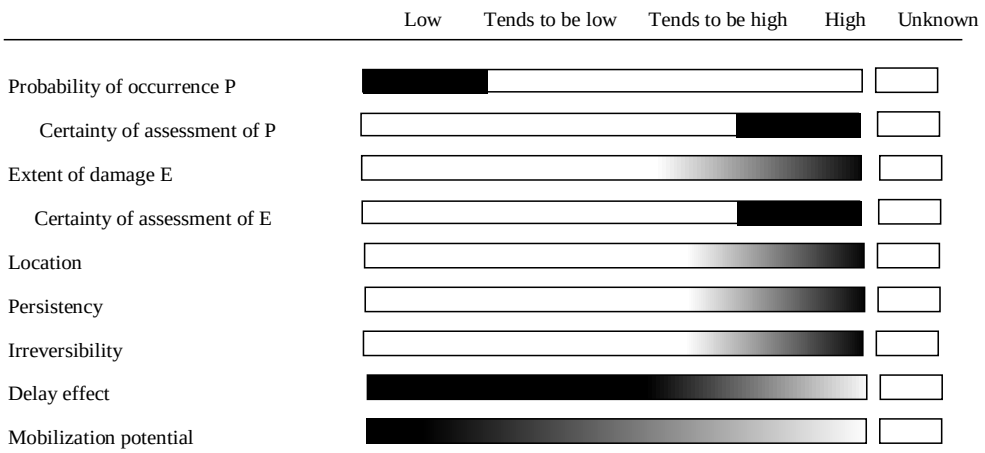

Fig. 6. An example of the application of the hazards evaluation criteria to the risk potential of nuclear energy; Damocles risk class

The properties of the criteria range from "low" to "high". The various meanings of ‘low’ and ‘high’ are briefly explained in the following, according to German Advisory Council for Global Change.

Unknown
Available knowledge does not permit any specific rating in the spectrum from low to high, nor a meaningful statement of confidence intervals (e.g. lies with a probability of 90% between x and y).

Probability of occurrence P
"Low" means "highly improbable" (approaching 0).
"Tends to be low" means "improbable".
"Tends to be high" means "probable".
"High" means "highly probable" (approaching 1).

Certainty of assessment of P or E
"Low" means "poor" certainty of assessment.
"Tends to be low" means "still relatively poor" certainty of assessment.
"Tends to be high" means "relatively good" certainty of assessment.
"High" means "good" certainty of assessment.

L*ocation:*
"Low" means "local".
"Tends to be low" means "regional".
"Tends to be high" means "transboundary".
"High" means "global".

Persistency:
"Low' means "short-term" (<1 year).
"Tends to be low" means "medium-term" (1–15 years).
"Tends to be high" means "long-term" (15–30 years).
"High" means "several generations" (>30 years).

Irreversibility:
"Low" means "restorable".
"Tends to be low" means "largely restorable".
"Tends to be high" means "only partially restorable".
"High" means "irretrievable".

Mobilization potential:
"Low" means "politically not relevant".
"Tends to be low" means "tends not to be politically relevant".
"Tends to be high" means "tends to be politically relevant".
"High" means "politically highly relevant".

Delay effect:
Self-explanatory

Extent of damage E:
Self-explanatory

Applicability of remote sensing technologies to the risk classification

Despite enormous progress in science and technology, most of the natural, environmental and man-made disasters are still unpredictable events.

According to Table 1 satellite systems are applicable mainly in the cases of phenomenon falling in *Achelous* and *Cyclops* risk classes.

Furthermore, according to the Figs. 3, 4 and 5 the usefulness of the satellite observations is highest in hazards evaluation criteria related to risk assessment and management [3, 8].

Conclusion

The performed approach to the WGBU classification shows the effectiveness in case of assessment using percentage of damages and percentage of GDP. The outlined areas – "normal", "transition" and "prohibited" can present the physical meaning of the risks. The areas are not clearly limited, but have dispersion around the different levels of the damages.

The report demonstrates classification with high practical applicability- If calculated risk for given event is "non-acceptable risk", the main goal is to shift it to "normal" area using most appropriate strategies and tools for action.

References

1. California Environmental Protection Agency. Toward the 21st century. Planning for protection of California's environment. Final Report. Sacramento, Ca.: EPA, 1994.
2. Frantzova, A. Remote sensing application in risk assessment and management for natural hazards, Ph.D. thesis, 2007, 170 pp.
3. Frantzova, A. Remote sensing application in risk assessment and management for natural hazards, Dr.Sc. thesis, 2013, 393 pp.
4. Kasperson, R., Renn, O., Slovic, P., Brown, H. S., Emel, J., Goble, R., Kasperson, J. X., and Ratick, S. The social amplification of risk. A conceptual framework. Risk Analysis, 1988, 8, 2, 177–87.
5. Kates, R. W. and Kasperson, J. X. Comparative risk analysis of technological hazards. A Review. Proceedings of the National Academy of Sciences 1983, 80, 7027.
6. German Advisory Council on Global Change (WBGU), World in Transition: Strategies for Managing Global Environmental Risks, Annual Report, Springer-Verlag, 1998, 359 pp.
7. UNISDR, Living with risk. A global review of disaster reduction initiatives. United Nation, Geneva, Switzerland, 2004, 59.
8. Mardirosjan, G. Osnovi na distancionnite aerokosmicheski tehnologii, NBU, 2015. ISBN 9789545358821. (in Bulgarian)

КЛАСИФИКАЦИЯ НА ПРИРОДНИТЕ И ТЕХНОГЕННИ РИСКОВЕ. ПРИЛОЖИМОСТ НА ТЕХНОЛОГИИТЕ ЗА ДИСТАНЦИОННИ ИЗСЛЕДВАНИЯ

А. Францова

Резюме

Настоящият доклад разглежда класификация на различните видове глобални рискове, свързани с промените в околната среда (природни, технологични, биологични и т.н), разработена от Германския консултативен съвет за глобални промени към Федералното Правителството на Германия. Класификацията е базирана на двата основни фактора (вероятност за възникване и потенциални щети) свързани с рисковите процеси и явления, които се развиват и протичат в т.н. „нормална област", „преходна зона" и „забранена област".

Създадената количествена класификационна система е свързана с предварително дефинираните области: „нормална област" (област на ниска вероятност и нисък разрушителен потенциал), „преходна област" на средни по стойност вероятности за случване и очаквани поражения и „забранена област" (област на високите вероятности и високи очаквани поражения.

На база така създадената и подобрена класификация е дефиниран и т.н. „приемлив" риск (ниво на потенциалните загуби, които дадено общество или общност счита за приемливи, като се има предвид съществуващите социални, икономически, политически, културни, технически и екологични условия), базирайки се предимно на експертни оценки.

За така създадената количествена класификационна система са използвани и сателитни данни и информация, съобразени със спецификата на природните опасности и бедствени явления.

Bulgarian Academy of Sciences. Space Research and Technology Institute.
Aerospace Research in Bulgaria. 32, 2020, Sofia

DOI: https://doi.org/10.3897/arb.v32.e03

WATER SURFACE DYNAMIC'S OF THE STUDENA DAM, PERNIK USING SENTINEL 2A AND 2B SATELLITE DATA

Georgi Jelev

Space Research and Technology Institute – Bulgarian Academy of Sciences
e-mail: g_jelev@space.bas.bg

Keywords: *Water Surface, Studena Dam, Sentinel-2*

Abstract

This article presents the results of a study of the dynamics of the surface water area of the Studena dam using satellite images from Sentinel 2A and 2B. The period considered is from the beginning of 2019 to January 2020. The collected 35 cloud-free images from a total of 80 captured are organized in a spatial database in a GIS environment. A water index - MNDWI (Modified Normalized Difference Water) was used to determine the boundary of the water surface. The calculated areas for all images and their trends are analyzed by graph. For about seven months from the maximum annual area (0.91 km^2) in June, a rapid decrease of 0.10 km^2 per month is observed until the beginning of 2020, when the lowest value was measured – 0.23 km^2.

Introduction

The *Studena* Dam is located at the western end of *Vitosha* Mountain. It was built in the period 1953–1955 and was put into operation in 1955 for the purpose of water supply to the town of Pernik and the region. It is located on the Struma River next to the village of *Studena* and is part of the water balance of *Vitosha* Nature Park, [1–3]. It is therefore not allowed to fish and is protected. The area is 145.6 ha (1.456 km^2) [I.1]. During its operation, the amount of water (volume) and contour of the water mirror varied greatly. In the period 1982–1994, it decreased by half, with a decrease below the dead volume recorded in December 1993 to March 1994 [4]. In their study [5], the authors identified periods and conditions of longer drought of the dam, considering the period 2001–2017. Due to the endangering low quantities of water remaining and the growing social problem, the use of remote methods gives us reliable and accurate information about the dynamics of the water surface of the dam.

Study area

The study area is the *Studena* Dam, located at the western end of *Vitosha* Mountain, southwest of *Sofia*, near *Pernik* (Fig. 1). The specific purpose of the study is to track and analyze the dynamics of the water surface of the dam for 2019.

Materials and Methods

Images of European Sentinel-2A and Sentinel-2B satellites [I.2], launched under the Copernicus program, formerly known as GMES (Global Monitoring for Environment and Security), and were used to study the dynamics of the water surface of *Studena* dam. It is the European Earth observation and monitoring capacity building program [I.3].

The data from this pair of satellites is appropriate because of its high temporal resolution – every 5 days. The images are 10 m, 20 m and 60 m in spatial resolution. Each of the satellites is equipped with a multispectral sensor (MSI) with 13 spectral channels in the visible, near infrared (VNIR) and shortwave infrared (SWIR) (Table 1). The available spectral channels are suitable for accurate determination of the water-land boundary [6, 7]. Access to the image databases from the Copernicus Open Access Hub is free [I.2].

Table 1. Sentinel-2 spectral bands and spatial resolutions [I.4]

Band number (ρ)	**Central wavelength (nm)**	**Band width (nm)**	**Spatial resolution (m)**
1	443	20	60
2	490	65	10
3 (GREEN)	**560**	**35**	**10**
4	665	30	10
5	705	15	20
6	740	15	20
7	783	20	20
8	842	115	10
8a	865	20	20
9	945	20	60
10	1380	30	60
11 (SWIR)	**1610**	**90**	**20**
12	2190	180	20

A GIS database was created – a geographic information system for monitoring the *Studena* dam by satellite images.

The use of satellite images gives a true idea of the objects on the Earth's surface and their change over time and is a reliable source of information [6–8]. In this article, they are used to accurately estimate the change in the water surface area

of the *Studena* dam for the last one year. To determine the maximum water surface of the dam, a topographic map K-34-059-1 – Pernik [I.5] and an image from Google Earth, Image © 2020 Maxar Technologies, dated July 30, 2013, were used (Fig. 1) [I.6].

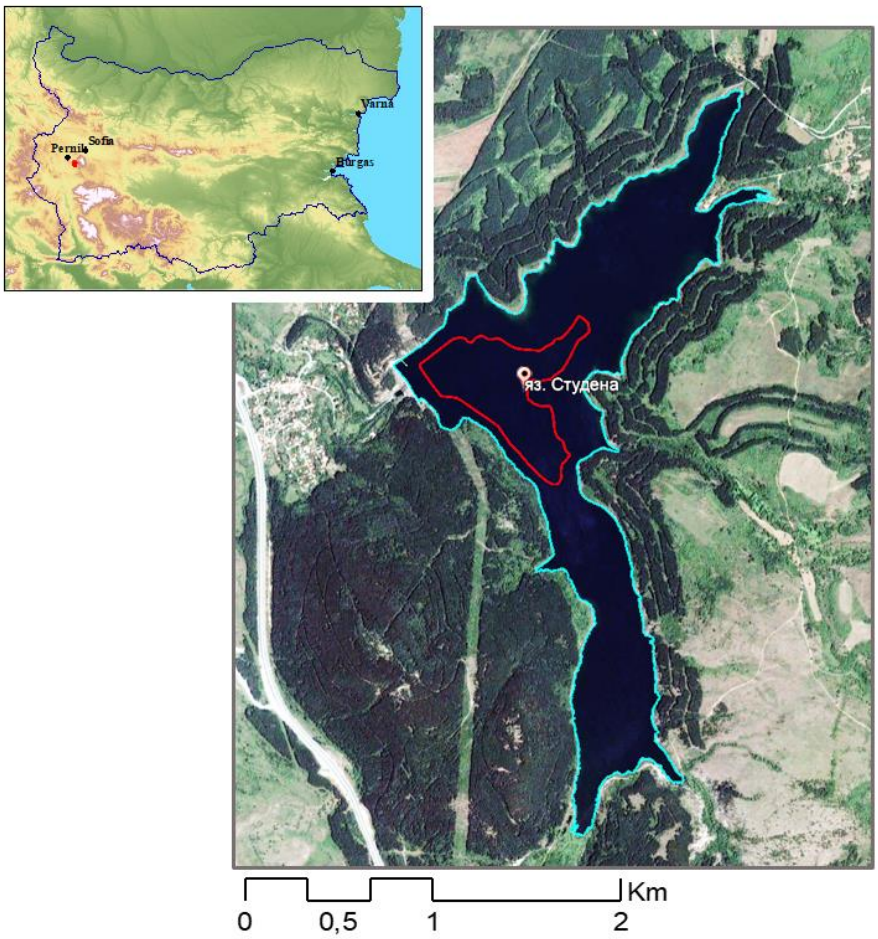

Fig. 1. Maximum (1.43 km^2, 30.07.2013) and minimum (0.23 km^2, 09.01.2020) water surface area of Studena dam [I.5]

Satellite data processing

For more accurate identification of the water surface, the generated water index – MNDWI (Modified Normalized Difference Water) was used, which combines the advantages of maximum absorption in the shortwave spectrum and

maximum reflection in the green spectral channel [9, 10]. The index is calculated by the formula:

1) $$MNDWI = \frac{\rho GREEN - \rho SWIR}{\rho GREEN + \rho SWIR'},$$

Where

$\rho GREEN$ is spectral channel 3 – green (560 nm),
$\rho SWIR$ is a spectral channel 11 – shortwave-infrared (1610 nm).

Geographic information systems (GIS) capabilities have been used to automatically calculate the index and extract the boundary of the water surface of the dam, and a model has been created for this purpose (Fig. 2).

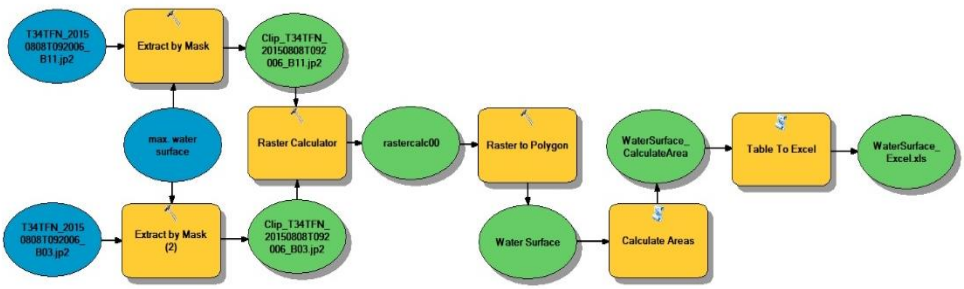

Fig. 2. Model water surface builder

Results and Discussions

The main problem with the satellite images used is the cloud cover masking effect. Only 35 cloudless images over the dam were studied from 80 taken from the Sentinel-2A and Sentinel-2B satellites during the study period (01/01/2019–29/01/2020). The normalized MNWI water index of formula 1) is calculated. On the basis of the obtained index images for each date, the contours of the water surface of the dam were extracted according to the model given in Fig. 2. The water surface areas have been calculated and the tendencies for stepwise decrease of their values and from there the quantities of water are clearly visible (Fig. 3).

The sharp decrease in the trends around the end of June and the beginning of July and the dates 01, 11 and 21 October is noticeable. The individual trends are characterized by a sharp decrease in the area of the water surface. The first decrease is at the end of July and is within 0.09 km^2. The second is with a greater difference of 0.24 km^2 and is observed in the first half of September. After 5–15 November until about 15 December, a steep decline was observed (a decrease of about 0.18 km^2), reaching a value of 0.23 km^2 at the end of the year. At the beginning of

2020 (09.01.2020) the minimum value of the water surface of the *Studena* Dam – 0.23 km^2 – was reported.

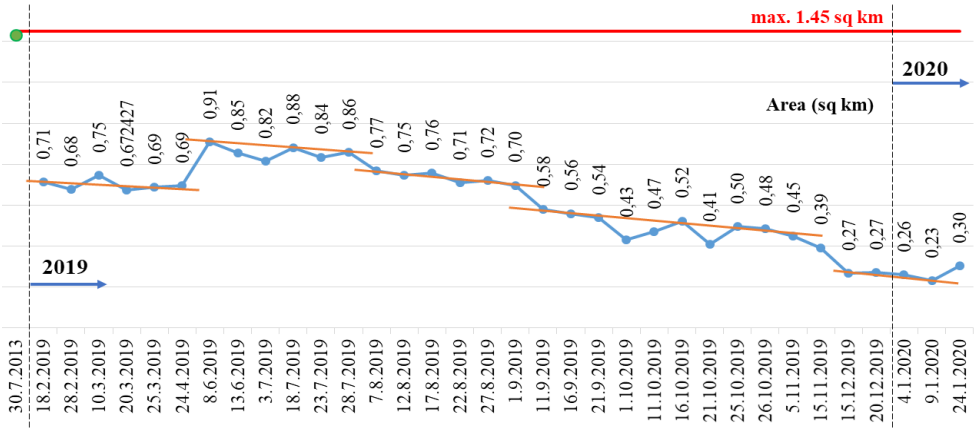

Fig. 3. Dynamics of the water surface area of the Studena dam in the studied period

In Fig. 1. the significant difference between the maximum measured in July 2013 and the minimum value in January 2020 of the water surface area of the dam is clearly visible.

The increase of the water surface at the end of January 2020, after the measures taken earlier, makes a positive impression.

The increase of the water surface area in May 2019 is clearly visible due to more rainfall (all images from May have a dense cloud cover).

Conclusion

In conclusion, the analysis of the satellite imagery data confirms the clear tendency to decrease the water surface area in 2019. There are clear sharp reductions in area and, accordingly, the amount of water around the dates 03 and 23 July, 01, 11 and 21 October, 15 December.

The upward trend at the end of January 2020 gives optimistic hope.

References

1. Bardarska, G. and H. Dobrev, 2003. Vlijanie na zasushavaneto sprjamo kachestvoto na povarhnostnite vodi, v Zasushavaneto v Balgarija: Savremenen analog za klimatichni promeni prirodni, ikonomicheski i socialni izmerenija na zasushavaneto 1982 – 1994 godina, (ed. by I. Raev, C. G. Knight and M. Staneva), 82–94. Publisher: BAS, Sofia, URL: https://www.solvo.bg/wp-content/ uploads/sush.pdf (in Bulgarian)

2. Monev, E., R. Marinov, I. Ilcheva, and A. Yordanova, Development of Control Monitoring for the Purposes of Integrated Water Resource Management of the Vitosha Natural Park, J. of Intern. Sci. Publicat., 2015, 9, 383–93. ISSN 1314-7234.
3. Irena, I., I. Niagolov, S. Balabanova, A. Yordanova, V. Rainova, A. Vatralova, and D. Georgieva. Water Resource Balance for the Vitosha Natural Park, Including Analysis Under Conditions of Climate Change and Extreme Phenomena, International Scientific Conference Proceedings - Sustainable Mountain Regions: Make Them Work, 2015, 246–53. Publisher: Fakel, ISBN 978-954-411-220-2.
4. Rajnova, V., I. Ilcheva, and A. Jordanova, 2017. Obezpechenost na vodosnabdjavaneto za nuzhdite na turizma v predelite na park Vitosha, Science & Technologies, Natural and Mathematical Science, 2017, VII, 3, 86–93. (in Bulgarian)
5. Irena, I., Y., Anna, and V. Rainova. Application of Standardized Status Index for Prolonged Drought Identification and River Basin Management. Socio Brains, 2019, 114–22. ISSN 2367-5721.
6. Mishra, K. and Prasad, P. R. C.. Automatic Extraction of Water Bodies from Landsat Imagery Using Perceptron Model, Journal of Computational Environmental Sciences, 2015, 903465, DOI:10.1155/2015/903465.
7. Jelev, G. and E. Roumenina. Monitoring the Studen kladenets reservoir using air and space images, Aerospace Researchin Bulgaria, 2001, 16, 97–106. SRI-BAS, http://journal.space.bas.bg/arhiv/n%2016/Volume_16.pdf.
8. Jelev, G. and E. Roumenina, Monitoring na Jaz. “Studen kladenec” s izpolzvane na aero i kosmicheski izobrazheniJa, In: Dokladi ot nauchna konferencija s mezhdunarodno uchastie v pamet na prof. d-r Dimitar Jaranov, 2002, 2, 244–54. (in Bulgarian)
9. Casadei1, S., S. Di Francesco, F. Giannone, and A. Pierleoni. Small reservoirs for a sustainable water resources management, Adv. Geosci., 2019, 49, 165–74, DOI:10.5194/adgeo-49-165-2019.
10. Xu, H., 2006. Modification of normalized difference water index (NDWI) to enhance open water features in remotely sensed imagery, Int. J. Remote Sens., 27, 3025–33, DOI:10.1080/01431160600589179.

Internet Sources

I.1. https://bg.wikipedia.org/ - Wikipedia, the free encyclopedia
I.2. https://scihub.copernicus.eu/dhus/#/home - Copernicus Open Access Hub
I.3. https://www.copernicus.eu/bg - Copernicus Home page
I.4. https://earth.esa.int/web/sentinel/technical-guides/sentinel-2-msi/msi-instrument - "Multi Spectral Instrument (MSI) Overview". Sentinel Online. ESA.
I.5. http://web.uni-plovdiv.bg/vedrin/details/K-34-059-1.html - Topographic map archives at 1: 50 000 scale.
I.6. https://www.google.com/maps/ - Google Earth map, Image © 2020 Maxar Technologies

ДИНАМИКА НА ВОДНАТА ПОВЪРХНОСТ НА ЯЗОВИР СТУДЕНА, ГР. ПЕРНИК С ИЗПОЛЗВАНЕ НА ИЗОБРАЖЕНИЯ ОТ SENTINEL 2A и 2B

Г. Желев

Резюме

В тази статия са представени резултати от изследване на динамиката на площта на водната повърхност на язовир „Студена“ с използване на спътникови изображения от Sentinel-2A, -2B. Разгледаният период е от началото на 2019 г. до януари 2020 г. Събраните 24 броя изображения са организирани в пространствена база данни в среда на ГИС. Използван е воден индекс – MNDWI (Modified Normalized Difference Water), с помощта на който е определена границата на водната повърхност. Изчислените площи за всички изображения и техните тенденции са анализирани чрез графика. За около седем месеца от максималната за годината площ през месец юни се вижда бързото намаляване със средно 0.10 km^2 месечно до началото на 2020 г., когато на 09 януари е измерена най-ниската стойност – 0.23 km^2.

Bulgarian Academy of Sciences. Space Research and Technology Institute.
Aerospace Research in Bulgaria. 32, 2020, Sofia

DOI: https://doi.org/10.3897/arb.v32.e04

SPATIAL MODELING OF ARCHAEOLOGICAL LANDSCAPES WITH UAV AND DIGITAL PHOTOGRAMMETRY

Jordan Tzvetkov

Space Research and Technology Institute – Bulgarian Academy of Sciences
e-mail: jordan.tzvetkov@gmail.com

Key worlds: *Archaeology, Landscape, UAV, Modeling, Digital Photogrammetry*

Abstract

The aim of this article is to present the results of spatial (2D and 3D) modeling of selected archaeological landscapes (Kaliakra, Chirakman, Provadia-Solnitsata, Debelt-Deultum, Halka Bunar) which was part of the project "Archaeological map of Bulgaria" during 2017 – 2018. To create these spatial models we used aerial (UAV) photography and digital photogrammetry. The main goal of this research was to prove the potential of UAV deployment of creating low-cost spatial models for archaeological tasks.

Introduction

Since archaeological excavation is a destructive process it's crucial scientific task to accurately document the entire process. One of the most important techniques for documenting is photographing the archaeological sites [1]. But along with ground photography aerial perspective is also very valuable so aerial photography and aerial reconnaissance started to be part of documenting the archaeological landscapes. This lead to develop new scientific branches like aerial archaeology and to distinguish new landscape features (crop marks, soil marks, shadow marks etc.) used to find new archaeological sites [2].

Modern technological development enriches this field with new methods for archaeological research like: satellite images; unmanned aerial vehicles (UAVs) also known as unmanned aircraft systems (UASs) or just drones; airborne laser scanning (LiDAR); digital photogrammetry; geographical information systems (GIS) [3–7]. Some of them are already used in Bulgaria for archaeological purposes [8–10]. Great opportunities to apply these methods are projects for national archaeological mapping existing in many European counties from Romania to Scotland [11, 12]. Bulgaria also has its archaeological map developed by National Archaeological Institute with Museum – NAIM (Bulgarian Academy

of Sciences – BAS) [13]. An important stage of its development was conducted by the project of BAS "Archaeological map of Bulgaria" during 2017 – 2018 [14].

The aim of this study (which also was part of the project "Archaeological map of Bulgaria") is to accomplish aerial photography and to create spatial (2D and 3D) models of five archaeological sites and their landscapes (specified by NAIM) with ground sampling distance (GSD) at 7.00 cm/pixel or higher. These archaeological landscapes are: (1) Kaliakra – antiquity and medieval site (Kavarna Municipality, Dobrich Province); (2) Chirakman – antiquity and medieval site (Kavarna Municipality, Dobrich Province); (3) Provadia-Solnitsata – prehistoric (chalcolithic) site (Provadia Municipality, Varna Province); (4) Debelt-Deultum – antiquity and medieval site (Sredets Municipality, Burgas Province); (5) Halka Bunar – antiquity site (Bratia Daskalovi Municipality, Stara Zagora Province).

Data and Methods

To conduct this research we use a combination of UAV photography and digital photogrammetry also known as UAV photogrammetry [15].

For aerial image acquisition we used UAV DJI Phantom 3 Advanced with RGB camera FC300S (sensor 1/2.3″, width 6.16 mm, height 4.62 mm, diagonal 7.7 mm, 4000 × 3000 pixels, 12 Megapixels) and software DJI Go and DJI Ground Station Pro (for flight mission planning).

Table 1. General specifications of the input data

Archaeological Site	Total Number of Images	Number of Images for 2D/3D Models	GSD (cm/pixel)	GCPs for Orthorectification
Kaliakra	587	435	5	No
Chirakman	514	188	7	No
Provadia-Solnitsata	512	427	6; 2; 3	Yes
Debelt-Deultum	3 624	3 069	6	Yes
Halka Bunar	1 237	968	6	No

For spatial modeling purpose we used 75% frontal overlap and 60% side overlap and regular grid for taking images. For the initial image dataset we provide quality check and removed blur images if they exist. Then we selected the image datasets used for spatial modeling excluding non-nadir images (Table 1). For some archaeological sites NAIM provided coordinates of existing Ground Control Points (GCPs) for high accuracy georeferencing. Some of them used an outdated Bulgarian coordinate system 1970 (Krasovsky 1942 ellipsoid) which we transformed to UTM zone 35N, datum WGS 1984 with BGSTrans v.4.2 coordinate transformation software (freely distributed by Bulgarian Geodesy, Cartography and

Cadastre Agency). Before image acquisition these GCPs were marked on the field. If no GCPs exist for image georeferencing we used the DJI geotagged photos with onboard GNSS/GPS.

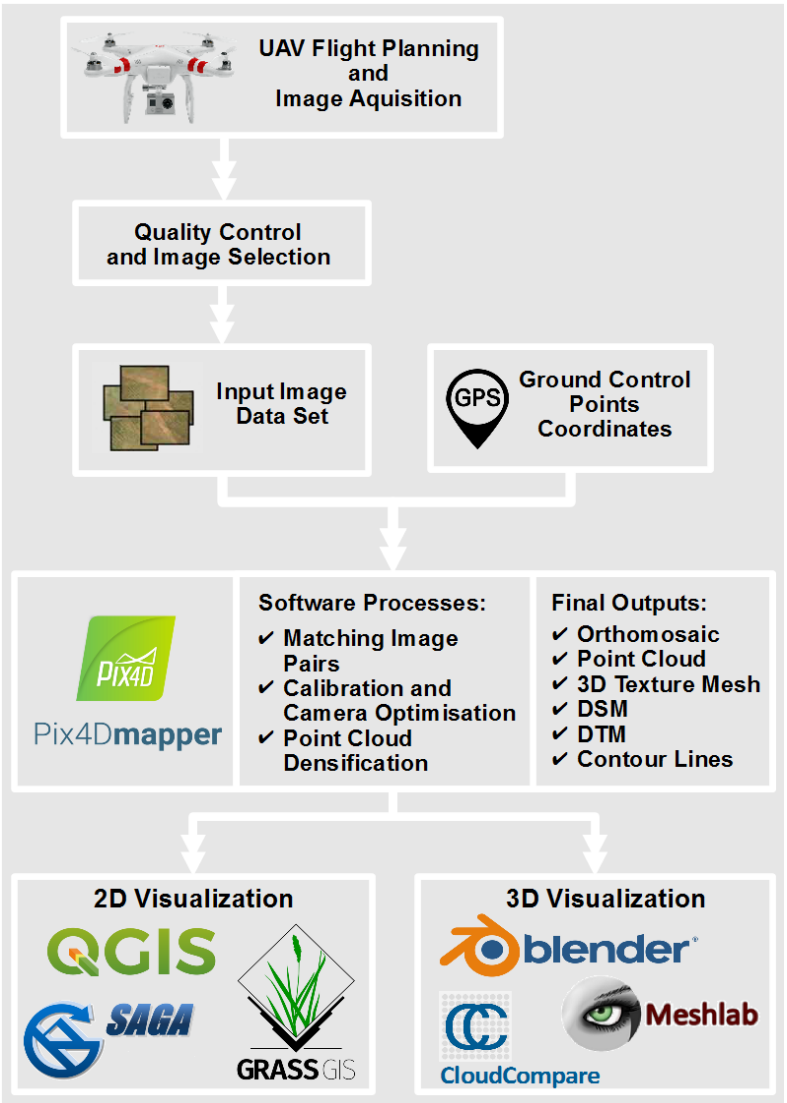

Fig. 1. Workflow of the data processing

The next step of the workflow was data processing. Since our goal was to create 2D and 3D spatial models we used digital photogrammetry and Structure

from Motion (SfM) algorithms [16–18]. For this task from several software opportunities we choose Pix4Dmapper software, because of its high quality in creation dense point clouds [19] and many other advantages including: designed for geospatial application; cloud service (avoiding high hardware system requirements for fast data processing) etc.

The entire workflow of the data processing is shown on Fig. 1. For all input data we apply same software settings to create outputs, including: point cloud, 3D texture mesh, orthophoto mosaic, digital surface model (DSM with resolution 1 × GSD), digital terrain model (DTM with resolution 5 × GSD) and contour lines.

Results

The total area we covered is approximate 10.75 km² (1 075 ha). For visualization of the final output models we used several free and open source software packages like QGIS for 2D and MeshLab for 3D visualization (Fig. 1).

The *Provadia-Solnitsata* archaeological landscape covers 0.78 km² (78 ha). The whole archaeological landscape (*Provadia-Solnitsata* 1) has 6 cm/pixel resolution and two different parts of it which are of special interest have greater resolution – 2 cm (*Provadia-Solnitsata* 2) and 3 cm (*Provadia-Solnitsata* 3) respectively. Georeferencing accuracy of the spatial models with GCPs by Pix4D reports is shown on Table 2. A visualization of the Provadia-Solnitsata mould (*Provadia-Solnitsata* 2) is shown on Fig. 2. *Debelt-Deultum* archaeological landscape is largest and covers 6.35 km² (635 ha). This landscape we divided to five separate parts with 6 cm resolution. Two of them have GCPs (Table 2). A visualization of one of them (*Debelt-Deultum* 5) is shown on Fig. 3. The *Chirakman* archaeological landscape covers 0.47 km² (47 ha). It has 7 cm spatial resolution and visualization is shown on Fig. 4. The Kaliakra archaeological landscape covers 0.82 km² (82 ha). It has 5 cm spatial resolution and visualization is shown on Fig. 5. The *Halka Bunar* archaeological landscape covers 2.33 km² (233 ha). It has 6 cm spatial resolution and visualization is shown on Fig. 6.

Table 2. Georeferencing accuracy of the spatial models with GCPs

Archaeological Landscape Models	Number of GCPs	RMS Error X (m)	RMS Error Y (m)	RMS Error Z (m)	RMS Error Mean (m)
Provadia-Solnitsata 1	13	0.070	0.132	0.445	0.203
Provadia-Solnitsata 2	4	0.007	0.062	0.070	0.045
Debelt-Deultum 3	3	0.323	0.453	8.764	0.484
Debelt-Deultum 5	3	0.069	0.039	0.123	0.068

Fig. 2. Provadia-Solnitsata archaeological site. Top: DSM visualization – multidirectional hillshade with color gradient (QGIS software). Bottom: 3D texture mesh visualization (MeshLab software)

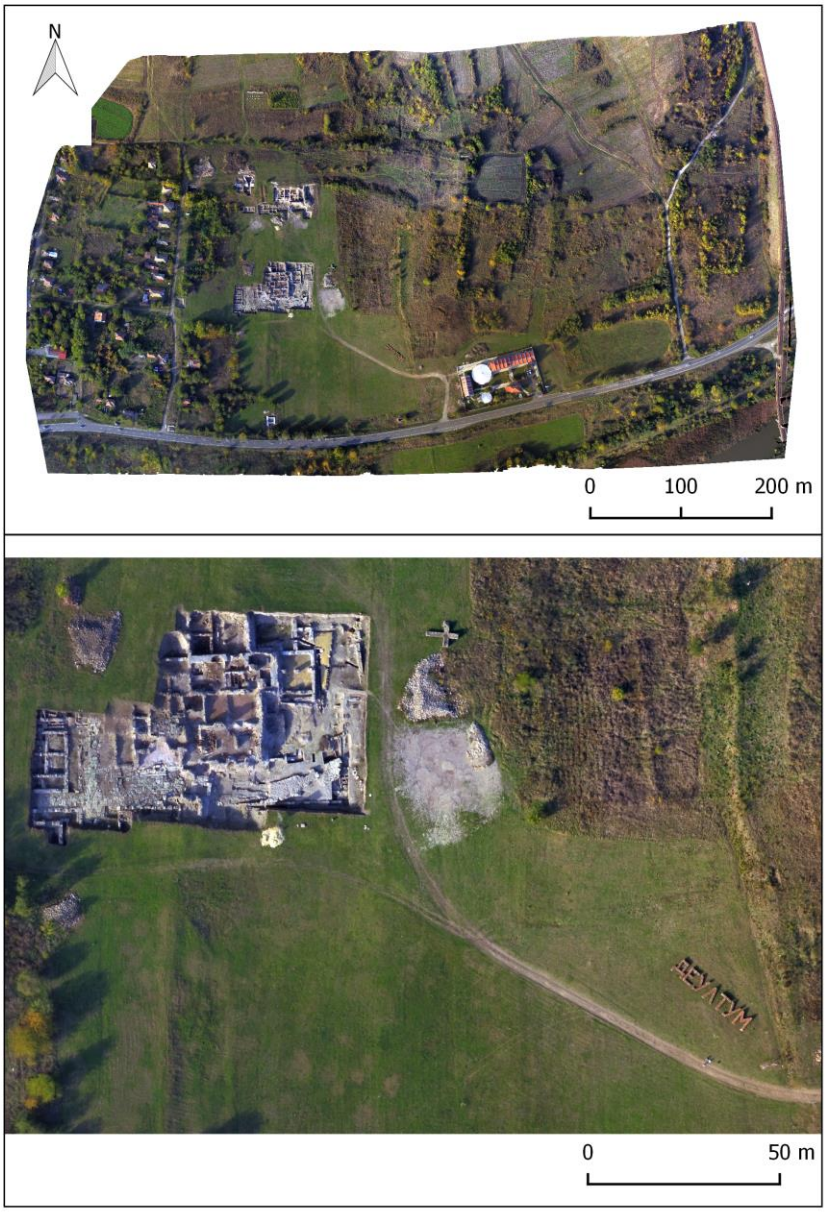

Fig. 3. Debelt-Deultum archaeological landscape. Orthophoto visualization – fragment for the east part at two different scales (QGIS software)

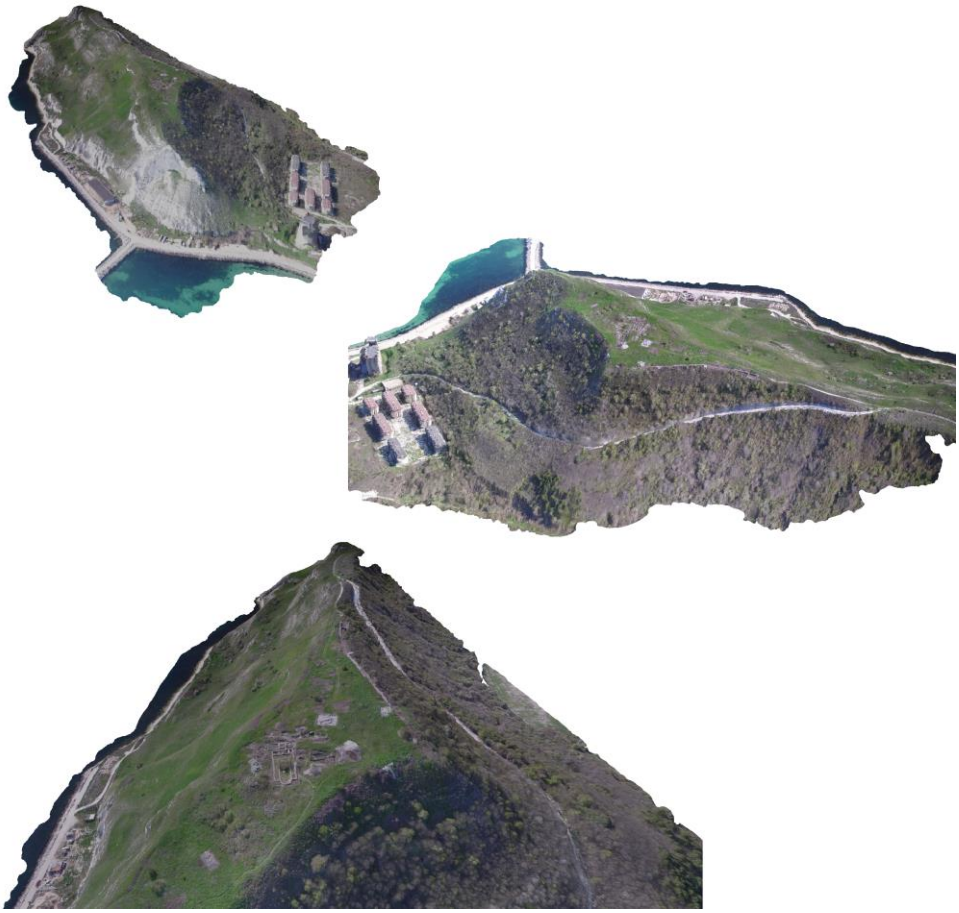

Fig. 4. Chirakman archaeological landscape. 3D texture mesh visualization (MeshLab and CloudCompare software)

Fig. 5. Kaliakra archaeological landscape. Top: Orthophoto visualization – fragment (QGIS software). Bottom: 3D texture mesh visualization (MeshLab software)

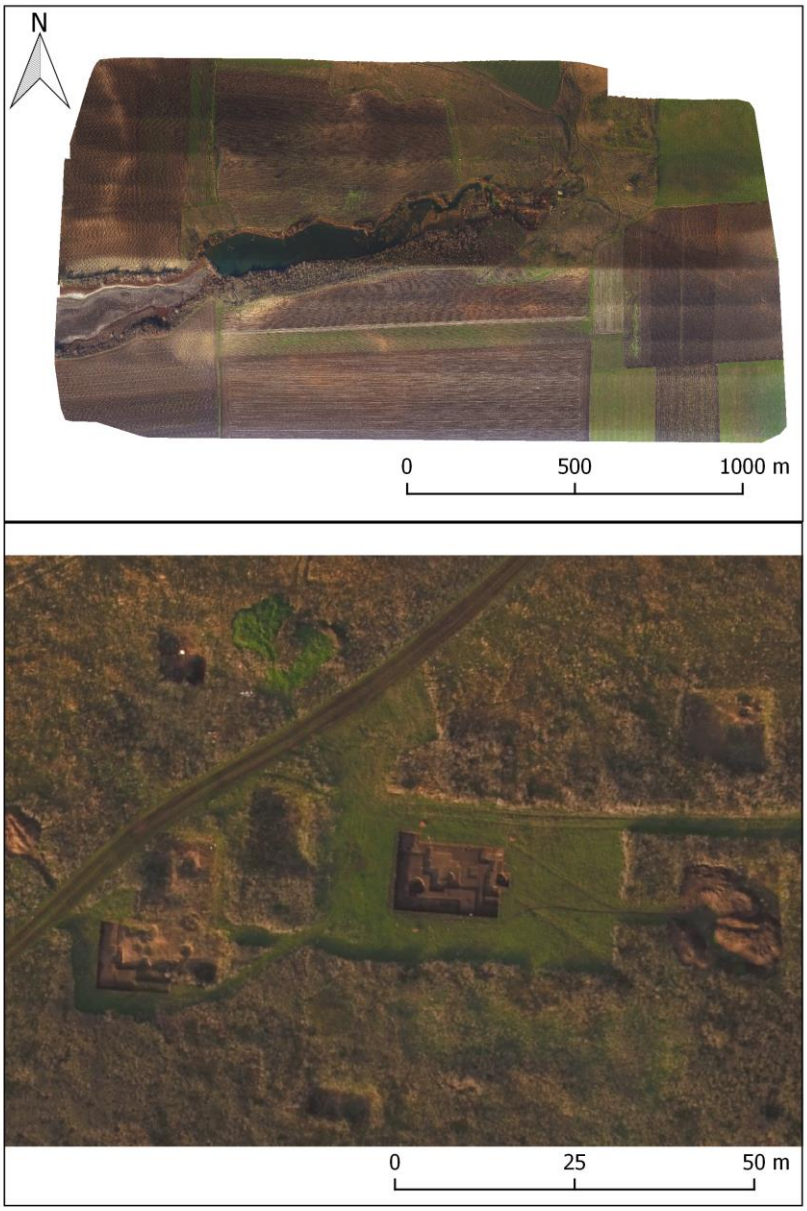

Fig. 6. Halka Bunar archaeological landscape. Orthophoto visualization at two different scales (QGIS software)

Conclusion

The presented above results are part of national level program of archaeological survey. The main goal of UAV deployment was to prove the potential of creating low-cost aerial photography and spatial modeling for archaeological tasks.

Some facilitation of field image acquisition was the lack of specific drone legal regulations in Bulgaria but this may change in near future.

The advantages of UAV deployment include low-cost high resolution photography; easy photography and aerial reconnaissance for terrains with difficult access; simple and fast 2D and 3D spatial modeling; many opportunities for visualization with different purposes: for future field investigations; for archaeology and cultural heritage popularization and preservation etc.

Future UAVs deployment in archaeology should include emphasis upon multispectral aerial reconnaissance for new archaeological site detection. Also an airborne laser scanning for the whole territory of Bulgaria will be of great concern.

Acknowlegments

I would like to express my gratitude to Bulgarian Academy of Sciences for funding this research; to National Archaeological Institute with Museum for creating the Project "Archaeological map of Bulgaria"; to Georgi Nekhrizov and Nadezhda Kecheva from NAIM-BAS; to Dimo Zafirov from Space Research and Technology Institute, Bulgarian Academy of Sciences (SRTI-BAS) for UAV image capturing on the field.

References

1. Dorrell, P. Photography in Archaeology and Conservation (2nd edn). Cambridge, Cambridge Univ. Press, 1994.
2. Musson, C., R. Palmer, S. Campana. Flights into the Past: Aerial Photography, Photo Interpretation and Mapping for Archaeology. Occasional Publ. No. 4 of the Aerial Archaeology Research Group, 2013. http://archiv.ub.uni-heidelberg.de/propylaeumdok/volltexte/2013/2009
3. Parcak, S. Satellite Remote Sensing for Archaeology. London, N. Y., Routledge, 2009.
4. Verhoeven, G. Beyond Conventional Boundaries: New Technologies, Methodologies, and Procedures for the Benefit of Aerial Archaeological Data Acquisition and Analysis. Doctoral Thesis, Ghent University. Zelzate (Belgium), Nautilus Academic Books, 2009. http://hdl.handle.net/1854/LU-631969
5. Lasaponara, R., N. Masini (eds). Satellite Remote Sensing: A New Tool for Archaeology. Springer Science & Business Media, 2012.
6. Corsi, C., B. Slapšak, F. Vermeulen (eds). Good Practice in Archaeological Diagnostics: Non-invasive Survey of Complex Archaeological Sites. Cham, Springer, 2013.

7. Opitz, R., D. Cowley (eds). Interpreting Archaeological Topography: Lasers, 3D Data, Visualisation and Observation. Oxford UK, Oxbow Books, 2013.
8. Stamenov, S. Remote sensing and GIS in Bulgarian archaeology. In: 30th EARSeL Symposium, Remote Sensing for Science, Education, and Natural and Cultural Heritage. UNESCO, Paris, 31 May – 3 June, 2010, 677–82.
9. Prahov, N., H. Angelova, A. Kotsev, et al. Predictive modeling in archaeology: world practice and Bulgarian perspectives. Bulgarian e-Journal of Archaeology, 2011, 1, 1, 71–121 (in Bulgarian). http://be-ja.org/index.php/Be-JA/article/view/48
10. Kunze, R., J. Abele, P. Leshtakov, et al. Archaeometallurgical prospections in the highlands of Medni Rid, southeastern Bulgaria. Preliminary report on fieldwork 2013-2015 with a focus upon remote sensing methods by means of LiDAR. Journal of Archaeological Science: Reports, 2018, 19, 596–617. DOI: 10.1016/j.jasrep.2018.03.021
11. Posluschny, A. (ed.). Sensing the Past: Contributions from the ArcLand Conference on Remote Sensing for Archaeology. Bonn, ArcLand, 2015. DOI:10.11588/ propylaeumdok.00002513
12. Banaszek, Ł., D. Cowley, M. Middleton. Towards national archaeological mapping. Assessing source data and methodology - A case study from Scotland. Geosciences, 2018, 8, 8, 272. DOI:10.3390/geosciences8080272
13. Kecheva, N. Archaeological Map of Bulgaria – Non-Destructive Methods for Field Archaeological Surveying and Applications of GIS. Ph.D. Thesis. Sofia, National Archaeological Institute with Museum, Bulgarian Academy of Sciences, 2018 (in Bulgarian).
14. Nekhrizov, G. Project "Archaeological map of Bulgaria". Bulgarian e-Journal of Archaeology, 2018, 8, 2, 197-212 (in Bulgarian). http://www.be-ja.org/index.php/ Be-JA/article/view/177/160
15. Eisenbeiß H. UAV Photogrammetry. Ph.D. Dissertation, ETH Zurich, ETH No 18515, 2009. URL: http://www.igp-data.ethz.ch/berichte/Blaue_Berichte_PDF/105.pdf
16. Remondino, F., S. Campana (eds). 3D Recording and Modelling in Archaeological and Cultural Heritage. Theory and Best Practices. BAR International Series 2598, 2014.
17. Historic England. Photogrammetric Applications for Cultural Heritage. Guidance for Good Practice. Swindon, Historic England, 2017. https://historicengland.org.uk/ images-books/publications/photogrammetric-applications-for-cultural-heritage/
18. Carrivick, J., M. Smith, D. Quincey. Structure from Motion in Geosciences. Chichester, John Wiley & Sons, 2016.
19. Federman, A., M. Santana Quintero, S. Kretz, et al. UAV photogrammetric workflows: A best practice guideline. The International Archives of the Photogrammetry, Remote Sensing and Spatial Information Sciences, Vol. XLII-2/W5. 26th International CIPA Symposium - Digital Workflows for Heritage Conservation, 28 August - 01 September, 2017, Ottawa, Canada. https://www.int-arch-photogramm-remote-sens-spatial-inf-sci.net/XLII-2-W5/237/2017/isprs-archives-XLII-2-W5-237-2017.pdf

ПРОСТРАНСТВЕНО МОДЕЛИРАНЕ НА АРХЕОЛОГИЧЕСКИ ЛАНДШАФТИ ЧРЕЗ БЛА И ЦИФРОВА ФОТОГРАМЕТРИЯ

Й. Цветков

Резюме

В статията са представени резултатите от въздушното заснемане и пространственото моделиране на избрани археологически ландшафти част от проекта на НАИМ-БАН „Археологическа карта на България" (2017–2018 г.). Въздушното фотографско заснемане е осъществено чрез БЛА (безпилотен летателен апарат) тип DJI Phantom 3, а пространственото моделиране е извършено чрез софтуер за цифрова фотограметрия Pix4Dmapper. Заснетите археологически ландшафти са „Калиакра", „Чиракман", „Провадия-Солницата", „Дебелт-Деултум" и „Халка Бунар" с обща площ 10.75 km². За всеки заснет обект е съставена серия от 2D и 3D модели: облак точки, 3D текстура, ортофото мозайка, цифров модел на повърхността (DSM), цифров модел на терена (DTM) и контурни линии. Резултатите от проучването доказват приложимостта и полезността на БЛА и цифровата фотограметрия като сравнително евтин и бърз метод за документиране и моделиране на археологически ландшафти за целите на археологическите разкопки, теренни проучвания в труднодостъпни местности и за целите на консервацията и популяризирането на културното наследство.

Bulgarian Academy of Sciences. Space Research and Technology Institute.
Aerospace Research in Bulgaria. 32, 2020, Sofia

DOI: https://doi.org/10.3897/arb.v32.e05

TROPHIC STATUS ASSESSMENT OF SMALL TURBID LAKES COMPARING REMOTE SENSING AND *IN SITU* DATA: CASE STUDY AT LOWER DANUBE FLOODPLAIN

Stefan Kazakov[1], Valko Biserkov[1], Luchezar Pehlivanov[1], Stoyan Nedkov[2]

[1]Insistitute of Biodiversity and Ecosystem Research – Bulgarian Academy of Sciences
[2]National Institute of Geophysics, Geodesy and Geography – Bulgarian Academy of Sciences
e-mail: skazakov.iber@gmail.com

Keywords: *Trophic Status, Sentinel 2 MSI, SNAP, Danube Floodplain Lakes, Chlorophyll*

Abstract

The aim of the study was to compare in situ and remote sensing data, in order to assess the applicability of satellite images in water quality monitoring of floodplain lakes. Two indicators of trophic status were compared: chlorophyll a and total suspended matter. Two lakes on Lower Danube floodplain were selected: Srebarna and Malak Preslavets. Data were obtained in july and august 2018. Sentinel 2 MSI L1c images were analyzed in SeNtinel Application Platform (SNAP), (v. 6.0). According to in situ data, Srebarna Lake indicated status of eutrophication, while Malak Preslavets experienced hypertrophic conditions. Satellite data indicated eutrophic conditions for both lakes. Comparing the results from in situ and satellite data, chlorophyll a showed higher correlation (r = 0.66) and comparable results. On the other hand, significantly overestimation of suspended matter according to satellite data were found, as well weaker correlation (r = 0.57) between both methods. Remote sensing i.e. Sentinel products are emerging as a powerful tool in environmental observation. Although weather conditions could have significant impact on environmental dynamic especially in floodplain lakes, combining and comparing of different methods could improve the preciseness of the methodology as well as assessment reliability.

Introduction

Eutrophication defined as nutrient enrichment mainly compounds of nitrogen and phosphorous leading to: increased growth, primary production and biomass of algae; changes in the balance of nutrients causing changes to the balance of organisms; and water quality degradation [1], is global threat to the aquatic ecosystems. The Water Framework Directive [2] requires measures for monitoring, restoration and preservation of eutrophication process enhanced by human activity. Water quality variables as water transparency, chlorophyll a and phosphorous concentration are the most used in the trophic status assessment of inland waters [3]. However, small, shallow, polymictic floodplain lakes are often prone to dynamics of the weather conditions, or a flood process, resulting in strong fluctuation of their

state. Achieving reliable results for the environmental conditions of floodplain lakes requires high-frequency monitoring, which could be expensive. Copernicus program offers freely available data from Sentinel-2 missions. Each satellites carry Multispectral Instrument (MSI) with a wide range of spectral channels, producing images with high spatial resolution (10 ÷ 60m), and a 5-day repeat cycle, providing regular long-term data array. European space agency (ESA) also developed user friendly SeNtinel Application Platform (SNAP) including large set of optical water processors, generating data about optically determined water quality parameters including chlorophyll-*a* and total suspended matter. Recent studies estimated good relationship between *in situ* and Sentinel MSI data along trophic state gradient [4, 5]. Sentinel 2 MSI L1C products are one of the newest and most precise data providers, although atmospheric conditions for example undetected clouds could significantly affect the results accuracy [6].

However, floodplain lakes due to their dynamic hydrology, wind resuspension, nutrient inflow, vegetation development, could experience fast shift in water consistent. Therefore, their optical properties are not limited to the chlorophyll produced by the algae (Case 1 waters), but interfere with higher amount of dissolved organic matter, minerals and sediments in the water, consequently defined as Case 2 waters [7]. The Case 2 Regional Coast Colour (C2RCC) processor developed as multi-mission ocean colour processor is applicable to the most of the produced satellite data, including Sentinel 2 MSI, representing good results for Case 2 waters [8]. Due to complex, inherit optical properties total suspended matter is still very often overestimated water quality parameter [9]. Hereafter *in situ* measurements are essential, considering light penetration especially in turbid lakes [10].

The aim of the study is to actualize the trophic status prerequisite of ecological state assessment of the two Lower Danube floodplain lakes, considering their importance as floodplain wetlands providing wide range of ecosystem services. The study also intend to compare and assess the reliability of the data obtained by remote sensing and *in situ* data in order of trophic state assessment of small turbid lakes.

Materials and methods

Two small and shallow floodplain lakes at Lower Danube were investigated as case study objects – *Malak Preslavets* Lake and *Srebarna* Lake (Fig. 1). *Malak Preslavets* is a former marsh, situated on Danube floodplain at 414 river km. After its embankment in the end of 1970's was transformed into small reservoir raising the water level above 14 m a.s.l., since than flooding by the Danube did not occurred. The maximum measured depth of the lake was over 3 meters with total water surface area of 35 ha. Development of fringing reed belt along the shore (varying between 2 to 5 meters wide) and densely developed canopy of floating vegetation mainly *Nimphea alba*, rooted in the central part of the lake, reduced its open water surface to less than 10 ha. *Srebarna* Lake is also situated on the *Danube* floodplain at

393 river km (Fig. 1). The lake was embanked and isolated from the *Danube* in 1949. Later in 1994 Srebarna was reconnected with *Danube* through inlet channel allowing flooding by the *Danube*, when the water level rises above 12 m a.s.l. at 393 rkm. The maximum depth of the lake varies between 1.8 and 3 meters according to the *Danube* flooding regime and the management of the channel facilities. The lake is characterized with open water area of about 129.66 ha, and several large adjacent pools with total area of 68.86 ha [11]. As the *Srebarna* Lake is more shallow and wider, situated in open flat area, it reflect in e greater extend the changes in the weather conditions, compared to *Malak Preslavets*, situated in a narrow valley surrounded by hills.

Five replicates were sampled from *Srebarna* Lake and three replicates were sampled from *Malak Preslaverts*, resuming totally eight samples (Fig. 2). Field sampling was conducted twice (on 18th of July and replicated on 20th of August 2018), generating overall 16 samples. As shallow polymictic lakes, samples were obtained subsurface from depth of 0.5 m. Water quality parameters such as chlorophyll-*a*; transparency (*Sechhi* depth); total suspended matter; turbidity; water depth and surface water temperature were measured. In order of obtaining necessary sample volume for determining the chlorophyll a and total suspended matter concentration between 0.1 and 0.35 litres of water were filtered, through CHMLAB GF-5 grade glass fiber filters for each method. Chlorophyll-a concentration was spectrophotometrically determined, extracted in 96% ethanol, following ISO 10260:1992. Total suspended matter assessment was performed according EN 872:2006. Turbidity was measured according ISO 7027-1:2016.

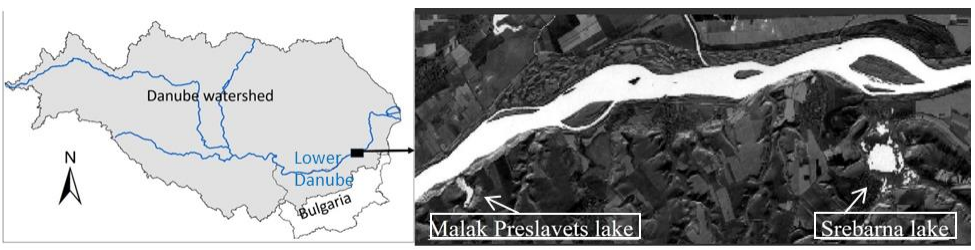

Fig. 1. Case study area: two small, shallow and turbid floodplain lakes - Malak Preslavets and Srebarna

Freely available satellite data were used for assessment of chlorophyll-*a* and total suspended matter (TSM) as indicators of eutrophication process. Sentinel 2 MSI_L1C products from 15 and 17 of July as well as from 19 and 21 of August were selected and downloaded from scihub.copernicus.eu. The mean time differences between *in situ* sampling and Sentinel-2 MSI sensing were approximately 2 days. The content of both chlorophyll a and total suspended matter (TSM) was determined by processing the images in SeNtinel Application Platform – SNAP (v 6.0.5) using

Case-2 Regional Coast Colour (C2RCC) MSI operator, with C2X neural networks recommended for turbid waters. Resampling by 20 m pixel resolution was performed before image processing. Atmospheric correction (AC) was automatically performed in C2RCC processor. *In situ* obtained environmental parameters such as surface water temperature, salinity and altitude were set in C2RCC operator. *In situ* GPS coordinates (Table 1) were used for match-up in pixels selection from Sentinel images, where 3 × 3 pixels were extracted for each sampling station and average values calculated (Fig. 2). *In situ* and satellite data were compared for the two analyzed water quality parameters (chlorophyll-*a* and total suspended matter), based on correlation analysis. T-test comparing two samples for means was used for detecting significant differences in the two sets of data.

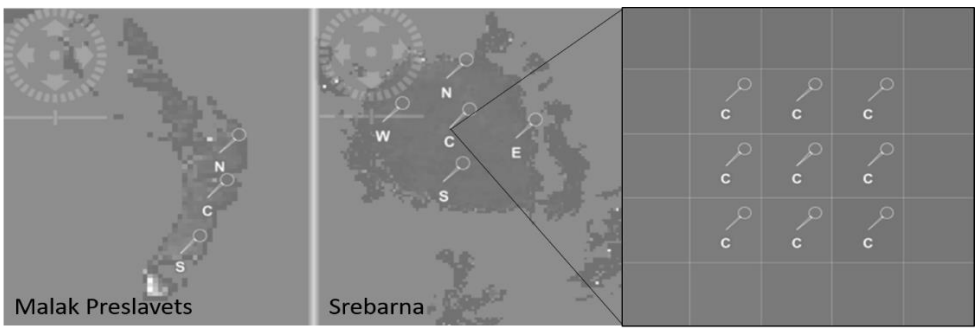

Fig. 2. Images of the Malak Preslavets lake and the Srebarna lake represented in SNAP. Pins indicate the sampling sites. Three sampling sites were selected for the open water area of the Malak Preslavets: N-North, C-Center, S-South (left pane) and five sampling stations were selected for the Srebarna considering its larger open water area: N-North, E-East, S-South, W-west, C-Center (middle pane). Data from 3 × 3 pixels around each station (right pane) were extracted and average values calculated.

Results

Higher average depth was recorded along the studied period in the *Malak Preslavets* – 2.26 (SD ± 0.58) m against 1.82 (SD ± 0.48) m in *Srebarna* lake (Table 1). Surface water temperature in both lakes registered relatively equal values 27.07 (SD ± 0.21) °C for *Malak Preslvets*, against 26.47 (SD ± 0.9) °C for *Srebarna*. Water transparency shows considerably lower values for *Malak Preslavets* 0.47 (SD ± 0.15) m and relatively higher values for *Srebarna* lake 0.89 (SD ±0.12) m. Turbidity was higher in *Malak Preslavets* registering 22.33 (SD ± 9.5) NTU against 6.17 (SD ± 1.46) NTU for *Srebarna* lake. Total suspended matter also registered higher values for *Malak Preslavets* 18.61 (SD ± 7.35) $g.m^3$, against 2.95 (SD ± 1.42) $g.m^3$ for *Srebarna*. Chlorophyll-*a* estimated higher concentration in *Malak Preslavets* 87.95 (SD ± 72.93) $mg.m^3$ and lower concentration in *Srebarna* lake 19.09 (SD ± 11.12) $mg.m^3$.

In seasonal trend average depth of *Srebarna* lake decrease from 1.9 (SD ±0.5) m in July to 1.7 (SD ± 0.5) m in August, while the depth of *Malak Preslavets* remained unchanged. Surface water temperature (at 0.5 m depth) was also more stable in *Malak Preslavets* with 27 ℃ in July and 27.13 ℃ in august, while *Srebarna* lake reported increase from 25.86 ℃ in July to 27.08 ℃ in August. *Malak Preslavets* registered significant increase in chlorophyll a concentration, where 21.88 mg.m^3 was measured in July and 154.00 mg.m^3 in August. Increase in chlorophyll a concentration in *Srebarna* Lake was also observed, registering 9.95 (SD ± 5.45) g.m^3 in July and 28.23 (SD ± 6.03) g.m^3 in August. The increase of other measured variables: turbidity, total suspended matter and transparency also was more expressed in *Malak Preslavets* compared to *Srebarna* lake.

Table 1. In situ measured water parameters: water temperature, depth, total suspended matter, transparency (Sechhi depth), turbidity and chlorophyll-a

		longitude	latitude	pin	sampling date	surface water temperature °C	CHL_a (mg.m^3)	TSM (g.m^3)	turbidity (NTU)	Secchi depth (m)	depth (m)
in situ data	Malak Presavets	26.83847	44.09422	N	18.07.2018	27	10.37	7.8	11	0.7	3.0
		26.83748	44.09187	C	18.07.2018	27	21.72	17.4	16	0.6	2.0
		26.83648	44.09043	S	18.07.2018	27	33.57	13.0	15	0.6	1.8
		26.83847	44.09422	N	20.08.2018	27	161.41	27.3	31	0.3	3.0
		26.83748	44.09187	C	20.08.2018	26.9	145.12	21.5	32	0.4	2.0
		26.83648	44.09043	S	20.08.2018	27.2	155.49	24.8	30	0.4	1.8
	Srebarna	27.07210	44.10745	C	18.07.2018	25.9	3.55	4.2	5	1.0	2.3
		27.07210	44.11105	N	18.07.2018	26.2	14.81	1.3	6	1.1	2.6
		27.06660	44.10764	W	18.07.2018	24.6	4.74	1.4	5	1.0	1.6
		27.07184	44.10349	S	18.07.2018	26.2	14.81	2.0	6	0.9	1.6
		27.07760	44.10709	E	18.07.2018	26.4	11.85	2.4	5	1.0	1.5
		27.07210	44.10745	C	20.08.2018	26.9	29.62	3.1	7	0.9	2.1
		27.07210	44.11105	N	20.08.2018	26.3	17.77	2.0	5	0.9	2.4
		27.06660	44.10764	W	20.08.2018	28	33.57	5.4	9	0.6	1.4
		27.07184	44.10349	S	20.08.2018	27.2	32.58	4.8	8	0.8	1.4
		27.07760	44.10709	E	20.08.2018	27	27.64	2.8	7	0.9	1.3

Results from the satellite data analysis also registered lower concentrations of both chlorophyll-*a* and total suspended matter in the *Srebarna* Lake, compared to higher values in *Malak Preslavets* (Table 2). Seasonal trend confirmed increasing concentrations of the chorophyll-*a* and total suspended matter from July to August (Table 2).

Table 2. Average values of chlorophyll a and total suspended matter retrieved from 9 pixels matched-up to coordinates of sampling sites. Sentinel 2 MSI L1C products processed in SNAP, and C2RCC processor.

		longitude	latitude	pin	sensing date	CHL_a (mg.m^3)	TSM (g.m^3)	CHL_a_unc	TSM_unc
Sentinel 2 MSI C2RCC C2X	Malak Presavets	26.83847	44.09422	N	15.07.2018	37.06	43.9	4.44	2.4
		26.83748	44.09187	C	15.07.2018	28.51	29.2	3.17	4.8
		26.83648	44.09043	S	15.07.2018	67.57	61.5	6.92	4.6
		26.83847	44.09422	N	19.08.2018	54.82	74.1	5.95	1.2
		26.83748	44.09187	C	19.08.2018	66.85	92.9	7.14	1.1
		26.83648	44.09043	S	19.08.2018	67.71	84.7	7.30	1.6
	Srebarna	27.07210	44.10745	C	17.07.2018	34.50	36.1	4.00	5.9
		27.07210	44.11105	N	17.07.2018	57.52	47.1	6.42	8.4
		27.06660	44.10764	W	17.07.2018	24.93	20.6	3.07	4.4
		27.07184	44.10349	S	17.07.2018	32.70	25.7	4.17	6.6
		27.07760	44.10709	E	17.07.2018	37.83	38.8	4.42	6.7
		27.07210	44.10745	C	21.08.2018	38.40	37.2	4.83	4.9
		27.07210	44.11105	N	21.08.2018	53.96	49.2	6.40	5.5
		27.06660	44.10764	W	21.08.2018	40.80	42.5	4.89	6.1
		27.07184	44.10349	S	21.08.2018	45.78	77.6	5.47	4.1
		27.07760	44.10709	E	21.08.2018	35.65	82.5	3.78	3.5

Satellite data reveal significant changes in concentration of chlorophyll and suspended matter in temporal scale (Fig. 3). Detailed information based on 244 pixels for the open area of *Malak Preslavets* and 2 144 pixels for the open water of *Srebarna* Lake outline well pronounced spatial heterogeneity for both lakes (Fig. 3).

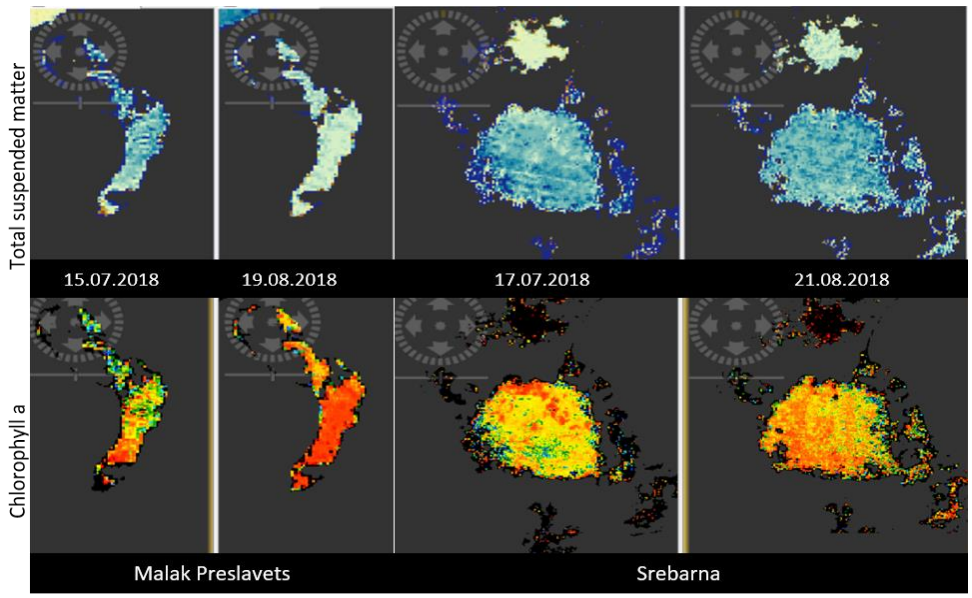

Fig. 3. Sentinel MSI images processed in SNAP representing chlorophyll a and total suspended matter retrieved by C2RCC operator using C2X neural networks. Malak Preslavets register higher concentration for both parameters chlorophyll a and total suspended matter than Srebarna lake. See the image from 19.08.2018 (on the left pane).

Correlation analysis revealed moderate relationship of concentration of total suspended matter between *in-situ* and satellite data (r = 0.57, p = 0.022, n = 16). Stronger relationship was determined for chlorophyll values (r = 0.66, p = 0.005, n = 16) (Fig. 4). However, less than 44% of the dispersion in chlorophyll data was explained comparing in-situ and satellite results, while only 32% of the dispersion was explained for total suspended matter (Fig. 4).

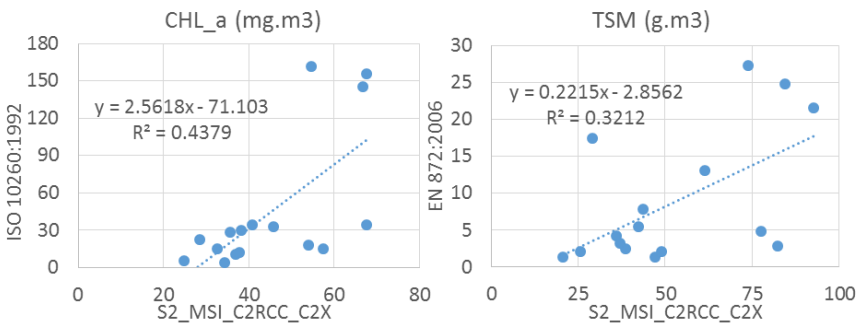

Fig. 4. Correlation between in situ values of chlorophyll a (left) and total suspended matter (right) against Sentinel 2 MSI data retrieved from C2X algorithm in C2RCC processor

Chlorophyll a concentration revealed similar mean values between Sentinel 2 data - 45.28 (SD ±14.22) mg.m^3 and *in situ* data – 44.91 (SD ±55.06) mg.m^3 (Fig. 5). However, *in situ* data set showed significantly higher variation, compared to Sentinel-2 data. Contrary, the total suspended matter revealed clear differences comparing the mean values obtained by the two methods. *In situ* samples registered mean values of 8.82 (SD ±8.98) g.m^3, while the Senitnel-2 C2X data set retrieved almost six folds higher mean values of 52.73 (SD ± 22.98) g.m^3 (Fig. 5).

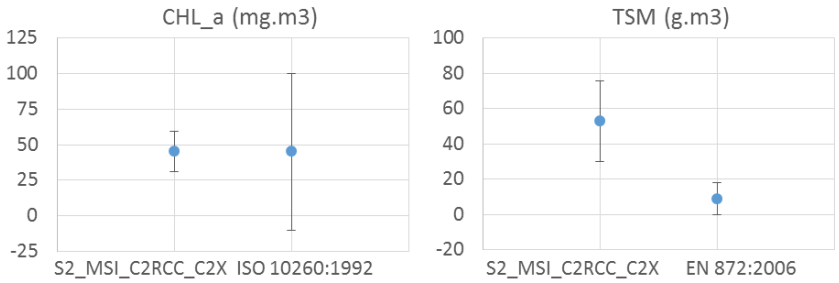

Fig. 5. Comparison between in situ values for chlorophyll a (left) and total suspended matter (right) against Sentinel 2 data based on C2RCC processor and C2X algorithm

T-test Paired Two Sample for Means, comparing chlorophyll-a concentration between both methods did not showed significant differences (t-stat = 0.03, one-tail p value = 0.49, t-Crit. = 1.75, n = 16). Contrary the total suspended matter registered significant differences between the two data sets (t-stat = 9.07, $p < 0.001$, t-Crit. = 2.13, n = 16).

Discussion

In situ data showed high values of chlorophyll-a and low water transparency indicating hypertrophic conditions of *Malak Preslavets*. Due to embankment, the water level of *Malak Preslavets* was significantly raised compared to *Danube* water level and no flood process occurs. The nutrient input from the local watershed is entrapped in the lake causing progressive eutrophication. Eutrophic state was registered in *Srebarna* Lake. The result confirmed last investigations [11, 13], indicating sustainable improvement of the environmental conditions as a result of maintenance of maximum water level and water volume.

Both methods showed pronounced spatial heterogeneity, especially in *Srebarna* Lake considering its larger surface water area. However, the concentration of chlorophyll a obtained by satellite data showed lower trophic state comparing to *in situ* data. The average time differences between the date of field sampling (*in situ* data) and remote sensing date (satellite data) was about 2 days. Taking into account that water parameters can change over a short period due to dynamic weather

conditions (mainly the strength and direction of the wind) reduction in data comparability could occurred.

Comparison of total suspended matter revealed higher values retrieved by satellite data. Concentration of coloured dissolved organic matter could also affect light absorption hereafter the values of measured parameter. Considering the small depth to transparency ratio of 3.22 and its high variability (SD ± 2.09), bottom reflectance also may have an influence on the water-leaving signal in the investigated shallow waters [10]. High density of submerged macrophytes in *Srebarna* [11], together with the large amount of suspended matter also could affect the light attenuation and colour of the water [12]. Hereafter, due to complex optical properties of turbid waters overestimation of total suspended matter is still in concern [9], therefore *in situ* studies have important role in local data verification.

Conclusion

Lake *Srebarna* experienced eutrophic conditions, indicating stabilization of the trophic status compared to previous years. On the other hand, in august 2018 *in situ* data revealed hypertrophic conditions in *Malak Preslavets*. The assessment of chlorophyll-*a* concentration according to both methods (satellite and in situ) showed comparable results. Contrary, six-fold higher concentration of the total suspended matter was determined by the satellite images and the used C2RCC operator, rather *in situ* obtained data. Nevertheless, remote sensing i.e. Sentinel 2 MSI data, emerged as valuable supportive tool for water quality monitoring, considering local validation.

Acknowledgements

The study was funded under "Program for Support of Young Scientists and PhD Students at the Bulgarian Academy of Sciences" (Grant No. DFNP-17-107/28.07.2017). The authors would like to thank to Momchil Petrov – RIEW-Ruse, administration of maintained reserve "Srebarna" and PhD student Galia Georgieva for the support in the field sampling.

References

1. IMAP. 2017. Integrated Monitoring and Assessment Programme of the Mediterranean Sea and Coast and Related Assessment Criteria. UNEP, Athens, 52 p.
2. Directive 2000/60/EC of the European Parliament and of the Council of 23 October 2000 established a framework for Community action in the field of water policy.
3. Carlson, R. E. A trophic state index for lakes. Limnology and Oceanography. 1977, 22, 2, 361–69.
4. Toming, K., T. Kutser, A. Laas, M. Sepp, B. Paavel, and T. Noges. First Experiences in Mapping Lake Water Quality Parameters with Sentinel-2 MSI Imagery. Remote Sensing. 2016, DOI:8.10.3390/rs8080640.

5. Ansper, A. and K. Alikas. Retrieval of Chlorophyll a from Sentinel-2 MSI Data for the European Union Water Framework Directive Reporting Purposes, Remote Sensing, 2018, 11. 64. DOI:10.3390/rs11010064.
6. Coluzzi, R., Imbrenda V., Lanfredi M., and Simoniello, T. A first assessment of the Sentinel-2 Level 1-C cloud mask product to support informed surface analyses, Remote Sensing of Environment, 2018, 217, 426–43, ISSN 0034-4257, DOI:10.1016/j.rse.2018.08.009.
7. Morel, A. Optical modeling of the upper ocean in relation to its biogeneous matter content (Case 1 waters). J. Geophys. Res., 1988, 93(C9), 10749–68.
8. Brockmann, C., R. Doerffer, P. Marco, K. Stelzer, S. Embacher, and A. Ruescas. Evolution of the C2RCC NeuralNetwork For Sentinel 2 and 3 For The Retrieval of Ocean. In Proceedings of the conference held LivingPlanet Symposium, Prague, Czech Republic, 9–13 May 2016.
9. Nechad, B., A-I. Dogliotti, K. Ruddick, and D. Doxaran. Particulate backscatter and suspended matter concentration retrieval from remotely-sensed turbidity in various coastal and riverine turbid waters. Proceedings of the 2016 ESA Living Planet Symposium held in Prague, Czech Republic, 9–13 May 2016, ESA Special Publication SP-740.
10. Luhtala, H. and H. Tolvanen. Optimizing the Use of Secchi Depth as a Proxy for Euphotic Depth in Coastal Waters: An Empirical Study from the Baltic Sea. ISPRS Int. J. Geo-Information, 2013, 2, 1153–68.
11. Biserkov, V., L. Pehlivanov L., Ivanova N., Hinkov G., and Zhelezov G. Updated Management Plan of the Srebarna Managed Reserve. Sofia, 2016, IBER-BAS: 257 p. (in Bulgarian)
12. Harvey, E. T. Bio-optics, satellite remote sensing and Baltic Sea ecosystems: Applications for monitoring and management. PhD thesis, Stockholm University, 2015, 58 p.
13. Kalchev, R., V. P. Vasilev, V. Tzavkova, and M. Beshkova. Water transparency, chlorophyll-a and plankton primary production in the course of Srebarna Lake recovery. In:Uzunov Y et al. eds: Ecosystems of the Biosphere Reserve "Srebarna Lake" 2012, Prof. Marin Drinov Academic Publishing House, Sofia, 57–68.

ОЦЕНКА НА ТРОФИЧЕН СТАТУС НА МАЛКИ МЪТНИ ЕЗЕРА ЧРЕЗ СРАВНЕНИЕ НА НАЗЕМНИ И ДИСТАНЦИОННИ МЕТОДИ НА ИЗСЛЕДВАНЕ: ЧАСТЕН СЛУЧАЙ ОТ ЗАЛИВНАТА ТЕРАСА НА ДОЛЕН ДУНАВ

С. Казаков, В. Бисерков, Л. Пехливанов, С. Недков

Резюме

Целта на проучването е да се оцени трофичното състояние на малки, плитки и мътни езера, сравнявайки *in situ* данни и данни от сателитни изображения. Обекти на изследване са езерата „Малък Преславец“ и „Сребърна“,

разположени заливната тераса на Долен Дунав. За оценка на трофичното състояние са използвани основни параметри за качество на водната среда като хлорофил-а, общо суспендирано вещество, прозрачност и мътност. Два от параметрите: хлорофил-а и общо количество суспендирана материя са използвани за сравнение с данни от сателитни изображения от продукти MSI L1C на сателитите Sentinel, с помощта на SeNtinel Application Platform (SNAP, v. 6.0). *In situ* резултатите индикират еутрофни условия в езерото „Сребърна“, докато в „Малък Преславец“ се регистрират хипертрофни условия. Сравнявайки резултатите от *in situ* и сателитните данни, и двата метода показват умерена корелация ($r = 0.66$) и съпоставими стойности в концентрацията на хлорофил-а. Стойностите на суспендирани вещества показва умерена корелация ($r = 0.57$) между двата метода. По отношение на суспендираните вещества резултатите, получени от сателитните данни, значително надценяват *in situ* резултатите. Продуктите на Sentinel 2 MSI, се очертават като перспективен източник на данни за околната среда, но е препоръчително резултатите от спътниците да се потвърдят от наземни данни.

Bulgarian Academy of Sciences. Space Research and Technology Institute.
Aerospace Research in Bulgaria. 32, 2020, Sofia

DOI: https://doi.org/10.3897/arb.v32.e06

MATHEMATICAL MODEL AND ALGORITHM OF OPERATION OF SYSTEM FOR RELEASE OF LOAD FROM AIRPLANE

Milen Atanasov

Aviation Faculty – "Vasil Levski" National Military University
e-mail: maatanasov@nvu.bg

Keywords: *Aviation Systems, Flight Parameters, Mathematical Model, Aircraft*

Abstract

The development of technology allows the accurate delivery of loads from an aircraft at a precise location using aboard aviation systems. For this purpose, a mathematical model and algorithm for a flight aviation system is proposed, which depending on the flight parameters and the coordinates of the load delivery point, automatically determines the release time.

Study area

The moment of load separation is determined by comparing the angular coordinates μ'_1, φ'_1 at the point (target-T) of delivery and μ'_{1d}, φ'_{1d} at the point of landing of the load (Fig. 1), [5]:

1) $f_\mu=\mu'_1-\mu'_{1d}=0$, $f_\varphi=\varphi'_1-\varphi'_{1d}=0$.

where Ox_Dyz is a distance-to-target coordinate system;

$Ox_1y_1z_1$ – associated coordinate system with the airplane.

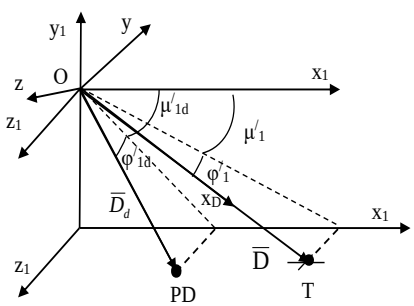

Fig. 1. Determination of angular coordinates in the coordinate system $Ox_1y_1z_1$

The current position of the target is determined by a tracking system. The position of the *Orij* coordinate system associated with the tracking device is determined with respect to the horizontally stabilized O_txyz coordinate system (Fig. 2) with the corners μ and φ.

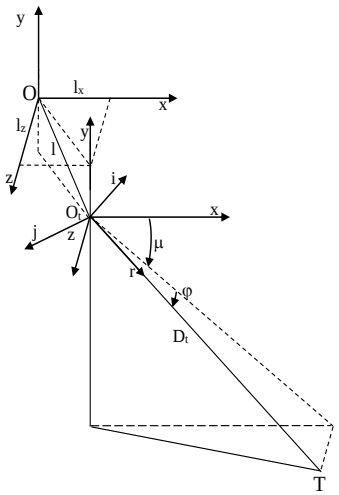

Fig. 2. Determining the position of Orij relative to O_txyz

Provided the target is mobile, the vector equation for determining the moment of release of the load from the airplane is determined by the vector scheme (Fig. 3):

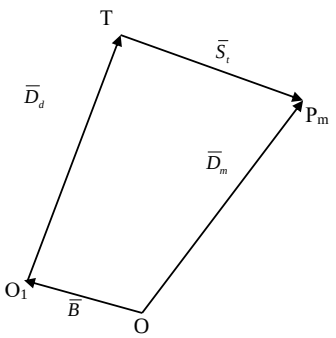

Fig. 3. Vector scheme for determining the moment of load release

2) $\overline{D}_d = \overline{D}_m - \overline{B} - \overline{S}_t$,

where $OO_1 = \overline{B}$ is the vector of the distance between the loading point and the center of gravity of the airplane;

$O_1T = \overline{D}_d$ - the distance vector to the target at the time of release;

$TP_m = \overline{S}_t$ - the vector of the road traveled by the load flight time;

$OP_m = \overline{D}_m$ - the vector of the distance to the point of encountering the load with the target.

The vector equation (2) is represented in scaled in the coordinate system $Ox_1y_1z_1$.

Vector projections $\left(\overline{S}_t\right)_1$ in the system $Ox_1y_1z_1$, are determined using the formula:

3) $$\left(\overline{S}_t\right)_1 = \begin{bmatrix} V_{tx1}T \\ V_{ty1}T \\ V_{tz1}T \end{bmatrix},$$

where T is time of load flight, $\left(\overline{V}_t\right)_1$ is the speed of the target in the system $Ox_1y_1z_1$.

The vector equation for determining the speed of the moving target is derived from Fig. 2 and Fig. 3 [5]:

4) $$\overline{V}_t = \overline{W} + \overline{\omega}_1 x \bar{l} + \frac{\tilde{d}\overline{D}_t}{dt} + \overline{\omega} x \overline{D}_t,$$

where $\bar{l}$ is the distance between the mass center of the aircraft and the center of the tracking device;

$\overline{W}$ - flight velocity vector of the aircraft;

$\overline{\omega}_1$ - vector of the angular velocity of the aircraft;

$\frac{\tilde{d}\overline{D}_t}{dt}$ - relative speed of the target to the tracking device;

$\overline{\omega}$ - vector of the angular velocity of the tracking device;

The projection of the target velocity $\left(\overline{V}_t\right)_1$ in a bound coordinate system $Ox_1y_1z_1$ is determined by the formula:

$$
\begin{aligned}
V_{tx1} &= W_{x1} - W_{rr}\left(\cos\vartheta\cos\mu\cos\varphi + \sin\vartheta\sin\mu\cos\varphi\right) - \\
&\quad - W_{ri}\left(-\cos\vartheta\sin\mu + \sin\vartheta\cos\mu\right) - \\
&\quad - W_{rj}\left(\cos\vartheta\cos\mu\sin\varphi + \sin\vartheta\sin\mu\sin\varphi\right); \\
V_{ty1} &= W_{y1} - W_{rr}\left(-\sin\vartheta\cos\gamma\cos\mu\cos\varphi + \cos\vartheta\cos\gamma\sin\mu\cos\varphi - \sin\gamma\sin\varphi\right) - \\
&\quad - W_{ri}\left(\sin\vartheta\cos\gamma\sin\mu + \cos\vartheta\cos\gamma\cos\mu\right) - \\
&\quad - W_{rj}\left(-\sin\vartheta\cos\gamma\cos\mu\sin\varphi + \cos\vartheta\cos\gamma\sin\mu\sin\varphi + \cos\gamma\cos\varphi\right); \\
V_{tz1} &= W_{z1} - W_{rr}\left(\sin\vartheta\sin\gamma\cos\mu\cos\varphi - \cos\vartheta\sin\gamma\sin\mu\cos\varphi - \cos\gamma\sin\varphi\right) - \\
&\quad - W_{ri}\left(-\sin\vartheta\sin\gamma\sin\mu + \cos\vartheta\cos\gamma\cos\mu\right) - \\
&\quad - W_{rj}\left(\sin\vartheta\sin\gamma\cos\mu\sin\varphi - \cos\vartheta\sin\gamma\sin\mu\sin\varphi + \cos\gamma\cos\varphi\right),
\end{aligned}
\qquad 5)
$$

where relative road speed $\overline{W_r}$ is calculated from formulas:

$$
\begin{aligned}
W_{rr} &= -\omega_{1i} l_j + \omega_{1j} l_i - \dot{D}_t; \\
W_{ri} &= \omega_{1r} l_j - \omega_{1j} l_r - \omega_j D_t; \\
W_{rj} &= -\omega_{1r} l_i + \omega_{1i} l_r + \omega_i D_t.
\end{aligned}
\qquad 6)
$$

Projection of the vector $\overline{D_m}$ in a coordinate system $Ox_1y_1z_1$ is determined by the formula:

$$
\left(\overline{D_m}\right)_1 = \begin{bmatrix} X_t\cos\vartheta - H\sin\vartheta \\ -X_t\sin\vartheta\cos\gamma - H\cos\vartheta\cos\gamma + Z_t\sin\gamma \\ X_t\sin\vartheta\sin\gamma + H\cos\vartheta\sin\gamma + Z_t\cos\gamma \end{bmatrix} \qquad 7)
$$

where X_t and Z_t are coordinates of the point of delivery of the load in the horizontally stabilized coordinate system Oxyz, calculated by the system of differential equations for body movement in space.

The vector $\left(\overline{B}\right)_1$ in a system $Ox_1y_1z_1$ is defined by the formula:

$$
\left(\overline{B}\right)_1 = \begin{bmatrix} B_{x1} \\ B_{y1} \\ B_{z1} \end{bmatrix}, \qquad 8)
$$

Projection of the distance vector is obtained by formulas (2), (3), (7) and (8)

$\left(\overline{D}\right)_1$:

$$\begin{bmatrix} D_{dx1} \\ D_{dy1} \\ D_{dz1} \end{bmatrix} = \begin{bmatrix} X_t \cos\vartheta - H\sin\vartheta \\ -X_t \sin\vartheta\cos\gamma - H\cos\vartheta\cos\gamma + Z_t \sin\gamma \\ X_t \sin\vartheta\sin\gamma + H\cos\vartheta\sin\gamma + Z_t \cos\gamma \end{bmatrix} - \begin{bmatrix} B_{x1} \\ B_{y1} \\ B_{z1} \end{bmatrix} -$$

9)
$$- \begin{bmatrix} W_{x1} - W_{rr}\left(\cos\vartheta\cos\mu\cos\varphi + \sin\vartheta\sin\mu\cos\varphi\right) - W_{ri}\left(-\cos\vartheta\sin\mu + \sin\vartheta\cos\mu\right) - \\ \quad - W_{rj}\left(\cos\vartheta\cos\mu\sin\varphi + \sin\vartheta\sin\mu\sin\varphi\right); \\ W_{y1} - W_{rr}\left(-\sin\vartheta\cos\gamma\cos\mu\cos\varphi + \cos\vartheta\cos\gamma\sin\mu\cos\varphi - \sin\gamma\sin\varphi\right) - \\ \quad - W_{ri}\left(\sin\vartheta\cos\gamma\sin\mu + \cos\vartheta\cos\gamma\cos\mu\right) - \\ \quad - W_{rj}\left(-\sin\vartheta\cos\gamma\cos\mu\sin\varphi + \cos\vartheta\cos\gamma\sin\mu\sin\varphi + \cos\gamma\cos\varphi\right); \\ W_{z1} - W_{rr}\left(\sin\vartheta\sin\gamma\cos\mu\cos\varphi - \cos\vartheta\sin\gamma\sin\mu\cos\varphi - \cos\gamma\sin\varphi\right) - \\ \quad - W_{ri}\left(-\sin\vartheta\sin\gamma\sin\mu + \cos\vartheta\cos\gamma\cos\mu\right) - \\ \quad - W_{rj}\left(\sin\vartheta\sin\gamma\cos\mu\sin\varphi - \cos\vartheta\sin\gamma\sin\mu\sin\varphi + \cos\gamma\cos\varphi\right) \end{bmatrix}.T$$

Angles μ'_{1d}, φ'_{1d} of the point of delivery of the load are determined by formulas (Fig. 1):

10)
$$\mu'_{1d} = arctg\left(\frac{D_{dy1}}{D_{dx1}}\right); \quad \varphi'_{1d} = arctg\left(\frac{D_{dz1}\sin\mu'_{1d}}{D_{dy1}}\right).$$

The structural scheme of the on-board aviation load delivery system (ADS) at a given point is based on the mathematical model (Fig. 4).

The structure of the ADS consists of:

- tracking system;
- a mathematical model for determining the target speed V_t;
- a ballistic model;
- a mathematical model for determining the distance to the point of encountering the load with the target D_t;
- a block for determining the angular coordinates μ'_{1d}, φ'_{1d} of the point of delivery of the load
- at the point of delivery of the load;
- ballistic block;
- block with input parameters;
- A head-up display (HUD);
- Specific Ground Range (SGR).

The algorithm of a flight aviation system operation, automatically defining the moment of separation, has been developed based on mathematical models (Fig. 5).

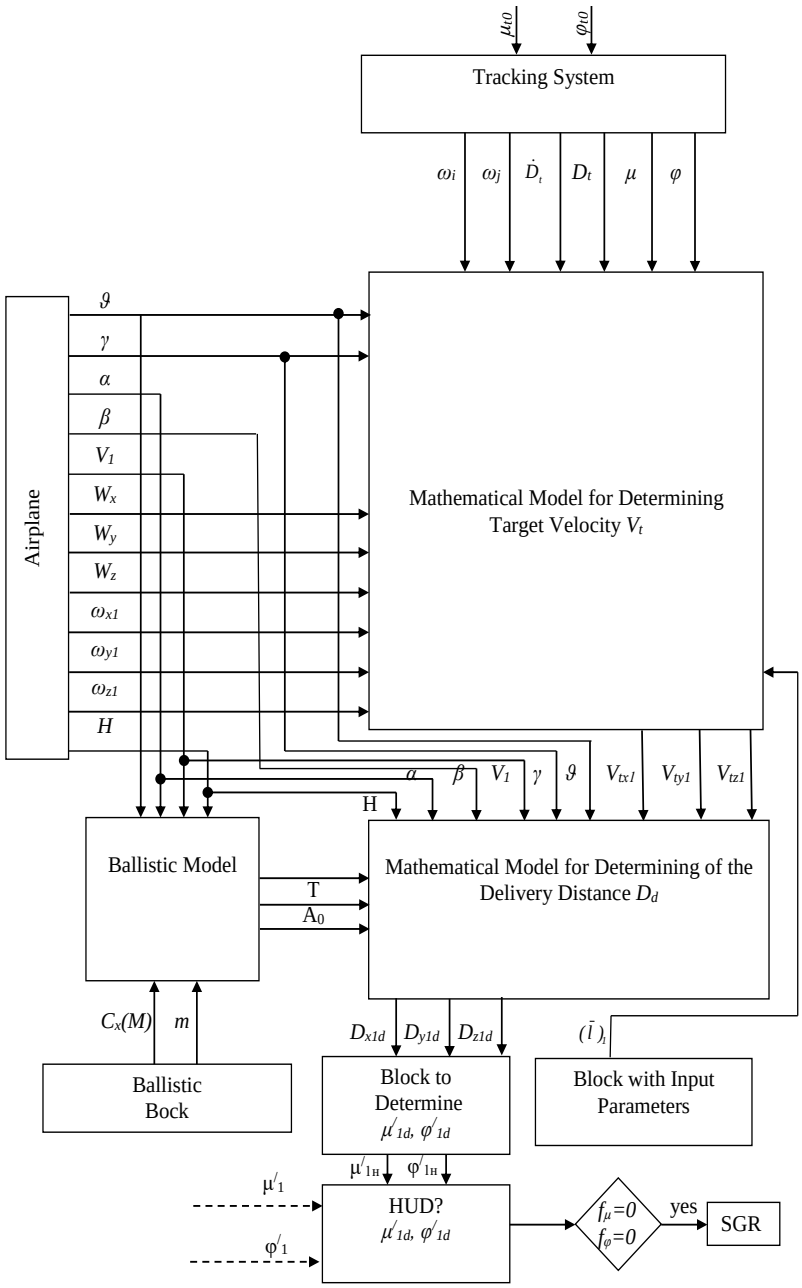

Fig. 4. Structural scheme of on-board aviation load delivery system

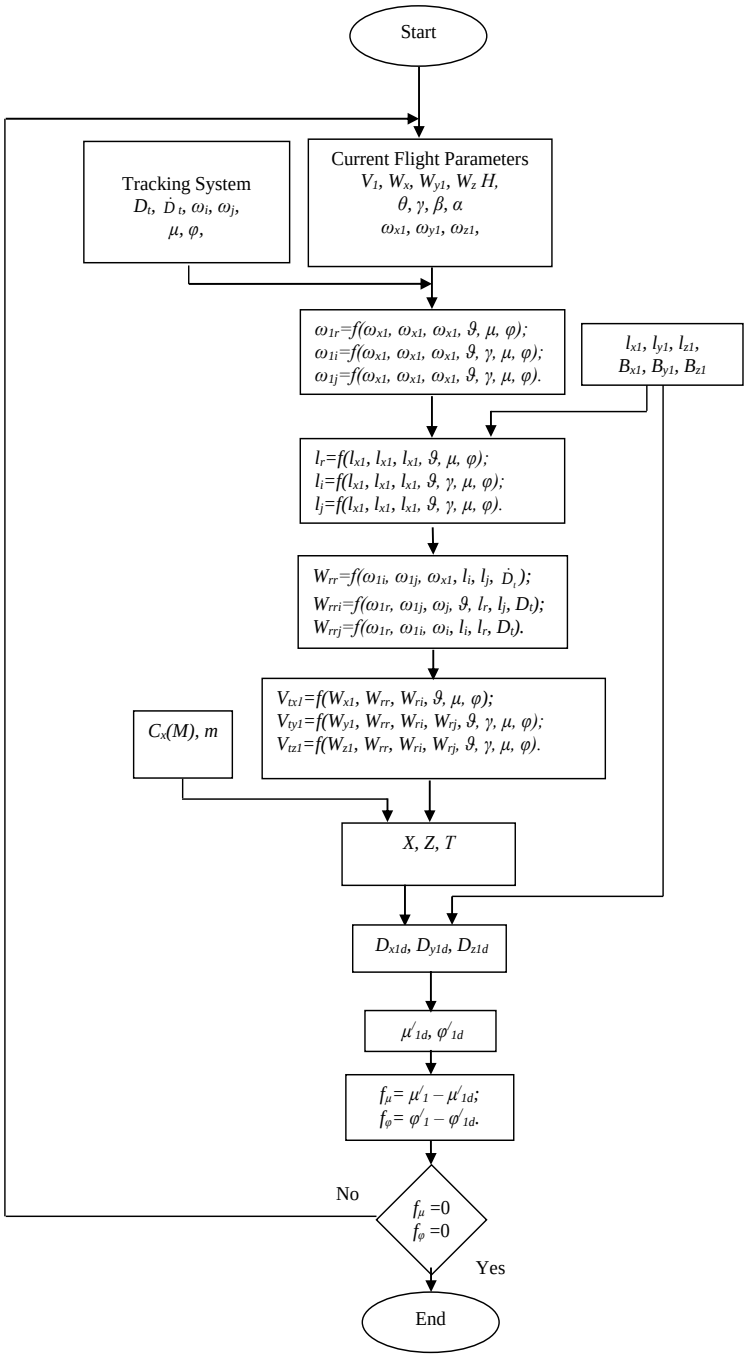

Fig. 5. Workflow algorithm of on-board aviation load delivery system

Using the developed mathematical model and operating algorithm of an aviation board system with a tracking system, the accuracy of load delivery is determined at a point that is mobile.The accuracy in horizontal flight of the load aircraft with the drag coefficient $C_x = 0.466$ [3].

Speed of the target is 60 km/h with course angle $\psi_t = 30^0$.

The test shall be carried out for the following load separation conditions:

- horizontal flight;
- speeds – V = 180; 200; 220; 240; 260 m/s;
- altitudes – H = 600; 900; 1 200; 1 500; 1 800 m.

Load separation error is the sum of a random and systematic error. As a consequence of this it is necessary to take some of its meanings. Considering that in most cases its sign is not of interest, the formula for the estimation of the accuracy of the load separation is used [1, 2, 4]:

11) $$\sqrt{\alpha_{2\Delta x}} = \sqrt{M^2[\Delta x] + D[\Delta x]},$$

where M[Δx] is the mathematical expectation of the error;

- D[Δx] is error dispersion.

The results of the conducted study are shown in Tables 1 and Fig. 6.

Table 1. The accuracy $\sqrt{\alpha_{2\Delta x}}$ of delivery of load at a moving point

λ= 0⁰ – horizontal flight					
$\sqrt{\alpha_{2\Delta x}}$ [m]	***V=180 [m/s]***	***200***	***220***	***240***	***260***
H=600 [m]	20.79	23.40	25.84	28.30	31.22
900	24.91	28.18	31.59	35.00	37.55
1200	29.40	33.10	36.71	40.77	44.32
1500	33.25	37.40	41.77	46.48	51.16
1800	37.35	42.54	46.45	51.69	56.87

As shown in Table 1 and Fig. 6:

- the accuracy $\sqrt{\alpha_{2\Delta x}}$ of delivery of load at a moving point when it is separated from a horizontal flight is in the range from 20.79 m to 56.87 m.

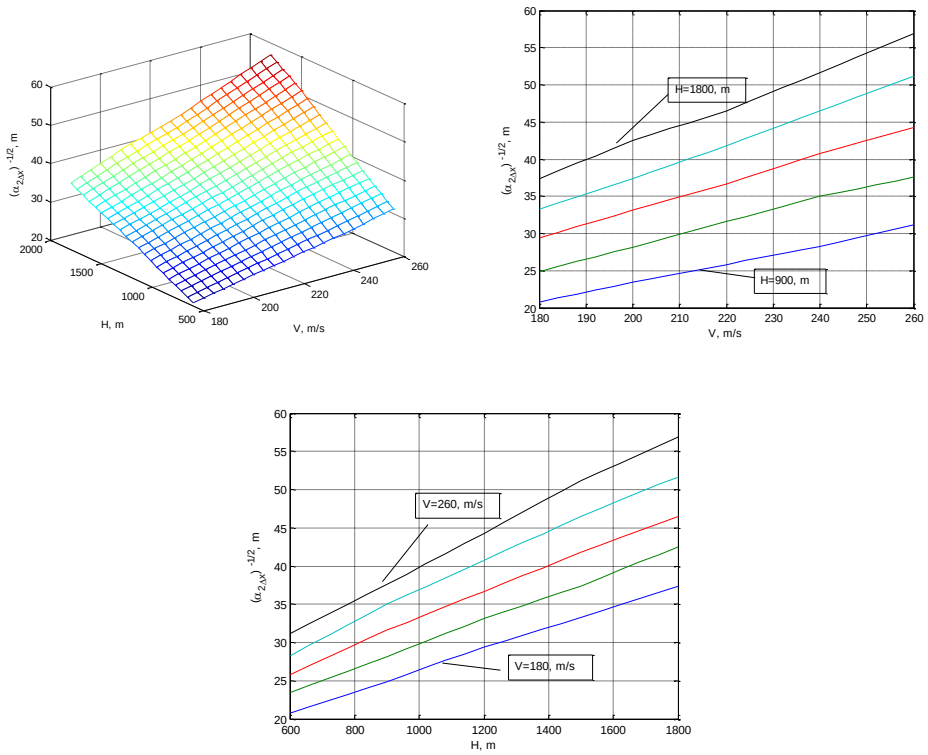

Fig. 6. Dependence of $\sqrt{\alpha_{2\Delta x}}$ *by V and H for delivering a load to a moving point*

The accuracy of load delivery (C_x= 0.466) at a point that is stationary when the load is loaded from a horizontal flight from an aircraft (Table 2 and Fig. 7).

Table 1. The accuracy $\sqrt{\alpha_{2\Delta x}}$ *of delivery of load at a fixed point*

λ= 0⁰ – horizontal flight					
$\sqrt{\alpha_{2\Delta x}}$ ***[m]***	***V=180 [m/s]***	***200***	***220***	***240***	***260***
H=600 [m]	*18.98*	*21.13*	*22.78*	*24.74*	*26.92*
900	*21.81*	*24.00*	*26.75*	*29.49*	*32.18*
1200	*24.65*	*27.62*	*30.37*	*33.41*	*36.21*
1500	*28.00*	*30.49*	*34.28*	*37.69*	*40.99*
1800	*30.48*	*34.37*	*37.50*	*40.92*	*45.93*

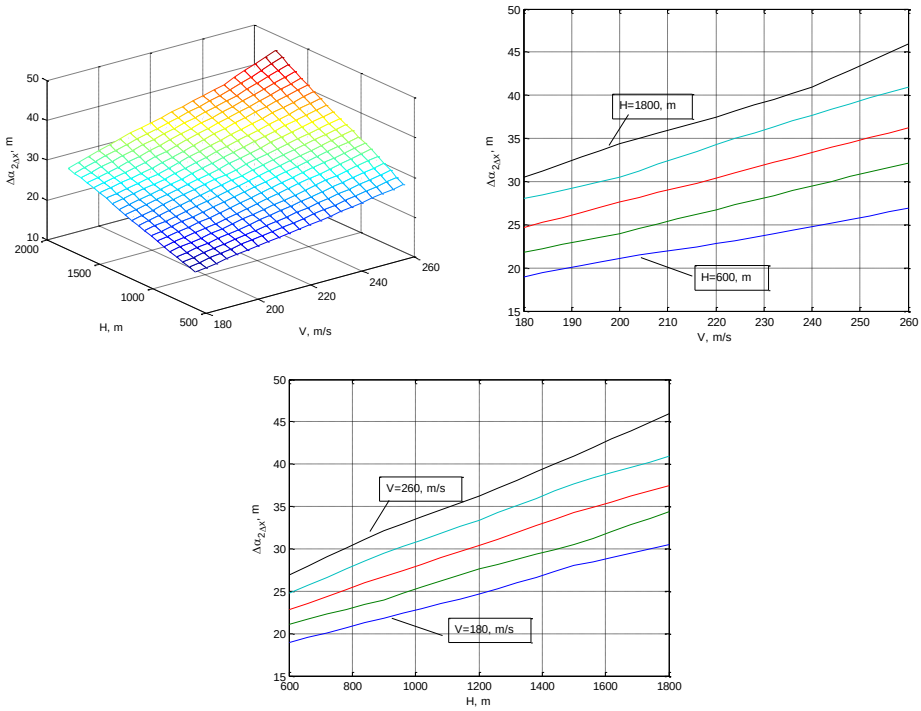

Fig. 7. Dependency of $\sqrt{\alpha_{2\Delta x}}$ *by V and H for delivering a load to a stationary point*

As shown in Table 2 and Fig. 7:

- the accuracy of delivering load $\sqrt{\alpha_{2\Delta x}}$ from a horizontal flight to a fixed point is in the range of 18.98 m to 45.93 m.

Conclusion

The use of a tracking system in aviation flight systems provides commensurate accuracy for delivering load to a mobile and stationary point. This accuracy is approaching that of using freight that can be self-directed.

The developed mathematical apparatus and operating algorithm of aviation aboard system provides the use of fire extinguishing equipment on mobile sea platforms and hard-to-reach terrestrial areas.

References

1. Stojkov, S. O, Stojkov O. S., Izchisljavane na verojatnostnite harakteristiki na tochnostta na bombopuskane s prinuditelno otdeljane na bombata, VI International scientific and technical conference, Engineering, Technologies, Education, Security, Proceedings, Vol. I, Military Science and Security, 27-29, Veliko Tarnovo, 2018, ISSN 2535-0315, 30–32 pp. 2018. (in Bulgarian)
2. Stojkov, O. S., Opredeljane na verojatnostnite harakteristiki na greshkata na bombopuskane, NVU "V. Levski", fakultet "Aviacionen", nauchna konferencija, Vol. 1, D. Mitropolija, 2011, pp. 46–53, ISBN 978-954-713-101-9. (in Bulgarian)
3. Stojkov, S. O., Izchisljavane na koeficienta na chelno s"protivlenie na prakticheska aviacionna bomba, Godishna mezhdunarodna nauchna konferencija na fakultet „Aviacionen" 2018, pp. 287–289, ISBN 978-954-713-114-9. (in Bulgarian)
4. Stojkov, O. S., Formula za opredeljane na verojatnoto otklonenie na popadenieto na bombata za unificiranija metod, 2010, NVU "V. Levski", fakultet "Aviacionen", nauchna konferencija, D. MitropoliJa, pp. 85–86, 978-954-713-094-4. (in Bulgarian)
5. Stojkov, O., Atanasov M., Aviacionni pricelni sistemi – Part 1, VGC, D. Mitropolija, 2009 г., ISBN 978-954-713-093-7. (in Bulgarian)

МАТЕМАТИЧЕСКИ МОДЕЛ И АЛГОРИТЪМ НА РАБОТА НА СИСТЕМА ЗА ОТДЕЛЯНЕ НА ТЯЛО ОТ ЛЕТАТЕЛЕН АПАРАТ

М. Атанасов

Резюме

Развитието на технологиите позволява точното доставяне на товари от летателен апарат на точно определено място с помощта на бордни авиационни системи. За тази цел е предложен математически модел и алгоритъм на работа на бордна авиационна система, която в зависимост от полетните параметри и координатите на точката за доставяне на товара се определя автоматично момента на отделяне.

Bulgarian Academy of Sciences. Space Research and Technology Institute.
Aerospace Research in Bulgaria. 32, 2020, Sofia

DOI: https://doi.org/10.3897/arb.v32.e07

AIRCRAFT NOISE LEVEL CALCULATION DURING TAKE-OFF

Hristina Georgieva

Mechanical Department – Technical University of Sofia
e-mail: hgeorgieva@tu-sofia.bg

Keywords: *Aircraft Trajectory, Departure, Modeling, Aircraft Noise, Calculation, Aperational Parameters*

Abstract

A mathematical model with 4 degree of freedom created in Matlab for aircraft departure trajectory is described in this article. As a reference aircraft a midsize commercial passenger aircraft similar to an Airbus A320 has been chosen. The aircraft is represented by the rigid body and the parameters of model are collected from Airbus and the simulated departure trajectory at the Munich airport is based on a Standard Instrumental Departure. A semi-empirical model of Stone for predicting the jet noise has been used. The proposed model is validated against 10 real flights obtained from aircraft noise and flight track monitoring system at Munich airport. The computed error between the real data and modelling is reported on. Obtained results are presented numerical and graphically. The observed effects of flight operational parameters affecting the aircraft noise emission level during take-off represent subjects of discussions in the paper.

Introduction

The air transport has risen in the recent years due to the steadily growing number of passengers. As aircraft operations continue to grow as the average size at the most congested airports increases, communities have become highly sensitive to aircraft noise and their environmental impact. Aircraft noise is considered to be one of the most significant environmental problem concerns the local communities of modern cities, affecting mostly people living near airports, the passengers on the airport and people worked on the airport. The aircraft noise causes sleep disturbance, general annoyance, children impairment and cardiovascular diseases. Aircrft can be considered as a complex set of noise sources. Especially during the take-off, the engine plays the main role because the thrust level is maximum, which generally causes the highest noise levels on the ground. Due to technological improvements the significant progress has been made in terms of reduction of aircraft noise. But the growing amount of air traffic in Europe shows that an important part of the population is still exposed to problematic noise levels. According to the European Aviation Environmental

Report for 2019 in the European Union (EU), aircraft noise is the third biggest source of noise exposure after road and rail traffic [1]. This is a critical issue that affects the sustainability of commercial aviation.

The aircraft noise depends on many different factors and it's very complex to control it. Significant research is currently being undertaken with the goal of reducing aircraft noise [2]. The theoretical models allow predicting and managing the real object. There are two types of models that are used to predict and analysis the aircraft noise in order to propose technology to reduce the impact of aircraft noise. The theoretical models of the first group are based on empirical data and use specialized software products [3, 4]. This work is focused on the second type of models that use the basic principles of aircraft modelling. They represent the aircraft as a point-mass model including the aerodynamics of the aircraft itself. The differential equations describe the aircraft position in space and allow finding an appropriate relationship between the investigated parameters. They allow the optimization of aircraft trajectories and determination also of noise level from these trajectories. The models that are used in the literature are with 4 to 6 degrees of freedom [5–7]. Khardi propose a 6-degree of freedom model of aircraft [5] simulating the aircraft departure trajectory in order to minimize aircraft noise levels at reception points around airports. The reduction of noise is achieved by changing the engine thrust. At work [6] an efficient trajectory parameterization for optimization of departure flight paths is described. The aircraft model used in the study has 6-degree of freedom and the noise level is decreased by varying the angle of climb and the thrust setting of the engine. Zhang et al. [7] with aid of 6 degree of freedom mathematical model simulated the aircraft departure trajectory describe that a lower climb speed for the initial acceleration and constant speed climb is preferred for a quieter departure. Paolo et al. [8] propose a simple model for predicting aircraft noise in a given reference point and taking into account some specific operational characteristics that have effect on noise impact on the ground. The model of Stone [9] is widely used in the literature to calculate the engine noise. This is a semi-empirical model which predicts the jet engine noise level for single and mixed dual jets up to bypass ratios of 15 as the main source. In general, the model can be applied to subsonic or supersonic flights up to Mach numbers of 2.5. J. E. Bridges et al. [10] an alyse the method and prove its applicability to modern engines with a high bypass ratio.

A mathematical model with 4 degree of freedom created in Matlab is described in the current work. It includes two sections: modelling the aircraft departure trajectory (take-off and climb), and modelling the engine jet noise level. The goal is to provide a simple model for calculating the engine jet noise levels from these trajectories in a given reference point. The model permits to develop an easy way to find flight operational parameters that effect on aircraft noise levels on the airports such as aircraft groundspeed and weight, and the angle of climb.

Methodolody

Data secelction for aircraft trakectory modelling

For the simulation an aircraft similar to the Airbus A320 is chosen, which is widely used for short to medium range flights [11]. The aircraft is equipped by CFM565A engine. This engine develops a maximum thrust force of 112 kN. According to performance training manual of Airbus [12] the aircraft take-off velocity varies as function of the aircraft weight, the airport elevation, the ambient conditions and it is limited by the tire maximum velocity. The take-off is supposed to be performed with CONF1+F flaps/slats configuration. In Tab. 1 is shown the selected parameters: the geometry of the aircraft and its engine, the runway elevation.

Table 1. Aircraft take-off trajectory modelling data

Data from	Parameter	Value	Unit
Aircraft	Wing span, b	35.8	m
	Wing are, S	122.6	m^2
	Wing aspect ratio, A	9.395	-
	Sweeper angle, χ	25	degree
Runway	Runway elevation, h_{runway}	498	m
	Coefficient of rolling resistance, μ	0.03	-
Engine	Thrust, T	112 000	N
	Thrust specific fuel consumption, *tsfc*	9.4444e-005	N/sN

The international airport of Munich is selected as a baseline airport. The airport is located around 30 km away from the Munich city centre. The airport consists of two runways and it is one of the ten busiest airports in Europe. Information about the track data and flight performances is provided by the aircraft noise and flight track monitoring system of the airport [13]. The noise monitoring network consists of 16 stationary measuring stations which are positioned at a radius of 20 km around the airport. Additionally, three mobile measurement stations are also used at places where no stationary measuring station provides information about aircraft noise pollution.

Data secelction for jet engine noise modelling

The engine jet noise model requires input data with respect to geometry and operational conditions of the engine (Table 2). From the Airbus technical data are taken the geometric parameters [11]. The aircraft altitude, aircraft velocity and the engine thrust setting determine the engine operation. According to the engine operation, specific engine thermodynamic parameters have to be generated. To calculate the parameters of ambient condition it has been used the International

Standard Atmosphere (ISA) [15]. The required specific design parameter of the engine for primary and secondary flow such as density, temperature and velocity of the jet a turbofan calculator is used [16].

Table 2. Engine noise modelling data

Data from	Parameter	Value	Units
Engine	Hydraulic diameter of inner contour, D_{19}	1.2	m
	Hydraulic diameter of outer contour, D_9	1.8	m
	Nozzle area of inner contour, A_{19}	Function of D_{19}	m^2
	Nozzle area of outer contour, A_9	Function of D_9	m^2
	Polar angle, α*	45	degree
	Jet velocity in inner contour, v_9	Vary	m/s
	Flow velocity in outer contour, v_{19}	Vary	m/s
	Jet Temperature in inner contour, T_9	Vary	K
	Flow Temperature in outer contour, T_{19}	Vary	K
Ambien condition	Air pressure, p_∞	90 811.7	Pa
	Air Temperature, T_∞	284.913	K
	Air density, ρ_∞	1.167	kg/m^3
	Air speed, c_∞	338.377	m/s
	Mach number, M	Vary	-

The subscripts 9, 19 correspond to the primary and secondary flow parameters.

Modelling of aircraft departure trajectory and jet engine noise

In order to calculate the noise level a mathematical model simulated the aircraft departure trajectory is developed. The aircraft departure trajectory includes two sections: take-off and climb trajectory. Fig.1 shows the aircraft used during the take-off modelling in which R is zero in the air.

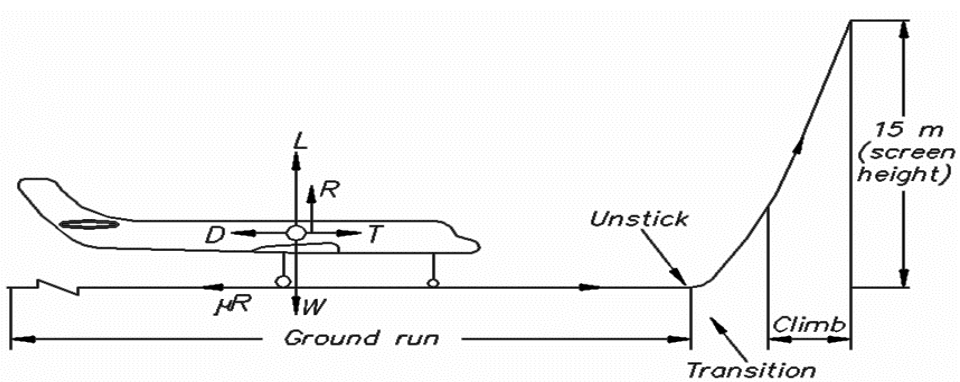

Fig. 1. Aircraft take-off trajectory

Modeling of aircraft departure trajectory

For the present scope the aircraft is modelled as a rigid body with varying mass, aerodynamics, thrust and gravitational forces. Some assumtions are made to simplify the problem:

- all forces acting on the aircraft through its centre of gravity;
- no slideslip;
- small angle of attack;
- no wind present;
- the earth is flat and nonrotating.

Therefore, the equations of motion can be expressed as:

For the take-off configuration in the horizontal plane (1) and in the vertical plane are (2):

1) $$\dot{V} = \frac{T\text{-}D - \mu R}{m}$$

2) $$0 = L\text{-}R\text{-}W$$

For the climb trajectory (3):

3)
$$\dot{x} = V\cos\gamma$$
$$\dot{h} = V\sin\gamma$$
$$\dot{V} = \frac{T\text{-}D}{m} - g\sin\gamma$$
$$\dot{\gamma} = \frac{(T\sin\alpha + L)}{mV} - \frac{g\cos\gamma}{V}$$

where (x, h) are the position of the aircraft, (V, γ) are respectively the velocity and the angle of the climb. The variables (T, $tsfc$, D, R, μR, m and g) are respectively the engine thrust, thrust specific fuel consummation, the drag force, the resultant vertical force with respect to the aircraft weight and wing lift, the rolling friction, the aircraft weight and gravity acceleration. Those variables are expressed as:

$$T=T_0\delta_x\frac{\rho}{\rho_0}\left(1-M+\frac{M^2}{2}\right)$$

4)
$$D=\frac{1}{2}\rho SV^2\left(C_{x0}+k_i C_{Z\alpha}^2\alpha^2\right)$$

$$M=\frac{V}{c}$$

with T_0 the full thrust, δ_x the throttle setting, ρ the density of air at altitude, ρ_0 the density of air at ground, M the Mach number, S the wing span, $C_{Z\alpha}$ the gradient of the lift depends on the high lift device, C_{x0} the drag coefficient for $\alpha = 0$, k_i the induced drag coefficient, c the speed of sound at the altitude h [17].

Modelling of aircraft engine jet noise

The ground noise levels on airports depend of many variables such as meteorological and runway characteristics, topographic conditions in the airport locations, etc. During the take-off phase, one of the main predominated aircraft noise sources is the jet noise. To model the aircraft engine jet noise in ths work is used a semi-empire model of Stone [9]. The model estimates the noise as a function of the exit velocity, pressure and temperature of the engine outflow. The model assumes a symmetric noise emission with respect to the engine reference axis.

5) $$L_{jet}=L_{norm}+\Delta L_{dir/spec}\left(Str_{c\text{-}jet},\alpha_{cor}^{*}\right)+\Delta L_{c\text{-}jet}$$

L_{norm} is a normalized sound pressure level and it is defined according to the atmospheric conditions, the nozzle shape and the operating conditions of the engine:

6)
$$L_{norm}=141.0+10\log10\left[\left(\frac{\rho_\infty}{\rho_{\infty,ISA}}\right)^2\left(\frac{c_\infty}{c_{\infty,ISA}}\right)^2\right]+10\log10\left(\frac{A_9}{d}\right)+$$
$$+75\log10\left(\frac{\overline{v_9}}{c_\infty}\right)-15\log10\left[\left(1+Ma_{con}\cos\left(\alpha^*\right)\right)^2+0.04Ma_{con}^2\right]-$$
$$-10\log10\left[1-Ma\cos\left(\alpha^*\right)\right]+3\log10\left(\frac{2A_9}{\pi\left(D_9\right)^2}+0.5\right)$$

where $\overline{v_9}$ is the effective jet speed defined as function of the jet exhaust velocity and aircraft velocity:

7) $$\overline{v_9} = v_9\left[1-\frac{V}{v_9}\cos\left(\alpha^*\right)\right]^{\frac{2}{3}}$$

ω is the density exponent applying to hot jets as function of the effective jet speed and the ambient speed of sound:

8) $$\omega = \frac{3.0\left(\overline{v_9}/c_\infty\right)^{3.5}}{0.6+\left(\overline{v_9}/c_\infty\right)^{3.5}} - 1$$

Ma_{con} is a convective Mach number and it is defined as function of aircraft velocity, jet exhaust velocity, the ambient speed of sound and the polar angle:

9) $$Ma_{con} = 0.62\frac{v_9 - V\cos\left(\alpha^*\right)}{c_\infty}$$

Str_9 is an effective Strouhal number.

$$Str_9 = f\frac{\sqrt{4A_9/\pi}}{\overline{v_9}}\left(\frac{D_9}{\sqrt{4A_9/\pi}}\right)^{0.4}\left(\frac{T_{t,9}}{T_{t,\infty}}\right)^{0.4\left[\left(1+\cos\left(\alpha^*_{cor}\right)\right)\right]}\left(1-Ma\cos\left(\alpha^*\right)\right)$$

10) $$\left[\frac{\left(1+0.62\left(\frac{v_9-v_\infty}{c_\infty}\right)\cos\left(\alpha^*\right)\right)^2+0.01538\left(\frac{v_9-v_\infty}{c_\infty}\right)^2}{\left(1+0.62\left(\frac{v_9}{c_\infty}\right)\cos\left(\alpha^*\right)\right)^2+0.01538\left(\frac{v_9}{c_\infty}\right)^2}\right]^{0.5}$$

with α^*_{cor} is a corrected directivity angle. It is defined as:

11) $$Ma_{con} = 0.62\frac{v_9 - V\cos\left(\alpha^*\right)}{c_\infty}$$

12) $$\alpha^*_{cor} = \alpha^*\left(v_9/c_\infty\right)^{0.1}$$

$\Delta L_{c\text{-}jet}$ is defined as

13) $$\Delta L_{c\text{-jet}} = 5\log 10\left(\frac{T_{t,9}}{T_{t,19}}\right) + 10\log 10\left[\left(1-\frac{v_{19}}{v_9}\right)^{m} + 1.2\left(\frac{1+\left(\frac{A_{19}}{A_9}\frac{v_{19}^2}{v_9^2}\right)^4}{\left(1+\frac{A_{19}}{A_9}\right)^3}\right)\right]$$

where the exponent *m* is defined as a function of the area ratio:

14) $$m = \begin{cases} 1.1\sqrt{A_{19}/A_9} & \text{for} \quad A_{19}/A_9 < 29.7 \\ 6.0 & \text{for} \quad A_{19}/A_9 > 29.7 \end{cases}$$

Results and discussion

To study the affect of the flight operational parameters on the jet noise levels, it was simulated different aircraft trajectories based on the Airbus A320 at Munich airport (Fig. 2). The parameters used in the simulations are listed in Table 1 and 2. The simulated departure trajectory was based on a Standart Instrumental Departure [14] and the calculation of the jet engine noise levels was made for 2 points from that trajectory – during the take-off and during the climb. The results regarding the noise levels were compared with the experimental data published by the aircraft noise and flight track monitoring system at Munich airport [13]. There are presented in Table 3 and 4.

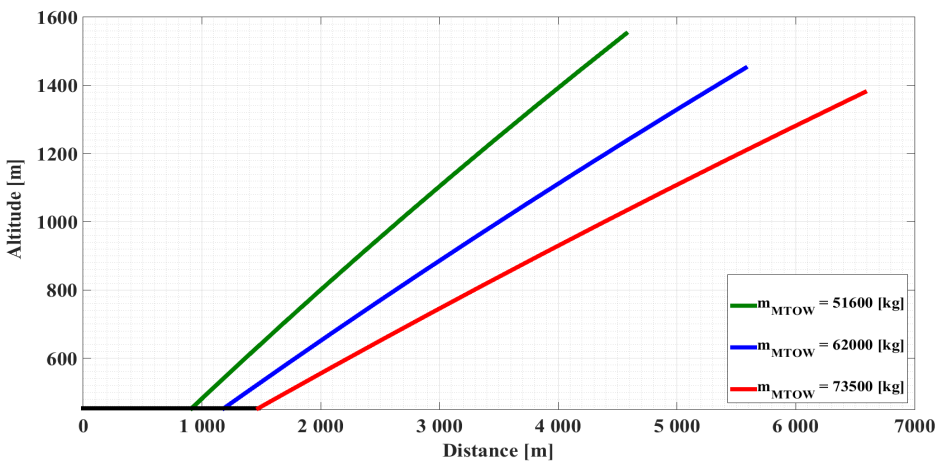

Fig. 2. Aircraft departure trajectory

Table 3. Obtained numerical value from aircraft trajectory

Parameter	Value			Unit
Weight	51 600	62 000	73 500	kg
V_{LOF}	55	65	75	m/s
Time of take-off	31	33	35	s
Take-off ground run distance	913	1 184	1 474	m
V_{CLIMB}	90	100	110	m/s
Climb altitude, h_{CLIMB}	1 552	1 451	1 380	m
Time of climb, t_{CLIMB}	65	65	65	s
Angle of climb, γ	15.36	11.82	9.52	degree

Table 4. Obtained numerical value from the jet engine model

Parameter	Value			Unit
Weight	51 600	62 000	73 500	kg
Noise level on the runway	63	68	72	dB
Noise level on the altitude	70	73	75	dB

According to the model:

- on the runway, at minimum take-off weight m_{MTOW} = 51 600 kg and aircraft groundspeed V_{LOF} = 55 m/s, the obtained level of jet engine noise is 63 dB;
- on the runway, at nominal take-off weight m_{MTOW} = 62 000 kg and aircraft groundspeed V_{LOF} = 65 m/s, the noise level from the jet engine increases up to 68 dB;
- on the runway, at maximum take-off weight m_{MTOW} = 73 500 kg and aircraft groundspeed V_{LOF} = 75 m/s, the noise level from the jet engine continues to increase up to 72 dB;
- on the initial climb with velocity V_{CLIMB} = 90 m/s and minimum aircraft weight m_{MTOW} = 51 600 kg, the noise level from the jet engine is 70 dB;
- on the initial climb with velocity V_{CLIMB} = 100 m/s and nominal aircraft weight m_{MTOW} = 62 000 kg, the noise level from the jet engine increase up to 73 dB;
- on the initial climb with velocity V_{CLIMB} = 110 m/s and maximum aircraft weight m_{MTOW} = 73 500 kg, the noise level from the jet engine continues to increase up to 75 dB.

The results of this work show that the engine jet noise levels are most affected by the actual take-off weight and the groundspeed reached by aircraft during the take-off and the inicial climb phase (Table 3 and 4). It can be noted that

aircraft noise level is directly proportional to the take-off weight (Table 3): heavier aircraft must increase engine thrust in order to reach the minimum speed for take-off. During departure as the engine is the main noise source this action leads to an increase in engine noise levels. It can also be obseved that noise is directly proportional to the aircraft groundspeed (Table 3). These variables are affected by adopted pilot technique. Analyzing the lowest and highest values of the take-off ground run distances that correspond to the lowest and highest values of the noise level it can be supposed that aircraft covers longer disnance on the ground reaches lower altitude during the climb with larger ground speed deteriorets the noise impact.

It was also able to use the experimental data from two noise monitoring stations (located at the airport and Pulling) for a real departure procedure of A320 from runway 08L/26R at Munich airport. The measured and calculated noise level, which are presented in Table 4 and Fig. 3 and 4, differ by 0.1 dB at the airport station and 1.8 dB at Pulling station. These results show that the model that was developed can be used with some confidence to predict noise level from aircraft in the vicinity of airports.

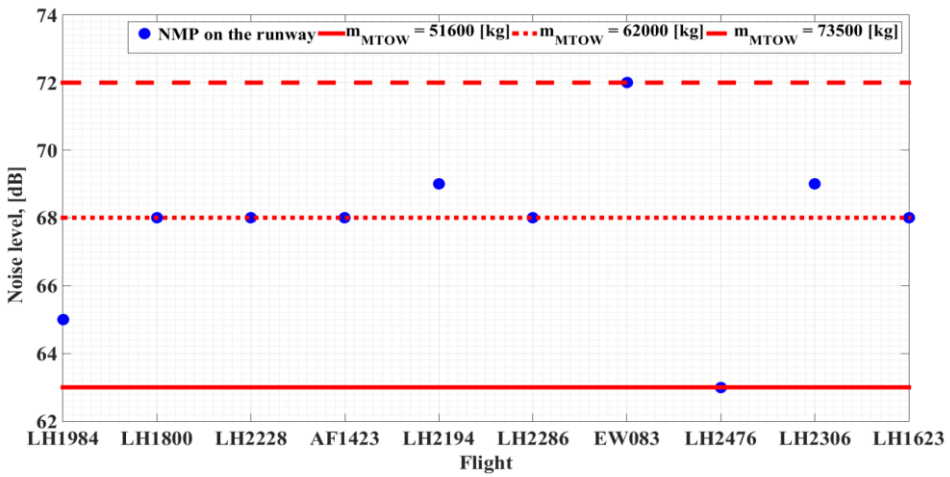

Fig. 3. Obtained results from the engine noise model and the real flight from the airport noise monitoring system, NMP on the runway

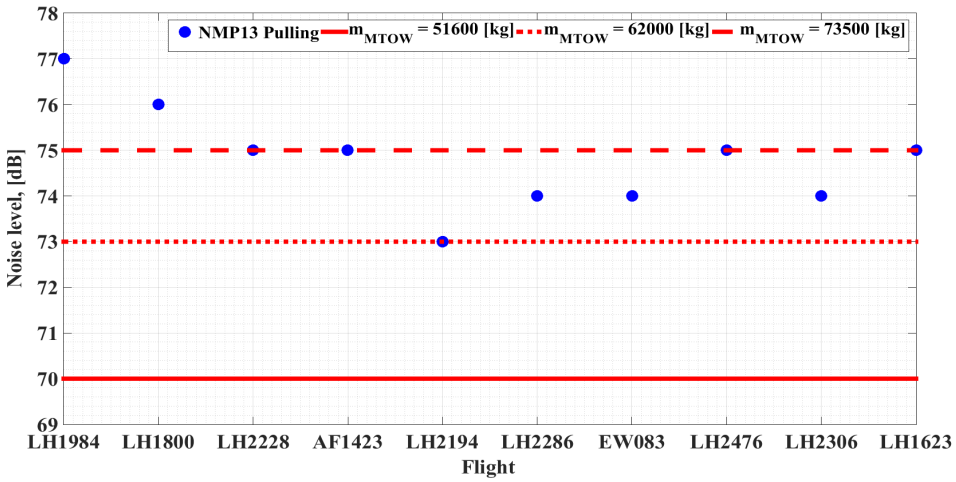

Fig. 4. Obtained results from the engine noise model and the real flight from the airport noise monitoring system, NMP 13 Pullin

Table 4. Data from the measurement stations at Munich airport runway 08L/26R on 29.04.2019 for the day period between 08:00 and 17:00

№	Flight		V_{LOF}, [m/s]	t_{LOF}, [s]	Noise, [dB]	
					NMP0	NMP13
1	Munich-Cologne	LH1984	75	35	65	77
2	Munich-Madrid	LH1800	80	28	68	76
3	Munich-Paris	LH2228	75	36	68	75
4	Munich-Paris	AF1423	75	34	68	75
5	Munich-Berlin	LH2194	80	32	69	73
6	Munich-Brussels	LH2286	75	36	68	74
7	Munich-Cologne	EW083	75	40	72	74
8	Munich-London	LH2476	75	30	63	75
9	Munich-Amsterdam	LH2306	80	38	69	74
10	Munich-Paris	LH1623	75	35	68	75

Conclusion

Aircraft noise is one the most detrimental environmental effect of aviation. The impacts of aircraft noise on people living in the vicinity of airports cannot be overestimated. In some airports, noise constrains air traffic growth. The main source of the aircraft noise during departure is assumed to be from its engine. In the current work is created a mathematical model simulated the aircraft departure

trajecrory (take-off and climb). The jet engine noise level from these trajectories is calculated. The trajectory model and the jet engine noise model are validated and demonstrate a correct physical behaviour. The suggested model could be integrated into noise-reduction measures that should take into account the interaction between the flight operation parameters and noise leves for a careful air traffic planning

In the future, the research will focus on:

- including the atmospheric factors in the trajectory model because of their non-negligible roles in flight performance during the take-off;
- creating a model to investigate the possibility of trajectory optimization during the departure trajectory in order to decrease the engine noise level.

Acknowledgments

This work has been supported by Research and Scientific Centre of Technical University of Sofia (Grant № 181ПР0012-04).

References

1. Eurocontrol. 2019, European Aviation Environmental Report 2019, ISBN 978-92-9210-214-2.
2. Futuresky. http://www.futuresky.eu/projects/noise (Accessed on 31.05.2019).
3. Boeker, E. R., E. Dinges, B. He, G, Fleming, C. J. Roof, P. J. Gerbi, A. S. Rapoza, and J. Hermann, Integrated noise model (INM) version 7.0 technical manual, FAA-AEE-08-01, 2008.
4. Krebs, W., Sound source data for aircraft noise simulation, Acta Acoustica united with Acustica, 2004, 91–100, 90p.
5. Khardi, S., Mathematical Model for Advanced CDA and Takeoff Procedures Minimizing Aircrft Environmental Impact, International Mathematical Forum, 2010, 5, 36, 1747–74.
6. Hartjes, S. and H. G. Visser, Efficient trajectory parameterization for environmental optimization of departure flight paths using a genetic algorithm, Journal of Aerospace Engineering, https://doi.org/10.1177/0954410016648980.
7. Zhang, M., A. Filippone; N. Bojdo. Using Trajectory Optimization to Minimize Aircraft Noise Impact, Inter.Noise, 27-30 August 2017, Honk Kong.
8. Gagliardi, P., L. Teti, and G. Licitra, A statistical evaluation on flight operational characteristics affecting aircraft noise during take-off, Applied Acoustics, 2018, 134, 8–15.
9. Stone, J. R., D. E. Groesbeck, and C. L. Zola, Conventional profile coaxial jet noise prediction, AIAA Journal, 1983, 21(1), 336–42.
10. Bridges, J. E., A. Khavaran, and C.A. Hunter, Assessment of Current Jet Noise Prediction Capabilities, 14th Aeroacoustics Conference, Vancouver, British Columbia, Canada, May 5–7, 2008.

11. Airbus-AC-A320, Aircraft Characteristics - Airport and Maintenance Planning. AIRBUS S.A.S. Customer Services, Technical Data Support and Services, 31707 Blagnac Cedex, FRANCE, 2016.
12. Airbus, Training & Flight Operation support and services, Flight crew performance course, A318/A319/A320/A321, Performance Training Manual, 31707 Blagnac Cedex, FRANCE, 2005.
13. https://travis-web01.munich-airport.de/data/travis.php?lang=en&_ga=2.41081378.185368683.1524577872-2134088401.1513440516 (Accessed at 31.05.2019).
14. EDDM. Muenchen Airport. https://skyvector.com/airport/EDDM/Muenchen-Airport (Accessed on 31.05.2019).
15. 1976 Standard Atmosphere Calculator. https://www.digitaldutch.com/atmoscalc/ (Accessed on 31.05.2019).
16. Turbofan Calculator. PIC-C. https://www.particleincell.com/2014/turbofan-calculator/ (Accessed on 31.05.2019).
17. Bos, Aircraft performance summary tables for the base of aircraft data (BADA) revision 3.0. EEC Technical / Scientific Reports.

РАСЧЕТ УРОВНЯ ШУМА ВОЗДУШНОГО СУДНА ПРИ ВЗЛЕТЕ

Х. Георгиева

Резюме

В этой статье описана математическая модель с 4 степенями свободы, созданная в Matlab для траектории вылета самолёта. В качестве эталонного самолёта был выбран коммерческий пассажирский самолёт среднего размера, подобный Airbus A320. Самолет представлен как твёрдое тело. Параметры модели получены из сайтов Airbus, а моделируемая траектория вылета в аэропорту Мюнхена, основана на стандартном инструментальном вылете. Для прогнозирования шума струи была использована полуэмпирическая модель Стоуна. Предложенная модель проверена на соответствие 10 реальным полетам, полученным из авиационного шума и системы мониторинга траектории полета в аэропорту Мюнхена. Рассчитывается ошибка между реальными данными и моделирование. Полученные результаты представлены численно и графически. Наблюдаемые эффекты эксплуатационных параметров полёта, влияющие на уровень шума воздушного судна во время взлета, являются предметом обсуждения в документе.

Bulgarian Academy of Sciences. Space Research and Technology Institute.
Aerospace Research in Bulgaria. 32, 2020, Sofia

DOI: https://doi.org/10.3897/arb.v32.e08

STEADY FLOW ANALYSIS OF A SLENDER WING BY LIFTING SURFACE METHOD

Konstantin Metodiev

Space Research and Technology Institute – Bulgarian Academy of Sciences
e-mail: komet@space.bas.bg

Key words: *Panel Method, Lifting Surface, Iterative Scheme*

Abstract

In the paper hereby, steady flow around a thin-walled wing is analysed by means of the Lifting Surface Method. In order to carry out tests, the wing has been divided into a finite number of quadrilateral panels. All panel edges in turn are replaced by discrete straight vortex segments which induce velocities within the flow field. The problem boils down to working out velocity circulation distribution on the wing surface. For this purpose, numerical realization has been developed in C by Minimalist GNU for Windows compiler and Code::Blocks IDE. To work out a solution to the linear non-homogeneous algebraic system, the Gauss – Seidel stationary iterative method has been applied. The obtained results for various angle of attack values are depicted by means of ParaView.

Introduction

The proposed study aims at displaying a fast algorithm for three-dimensional smooth flow analysis. A straight slender wing with finite span has been chosen for the test purposes. It has an exact resemblance to HAWK-2M Unmanned aerial Vehicle (UAV) wing upper surface. The UAV is produced by Aviotehnika Ltd. in Bulgaria. Although, the utilized algorithm is relatively old (it is also widely known as the Lifting Surface Method), it is seldom used in conjunction with iterative schemes for working out a solution to the linear algebraic system. In addition, the lack of specific aerodynamic data motivates the proposed study, so does development of a nonproprietary source code.

Method

The utilized approach towards working out a numerical solution follows procedure thoroughly described in [1]. The wing is divided into finite number of quadrilateral panels. Each panel is replaced afterwards by a vortex ring consisting of four straight vortex segments with constant intensity Γ. The rings purpose is to replace the actual geometry by inducing velocities within the flow field. In this

way, discontinuities of the velocity field magnitude are introduced which is what the actual wing is designed for. Each panel centroid is considered a collocation point. The velocities induced by all panels are computed successively at each collocation point and a linear algebraic system is formed afterwards in terms of velocity circulation distribution on the wing surface. A solution to the system is worked out numerically employing the Gauss – Seidel's stationary iterative scheme. Validation of the implemented algorithm has also been carried out.

The Biot – Savart law applied to a straight vortex element

The velocity induced at point P, fig. 1, by a straight vortex element with finite length r_0 might be computed by means of following formula, [1]:

$$\mathbf{q}_{1,2} = \frac{\Gamma}{4\pi} \frac{\mathbf{r}_1 \times \mathbf{r}_2}{\left|\mathbf{r}_1 \times \mathbf{r}_2\right|^2} \cdot \mathbf{r}_0 \cdot \left(\frac{\mathbf{r}_1}{r_1} - \frac{\mathbf{r}_2}{r_2} \right) \tag{1}$$

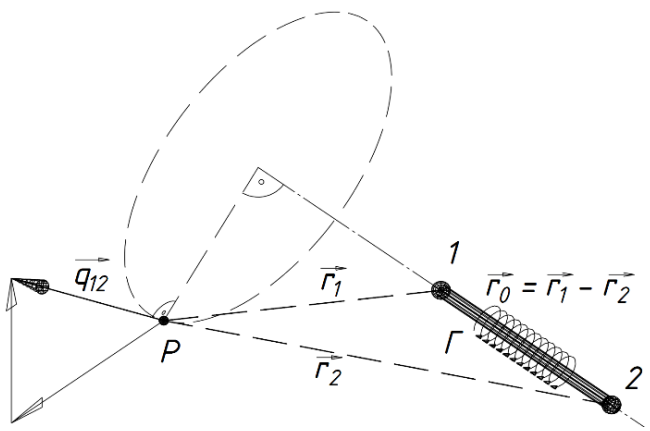

Fig. 1. Velocity induced by straight vortex element

Formula (1) is an alternative expression of the Biot-Savart law, which establishes a relationship between the induced velocity and the vortex element geometry. This formula is mainly used about further computations, which are to be made in the paper. It should also be noted that the velocity vector $\mathbf{q}_{12}$, Fig. 1, is orthogonal to the plane formed by vectors $\mathbf{r}_1$ and $\mathbf{r}_2$ which statement intuitively follows taking into account the cross product in (1).

Computation of influence coefficients

The boundary condition imposed on the problem under consideration implies that normal flow component is not allowed through the wing surface. The

normal velocity component at each point of the wing could be divided into a self-induced and a free-stream part, [1], i.e.

$$(2) \qquad \left(\mathbf{u}+\mathbf{Q}_{\infty}\right)\mathbf{n}=0\,.$$

The self-induced part is a linear combination of the so-called influence coefficients, which must be computed at each collocation point. These coefficients are defined as velocity components normal to the surface due to singularity element (vortex ring in our case) with unit strength, [1]. What is more, the velocity components induced by a single vortex ring at given collocation point are defined as an algebraic sum of velocities induced by all straight vortex segments comprising the ring. For instance, the influence coefficient at collocation point 1 due to vortex ring *j* is defined as dot product (3) between induced velocity **u** and panel normal vector **n**,

$$(3) \qquad a_{1j}=\mathbf{u}_{1j}\,\mathbf{n}_1\,.$$

At given collocation point, velocities induced by all vortex rings that the wing contains must be added to each other. At that point, the left hand side of (2) is represented by the sum (4),

$$(4) \qquad \sum_{j=1}^{N} a_{1j}\Gamma_j=\sum_{j=1}^{N}\mathbf{u}_{1j}\mathbf{n}_1\Gamma_j=-\mathbf{Q}_{\infty}\mathbf{n}_1\,.$$

In formula (4) circulation value Γ_j is unknown. In addition, the induced velocity computed by means of (1) takes value of $\Gamma = 1$.

Having traced all vortex rings influence upon all collocation points, following linear non-homogenous algebraic system with constant coefficients is formed:

$$(5) \qquad \begin{Vmatrix} a_{11} & a_{12} & a_{13} & \dots & a_{1N} \\ a_{21} & a_{22} & a_{23} & \dots & a_{2N} \\ a_{31} & a_{32} & a_{33} & \dots & a_{3N} \\ \vdots & \vdots & \vdots & \ddots & \vdots \\ a_{N1} & a_{N2} & a_{N3} & \dots & a_{NN} \end{Vmatrix} \begin{Vmatrix} \Gamma_1 \\ \Gamma_2 \\ \Gamma_3 \\ \vdots \\ \Gamma_N \end{Vmatrix} = \begin{Vmatrix} RHS_1 \\ RHS_2 \\ RHS_3 \\ \vdots \\ RHS_N \end{Vmatrix}.$$

In system (5), the right-hand side (RHS) is computed at current collocation point as

$$(6) \qquad RHS_i=-\mathbf{Q}_{\infty}\,\mathbf{n}_i\,.$$

The approach described above is illustrated in Fig. 2 adopting double indexing notation.

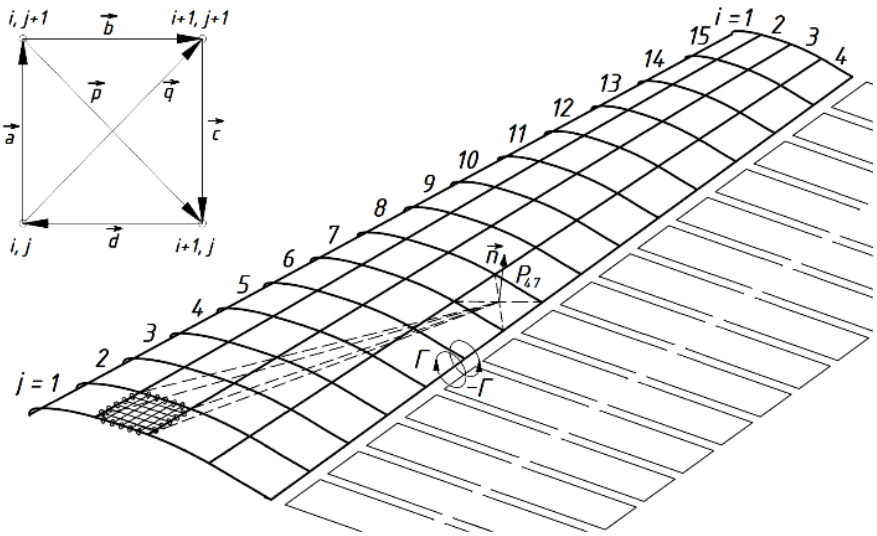

Fig. 2. Velocity induced at collocation point P47 due to panel i = 2, j = 1

In order to put the system (5) together, normal unit vectors at each panel must be computed in advance. This could be easily done recalling that the panel area equals half the cross product

$$\mathbf{S}_{ij} = 0.5(\mathbf{p} \times \mathbf{q}). \tag{7}$$

The vectors **p** and **q** form diagonals of the quadrilateral panel, Fig. 2, upper left corner. Hence, the unit vector is

$$\mathbf{n}_{ij} = \frac{\mathbf{S}_{ij}}{|\mathbf{S}_{ij}|}. \tag{8}$$

Solving a linear algebraic system

Having computed the influence coefficients, a non-homogenous linear algebraic system (5) is obtained in terms of circulation Γ distribution on the wing surface. The system is said to be strictly diagonal dominant if the absolute value of each main diagonal element is greater than sum of the absolute values of remaining entries in the current row respectively, i.e.

(9) $$|a_{ii}| > \sum_{\substack{j=1 \\ j\neq i}}^{n} |a_{ij}|$$

If the requirement (9) is met, then the following stationary iterative method, [2]

(10) $$x_i^k = \frac{1}{a_{ii}}\left(b_{ii} - \sum_{j=1}^{i-1} a_{ij} x_j^k - \sum_{j=i+1}^{n} a_{ij} x_j^{k-1} \right) \quad i = 1,2,\ldots,n \quad k = 1,2,3,\ldots$$

for working out a solution to the system (5) is said to converge unconditionally. Method (10) is named after Gauss and Seidel who used it as a modification of the widely known Jacobi method, [3].

(11) $$x_i^k = \frac{1}{a_{ii}}\left(b_{ii} - \sum_{\substack{j=1 \\ j\neq i}}^{n} a_{ij} x_j^{k-1} \right) \quad i = 1,2,\ldots,n \quad k = 1,2,3,\ldots$$

The convergence criterion used in the algorithm is the relative difference

(12) $$\max \left| \mathbf{x}^k - \mathbf{x}^{k-1} \right| \Big/ \left| \mathbf{x}^k \right| < 10^{-3}$$

Both iterative schemes (10) and (11) require initial guess for the vector **x**.

Secondary quantities

After computing the velocity circulation distribution, it becomes possible to work out lift *L*, pressure distribution *p*, and drag due to lift *D* values. Following formulae are recommended, [1]:

- Lift on each bound vortex segment:

(13) $$\begin{aligned} \Delta L_{ij} &= \rho Q_\infty \left(\Gamma_{ij} - \Gamma_{i-1\,j} \right) \Delta y_{ij} \quad & i > 1 \\ \Delta L_{ij} &= \rho Q_\infty \Gamma_{ij} \Delta y_{ij} & i = 1 \end{aligned}$$

- Static pressure distribution:

(14) $$\Delta p_{ij} = \Delta L_{ij} \Big/ \Delta S_{ij}$$

- Induced drag due to trailing vortex segments of each panel:

$$\Delta D_{ij} = -\rho w_{ij}\left(\Gamma_{ij} - \Gamma_{i-1\,j}\right)\Delta y_{ij} \quad i > 1$$
$$\Delta D_{ij} = \rho w_{ij}\Gamma_{ij}\Delta y_{ij} \quad i = 1 \tag{15}$$

where w is the induced velocity on the wing surface. Eventually, for total values it yields:

- Total drag:

$$D = \sum_{i=1}^{M}\sum_{j=1}^{N}\Delta D_{ij} \tag{16}$$

- Total lift:

$$L = \sum_{i=1}^{M}\sum_{j=1}^{N}\Delta L_{ij} \tag{17}$$

Since the fluid is assumed ideal, any other kind of drag force is expected to be zero due to d'Alembert paradox.

Source code description and validation

The source code has been developed in C. It utilizes two main structures shown in Fig. 3. Firstly, a structure storing quantities due to one straight vortex segment is created. In addition to geometry and velocity data, it contains a pointer to a function working out the induced velocities $\mathbf{q}_{12}$ according to formula (1). Then, another structure is created to store quantities related to one vortex ring. Since one ring contains four segments, four pointers to the former structure are declared within the latter. In this way, an inheritance is implemented facilitating code development process and making it possible to clarify vortex segments pertaining to the current ring and their location on the mesh. According to author's experience, double indexing of the panels in both curvilinear directions is the best approach as it is shown in Fig. 2.

The source code reads a text file containing grid point coordinates. Having read the data, the code passes them to aforementioned structures for further processing. All data blocks such as structures and arrays are dynamically allocated and assigned to pointers thereafter, which lets developer make use of the program with arbitrary number of panels. Both the number of wake panels and their geometry are computed automatically. Having completed the calculations, all data blocks are set free.

The source code has been developed by means of Minimalist GNU for Windows v.4.9.2, [4] and Code::Blocks IDE v.17.12, [5]. The 3rd party software used is ParaView to visualize obtained data, [6].

```
#ifndef DEFS_H
#define DEFS_H
#define PI_180 4. * atan(1.) / 180.
#define I 10
#define J 32
#define AOA 10 //deg
#define IW 2   // wake points along I

typedef double real;
typedef int int_t;

typedef struct oneSegment {
        struct oneSegment *that;
        real u, v, w, x1, y1, z1, x2, y2, z2;
        int_t (*q12)(struct oneSegment*, real, real, real, real);
} mySegment;

typedef struct onePanel {
        struct onePanel *that;
        real S, nx, ny, nz;
        mySegment *East, *West, *North, *South;
} myPanel;

real **x, **y, **z, **xP, **yP, **zP, **xW, **yW, **zW, *A, *b, **Gamma;
myPanel ***panel, ***panelW;

real** make2DArray(int_t X, int_t Y);
int_t delete2DArray(real **foo, int_t X);
int_t q12Common(mySegment *foo, real xP, real yP, real zP, real G);
myPanel* makePanel(int_t i, int_t j, real **x, real **y, real **z);
int_t killPanel(myPanel *foo);
int_t LHS(real *pA, real **G, int_t knob);
int_t RHS(real *pb);
int_t solveLS_GS(real *a, real *b, real **G);

#endif // DEFS_H
```

Fig. 3. Main header file used in the developed software

In order to estimate the program ability to work out a solution in advance, a few validation cases were carried out. Firstly, the iterative scheme (10) was tested with exact solution of small-sized system of linear non-homogenous equations, precisely 3 and 4. The Gauss-Seidel method proved to be about three times faster than Jacobi's, as expected.

The proposed algorithm is tested further by means of a thin rectangular wing divided into a mesh of 4 times 26 panels. This problem has been solved in [1] by means of a FORTRAN code published in Appendix D.2. Unlike the presented study, Gauss eliminations were used in [1] to solve the linear system of equations.

Both results for circulation Γ distribution on the wing surface are shown in Fig. 4 and Table 1.

Numerical results

In Table 1 and Fig. 4, results from presented code validation are shown. In Fig. 4, the wing semi span is solely depicted due to symmetry.

Table 1. Exemplary serial computations

	Gamma, m^2/s, Katz and Plotkin, [1]				Gamma, m^2/s, presented code			
R/C	1	2	3	4	1	2	3	4
1	0.491	0.699	0.822	0.889	0.491	0.698	0.822	0.889
2	0.490	0.697	0.820	0.887	0.490	0.697	0.819	0.887
3	0.487	0.693	0.815	0.882	0.488	0.693	0.815	0.882
4	0.484	0.688	0.808	0.875	0.484	0.688	0.808	0.874
5	0.479	0.680	0.799	0.864	0.479	0.680	0.799	0.864
6	0.472	0.670	0.786	0.850	0.472	0.670	0.786	0.850
7	0.463	0.656	0.769	0.830	0.463	0.656	0.769	0.830
8	0.451	0.637	0.746	0.805	0.451	0.637	0.746	0.805
9	0.435	0.613	0.715	0.771	0.435	0.613	0.715	0.770
10	0.413	0.579	0.674	0.724	0.413	0.579	0.674	0.724
11	0.383	0.532	0.615	0.659	0.383	0.532	0.615	0.658
12	0.337	0.460	0.526	0.561	0.337	0.460	0.526	0.561
13	0.255	0.336	0.378	0.400	0.255	0.336	0.378	0.400

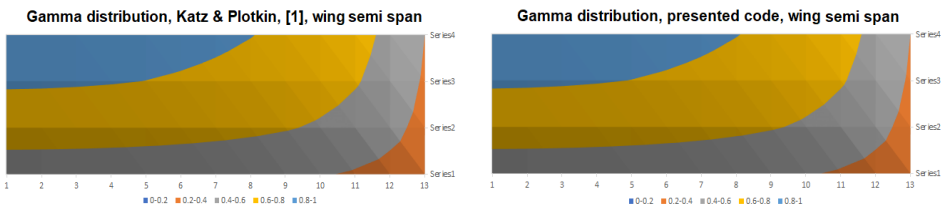

Fig. 4. Program validation, α = 5 deg, Q_∞ = 1 m/s

In Fig. 5, numerical results are shown for lift force distribution along upper surface of the Hawk-2M wing. In this case, the Gauss-Seidel numerical routine (10) has been used to work out a solution to system (5). In case of angle of attack α = 10 deg, Q_∞ = 16.7 m/s, ρ = 1.225 kg/m^3, the total lift is L = 147 N. In addition, the total lift coefficient is C_L = 1.358. In Fig. 6, a screenshot taken during numerical computations is depicted regarding same computational case. In the figure, upper left corner of the coefficient matrix taking part in system (5) is clearly visible. It is evident that the main diagonal elements are dominant with respect to

the order of magnitude. In Fig. 7, the root wing foil of Hawk-2M UAV is depicted. The wingfoil upper surface has been extruded along the semi span so as to obtain the 3D slender wing used in the present study.

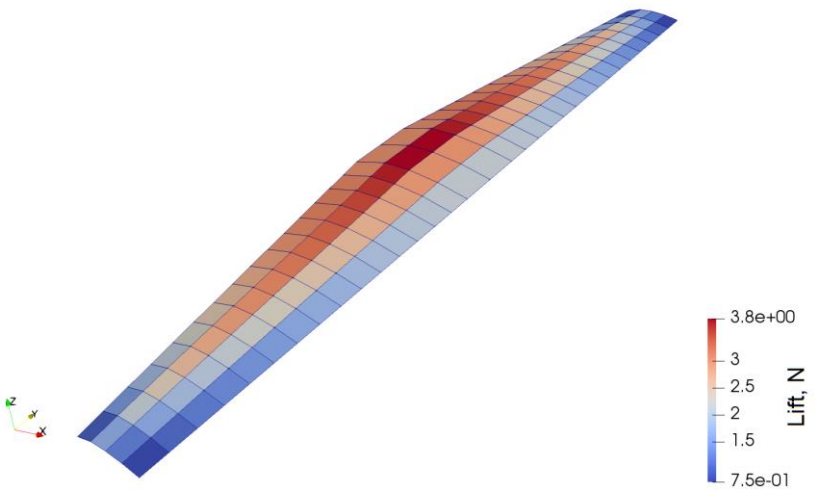

Fig. 5. Lift force distribution, N

"C:\Users\Prokopy\Desktop\Desktop\Lifting Surface Method\lift3DH3D\bin\Debug\lift3DH3D.exe"

-1.126e+001	8.969e-001	8.536e-002	2.545e-002	1.117e-002	5.985e-003
8.659e-001	-1.069e+001	9.490e-001	9.085e-002	2.698e-002	1.179e-002
7.532e-002	9.197e-001	-1.023e+001	9.978e-001	9.618e-002	2.845e-002
2.089e-002	8.111e-002	9.698e-001	-9.840e+000	1.044e+000	1.013e-001
8.606e-003	2.254e-002	8.669e-002	1.018e+000	-9.515e+000	1.086e+000
4.358e-003	9.292e-003	2.413e-002	9.217e-002	1.061e+000	-9.238e+000
2.506e-003	4.706e-003	9.953e-003	2.570e-002	9.740e-002	1.102e+000
1.572e-003	2.706e-003	5.042e-003	1.061e-002	2.721e-002	1.025e-001
1.050e-003	1.698e-003	2.900e-003	5.375e-003	1.124e-002	2.869e-002
7.362e-004	1.134e-003	1.819e-003	3.092e-003	5.697e-003	1.186e-002
5.359e-004	7.951e-004	1.216e-003	1.940e-003	3.279e-003	6.013e-003
4.022e-004	5.789e-004	8.524e-004	1.297e-003	2.058e-003	3.461e-003
3.096e-004	4.345e-004	6.206e-004	9.093e-004	1.375e-003	2.173e-003
2.434e-004	3.345e-004	4.659e-004	6.622e-004	9.647e-004	1.453e-003
1.948e-004	2.630e-004	3.588e-004	4.972e-004	7.026e-004	1.019e-003
1.510e-004	2.001e-004	2.671e-004	3.608e-004	4.945e-004	6.912e-004
1.145e-004	1.489e-004	1.945e-004	2.564e-004	3.415e-004	4.614e-004
9.251e-005	1.187e-004	1.528e-004	1.981e-004	2.587e-004	3.418e-004
7.902e-005	1.005e-004	1.280e-004	1.640e-004	2.114e-004	2.751e-004
6.800e-005	8.576e-005	1.083e-004	1.372e-004	1.749e-004	2.244e-004
5.891e-005	7.374e-005	9.231e-005	1.159e-004	1.462e-004	1.854e-004
5.135e-005	6.384e-005	7.932e-005	9.879e-005	1.234e-004	1.548e-004
4.503e-005	5.563e-005	6.864e-005	8.484e-005	1.051e-004	1.306e-004

Fig. 6. Matrix A upper left corner

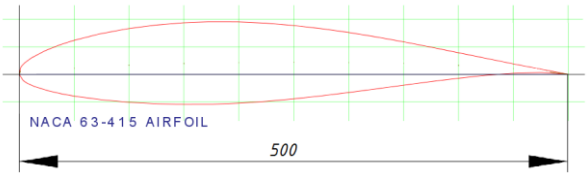

Fig. 7. NACA 63-415, 15%

4. Discussion

It is somewhat appropriate to note that velocities induced at given collocation point by an arbitrary vortex ring are highly dependent of the distances $\mathbf{r}_1$ and $\mathbf{r}_2$, Fig. 1, dashed lines, Fig. 2. The longer the distance the least the influence. Therefore, the biggest velocities are induced by a ring, which overlaps the collocation point. This in turn implies that the user is expected to get a diagonally dominant system of linear equations because diagonal elements with same indices all in (5) are obtained whenever the collocation point and vortex ring coincide.

In Fig. 2, a set of vortex rings (wake) is depicted right behind the wing trailing edge. Essentially, this implements the Kutta condition implying that the rear stagnation point should be held at the trailing edge. At that point, the flow velocity takes zero value. The vortex straight segments in Fig. 2 along the trailing edge replace the initial vortex. They would remain uncompensated if the vortex wake were absent. It is well known fact that the velocity vector circulation makes up for the initial vortex to preserve angular momentum of the mechanical system. Having encountered the trailing edge panels, the algorithm appends wake rings influences in order to impose the Kutta condition. For all that, the wake is a major source of numerical errors, which is why it is recommended for its length to be no less than 20 chords, [1].

In Table 1, Fig. 4, slight differences might be observed between results. The explanation might be found the digit precision. In book [1], single precision variables were used whilst in presented study results are quoted using double digit precision. In Fig. 5, the numerical results are shown for angle of attack $\alpha = 10$ *deg*. It may be figured out that the lift force decreases dramatically in the vicinity of ailerons thus reducing their efficiency. This is notably the case of take-off and landing. Efficiency of Hawk-2M aileron has been already thoroughly discussed in paper [7].

According to Fig. 6, the coefficient matrix is expected to be noninvertible. The matrix determinant has been computed in addition by means of GNU Scientific Library, [8], “gsl_linalg_LU_det” routine. The obtained order of result was quite small which makes the iterative scheme preferable to some direct methods such as the Cramer’s rule.

A possible algorithm extension would be simulating an unsteady flow around the wing. In this case, the wake shape evolution should be computed in addition. Also, it is advisable to study the topic of winglets design for this particular wing. Unfortunately, it is not possible to dive into all details of the source code due to the limited paper size. However, the source code is extensively commented and distributed by the author on demand.

Some additional tests carried out by means of Jacobi's and Gauss-Seidel's methods might be found in [9].

References

1. Katz, J. and A. Plotkin, Low-Speed Aerodynamics, Cambridge University Press, NY, 2010.
2. Fadugba, S. E., On Some Iterative Methods for Solving Systems of Linear Equations, Computational and Applied Mathematics Journal, 2015, 1, 2, 21–28. AASCIT
3. Larson, R., Elementary Linear Algebra, 7th edition, Brooks/Cole, CENGAGE Learning, MA, 2013.
4. MinGW. http://www.mingw.org/ (Accessed on 05 November 2020)
5. Codeblocks. http://www.codeblocks.org/ (Accessed on 05 November 2020)
6. Paraview. https://www.paraview.org/ (Accessed on 05 November 2020)
7. Metodiev, K., A New Aileron Designed for Hawk–2M Unmanned Aerial Vehicle, Journal of the Technical University–Sofia, Plovdiv branch, "Fundamental Sciences and Applications", 2015, 21.
8. GSL - GNU Scientific Library. https://www.gnu.org/software/gsl/ (Accessed on 05.11.2020)
9. Solution of Linear Equations by Stationary Iterative Methods. http://www.space.bas.bg /acsu/Ax_b/ (Accessed on 05 November 2020)

АНАЛИЗ НА СТАЦИОНАРНО ТЕЧЕНИЕ ОКОЛО ТЪНКО КРИЛО ПО МЕТОДА НА НОСЕЩАТА ПОВЪРХНОСТ

К. Методиев

Резюме

В настоящата статия стационарно течение около тънко крило е анализирано по Метода на носещата повърхност. За да се проведат числени експерименти, крилото бе разделено на краен брой квадратични панели. Всички страни на панелите на свой ред са заменени от дискретни прави вихрови сегменти, които индуцират скорости в полето на течението. Задачата се свежда до намиране на разпределението на циркулацията по повърхността на крилото. За целта бе разработена числена реализация на език С посредством компилатор Minimalist GNU for Windows и развойна среда Code::Blocks. За да се намери решение на линейната нехомогенна алгебрична система бе приложен итеративен метод на Гаус – Зайдел. Получените резултати за различни ъгли на атака са визуализирани посредством ParaView.

Bulgarian Academy of Sciences. Space Research and Technology Institute.
Aerospace Research in Bulgaria. 32, 2020, Sofia

DOI: https://doi.org/10.3897/arb.v32.e09

LONG ENDURANCE ELECTRIC MULTIROTOR UNMANNED AERIAL VEHICLE

Dimo Zafirov

Space Research and Technology Institute – Bulgarian Academy of Sciences
e-mail: zafirov@space.bas.bg

Key words: *Multi-Rotor UAV, Long Endurance, LiPo, LiION*

Abstract

The article presents an algorithm for development of a Long endurance electric multirotor unmanned aerial vehicle. Calculations for usage of different types of electric batteries have been made and dependencies of flight time for different weights of batteries have been obtained. Options for quadcopter and sixcopter have been considered.

Notation

C_D – coefficient of drag force;
C_L – coefficient of lift force;
D – drag force of the aircraft;
E_{bat} – energy of the batteries;
$\overline{E_{bat}}$ – specific energy of the batteries;
F – thrust of the propulsions;
g – acceleration of gravity;
K – glade ratio;
K_e – glade ratio by maximum endurance;
K_R – glade ratio by maximum distance;
L – lift force of the aircraft;
m_0 – take-off mass;
m_p – mass of the payload;
m_{bat} – mass of the batteries;
m_{empty} – empty mass of the aircraft;
$\overline{m_{bat}}$ – specific mass of the batteries;

$\overline{m_p}$ – specific mass of the payload;

$\overline{m_{empty}}$ – specific mass of the empty aircraft;

P – power;

P_1 – power for 1 motor;

R – distance of the flight;

t – flight time;

t_e – endurance time;

V – air speed of the aircraft;

V_c – cruise speed of the aircraft;

W_0 – take-off weight;

ρ – air density.

1. State of the Art

In the past years, sales of multi-rotor unmanned aerial vehicles (UAV) (copters) represent a major part (over 90%) of total sales of such aircraft. This is due to UAV capability to perform take-off and landing on small non-equipped areas, to carry out motionless hovering, and to be easily maintained. The only disadvantage is their relatively short flight endurance due to low energy efficiency. Opportunities for improvement of their aerodynamic and thrust efficiency are almost run out. It is expected that the flight endurance will be increased by developing batteries with higher specific energy $\bar{E} = \frac{E}{m_{bat}}$.

This paper presents a simple and efficient algorithm for development of copters that fulfil customer requirements.

2. Initial Requirements

Customers most frequency requires copters with long endurance at the payload used, which are relatively cheap, that possess high level of reliability and simple maintenance [5–7].

3. Mathematical model

Basic properties and features

Copter mass can be presented as the sum of the masses of individual subsystems:

(1) $$m_o = m_{con} + m_{prop} + m_a + m_p + m_{bat}\ [g].$$

Required thrust for motionless hovering is a multiplication of required thrust of one propulsor by the number of propulsor:

(2) $F_r = F_1 n\ [N].$

Required thrust of one propulsor is calculated according to the formula by accepting that 4% of the thrust is used to limit displacements caused by air movement:

(3) $F_1 = 1.04 \frac{m_o g}{n}\ [N].$

Total required power is:

(4) $P_r = nf(F_1)\ [W].$

Required power of one motor for motionless hovering depends on required thrust. This dependence is presented by manufacturers of electric motors for copters in tables with experimental data. In tables, for a specific motor, propeller and battery voltage, depending on revolutions, are presented data for power consumption and achieved thrust.

According to data by using a parabolic regression we can find the dependence:

(5) $P_1 = f(F_1)\ [W],$

(6) $E = P_r t = \bar{E} m_{bat}\ [Wh],$

(7) $t = \frac{E}{60nP_1} = \frac{\bar{E} m_{bat}}{60nP_1}\ [min].$

For the electric motor U8lite KV150, with the propeller G28*9.2CF and batteries with a voltage of 24 V, the following dependence between power consumption and required thrust can be found:

Table 1

F1, N	**P1, W**
11.54	69.6
12.13	74.4
13.27	84.0
14.37	93.6
15.31	103.2
16.17	110.4
17.51	124.8
18.69	134.4
19.68	146.4
21.12	160.8

F1, N	P1, W
21.85	168.0
22.90	180.0
24.03	194.4
25.01	206.4
26.74	230.4
28.22	247.2
30.89	283.2
34.13	326.4
39.81	415.2
47.86	552.0

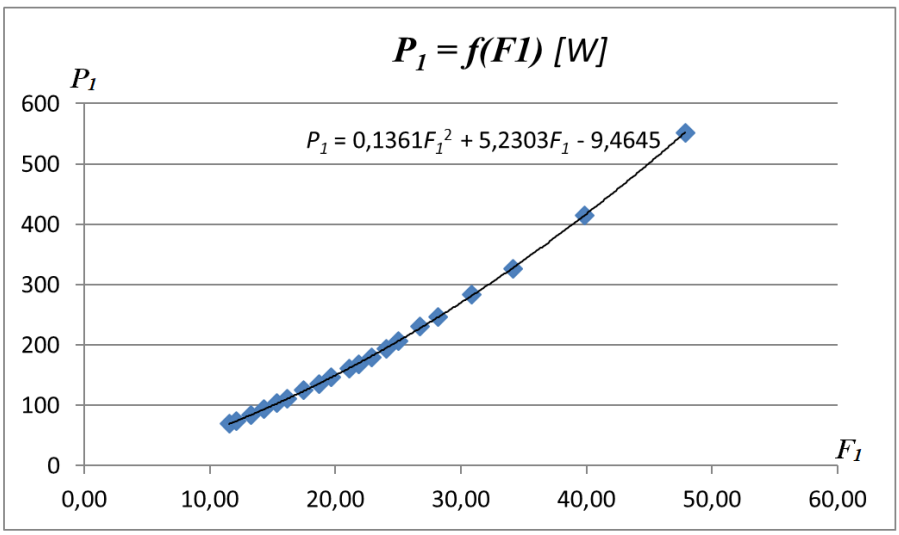

Fig. 1. Parabolic regression

For dependence between power consumption and required thrust of the electric motor U8lite KV150, with the propeller G28*9,2CF and batteries providing 24 V.

When looking at a specific example about designing of an industrial copter, some dependence can be found, which can be used for development of a copter fulfilling customer requirements.

An example is considered where a customer requires a copter capable to carry a payload with gimbal mass of $m_p \leq 1\,500$ g and have a flight time of

$t \geq 90\ min$. Calculations have been performed for two basic copter configurations with four rotors (quadcopters) and six rotors (sixcopters), which are the most frequency used for these payloads. It should be noted that this copter are able to carry higher loads at the expense of a reduced flight time.

After analysis of the masses of the structure, we accept:

- $m_{con4} = 1\ 350$ g for quadcopter;
- $m_{con6} = 2\ 700$ g for sixcopter;
- $m_a = 500$ g for avionics.

An option with a highly effective propulsion system has been considered. The system consists of brushless electric motors U8lite KV150, a propeller G28*9,2CF and batteries with a voltage of 24V. Flight times with different types of batteries and specific electric energy have been compared: ***LiPo*** with $\bar{E} = 200\ Wh/kg$, ***LiION*** with $\bar{E} = 250\ Wh/kg$ and promising batteries which are expected to be used in 2026 with $\bar{E} = 1\ 200\ Wh/kg$.

Table 2

m_{bat}	Quadcopter					
	m_0	F_1	P	$\bar{E}$		
				200	250	1 200
g	g	N	W	*t*, min		
1 500	6 277	16	437	41.22	51.53	247.33
1 750	6 527	17	461	45.52	56.90	273.12
2 000	6 777	17	486	49.34	61.67	296.02
2 250	7 027	18	512	52.73	65.92	316.40
2 500	7 277	19	538	55.76	69.70	334.56
2 750	7 527	19	564	58.46	73.08	350.77
3 000	7 777	20	591	60.88	76.10	365.26
3 250	8 027	20	619	63.04	78.79	378.22
3 500	8 277	21	646	64.97	81.21	389.81
3 750	8 527	22	675	66.70	83.37	400.18
4 000	8 777	22	703	68.24	85.31	409.47
4 250	9 027	23	732	69.63	87.04	417.77
4 500	9 277	24	762	70.87	88.58	425.19
4 750	9 527	24	792	71.97	89.96	431.82
5 000	9 777	25	822	72.95	91.19	437.73

m_{bat}	Quadcopter					
	m_0	F_1	P	$\bar{E}$		
				200	250	1 200
g	g	N	W	*t*, min		
5 250	10 027	26	853	73.83	92.29	442.99
5 500	10 277	26	885	74.61	93.26	447.65
5 750	10 527	27	916	75.30	94.12	451.78
6 000	10 777	27	949	75.90	94.88	455.42
6 250	11 027	28	981	76.43	95.54	458.61
6 500	11 277	29	1 014	76.90	96.12	461.39
6 750	11 527	29	1 048	77.30	96.63	463.81
7 000	11 777	30	1 082	77.65	97.06	465.88
7 250	12 027	31	1 116	77.94	97.43	467.64
7 500	12 277	31	1 151	78.19	97.73	469.12
7 750	12 527	32	1 186	78.39	97.99	470.33
8 000	12 777	33	1 222	78.55	98.19	471.30
8 250	13 027	33	1 258	78.68	98.34	472.05
8 500	13 277	34	1 295	78.77	98.46	472.60
8 750	13 527	35	1 332	78.83	98.53	472.96
9 000	13 777	35	1 370	78.86	98.57	473.15
9 250	14 027	36	1 408	78.86	98.58	473.17
9 500	14 277	36	1 446	78.84	98.55	473.06
9 750	14 527	37	1 485	78.80	98.50	472.80
10 000	14 777	38	1 524	78.74	98.42	472.43
10 250	15 027	38	1 564	78.66	98.32	471.93
10 500	15 277	39	1 604	78.56	98.20	471.34
10 750	15 527	40	1 645	78.44	98.05	470.64

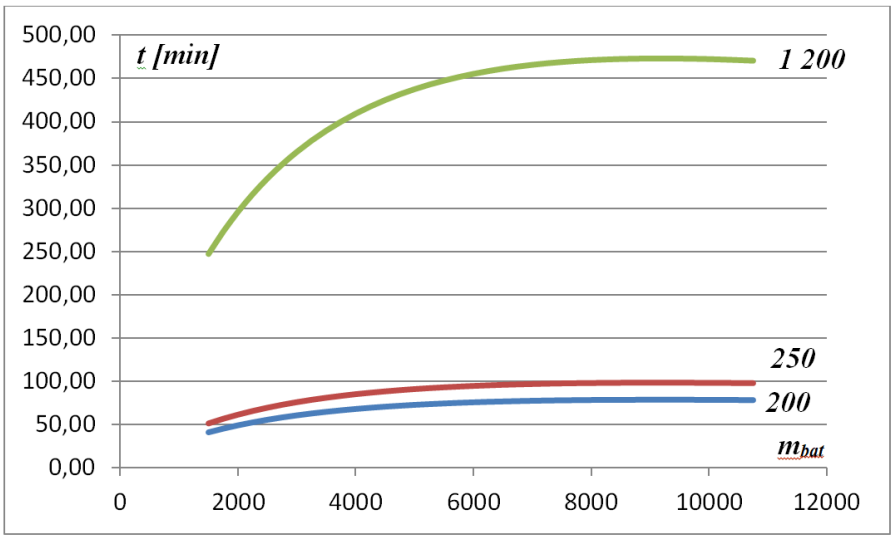

Fig. 2. Flight endurance of a quadcopter
according to the mass of batteries at $\bar{E} = 200, 250$ *and* $1200\ Wh/kg$

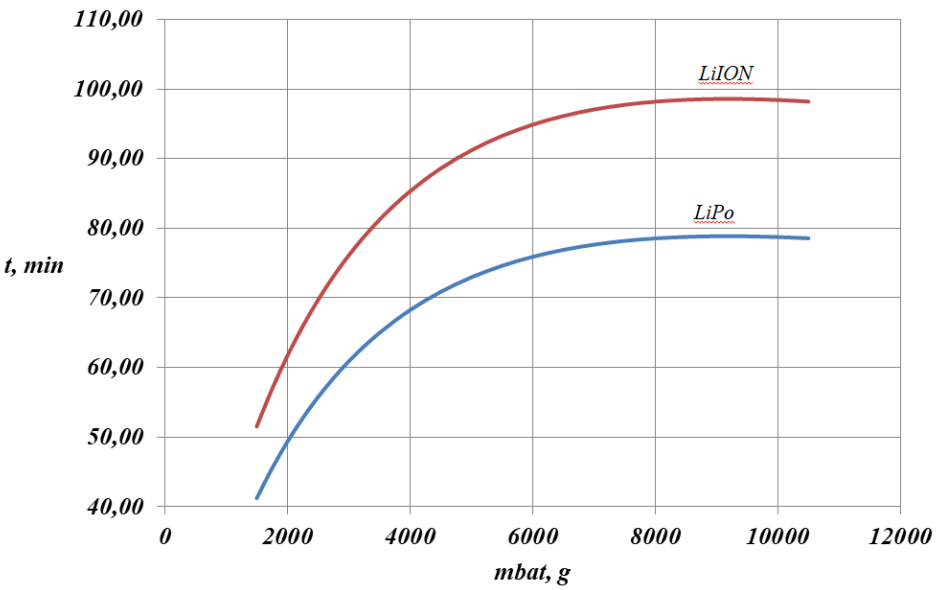

Fig. 3. Flight endurance of a quadcopter
with a battery ***LiPo*** *at* $\bar{E} = 200$ *and* ***LiION*** *at* $\bar{E} = 250 Wh/kg$
according to the mass of batteries

Following conclusions can be drawn according to table data and figures:

- The maximum endurance with *LiPo* batteries is less than 80 min which do not fulfill customer requirements;
- Required flight time can be only achieved when using ***LiION*** batteries with a mass of $m_{bat} = 5\,000$ g and $m_0 = 9\,777$ g. By using these types of batteries with a higher mass, the flight endurance increases slightly. Maximum endurance of 98,58 min is reached by using batteries with a mass of $m_{bat} = 9\,850$ g and $m_0 = 14\,027$ g;
- With promising batteries, the required endurance will be achieved at $m_{bat} \leq 1\,500$ g and $m_0 \leq 6\,000$ g. Promising batteries will provide flight endurance over 8.5 hours so that the usage of other sources of energy will be inefficient.

When designing, several copter configurations should be explored in order to achieve the best solution. In this case, the scheme of a sixcopter is considered.

Table 3

mbat	**Sixcopter**					
	m0	**F1**	**P**	**Espec**		
				200	**250**	**1 200**
g	**g**	**N**	**W**	**t, min**		
1 500	8 341	21	654	27.54	34.42	165.24
1 750	8 591	22	682	30.79	38.49	184.77
2 000	8 841	23	711	33.77	42.21	202.61
2 250	9 091	23	740	36.49	45.61	218.94
2 500	9 341	24	770	38.98	48.73	233.89
2 750	9 591	24	800	41.27	51.58	247.59
3 000	9 841	25	830	43.36	54.20	260.17
3 250	10 091	26	861	45.28	56.61	271.71
3 500	10 341	26	893	47.05	58.81	282.30
3 750	10 591	27	925	48.67	60.84	292.04
4 000	10 841	28	957	50.16	62.71	300.99
4 250	11 091	28	990	51.54	64.42	309.21
4 500	11 341	29	1 023	52.80	65.99	316.78
4 750	11 591	30	1 056	53.95	67.44	323.73
5 000	11 841	30	1 091	55.02	68.77	330.11
5 250	12 091	31	1 125	56.00	70.00	335.98

mbat	Sixcopter					
	m0	F1	P	Espec		
				200	250	1 200
g	g	N	W	t, min		
5 500	12 341	31	1 160	56.89	71.12	341.37
5 750	12 591	32	1 195	57.72	72.15	346.31
6 000	12 841	33	1 231	58.47	73.09	350.84
6 250	13 091	33	1 268	59.17	73.96	355.00
6 500	13 341	34	1 304	59.80	74.75	358.80
6 750	13 591	35	1 342	60.38	75.47	362.27
7 000	13 841	35	1 379	60.91	76.13	365.44
7 250	14 091	36	1 417	61.39	76.73	368.32
7 500	14 341	37	1 456	61.82	77.28	370.94
7 750	14 591	37	1 495	62.22	77.77	373.32
8 000	14 841	38	1 534	62.58	78.22	375.46
8 250	15 091	38	1 574	62.90	78.62	377.39
8 500	15 341	39	1 614	63.19	78.98	379.13
8 750	15 591	40	1 655	63.45	79.31	380.67
9 000	15 841	40	1 696	63.67	79.59	382.04
9 250	16 091	41	1 738	63.88	79.84	383.25
9 500	16 341	42	1 780	64.05	80.06	384.31
9 750	16 591	42	1 822	64.20	80.26	385.23
10 000	16 841	43	1 865	64.33	80.42	386.01
10 250	17 091	44	1 909	64.44	80.56	386.67
10 500	17 341	44	1 952	64.53	80.67	387.20
10 750	17 591	45	1 997	64.61	80.76	387.64

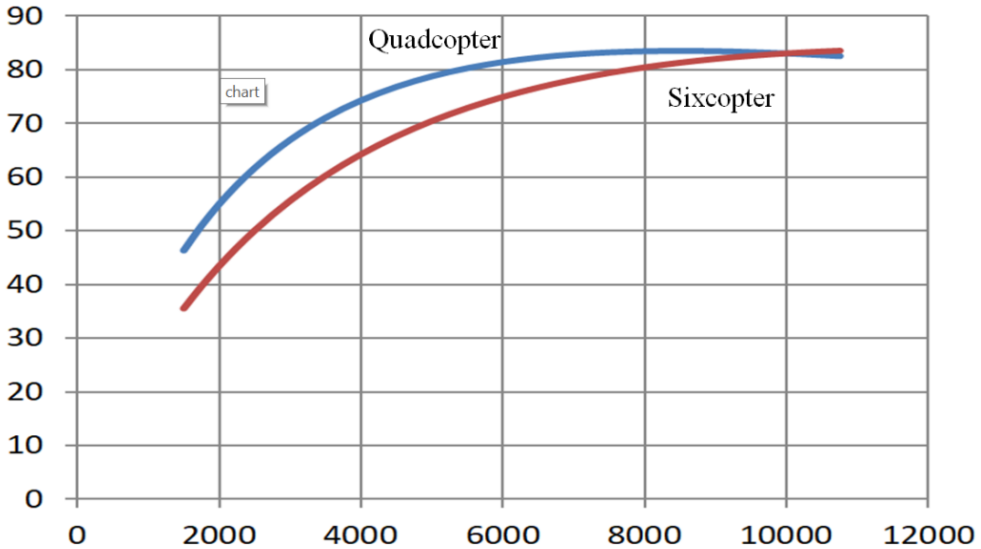

Fig. 4. Flight endurance of a quadcopter and sixcopter according to the mass of batteries at $\bar{E} = 200\ Wh/kg$

The tables and diagrams show that a sixcopter is not able to provide the required flight endurance.

Conclusion

The algorithm allows to find options that fulfil customer requirements and to eliminate options which do not fulfil these requirements and also are not competitive.

Acknowledgements

Set up under the project 9иф-02-4/28.11.2018 “Development of an innovative drone with long endurance and high altitude”, financed by the National Innovation Fund of Ministry of Economic of Republic of Bulgaria.

References

1. U8 Lite KV150. T-Motor. http://store-en.tmotor.com/goods.php?id=469
2. Stojkov, O., I. Kamburov. Matematicheski model na eksploatacijata na sistemite za upravlenie na aviacionnoto v"or"zhenie. 1983 Nauchni trudove “VNVVU G. Benkovski”, No. 44, VI, Sofia. (in Bulgarian)

3. Stojkov, O. Kompleksna obrabotka na informacijata poluchavana ot razlichni datchici. 1988 Nauchni trudove “VNVVU G. Benkovski”, No. 51, VI, Sofia. (in Bulgarian)
4. Stojkov, O. Optikoelektronni sistemi. NVU “V. Levski”, fakultet “Aviacionen”, Jubilejna nauchna sesija. 2005, Vol. 1, Dolna MitropoliJa, 164–170, ISBN 954-713-071-4. (in Bulgarian)

МНОГОРОТОРЕН БЕЗПИЛОТЕН ЛЕТАТЕЛЕН АПАРАТ С ГОЛЯМА ПРОДЪЛЖИТЕЛНОСТ НА ПОЛЕТА

Д. Зафиров

Резюме

В тази статия се предлага алгоритъм за проектиране на многороторен безпилотен летателен апарат с голяма продължителност на полета. Направени са пресмятания за използването на различни видове батерии, като са получени зависимости на полетното време за различни техни маси. Разгледани са варианти за четирироторен и шестроторен безпилотни летателни апарати.

Bulgarian Academy of Sciences. Space Research and Technology Institute.
Aerospace Research in Bulgaria. 32, 2020, Sofia

DOI: https://doi.org/10.3897/arb.v32.e10

TRANSONIC FLOW STUDY IN A CENTRIFUGAL COMPRESSOR USING PERFORATED AIRFOILS

Bogdan Gherman[1], Oana Dumitrescu[1,2], Valeriu Dragan[1]

[1]National Research and Development Institut for Gas Turbine COMOTI - Romania
[2]University POLITEHNICA of Bucharest
e-mail: bogdan.gherman@comoti.ro

Key words: *Centrifugal Compressor, Numerical Simulation, Airfoil*

Abstract

In this paper, the effect on a perforated plate on a centrifugal compressor is investigated using numerical simulation. The performances and fluid flow are compared for two different vaned diffusers, a base case where there are no perforated plates and a case where a perforated plate is inserted in the rotor casing at exit and the stator blade. The impact of this geometry change on the compressor performances it is studied in the case of adverse angles of attack at stator vane. Near wall refinement ensures the accuracy resolution of the boundary layer with a y+ value of one unit corroborated with a growth ratio of 1.1:1. Menter's SST model was used in all numerical cases performed, as implemented in ANSYS CFX. Following the results of the baseline diffuser, the optimal position of the perforated cavity was determined.

Introduction

In recent decades, the compressor design technique has been constantly improved, especially due to the development of CFD technology. Significant improvements in the performance of compressors have been achieved by solving three-dimensional equation for the impeller exit flow. Experimental studies and numerical ones have shown that diffuser have a significant importance on stability limit of a centrifugal compressor, depending on the impeller design and the interface between the impeller and diffuser [1].

Performances of compression system are limited by the occurrence of aerodynamic flow instabilities, which may lead to propulsion system instabilities or, in some extreme case, machine damage. Trebinjac et al. [2] analyzed a transonic centrifugal compressor stage, especially the space between the vaneless and semi-vaneless space where the surge originates. Komatsubara [3] investigate the surge and rotating stall in a centrifugal compressor using a phase portrait reconstruction method, to clarify the cycle behavior of surge. Another study was realized by Bousquet et al [4] who analyzed a 2.5 pressure ratio centrifugal

compressor stage to achieve a comprehensive description of the flow field from peak efficiency to near stall. In the work by Lennemann and Howard [5], on the appearance of stall, the hydrogen bubble technique is used to determine the flow pattern in an impeller which is in stall. Jansen [6] was probably the first to show that the separation of the boundary layer precedes the initiation of the surge into a vaneless stator. He was able to anticipate cell velocity and speed distribution, but not the number of cells.

Surge into the vaned diffuser is initiated in the vaneless space at the entrance into the diffuser. Due to the increase in static pressure and the increased incidence angle on the leading edge, the flow decreases. Together with the expanded range of vaneless diffusers, the specific speed of the rotor significantly influences the behavior of the stage in unstable conditions at low mass flow rates. A specific low velocity (corresponding to a low flow rate coefficient) can lead to unstable rotor under low flow conditions [7]. This is supported by the fact that the angle of the volute tongue is much more important in the case of high specific speed stages [8]. The conventional approach to pumping industry is to maintain a safety margin on a pump anticipation line (usually 10% of the air flow rate: which means that the distance from the pump line to the edge is 10% of the flow rate If the pumping line is at 0.5 kg/s, then the pumping edge is 0.55 kg/s).

In the cases of high-pressure ratio stages, the speed of sound may be exceeding, thus leading to formation of shock waves. Hence, control of shock waves plays an important role in high speed compressor performance. Savu [9] proved that a perforated airfoil can reduce shock wave intensity and the noise associated with it. Fig. 1 depicts the concept geometry and a shadowgraph proof of concept. Also, porous layers are used to control the incompressible flow around bodies, reducing drag. Bruneau et al. [10] developed a passive control method, in order to establish the proper position of a porous layer, having as limits being the fluid and the bluff-body. A suitable position of porous layer, can lead to a 40% decreasing in drag coefficient. Another aspect is the complexity of structured grids for porous geometries leading to high computational costs. Thus, Frink [11] developed a new boundary condition, eliminating the grid construction for the plenum, simplifying the model. Solving the Navier-Stockes equations, the influence of porous surfaces on aerodynamic performances was analyzed for supercritical flow [14]. Experimental measuraments revealed that for porous airfoils displacement thickness increases with a lower flow resistance [15].

Studies regarding shock wave control, shape and position of bumps, slots and other passive control devices have been realised over the years, having as purpose a weaker lambda shock wave. Position and bump shape were investigated by Zhou [12] using a sequential quadratic programming optimization method coupled with adjoint method. Another approach regarding porous surfaces is Drăgan's [13], which based on super circulation and Coandă effect, developed a new rotary wing concept, with a channel imbedded inside the wing.

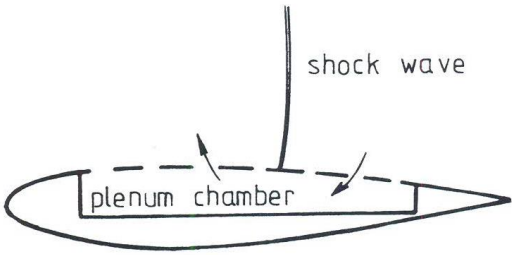

a)

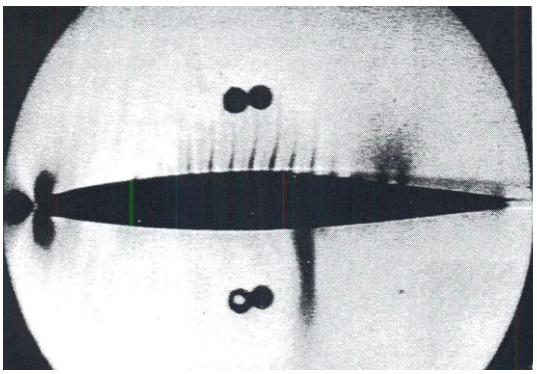

b)

Fig. 1. Suppression of shocks by a permeable surface concept airfoil (a) and Schlieren image of the experiment (b) (M = 0.785, α = 00) [9]

The main focus of the research is to determine the effectiveness of a perforated cavity incorporated on a rotor casing surface and diffuser vane surface, for transition regime flow mitigation and increase perfomances at adverse angles of attack, see Fig. 3. This comoressor that it is studied here it is subject to extreme conditions near surge. In this case a steady regime it is chosen to quatify as a first step the behavior of porous solution and the mass flow that it is need to modify the flow structure. The idea is to obtain a stable regime with an extra connection between rotor and stator. The air will be extracted from the rotor casing near the exit, where the flow is fully turbulent and secondary flow and tip flow are occurring. It will be studied the possibility to insert the air extracted from rotor casing into the stator blade porous section. In order to provide quantitative data for this type of passive control device, numerical simulations were conducted and compared with a normal diffuser vane.

Computational modeling

Compressor design specifications are presented in Table 1, mentioning number of blades, diameters and boundary conditions. For the present paper, just one channel was numerical studied, Fig. 2, in order to validated the concept.

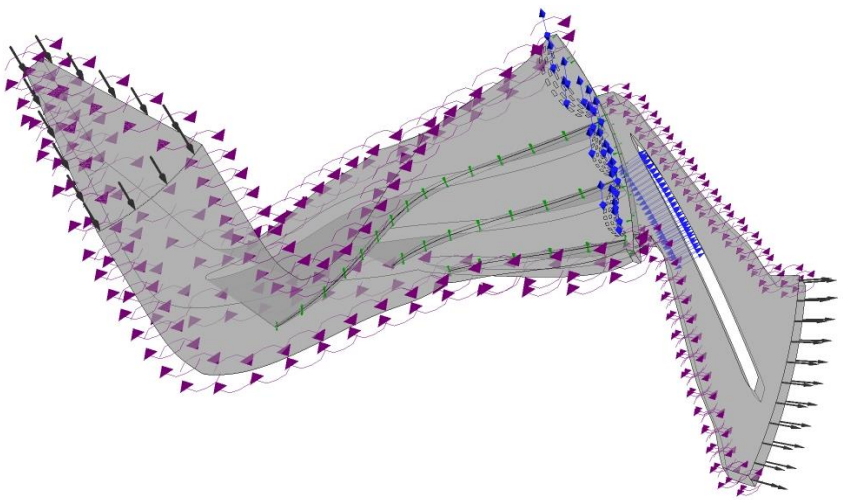

Fig. 2. Computational domain of the centrifugal diffuser

Table 1 presents the specific parameters of the centrifugal compressor.

Table 1. Specifications of the compressor

Design operating condition	
Inlet pressure	1 bar
Inlet temperature	288 K
Pressure ratio	3.5
Design rotational speed	37 550 rpm
Design mass flow rate	0.7 kg/s
Impeller	
Blade count	11 main + 11 splitter +11splitter
Inlet diameter	110.8
Exit diameter	219
Exit blade height	6.4 mm
Vaned diffuser	
Blade count	18
Outlet diameter	298.8 mm
Vanes height	5.6 mm

Impeller and diffuser, spatial discretization was performed using a structured multi-block meshing strategy, realized by the mesh generator for turbomachinery CFX TurboGrid. In order to capture the viscous and turbulent effects near the compressor blades and wall, the mesh discretization is performed such as y+ is equal to 1, increasing the mesh near the wall. Table 2 presents the mesh statistics.

Table 2. Mesh statistics

Number of nodes	1.7 mil.
Number of elements	1.63 mil.

The computational fluid dynamics solver used in this case is ANSYS CFX. As working fluid, ideal gas was chosen. For the blades and hub/shroud walls a nonslip and adiabatic wall boundary conditions are applied. Between the impeller/diffuser a stage connection was established.

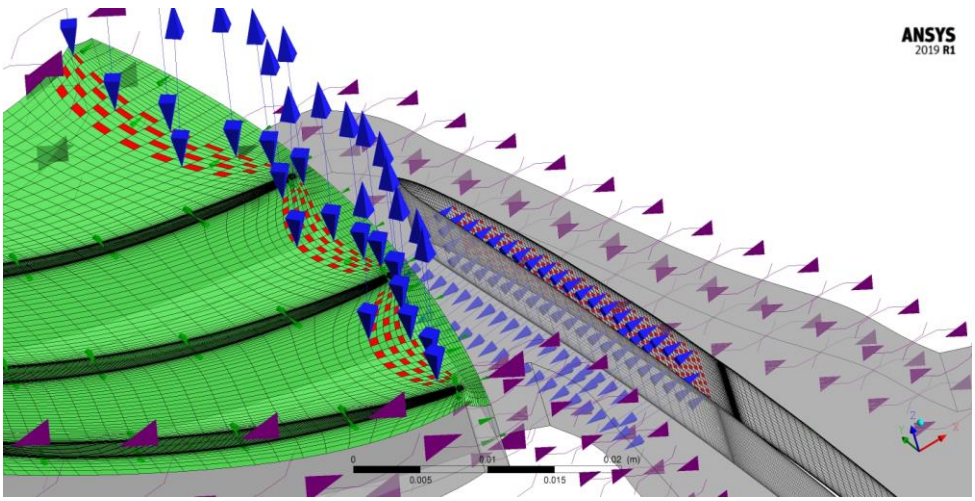

Fig. 3. Grid structure: a) Impeller casing and Diffuser porous zone

The turbulence model used for this analysis is the k-omega SST (Shear Stress Transport). This model has been shown to yield accurate results, and is more suitable for such cases where it is important to capture both the phenomena occurring near the walls and those of the entire field of computing.

Table 3 illustrates the boundary conditions used for the numerical simulation.

Table 3. Porous Boundary conditions

Rotor casing porous boundary condition	
Openning	Entrainment
Relative Pressure	1 bar
Openning Temperature	430 K
Diffuser porous boundary condition	
Openning	Entrainment
Relative Pressure	0.8 bar
Openning Temperature	428 K

Results and Discussions

The numerical results obtain shows a non-transient behavior of the flow when the porous structure it is employed. Also, it was considered that a mass flow of 6% of the entire mass flow rate should be extracted from the rotor and inserted in the stator blade. The streamlines distribution inside the rotor shows no impact on the flow close to exit in both cases.

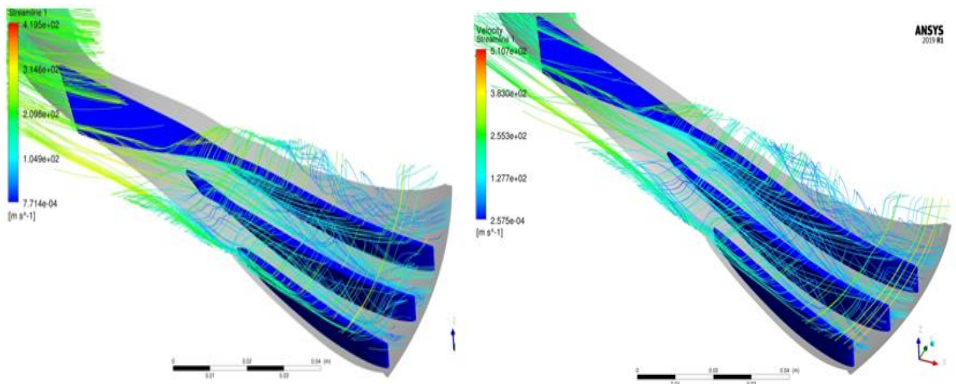

a) *b)*

Fig. 4. Streamlines inside rotor: a) with porous, b) base case

Also, the static pressure distribution shows that the porous material has an impact in the region where it is used, but towards the exit of the compressor stage the pressure distribution it is not modified, see Fig. 5.

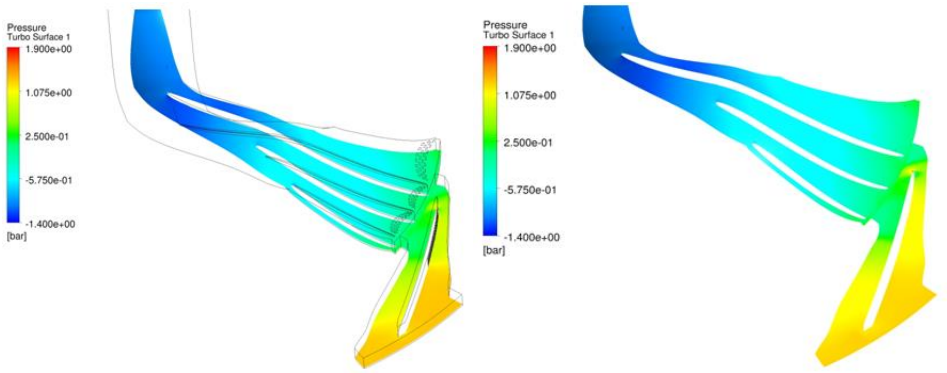

a) *b)*

Fig. 5. Pressure distribution inside the domain at 0.5 of the blade height: a) with porous, b) base case

The compressor regime studied in this case experience an adverse angle of attack at the vane diffuser inlet and a high Mach number; see Fig. 6, 7, and 8. In Fig. 6 it can be seen the low Mach number region on the diffuser blade, suction side. The comparison between the two cases shows that in the porous case (Fig. 6a) the low Mach number region is deacresed and it appears only at the end of the blade.

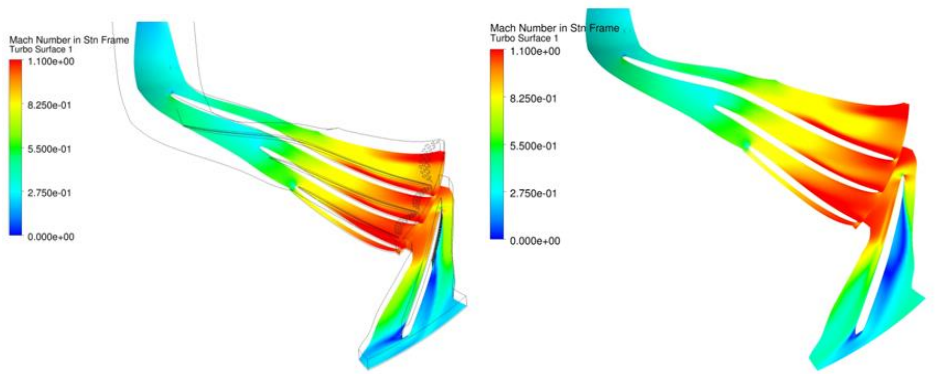

a) *b)*

Fig. 6. Mach number distribution at 0.1 of blade height: a) porous case, b) base case

Also, at 0.5 of blade height, Fig. 7, it can be seen that the low Mach region it is still present on the same place. The porous region manages to deacrease the region area, thus increase the mass flow rate through that section.

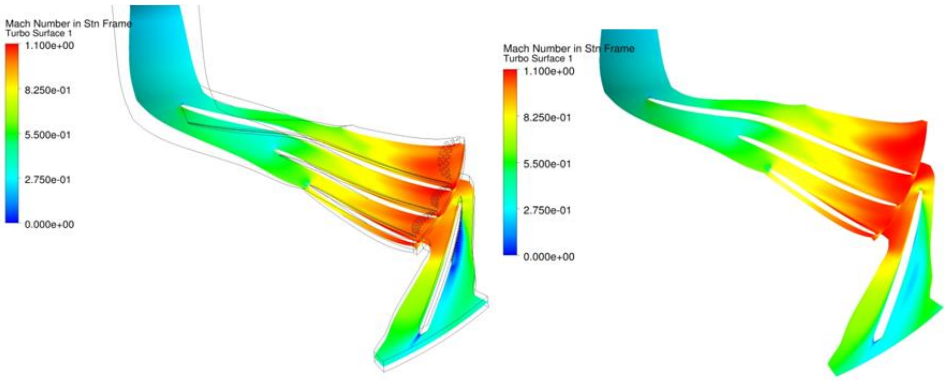

a) *b)*

Fig. 7. Mach number distribution at 0.5 of blade height: a) porous case, b) base case

When it comes to the tip of the blade region it can be seen a different scenario, see Fig. 8, when there is no Low Mach number region present in the base case, the extra flow rate that enters through the porous region has a negative impact on the flow structure.

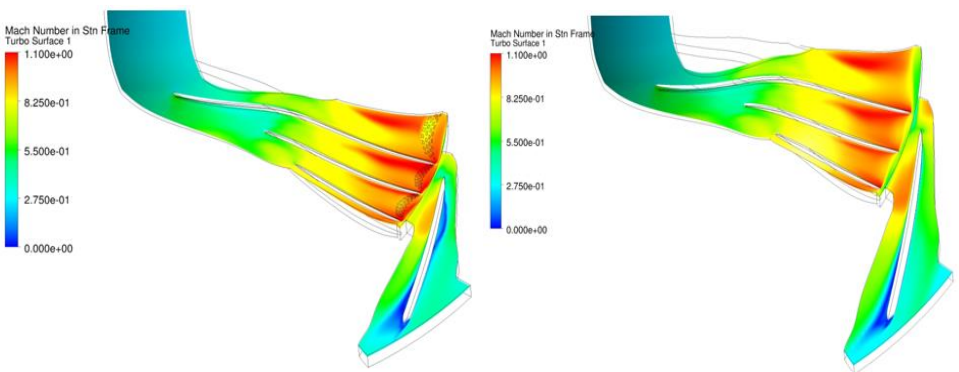

a) *b)*

Fig. 8. Mach number distribution at 0.9 of blade height:
a) porous case, b) base case

The idea was to destabilize or reduce the low Mach number zone that forms inside the diffuser by inserting a small amount of air. The results show a mofidication of the low Mach number zone.

Another difference observed between the two cases is the turbulent kinetic energy plot. There it can be observed a high level of this energy where the flow leaves the rotor and enters the vane diffuser. In the porous case there are two

regions in that are instead of one due to porous material in that region. These two regions have a low level of turbulent kinetic energy compared to the base case.

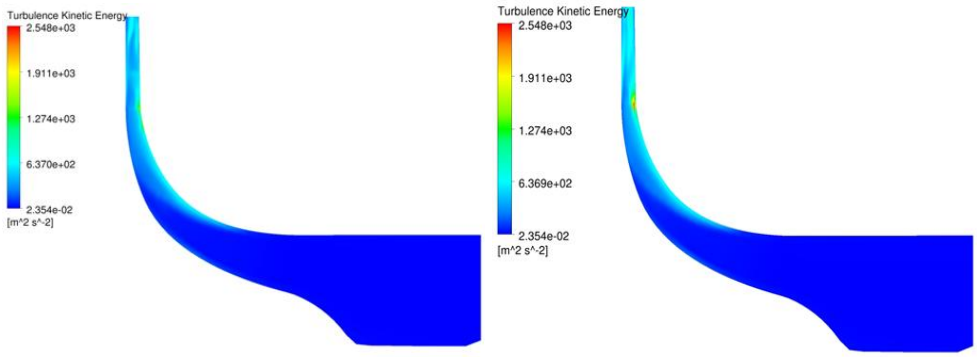

a) *b)*

Fig. 9. Turbulent Kinetic Energy distribution on the meridional plane: a) porous case, b) base case

Also, in Fig. 10 it can be observed a reduction of static entropy levels in the porous case.

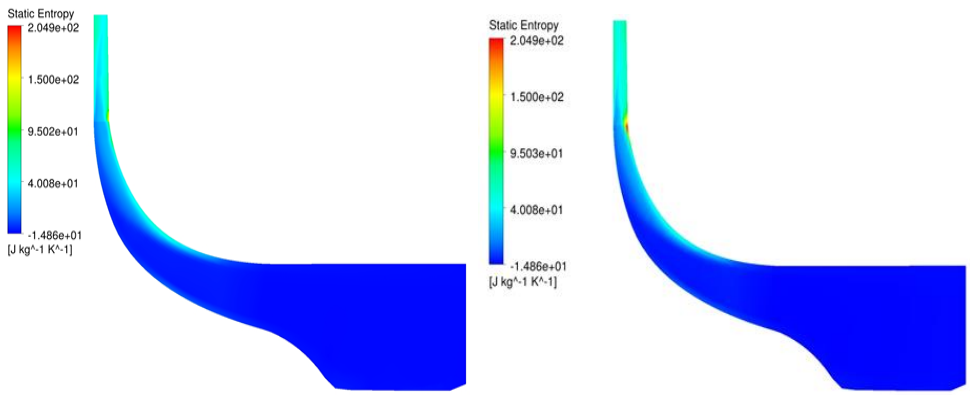

a) *b)*

Fig. 10. Static entropy meridional distribution: a) porous case, b) base case

The velocity in stn frame plot shows no difference between the two cases, see Fig. 11.

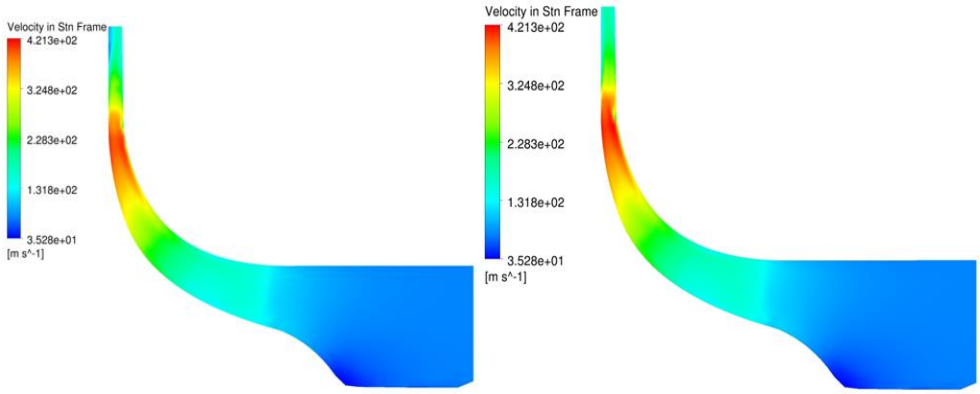

a) *b)*

Fig. 11. Velocity in stn frame meridional distribution: a) porous case, b) base case

Another important aspect is the static pressure distribution inside the compressor stage. As it can be seen there is a slite increase at the exit of the rotor in the porous case, however the trend is similar as in the base case, see Fig. 12.

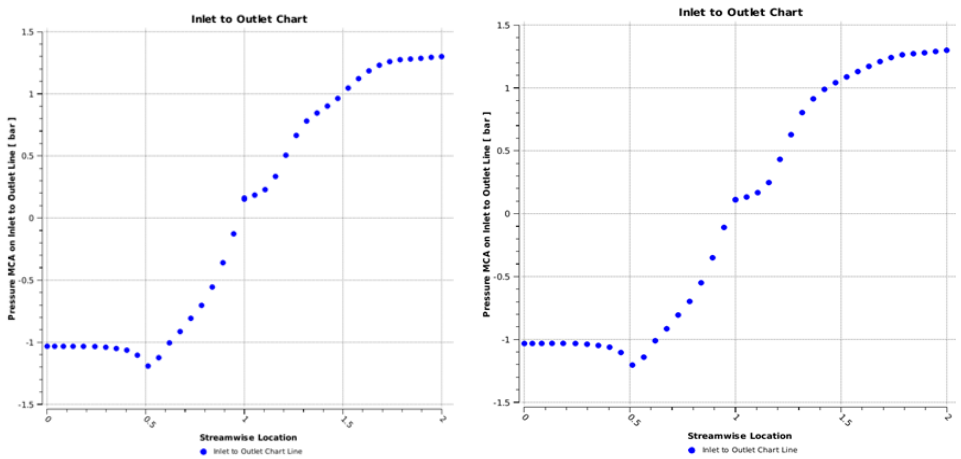

a) *b)*

Fig. 12. Static pressure (mass avereged) from inlet to outlet: a) porous case, b) base case

The geometry changes made to the compressor stage modified the performances at this regime, compared to the base case. Although the rotor polytropic efficiency did not change, ~ 92%, so the extraction of air from the rotor exit had no impact. In the stator case the insertion of air increased the polytropic efficiency 2%, reaching 85%.

Conclusion

The numerical analysis performed in this study to see the impact of perforated casing, for rotor, and perforated airfoil in the case of the stator blade. The scenario simulated in this case was to use the air extracted from the rotor exit and inserted in the stator through the perforated airfoil. The idea was to destabilize the low Mach number zone that formed in that area of the blade surface, thus increase the channel witdth. The entrainment boundary condition simulated a perforated airfoil where the pressure was not constant on the entire surface. Thus, where the pressure was higher the mass flow rate entering the stator domain was smaller and viceversa. This can be seen on the entire height of the stator blade. This scenario increased the efficiency on the stator part while did not changed the rotor performances.

In conclusion this idea has potential but more studies have to be performed especially for transient regimes.

References

1. Waleed, Al-Busaidi, Pericles Pilidis, Techno-Economic Optimization of Diffuser Configuration Effect on Centrifugal Compressor Performance, American Journal of Energy Research, 2015, 3, 2, 37–48.
2. Trebinjac, I., N. Bulot, X. Ottavy, and N. Buffaz, Surge inception´ in a transonic centrifugal compressor stage, Proceedings of the ASME Turbo Expo, pp. GT2011–G45116, June 2011.
3. Komatsubara, Y., S. Mizuki, Dynamical System Analysis of Unsteady Phenomena in Centrifugal Compressor, Journal of Thermal Science, 1997, 6, l.
4. Bousquet, Y., X. Carbonneau, G. Dufour, N. Binder, and I. Trebinjac, Analysis of the Unsteady Flow Field in a Centrifugal Compressor from Peak Efficiency to Near Stall with Full-Annulus Simulations, International Journal of Rotating Machinery, Volume 2014, Article ID 729629, 11. DOI:10.1155/2014/729629
5. McDonald, G. B., E. Lennemann, J. H. G. Howard, Measured and Predicted Flow Near the Exit of a Radial-Flow Impeller, J. Eng. Power, 1971, 93, 4, 441–46. DOI:10.1115/1.3445604
6. Jansen, W., Rotating Stall in a Radial Vaneless Diffuser, J. Basic Eng., 1964, 86, 4, 750–58. DOI:10.1115/1.3655945
7. http://pt.slideshare.net/soulstalker/easa-part-66-module-154compressors?smtNoRedir=1
8. Frigne, P., and R. van den Braembussche, One Dimensional Design of Centrifugal Compressors Taking into Account Flow Separation in the Impeller, Von Karman Institute for Fluid Dynamics Turbomachinery Department, June 1978.
9. Savu, G., Trifu O., and Dumitrescu, L. Z. Supresssion of shocks on transonic airfoils, In: Proceedings of 14th International Symp. “Shock tubes & Waves”, Sydney, Australia, 1983, NSW university press, 1984, 92–101.
10. Bruneau, C. H., I. Mortazavi, Numerical modelling and passive flow control using porous media, Computers & Fluids, 2007, 37, 5, DOI:10.1016/j.compfluid.2007.07.001

11. Frink, N. T., D. L. Bonhaus, V. N. Vatsa, and S. X. S. Bauer, A boundary condition for simulation of flow over porous surfaces, 19th Applied Aerodynamics Conference June 11-14, 2001/Anaheim, California.
12. Ling Zhou, Dehua Chen, Yang Tao, Guangyuan Liu, Shuheng Song, Shidong Zhong, Paasive shock wave/boundary layer control of wing at transonic speeds, Theoretical&Applied Mechanics Letters, 2017, 7, 325–30.
13. Dragan, V., Contributions Regarding the Design of a Self Super Circulated Rotary Wing, 16th International Conference on Modern Technologies, Quality and Innovation.
14. Jixiang, S., Ling, Z., Xin, P., & Shidong, Z. Computational Analysis on Porosity Effect on Aerodynamic Characteristic of Supercritical Airfoil, In: 5th International Conference on Intelligent Systems Design and Engineering Applications, 2014, 310–13.
15. Geyer, T., E. Sarradj, and C. Fritzsche, Porous Airfoils: Noise Reduction and Boundary Layer Effects, 15th AIAA/CEAS Aeroacoustics Conference (30th AIAA Aero-acoustics Conference), 11-13 May 2009, Miami, Florida.

Bulgarian Academy of Sciences. Space Research and Technology Institute.
Aerospace Research in Bulgaria. 32, 2020, Sofia

DOI: https://doi.org/10.3897/arb.v32.e11

2.5D LES SIMULATION OF AN AIRFOIL SHOCK WAVE REDUCTION BY USING POROUS MEDIA

Ion Malael, Ioana Octavia Bucur, Valeriu Dragan

National Research and Development Institute for Gas Turbines COMOTI, Romania
e-mail: ioana.bucur@comoti.ro

Key words: *Airfoil, Numeric Simulations*

Abstract

Supersonic flight has become a practical reality since the 1950s. One of the first ways to study high speed effects of the shock waves is to evaluate the aerodynamic coefficients of an airfoil. The work described herein refers to a series of 2.5D LES numeric simulations, to investigate the behavior of the shock wave on the airfoil. To reduce the unwanted effects, a porous surface is placed on 80% of suction and pressure side of a NACA 0012 airfoil. Solving the motion equations was carried out with Ansys Fluent. Qualitative comparison consists in the pressure contours visualization for different angles of attack, showing how shock waves form on the airfoil surfaces. After plotting the polar diagrams, CL = f(AoA) and CL = f(CD), a quantitative comparison was made between the baseline airfoil and the same airfoil but with porous media on each surface side.

Introduction

Current literature regarding porous media focuses mainly on the flow through such a medium and its engineering applications, such as thermal transfer or acoustic lining [1]. One approach to define and characterize porous media is presented by W. Ehlers and J. Bluhm [2]. A review of thin porous media state of the art is briefly analyzed in [3], with a main focus on new developed theories that address the matter, such as GDL (Gas diffusion layers), MPN (molecular pore network), PTM (pore topology method). With this baseline, experiments and numerical applications were conducted in the medical field and biotechnology [4, 5] and innovative technologies in the energetic field [6]. Recent studies show how applications of porous media can improve flow in a wind tunnel. Khalid et al. use porous boundaries and manage to obtain better results when simulating the flow through a wind tunnel. Porous media was used in their paper [7] to reduce the wall interference effects.

A lesser known application of porous media is the behavior of shock waves in regard to it and may provide genuine optimization solutions. A study referring to steady shock waves in porous aluminum that concentrates mainly on the interaction

between the metal and the shock wave is presented in [8]. Its conclusions sustain the theory that porous metals help in the mitigation of shock waves formation. Furthermore, alongside with researches regarding porous metals, there are also papers analyzing the behavior of shock waves in porous plastic solids [9]. Cohen and Durban attempt to determine the influence of porosity on plastic solids using as a baseline the Gurson model from 1977. Their findings in [9] conclude that porous medium can influence the presence of shock waves by delaying their appearance and also such a medium slows down their propagation speed.

G. Savu published his research regarding the porous airfoil in transonic flow in the early 80's. He and his colleague carried on numerical and experimental work on the behavior of a porous airfoil with a plenum chamber placed on the suction side. They observed, in a supersonic wind tunnel, that the shock wave formed on the upper surface of the airfoil can be splitted in smaller waves by using porous media on that surface [10].

Another relevant point of view is offered by Gubin in his paper [11], in which he states that when the porous area expands and becomes greater than that of the shock wave, the technique will have a greater impact.

In order to study the flow over an airfoil with porous media on the suction side it is necessary to review the patterns regarding shock wave formation over a standard airfoil model. This phenomenon is analyzed in [12], where the author uses a NACA 0012 airfoil and considers angles of attack varying from 0° to 5° in a transonic regime with Mach numbers in the range of 0.2 and 0.8.

In previous years, due to software development in the field of computational fluid dynamics, the technology advances made it possible to detect shock waves through some specific methods, more accurately than in the early case studies. These methods include density gradient maxima, normal Mach number and characteristics which are briefly presented with their advantages and disadvantages in [13]. Based on these methods, researchers have determined other optimized ways to detect shock waves, taking into account its mathematical definition and implying the use of eigenvectors and the Riemann invariants [14].

The 2.5D LES (Large Eddy Simulations) are known to give more accurate results and be more efficient in comparison with other CFD approaches, such as 2D URANS (Unsteady Reynolds-Averaged Navier-Stokes) or 2.5D URANS, in terms of aerodynamic performance evaluations [15–17].

This paper is aiming to investigate the behavior of the shock wave formed on an airfoil placed in a high speed flow. The 2.5D LES simulations was carried to cover a set of geometrical and aerodynamic configurations representative for shock wave regime.

CFD Setup

With a physics-based understanding of the flow instabilities that occur at high speeds over an airfoil, we can develop a viable control technology for flow

instabilities that will allow the airfoil to operate at an increased efficiency in that regime. Due to the dimensional nature of the unsteady aerodynamic phenomenon occurring during the appearance of a shock wave, the full extent of the implications and interactions can be captured by fully viscous 2.5/3D unsteady CFD simulations. However, lower order models are known to provide valuable guidelines regarding the properties of unstable flow patterns in flow around airfoils.

High-fidelity computational approaches like Large Eddy Simulation (LES) [18] or Detached Eddy Simulation (DES) [19] are suitable for understanding flow dynamics associated with aerodynamic flows. They are resolving (not modelling) a large range of flow scales.

The CFD used in this study integrates the LES discretized fully compressible Navier-Stokes equations describing the conservation of mass, momentum and total energy. Therefore, the Navier-Stokes equations have to be filtered with respect to the grid size in order to obtain the LES governing equations [20].

(1)
$$\frac{\partial \bar{u}_i}{\partial x_i} = 0$$
$$\frac{\partial \bar{u}_i}{\partial t} + \frac{\partial}{\partial x_j}\left(\overline{u_i u_j}\right) =$$
$$= -\frac{1}{\rho}\frac{\partial \bar{p}}{\partial x_i} + \nu \frac{\partial}{\partial x_j}\left(\frac{\partial \bar{u}_i}{\partial x_j} + \frac{\partial \bar{u}_j}{\partial x_i}\right) =$$
$$= -\frac{1}{\rho}\frac{\partial \bar{p}}{\partial x_i} + 2\nu \frac{\partial}{\partial x_j} S_{ij}$$

In this paper three cases were numerically investigated starting with the NACA 0012 baseline airfoil. In the other two cases the structure of porous media was changed: in the first case the airfoil was perforated on 80% of its upper/lower surface, fourteen times and in the second case the airfoil has twenty-six holes to simulate a porous media. Fig. 1 presents the geometries of the studied cases.

a) *b)* *c)*

Fig. 1. Cases geometry: a) baseline, b) porous media case with 14 holes, c) porous media case with 26 holes

Accurate CFD methods require domains large enough to minimize the boundary effects on the resulted prediction of the shock wave evolution. In Fig. 2, the computational domain used in all three simulations is presented. In terms of boundary conditions, pressure far field condition with Mach number value at the domain border was imposed while for the airfoil, a no-slip wall BC was used.

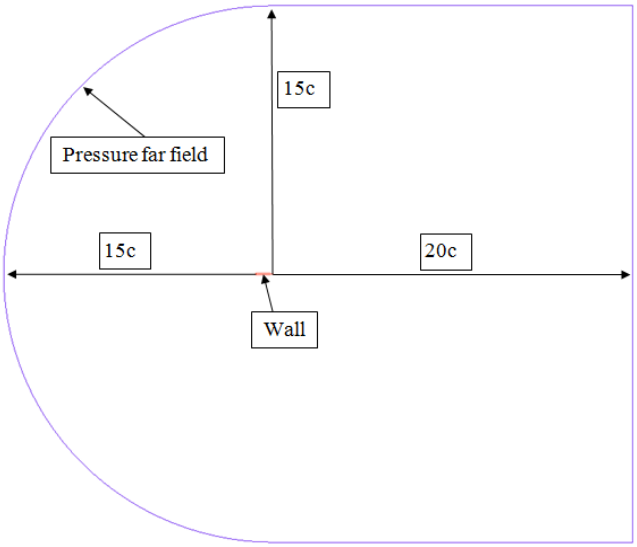

Fig. 2. Computational domain

Mesh quality is a major factor in order to avoid slow convergence, or even convergence problems. Because of its complex dimensional structure, producing a good mesh of is not trivial.

The mesh was generated with ICEM CFD using block-structured meshing, controlled in terms of skewness, growth and aspect ratio. For representation purposes only, a course mesh generated by ICEM CFD for this study can be found hereafter.

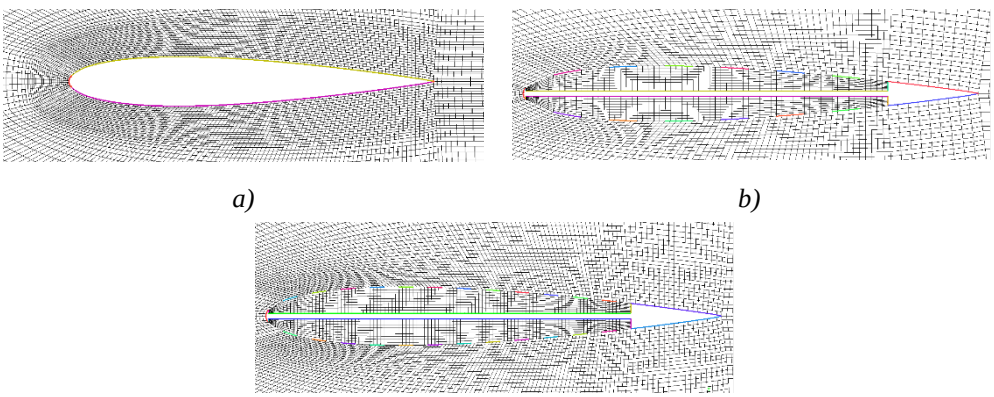

Fig. 3. Mesh: a) baseline, b) 14 holes porous media, c) 26 holes porous media.

The target final mesh size will be about 2.5 million grid cells for a case, with a ratio between two neighbour cells around 1.05. The first wall cell size was defined in order to reach a y^+ of the order of unity at the first point away from the solid walls.

Results

In order to determine the best size and ratio of the porous wall placed on an airfoil, in reducing the shock wave, several simulations were carried out, using the LES methods. It is a well known issue that on the airfoil in a high speed flow the shock wave has a bad influence on aerodynamic efficiency, generating entropy and leading to boundary layer interactions which are difficult to control in flight. For the baseline, the NACA 0012 was used and after that it was modified for the other two cases, where PM was installed on 80% of the airfoil surface. In Fig. 4 the static pressure flow field for the three studied cases it's presented at different angle of attack.

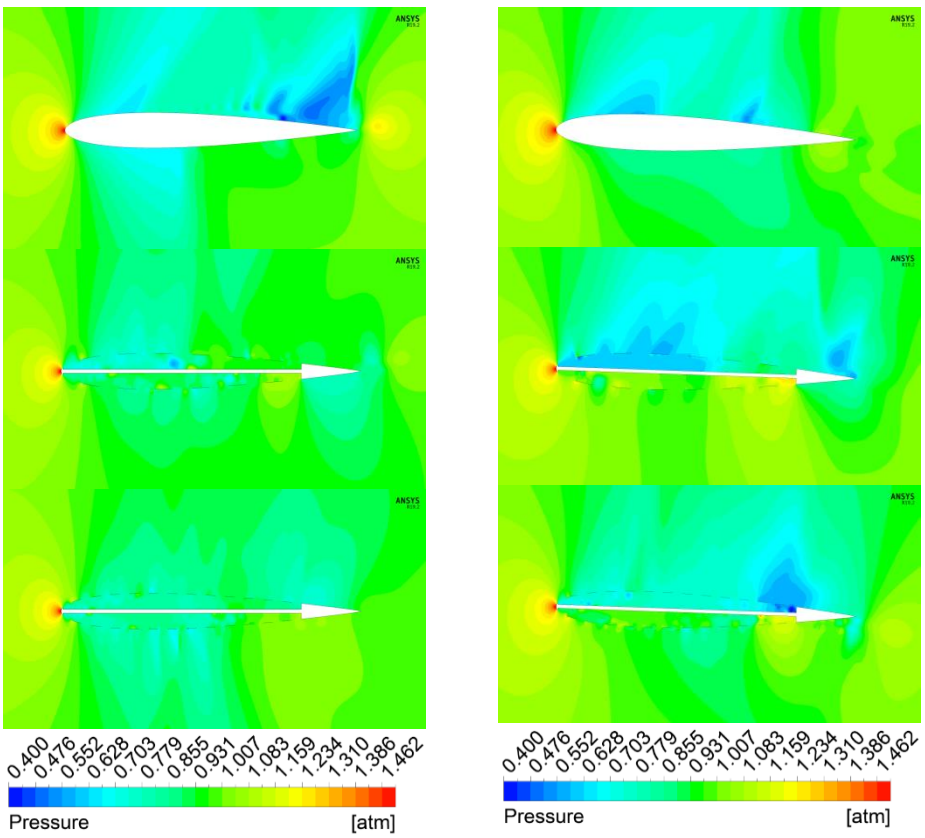

a) 0º AoA *b) 2º AoA*

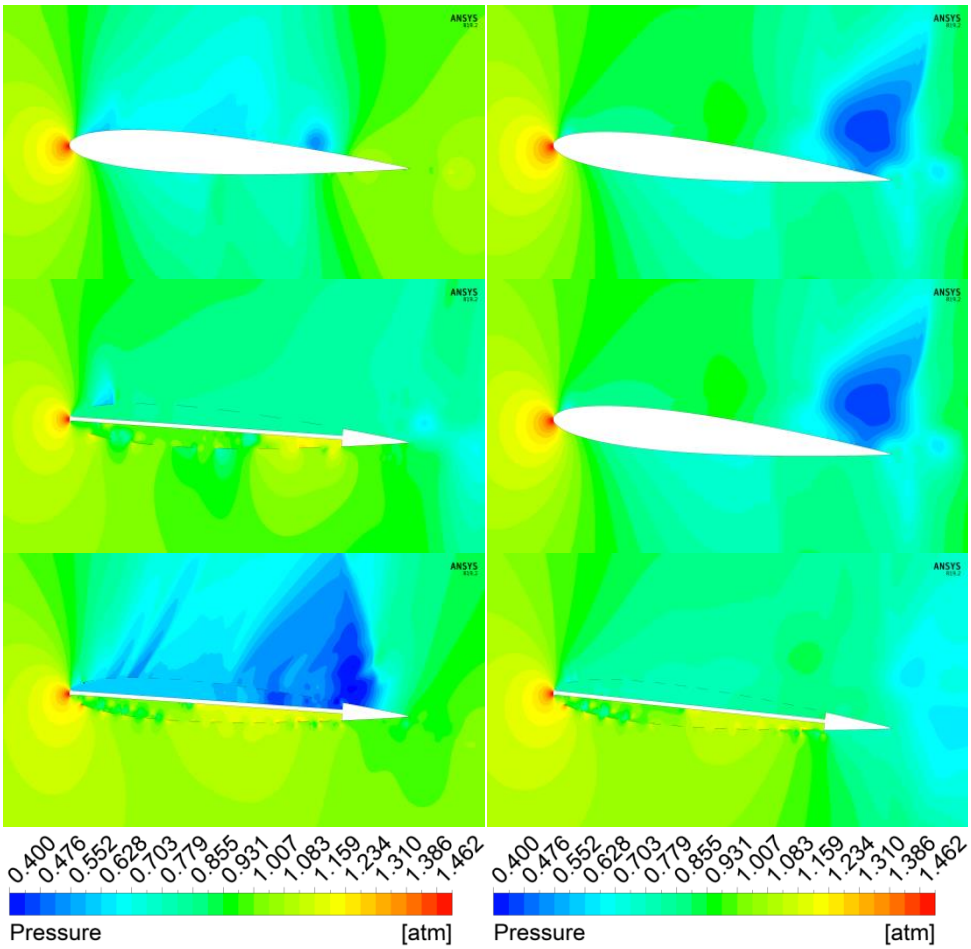

c) 4º AoA

d) 6º AoA

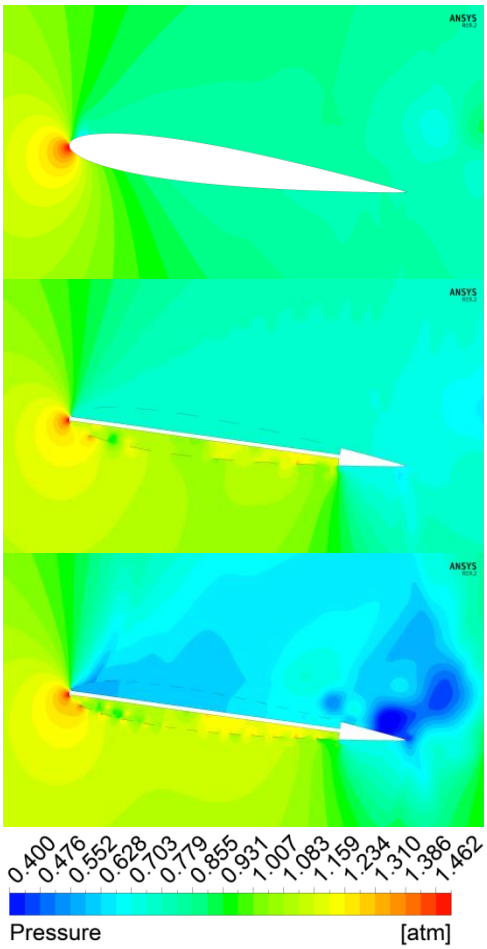

e) 8º AoA

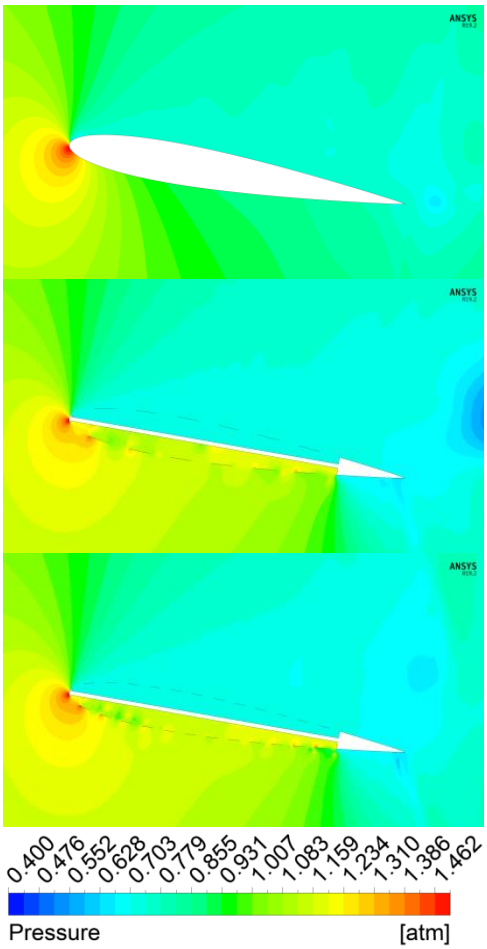

f) 10º AoA

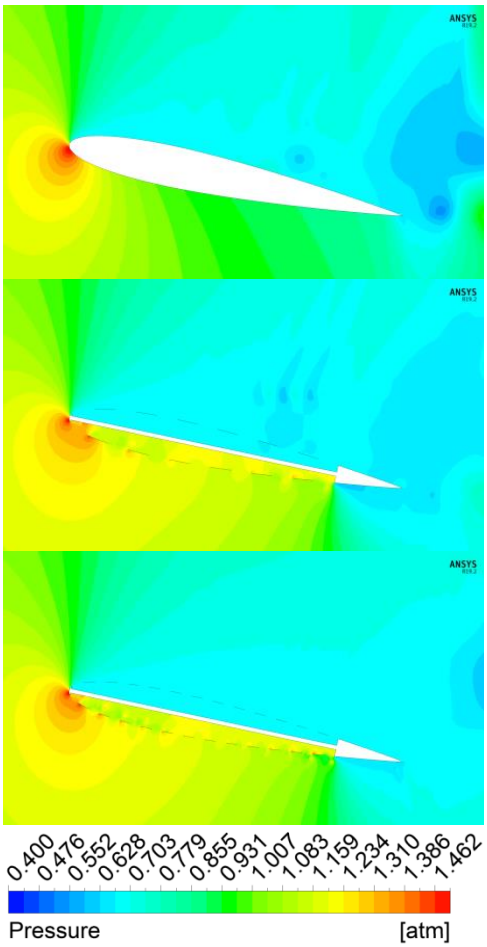

g) 12º AoA

Fig. 4. Static pressure flow field at: a) 0º AoA, b) 2º AoA, c) 4º AoA, d) 6º AoA, e) 8º AoA, f) 10º AoA, g) 12º AoA.

Fig. 5 shows the variation of the lift coefficient for different angles of attack. The maximum value for the airfoils with PM is obtain at AOA = 4 degrees, compared to the baseline where the CL max is at AOA = 2 degrees. A note must be made that the NACA 4 series is not suitable for high Mach number; hence the atypically low angles of attack.

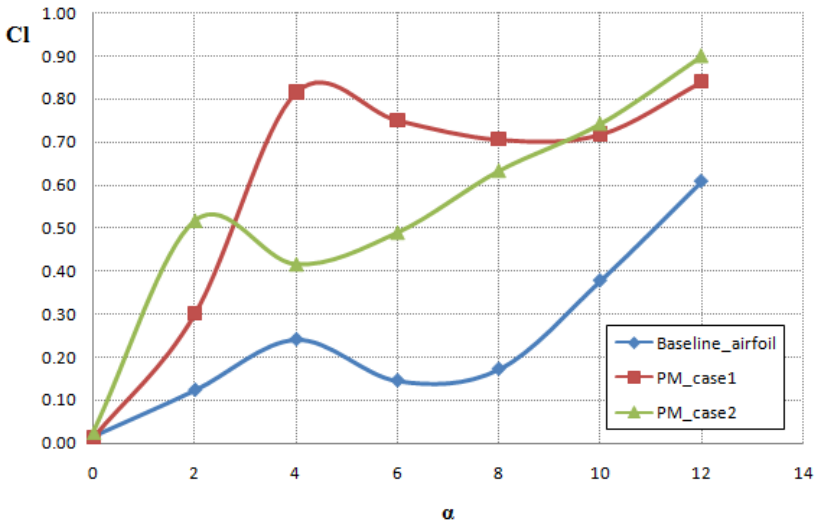

Fig. 5. Lift coefficient variation as function of AoA

Regarding the drag coefficient variation, figures 6 and 7 depict the impact on lift and lift to drag ratio evolution of the various porous configurations.

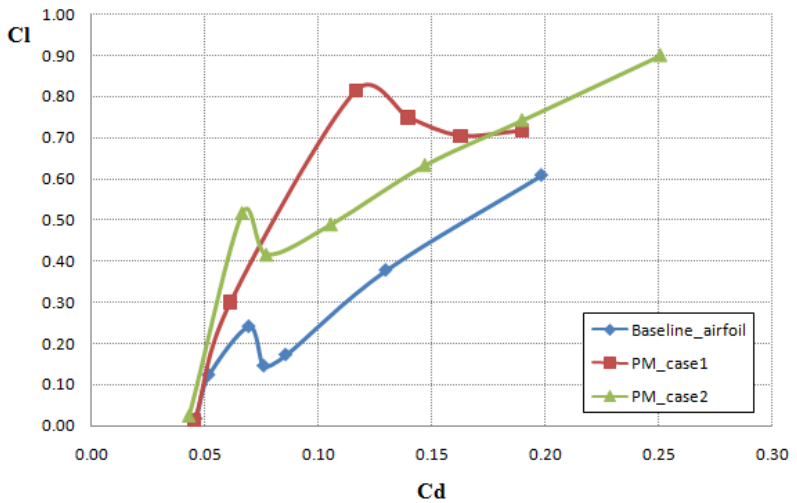

Fig. 6. Lift coefficient variation as function of drag coefficient – note the "drag bucket" extension of PM1

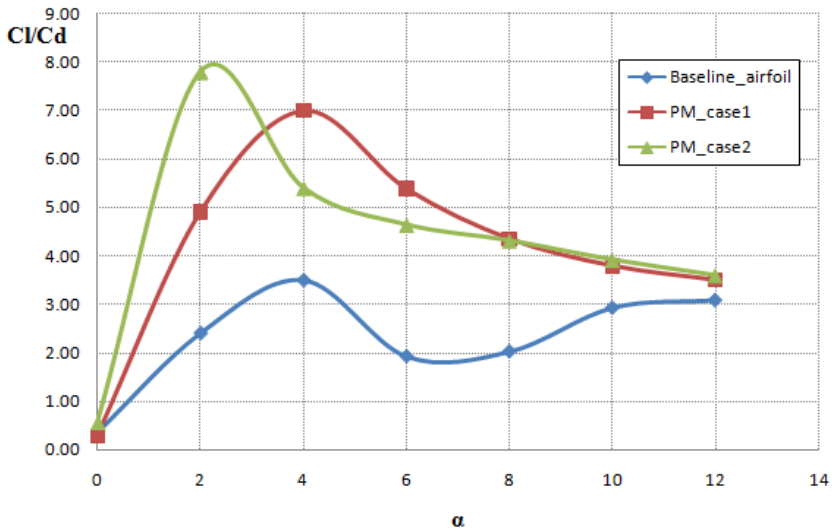

Fig. 7. Lift to Drag ratio variation as function of drag AoA

Conclusion

The first major conclusion that can be drawn from this study is that porous walls have a definite effect on the high speed aerodynamics of airfoils.

Lift coefficients improved on both cases, with a finer orifice airfoil having a maximum at lower AoA compared to the other cases. Due to the greater size of the orifices, the first porous wall case PM1 behaved similar to a flat plate with a qualitative evolution similar to the baseline - although with better quantitative values. The more fine porous wall, PM2, also showed clear improvement in both lift and lift-to-drag ratio, but with the added note that the peak performance was registered at a lower value of the AoA than the baseline and PM1.

Not very intuitively, the drag bucket of PM2 was more similar to that of the baseline - to the extent that one can define such a notion when using this family of airfoils under these conditions. The coarser orifice wall of PM1 leads to the overall extension of this region of interest, therefore making it more useful to the designers who must factor in stability and range of motion.

It is unclear wheather or not the shape of the plenum is relevant to the overall performance but this parameter is worth further investigation.

Future Work

As future studies an experimental model of a centrifugal stator with porous media on the blades will be manufactured using the National Research and Development Institute for Gas Turbine – COMOTI technological research

infrastructure (Fig. 8a). After that a tests campaign will be carried out to validate the numerical results (Fig. 8b).

a) *b)*

Fig. 8. a) CNDMU 70 Deckel Maho machine, b) NRDI COMOTI centrifugal compressor testing facilities

Acknowledgement

This work was carried out within *"Increasing Excellence in Research - Development of RRDI for Gas turbine* – COMOTI" Project CREaROR", supported by the Romanian Minister of Research and Innovation, project number Ctr. 3PFE/2018.

References

1. Bear, J. Dynamics of Fluids in Porous Media. Michigan, American Elsevier Publishing Company, 1972, 764 p.
2. Ehlers, W., J. Bluhm. Porous Media: Theory, Experiments and Numerical Applications. Berlin, Springer-Verlag, 2002, 459 p.
3. Yeghiazarian, L., K. Pillai, and R. Rosati. Thin Porous Media. Transport in Porous Media, 2016, 115, 3, 407–10.
4. Vafai, K. Porous Media: Applications in Biological Systems and Biotechnology. Florida, CRC Press, 2010, 632 p.
5. De Lemons, M. Turbulence in Porous Media: Modeling and Applications, Second Edition. Amsterdam, Elsevier, 2012, 408 p.
6. Mujeebu, M. A., M. Z. Abdullah, M. Z. Abu Bakar, A. A. Mohamad, and M. K. Abdullah. Applications of porous media combustion technology – A review. Applied Energy, 2009, 86, 9, 1365–75.
7. Khalid, M., K. A. Juhany, and S. Hafez. Computational modeling of the flow in a wind tunnel. Aircraft Engineering and Aerospace Technology, 2018, 90, 1, 175–85.
8. Czarnota, C., A. Molinari, and S. Mercier. The structure of steady shock waves in porous media. Journal of the Mechanics and Physics of Solids, 2017, 107, 204–28.

9. Cohen, T., D. Durban. Steady shock waves in porous plastic solids. International Journal of Solids and Structures, 2015, 71, 70–78.
10. Savu, G., O. Trifu. Porous Airfoils in Transonic Flow. American Institute of Aeronautics and Astronautics Journal, 1984, 22, 7, 989–91.
11. Gubin, S. A. Shock waves in porous media. Jorunal of Physics: Conference Series, 2018, 1099.
12. Leite, H. F., A. C. Avelar, J. B. P. F. Filho, and R. G. A. da Silva. Experimental Study of Shock Wave Patterns over an Airfoil. American Institute of Aeronautics and Astronautics: Conference Paper – Shock Dominated Flows I, 2016, DOI: https://doi.org/10.2514/6.2016-3935.
13. Ziniu, W., X. Yizhe, W. Wenbin, and H. Ruifeng. Review of shock wave detection method in CFD post-processing. Chinese Journal of Aeronautics, 2013, 26, 3, 501–13.
14. Kanamori, M., K. Suzuki. Shock Wave Detection based on the Theory of Characteristics for CFD Results. 20th AIAA Computational Fluid Dynamics Conference, 2011, DOI: https://doi.org/10.2514/6.2011-3681
15. Li, C., S. Zhu, Y. Xu, and Y. Xiao. 2.5D large eddy simulation of vertical axis wind turbine in consideration of high angle of attack flow, Renewable Energy, 2012, 51, 317–30.
16. Zhang, Y., H. Chen, S. Fu, and W. Dong. Numerical Study of an airfoil with riblets installed based on large eddy simulation. Aerospace Science and Technology, 2018, 78, 661–670.
17. Oro, J. M. F., A. Meana-Fernández, M. G. Vega, B. Pereiras, and J. G. Pérez. LES-based simulation of the time-resolved flow for rotor-stator interactions in axial fan stages. International Journal of Numerical Methods for Heat & Fluid Flow, 2019, 29, 657–681.
18. Rumsey, C. L., T. Nishino. Numerical study comparing RANS and LES approaches on a circulation control airfoil. International Journal of Heat & Fluid Flow, 2011, 32, 5, 847–864.
19. Szydlowski, J., M. Costes. Simulation of Flow Around a Static and Oscillating in Pitch NACA 0015 Airfoil Using URANS and DES. ASME 2004 Heat Transfer/ Fluids Engineering Summer Conference, 2004, 2, 891–908. DOI: https://doi.org/10.1115/HT-FED2004-56437.
20. Sagaut, P. Large Eddy Simulation for Incompressible Flows (3rd Edition). Berlin, Springer-Verlag, 2006, 575 p.

Bulgarian Academy of Sciences. Space Research and Technology Institute.
Aerospace Research in Bulgaria. 32, 2020, Sofia

DOI: https://doi.org/10.3897/arb.v32.e12

XZ-SERIES OF UNMANNED AERIAL VEHICLES IN 2020

Svetoslav Zabunov

Space Research and Technology Institute – Bulgarian Academy of Sciences
e-mail: SvetoslavZabunov@gmail.com

Key words: *Multi-Rotor Unmanned Aerial Vehicles, XZ-Series of Drones*

Abstract

The XZ-series of unmanned aerial vehicles was initiated in 2014 initially as an endeavour of theoretical development of multirotor unmanned aircraft models. The idea and major work was done by the author of the current article, and now, by the year of 2020, the series is still in constant process of inventing new designs. Most of the models were patented at the Bulgarian Patent Office through patents for inventions or utility models. In the recent years, publications on the XZ-series models have appeared in foreign scientific journals with high scientific impact metric.

The XZ-series of flying machines includes various types of multi-rotor machines such as standard multi-rotors, fixed wing multi-rotors and compound multi-rotors.

This article is a concise guide, as concise as it can be, to the XZ-series of unmanned aerial vehicles as of middle 2020 and, as such, it shall be followed in the future by sequels, published regularly, summarizing the ongoing process of the XZ-series aircraft model development.

Introduction

Found in 2014, the XZ-series of unmanned aerial vehicles is in constant development today. The idea for the series belongs to the author of the current publication. Although started as a theoretical enterprise in originating novel multi-rotor unmanned aircraft models, it evolved into full-featured aircraft design process implementing all the needed on-board avionics, including a developed by the author autopilot (Z-pilot), dynamic reconfiguration battery module [2], motor controllers for brushless direct current electric motors, etc. A few models were brought to prototype stage and laboratory testing [1]. Many of the models were patented at the Bulgarian Patent Office through patents for inventions or utility models.

The XZ-series of aircraft includes multi-rotor aircraft of various types such as standard multi-rotor machines, fixed wing multi-rotor aircraft and compound helicopter multi-rotors. In the current article the XZ-series models are described

systematically in thematic groups related to their technological background and are summarized in an extended table for the sake of ease of reference.

In contrast to previous publications by the author, the current material does not compare the XZ-series models to classical multi-rotors of other inventors, but still does attempt to disclose the major advantages of the XZ-series models. There are other specific publications, aiming at detailed and elaborate presentation of each model to the scientific community and to the general public. These publications do compare the XZ-series models to the known state of the art technological achievements of the present day.

Information found in the table

As already mentioned, the models are divided into three major groups in respect to their construction and paradigm: standard multi-rotors, fixed-wing multi-rotors, and compound multi-rotors (see Fig. 1).

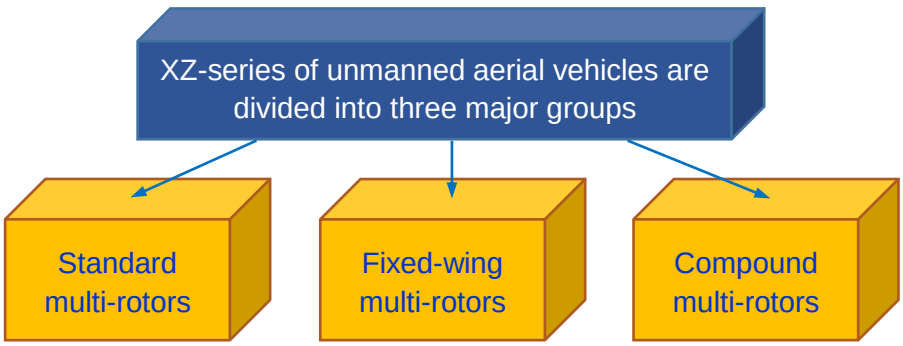

Fig. 1. XZ-series unmanned aerial vehicles are divided into three major groups

Standard multi-rotor aircraft are based on an airframe, which has no aerodynamic lifting properties but only supporting ones. The lift is generated by horizontal or close to horizontally oriented rotors and attitude control is attained by altering the speed of rotation of each individual rotor. In some cases, this group encompasses models having aerodynamic surfaces employed for attitude control only, but not for creating lift. Vertical or close to vertical rotors are also employed for attitude control.

Fixed wing multi-rotors are distinguished from the former group by having a fixed wing that generates lift in flight. These multi-rotors are still taking off and landing vertically not utilizing the fixed wing. The latter is relied on during forward flight only.

The last group of aircraft includes the so called compound multi-rotors. They employ vertical and horizontal rotors and no fixed wing. The horizontal rotors are used to generate lift, while the vertical rotors are engaged after take-off in order to generate horizontal trust and accelerate the aircraft in a horizontal motion without having the airframe inclined as with the standard multi-rotors to achieve horizontal propulsion.

The XZ-series of unmanned aerial vehicles as of 2020

Table 1. XZ-series of unmanned aerial vehicles complete list as of 2020

Model	Description and images
Model: **XZ-1** Group: **Standard** Topology: **H-frame** Rotors: **4** Year: **2014**	 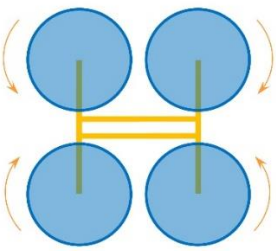 XZ-1 is a four rotor multi-copter based on the H-frame paradigm. It is the first model in the series and was used as a testbed for experimenting with the evolving idea of the edge-controller [3]. The model was also a testbed for the first version of Z-Pilot autopilot. The prototype is powered by lithium polymer batteries, 3 cell, 11.1 V nominal voltage. Radio control is established in the standard 2.4 GHz band. The employed brushless direct current electric motors are with KV rating of 1300 and maximum power of 60 W each. The used propellers are 11 inches in diameter.

Model	Description and images
Model: **XZ-1B** Group: **Standard** Topology: **H-frame** Rotors: **4** Year: **2014**	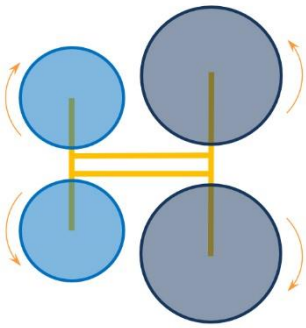 XZ-1B model is a variant of XZ-1 with asymmetric rotor design where two of the rotors on both sides of the main beam are larger and thus responsible for creating the main portion of the lift. The centre of mass in this model does not coincide with the geometric centre of the airframe and the smaller two rotors are used mainly for attitude control. All rotors are mounted above the fuselage.
Model: **XZ-1C** Group: **Standard** Topology: **T-frame** Rotors: **4** Year: **2014**	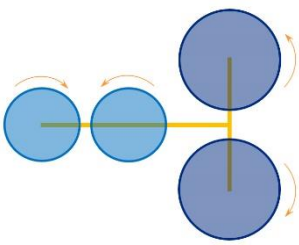 While the XZ-series does not include tri-copters, it does rely on T-frame paradigm of designing the airframe for some of its models. Such an example is the XZ-1C quadcopter. It is similar to XZ-1B for having two larger and two smaller rotors mounted above the fuselage, but the airframe is "T"-shaped.
Model: **XZ-1D** Group: **Standard** Topology: **T-frame** Rotors: **4** Year: **2014**	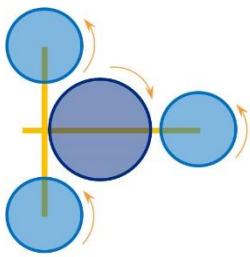 Another T-frame topology drone of the XZ-series with four rotors. Approximately half of the lift comes from the larger rotor, which is situated in the middle of the airframe while the rest of the rotors are used for the other portion of the lift and for attitude control. The rotors are mounted above the fuselage. The development stage is concept.

Model	Description and images
Model: **XZ-1E** Group: **Standard** Topology: **T-frame** Rotors: **4** Year: **2014**	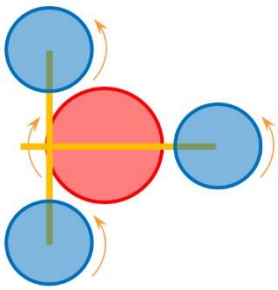 Still another T-frame topology drone and very similar to the previous design, the XZ-1D. The difference is that the larger rotor is mounted under the fuselage. This mounting strategy eliminates the possibility for carrying large payloads under the fuselage at its centre of lift or at its cross point, but reduces the downwash aerodynamic pressure on the airframe this improving flight efficiency. The development stage is concept.
Model: **XZ-1F** Group: **Standard** Topology: **Star** Rotors: **4** Year: **2014**	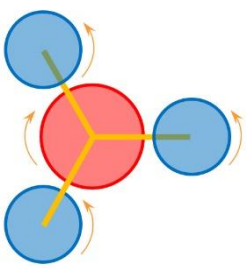 The XZ-1F is a Star-topology aircraft. This paradigm of building an airframe is untypical for the XZ-series, but was utilized in this model for the sake of implementing a symmetric construction for a tri-copter like design with the addition of a centre large propeller, responsible for the generating of roughly half of the lifting force. The latter rotor is undermount, thus guaranteeing the same benefits as with the previous model.
Model: **XZ-1G** Group: **Standard** Topology: **T-frame** Rotors: **4** Year: **2014**	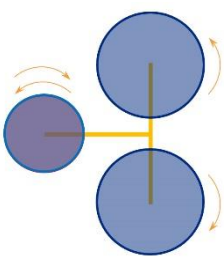 The XZ-1G is still another T-frame multi-rotor following the concept of XZ-1C, but having its two smaller rotors mounted coaxially, one over the other at its tail. The latter two propellers are contra-rotating. The two larger rotors are over-mount. This approach leads to smaller overall dimensions of the aircraft in comparison to XZ-1C.

Model	Description and images
Model: **XZ-1H** Group: **Standard** Topology: **T-frame** Rotors: **4** Year: **2014**	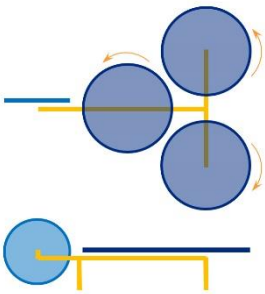 The XZ-1H is a design hybrid taking the approach of the tri-copter paradigm along with the T-frame topology of the fuselage, but also borrowing the idea from classic helicopters of a vertical attitude control rotor mounted at the tail. The major three propellers have same sizes and are horizontally mounted.
Model: **XZ-1J** Group: **Standard** Topology: **T-frame** Rotors: **4** Year: **2014**	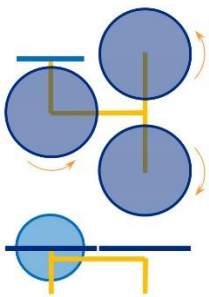 The XZ-1J multi-rotor is a development from the previous design XZ-1H. The new approach minimizes the dimensions of the copter by placing the vertical tail rotor on a supporting beam to one side of the central horizontal rotor, thus saving space. Stage of development is concept.
Model: **XZ-1A** Group: **Standard** Topology: **H-frame** Rotors: **5** Year: **2014**	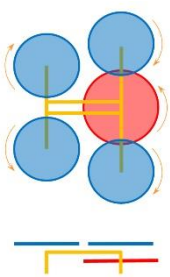 XZ-1A is an H-frame model that elaborates on the first representative of the series, the XZ-1 by adding an undermount rotor at one of the cross points of the fuselage. The additional rotor is larger and supports an increased payload of battery load, thus increasing the lifting and carrying capabilities of the aircraft. The dimensions are minimally enlarged, because the undermount rotor disc partially overlaps with the discs of the two neighbouring overmount rotors.

Model	Description and images
Model: **XZ-5** Group: **Standard** Topology: **H-frame** Rotors: **6** Year: **2014**	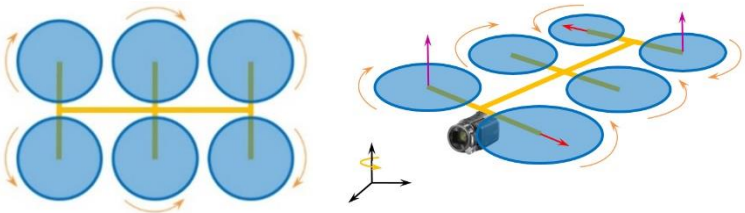 The design of XZ-5 multi-rotor is highly conceptual and theoretical. Although it is unpromising for real development for being constructively non-rigid, it serves the purpose of basis for further desings of multicopters with 6 or more rotors based on the H-frame paradigm. The characteristic payload hard-point position is shown in the above figure on the right. H-frame based aircraft are offering this type of hard-point, which is suitable for different types of payloads especially for a camera-based payload requiring large fields of view. All rotors are overmount.
Model: **XZ-5A** Group: **Standard** Topology: **H-frame** Rotors: **7** Year: **2014**	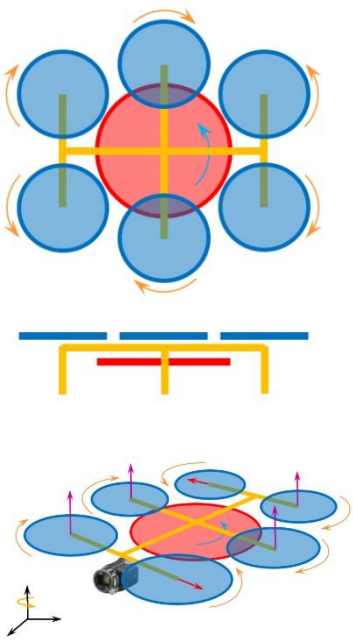 Evolving from the previous design XZ-5, another H-frame based multi-rotor is constructed – the XZ-5A model. A seventh rotor with larger dimensions is added at the centre of the fuselage and is undermount. This approach, as in previous design of the XZ-series, increases the lifting capabilities of the aircraft with little sacrifice of its dimensions, enlarging them at the centre along the smaller dimension. Such an aircraft is suitable for lifting larger payloads mounted at the centre of the fuselage. Again, certain measures should be followed to guarantee rigidity of the fuselage along its axis of symmetry by establishing a specifically suitable structure of the main beam of the fuselage, should the model be implemented in prototype design.

Model	Description and images
Model: **XZ-2** Group: **Standard** Topology: **H-frame** Rotors: **8** Year: **2014**	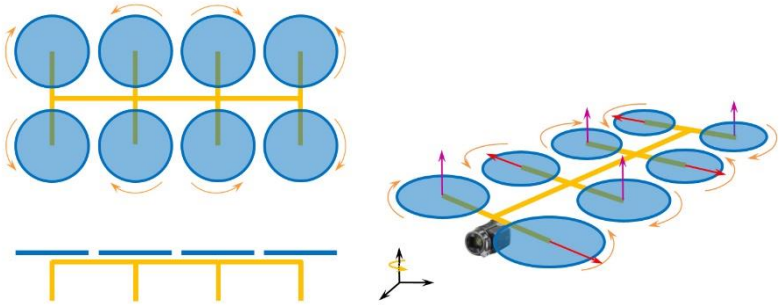 The XZ-2 model is development from the XZ-5. It adds another pair of rotors on the same type of H-frame based fuselage elongating it even further. This model is highly conceptual, similar to XZ-5, and serves for further developments of other more practical designs. All rotors are overmount.
Model: **XZ-3** Group: **Standard** Topology: **X-frame** Rotors: **8** Year: **2014**	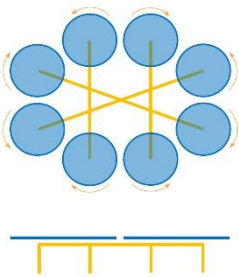 XZ-3 is a practical model with crossed beams in the fuselage in triangular structures insuring rigidity of the airframe. It is an eight-rotor aircraft. The ever increasing number of rotors in the consecutive models of the series aims at higher stability, quicker response to external factors, lower noise and vibrations and higher safety of operation. All rotors are overmount. The stage of development is concept.
Model: **XZ-6** Group: **Standard** Topology: **Honey comb** Rotors: **12** Year: **2014**	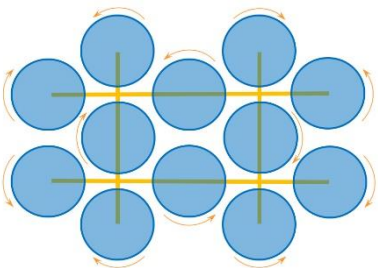 XZ-6 is the first model in the XZ-series designed along the honey comb paradigm. The approach guarantees optimal geometric covering of the horizontal plane with rotor discs thus minimizing the size and weight of the airframe structure and consequently improving the lifting capabilities of the aircraft and also its flying time and range. XZ-6 is again a practical design that led to the development of a few multi-rotors along the honey comb paradigm that reached prototype stage. All rotors are overmount. Its own stage of development is concept.

Model	Description and images
Model: **XZ-7** Group: **Standard** Topology: **Honey comb** Rotors: **12** Alias: **Bulgarian Knight** Year: **2015**	 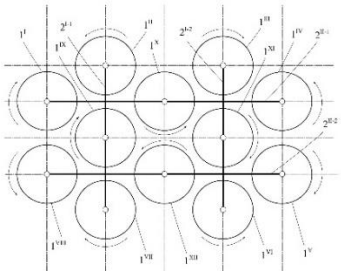 Bulgarian Knight multi-rotor is an award winning design and an article on this model was published in recently [1]. The model won a gold medal at the international inventions exhibition Tesla Fest 2016. Based on the same honey comb paradigm [10], the multi-rotor XZ-7 was the first aircraft to prove in practice the design benefits of the optimal covering approach and also of the undermount rotors scheme. Both ideas were shown to bring adventages of significant merit through the development of the *Bulgarian Knight* prototype and its laboratory tests. The stage of development is prototype. The aircraft was also used as a testbed in the early steps of the Z-Pilot Nano V1.0 development – the first version of a nano-drone variant of the Z-Pilot series of autopilots.
Model: **XZ-7-n-m** Group: **Standard** Topology: **Honey comb** Rotors: **R (see eq. 1.)** Year: **2015**	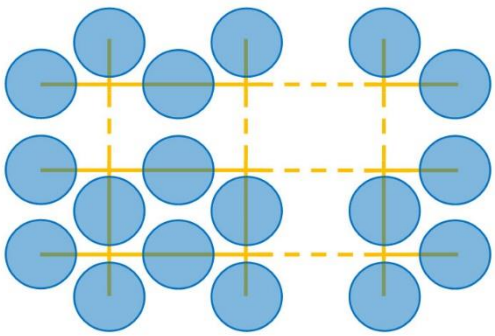 The **n** and **m** indices in the model designation denote respectively the number of rows and columns of beams making up the airframe. XZ-7-2-2 is equivalent to XZ-7 Bulgarian Knight multi-rotor. The XZ-7-n-m family of drones has its rotors under the airframe. The number of rotors in a given model variant is calculated after the observation that on each beam there are as many rotors as is the number of parallel beams to it plus one. Hence, the number of rotors R is: (1) $R = n * (m + 1) + m * (n + 1) = 2 * n * m + n + m$

Model	Description and images
Model: **XZ-14** Group: **Standard** Topology: **Tandem helicopter** Rotors: **6** Year: **2015**	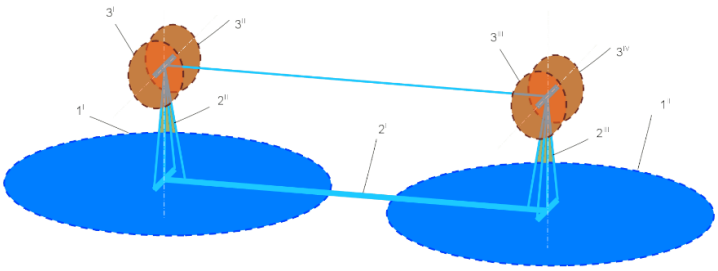 XZ-14 is a model belonging to the well-known tandem rotor helicopters group. This model, as all current XZ-series models, employs only fixed pitch propellers, hence for attitude control it requires 4 additional small vertical rotors, mounted on vertical beams. The large horizontal rotors, creating the lift force, are undermount in respect to the fuselage. XZ-14 is aerodynamically stable [5], in spite of its long vertical beams and the four small rotors mounted at their tops, because the centre of mass coincides with the aerodynamic centre of the aircraft. The model is an award winning invention and has won a gold medal at the international inventions exhibition Tesla Fest 2016, Novi Sad, Serbia.
Model: **XZ-15** Group: **Hybrid** Topology: **Tandem helicopter** Rotors: **6** Year: **2019** Alias: **Storm**	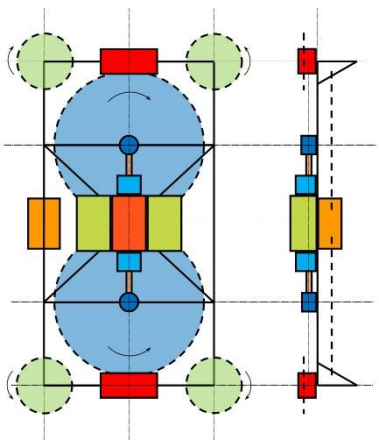 XZ-15 model is a development from the XZ-14 tandem multi-copter [9]. It is the only hybrid model in the XZ-series having an internal combustion engine as the main source of power. The engine is situated in the centre of the aircraft and is marked with red-orange colour in the figure to the left. The fuel tanks are the two green rectangles surrounding the engine. Along two transmission lines the torque of the engine is transferred to the fixed pitch large undermount horizontal rotors that are driven directly by the engine. On the transmission shafts two electric generators are employed generating electrical power that is buffered using batteries (red rectangles). The four small rotors have horizontal or close to horizontal orientation and are positioned at the edges of the fuselage. These rotors are driven by electric motors powered by the generators and the batteries. The latter rotors are used for attitude control, while the main two large rotors are employed in generating lift.

Model	Description and images
Model: **XZ-16** Group: **Standard** Topology: **Honey comb** Rotors: **16** Alias: **Emerald** Year: **2019**	 The XZ-16 multi-rotor is again an example of a honey comb structure drone. The honey comb approach seems very promising in creating new models with superior characteristics and performance. The XZ-16 was named Emerald and a prototype is under active development. The aircraft facilitates 16 rotors, horizontal in disposition and undermount in respect to the fuselage. The airframe has a rhombic shape, meaning the fuselage is elongated along the longer rhombus diagonal. Exactly this feature of XZ-16 led to the specific implementation of the aircraft, among others, as a stereo camera payload platform [6]. In this role the multi-rotor carries two cameras at the ends of its longest beam as shown with orange squares in the figure below. 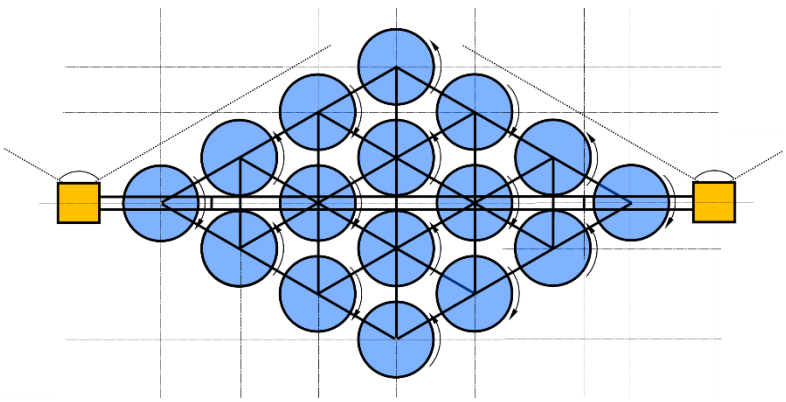 The developed prototype is of micro-drone dimensions weighing in the proximity of 160 g and employing rotors with propeller diameters of only 55 mm. This very realization of the model is suitable for reconnaissance tasks due to the small visibility footprint of the tiny aircraft and its superior noise characteristics. The aircraft's current prototype is also very safe to operate with, although not completely safe.

Model	Description and images
Model: **XZ-18** Group: **Standard** Topology: **Honey comb** Rotors: **18** Alias: **Diamond** Year: **2019**	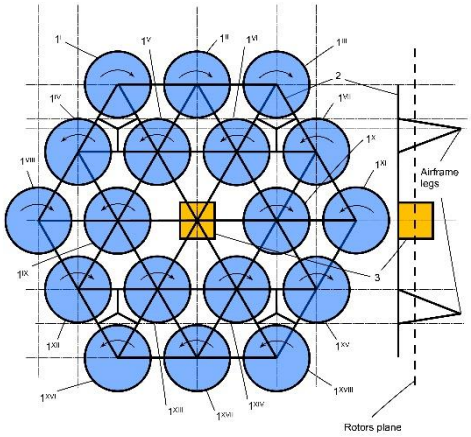 The Diamond model (XZ-18) is the latest model of the series. As it was mentioned above, the honey comb approach proved to be superior to other rotor schemes. As advancement in respect to the Bulgarian Knight drone the newer models that follow the honey comb paradigm do not rely of square beam airframes. Instead they are based on traingular beamed airframes (XZ-16 also) as the latter are considerably more rigid [7]. XZ-18 has 18 rotors, which are undermount. The under-mounting of the rotors increases the efficiency of lift and flight by 5% to 12% with different models and for XZ-18 the efficiency gain is expected to be 9%. Hence this mounting strategy is the preferred way of installing the rotors on multi-rotor aircraft in the recent XZ-series models. Further, the newer models have large numbers of rotors, exceeding 12 and thus allow the mounting of rotors under the fuselage without incurring any consequential problems with the implementation of landing legs and gear and utilizing hard-points for payloads. The hard-point for the payload in the Diamond multi-rotor UAV is in the centre of the fuselage structure. The aircraft relies on four legs for landing, each constructed out of three beams. For these reasons the multi-rotor is suitable mostly for payloads not requiring horizontal field of view, for example cameras photographing the terrain directly below the aircraft or other instrumentation such as ionizing radiation sensors, meteorological data acquisition systems, ground sensing radar or any other devices that are not dependant on the obstructed horizontal visibility. The Diamond multi-copter was conceived as a platform for testing the new micro- and nano-drone ionizing radiation sensors being under development with the purpose of designing drones and robots used for disaster management and ionizing radiation sources control. The first prototype is planned to be developed in the early 2020 and shall be again a nano-drone in the 200–250 g range of total weight.

Model	Description and images
Model: **XZ-4** Group: **Fixed-wing** Topology: **Tail-sitter** Rotors: **6** Year: **2014**	The first model of a series of fixed-wing multi-rotor aircraft having no moving control surfaces and relying only on the rotors rotations per minute to attain attitude control, because, as stated above, currently no model in the XZ-series implements variable pitch propellers. 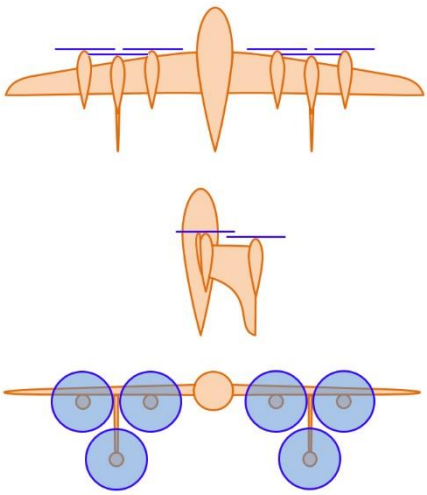 The XZ-4 [4] is a tail-sitter airplane that takes-off and lands on its tail – vertically as a multi-rotor drone and flies either vertically or horizontally. The horizontal mode is much more efficient and also offers higher speeds than the vertical regime of flight. In horizontal flight mode the aircraft is inherently unstable and relies on the autopilot to be stabilized. The current stage of development is concept, but due to the estimated superiority in comparison to existing vertical take-off and landing aircraft the model is planned for prototype development and laboratory and field testing. Because 6 rotors are employed, the failure of one of the four rotors mounted near the wing will not render the aircraft unconditionally uncontrollable. Nevertheless, the aircraft is not immune to catastrophic failure in case of propeller disintegration or a motor malfunction. The fixed-wing multi-rotors of the XZ-series are award winning inventions from Archimedes 2015, Inventarium Science 2015 and Tesla Fest 2015 international inventions exhibitions.

Model	Description and images
Model: **XZ-4A** Group: **Fixed-wing** Topology: **Tail-sitter** Rotors: **6** Year: **2014**	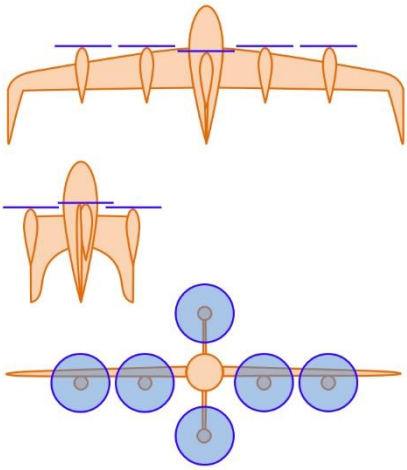 This model is similar to the XZ-4 aircraft, but exhibits a larger margin for rotor failure. Due to the mounting of the off-wing propellers not on one side, but on both sides of the wing, the failure of any rotor is in general terms manageable. The design proposes higher rigidity of the off wing rotor nacelles as they are mounted at the fuselage instead of at the wing, thus relieving the wing structure from excessive structural tension and the following structural strength require-ments. Stage of development is concept.
Model: **XZ-4B** Group: **Fixed-wing** Topology: **Tail-sitter** Rotors: **4** Year: **2014**	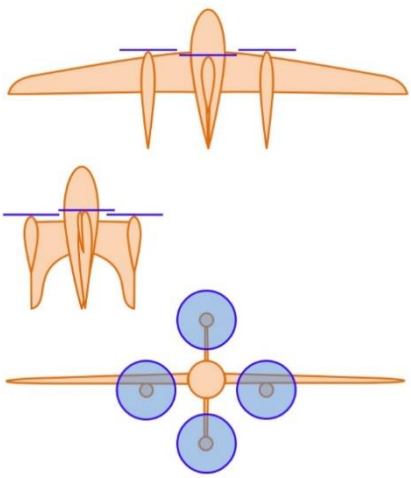 The XZ-4B is still another fixed-wing multi-rotor aircraft having only four rotors, instead of 6 as with the previous two models. The airplane is thus lighter, simpler and easier to maintain, but is prone to catastrophic failure if one of the rotors suffers a damage. XZ-4B is nevertheless a valuable testing platform for the vertical take-off and landing approach in the field of fixed pitch propeller multi-rotors. It also does not rely on moving aerodynamic surface for attitude control which makes it one of the simplest and cheapest aircraft in its class. The stage of development is concept.

Model	Description and images
Model: **XZ-5B** Group: **Compound** Topology: **H-frame** Rotors: **7** Year: **2014**	 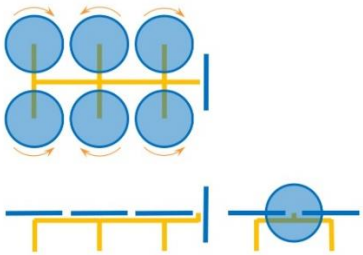 The XZ-series of drones includes compound helicopters. These are multi-rotors that rely on horizontal rotors for creating lift and at the same time they use vertical rotors for creating horizontal trust and moving the aircraft horizontally like an airplane. The benefits of this approach are numerous and large helicopter companies are evaluating this it such as Sikorski Aircraft and JSC Kamov. In the field of small UAVs such a design is novel and was pioneered by the XS-series through several of its models.
Model: **XZ-2A** Group: **Compound** Topology: **H-frame** Rotors: **9** Year: **2014**	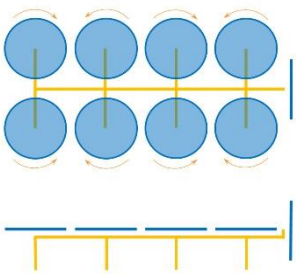 The XZ-2A model is again a development from XZ-2 which was turned into a compound multi-rotor. The model is again conceptual in its nature and serves only as a basis for the creation of practical compound multi-copters. The aircraft has 9 rotors, one of which is vertical at its tail and is used for horizontal propulsion.
Model: **XZ-2B** Group: **Compound** Topology: **H-frame** Rotors: **10** Year: **2014**	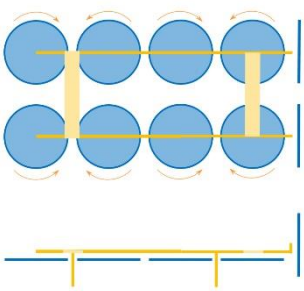 XZ-2B is the first compound model from the XZ-series that is created with the idea of complete realization and extensive prototype testing. This model is not only following the compound helicopter paradigm, but it is also designed for rigidity and speed. It is aerodynamically sound, has stable fuselage construction and its horizontal rotors are undermount in respect to the airframe.

Model	Description and images
Model: **XZ-6A** Group: **Compound** Topology: **Honey comb** Rotors: **12** Year: **2014**	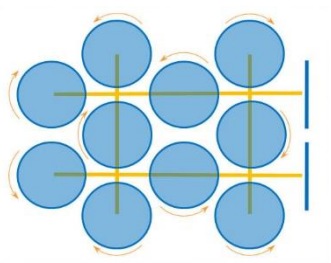 The XZ-6A model is a reduction from the XZ-6. Two of the horizontal rotors are removed and two vertical rotors are mounted instead in their places aimed at horizontal propulsion. The model benefits from the honey comb paradigm for optimal geometric covering of the horizontal rotors and also improves its horizontal speed properties by employing vertical rotors at its tail. The stage of development is concept.
Model: **XZ-2C** Group: **Compound** Topology: **H-frame** Rotors: **10** Alias: **Thunder** Year: **2019**	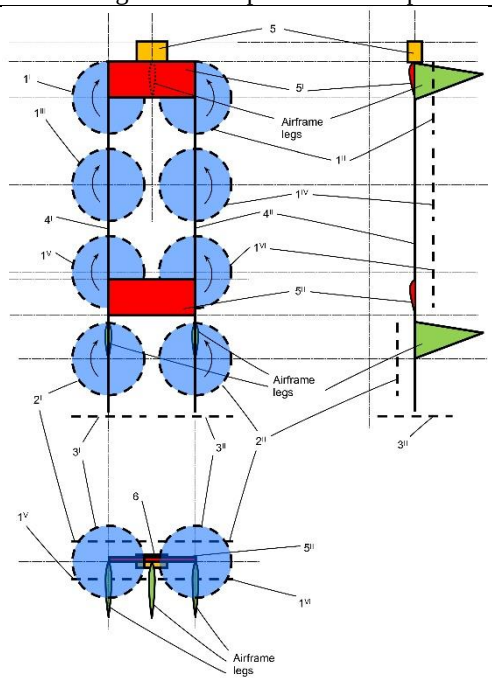 Still further improvement on the XZ-2B model is one of the latest developments in the XZ-series – the XZ-2C aircraft [8]. This multi-rotor has 10 rotors, 2 of which are used for horizontal propulsion and are mounted at the tail of the fuselage. The 8 horizontal rotors are mounted on two parallel longitudinal beams. The front 6 rotors are undermount while the rears 2 are over mount in respect to the beams, thus minimizing mutual interference among the horizontal rotors during forward flight. The two beams are connected using horizontal flat aerodynamic surfaces exhibiting aerodynamic lift when the aircraft is in fast forward flight. The aircraft lands on three flat streamlined legs. The payload is positioned at the front of the fuselage. This hard-point placement allows wide field of view in case of cameras used as payloads. The horizontal rotors' rotation directions are chosen in such a way that the non-stalled sections of the rotors are in minimal mutual interference. The current stage of development is concept with the aim of prototype development.

Conclusion

The XZ-series is in constant development during the last five years and is an evolving project. It is oriented towards multi-rotor aircraft in different variants and paradigms regarding multi-copters.

Multi-rotors require innovative development because this technology hides a significant potential for modern inventions. The field, although initiated during World War I, is still lacking significant scientific attention and one should be sparked.

The described developments are mostly theoretical, although not exclusively. Nevertheless, the focus on the work has moved towards real experiments with prototypes and flight tests.

The series has covered an astonishing variety of presentations in the scientific media acquiring publications with all kinds of scientific metric such as patents, international medals and awards received from exhibitions, conference reports, and scientific articles published in high impact journals.

References

1. Zabunov, S., and G. Mardirossian, Innovative Dodecacopter Design – Bulgarian Knight. International Journal of Aviation, Aeronautics, and Aerospace, 5, 4. https://doi.org/10.15394/ijaaa.2018.1293.
2. Zabunov, S. and G. Mardirossian, In-flight Reconfiguration of Lithium-ion Cells Aimed at Extending Flight Times and Range of Electrically Powered UAVs, International Journal of Intelligent Unmanned Systems, 7, 3, 98–111. https://doi.org/10.1108/IJIUS-08-2018-0026.
3. Zabunov, S. and Nedkov, R. (2019), "Edge controller – a small UAVs distributed avionics paradigm", Aircraft Engineering and Aerospace Technology, Vol. 92 No. 2, 229–236. https://doi.org/10.1108/AEAT-04-2019-0087.
4. Zabunov, S., P. Getsov, and G. Mardirossian, Vertical Take-off and Landing Airplane, Bulgarian Patent Office Utility model reg. № 2765 / 12.05.2014.
5. Zabunov, S., G. Mardirossian, and P. Getsov, Tandem Helicopter, Bulgarian Patent Office Utility model reg. № 3223 / 05.08.2019.
6. Zabunov, S., G. Mardirossian, and R. Nedkov, Multi-copter for Stereo Observations, Bulgarian Patent Office Utility model reg. № 3170 / 21.01.2019.
7. Zabunov, S., G. Mardirossian, R. Nedkov, 18-rotor Multi-copter, Bulgarian Patent Office Utility model reg. № 3169 / 23.01.2019.
8. Zabunov, S., G. Mardirossian, and R. Nedkov, 10-rotor Compound Multi-copter, Bulgarian Patent Office Utility model reg. № 3200 / 24.06.2019.
9. Zabunov, S., G. Mardirossian, Hybrid Multi-copter, Bulgarian Patent Office Utility model reg. № 3175 / 07.03.2019.
10. Zabunov, S., G. Mardirossian, Twelve-rotor Drone for Remote Sensing Applications, Bulgarian Patent Office, submitted on 11.10.2019.

XZ-СЕРИЯ БЕЗПИЛОТНИ ЛЕТАТЕЛНИ АПАРАТИ ПРЕЗ 2020

С. Забунов

Резюме

Серията XZ безпилотни летателни апарати стартира през 2014 г. първоначално като начинание, целящо теоретични разработки на мулти-роторни безпилотни летателни модели. Идеята и основната работа беше осъществена от автора на настоящата статия и сега, в 2020 г., серията е все още в непрекъснат процес на изобретяване на нови модели. Повечето модели са патентовани в Българското патентно ведомство чрез патенти за изобретения или полезни модели. През последните години се появиха публикации относно серията XZ в чуждестранни научни списания с висок наукометричен статус.

Серията от летящи машини XZ включва различни мулти-роторни летателни апарати като стандартни мулти-ротори, мулти-ротори с фиксирано крило и съставни мулти-роторни летателни машини.

Тази статия е кратко ръководство, толкова кратко, колкото може да бъде, върху състоянието на серията XZ безпилотни летателни апарати към 2020 г. Очаква се тя ще бъде последвана в бъдеще от продължения, публи-кувани редовно, които ще обобщават продължаващия процес на разработка на нови модели в серията XZ.

Bulgarian Academy of Sciences. Space Research and Technology Institute.
Aerospace Research in Bulgaria. 32, 2020, Sofia

DOI: https://doi.org/10.3897/arb.v32.e13

QUANTITATIVE ASSESSMENT OF PILOTING TECHNIQUE BY FLIGHT DATA RECORDER

Assen Marinov[1], Georgi Yordanov[2], Martin Kambushev[1], Stefan Biliderov[1], Kiril Kambushev[1]

[1]Aviation Faculty, National Military University
[2]Bulgarian Air Force
e-mail:asen_aerodynamics@abv.bg

Keywords: *Aircraft, Piloting Technique, Flight Activity, Flight Data Recorder*

Abstract

Flight training is a complex and responsible training process for pilot and requires experienced specialists, good organization and quality control of flight activity. Its main purpose is to create highly qualified personnel with long-term professional skills in the techniques of piloting, aircraft flying and the combat use of aircraft.

Assessment is an important part of the training process for young cadets. It determines the extent to which trainees have been able to perceive, learn and comprehend their new flying activity and their ability to apply the acquired knowledge in tense conditions. Assessment is directly related to the quality of the flight training, and it should show the trainees the mistakes they have made and encourage them to upgrade their knowledge and skills. The trainees should be well versed in the assessment methodology and understand its purpose, otherwise the grades obtained will not be an indicator of their ability.

1. Introduction

The high quality of training requires continuous improvement of the methodology for flight preparation and the use of modern technical means. The use of computer-based training tools and automated training systems have become important nowadays.

In order to determine the knowledge gained and the level of training, trainees should be assessed. Assessment is complex and involves assessing their theoretical knowledge, their practical skills, and their physical endurance and discipline.

Evaluation of the piloting technique is of paramount importance in forming the final assessment of the trainee. It is done after each flight, evaluating all the elements of the exercise. The rating is the arithmetic mean of the assigned performance estimates and has a different weight depending on the type of flight. For this purpose, an assessment sheet is completed, which together with other

documentation related to flight task is stored in student's personal file. The overall rating of the piloting technique is the arithmetic mean of the estimates of each flight.

The evaluation of the piloting technique by flight data recorder is performed on two levels – qualitative analysis of the elements of the exercise and quantitative assessment. Important for its determination are the records of parameters – speed, height and load factor.

Qualitative analysis includes:

- determining flight stages;
- defining completed elements;
- the order of completion of the assignment;
- determining the deviations and errors in the piloting technique.

In the quantification of the piloting technique, each element is evaluated as values of the recorded parameters, at certain stages of the executed element (the so-called control points), are compared with the set ones. Any deviations of parameters from setpoints are determined and evaluated accordingly.

In order to maintain the high quality of the training and to ensure that the assessment is correct, the training methodology must be continuously improved and assessment optimized. The main steps to increase the level of the training are:

- updating of the manuals regulating flight activity;
- realism, efficiency and flexibility in preparation;
- clear training methodology;
- up-to-date and accessible training programs;
- use of modern computer systems;
- use of flight simulators;
- clear standards for the evaluation of piloting techniques;
- updated student evaluation criteria;
- quality control.

2. Main purpose of optimization of flight technique' assessment

The main goal in optimizing the assessment of piloting techniques is to reduce the subjective factor in evaluating learners and improve the quality of training, using modern computer models and applications. The subjective factor can be reduced by correctly assessing the accomplished elements of the flight task in accordance with the approved assessment standards. Doing this after each flight (during the analysis of the exercise performed) or at the end of the flight, facilitates the work of the instructor staff.

In order to achieve this goal, the following main tasks must be accomplished:

- to create a computer application for research and storage of the data recorded by the aircraft flight data recorder;
- to create an algorithm for processing the recorded data and assessing the piloting technique;
- to create a computer model to compare the recorded flight parameters with their setpoints.

Another main objective is to create an electronic database for storing information and evaluations of completed flight tasks. In this way, students' personal files can be made electronic.

3. A computer application model for flight assessment

The computer application for flight tasks assessment allows, using the records from the flight data recorder of the aircraft, to perform a qualitative analysis of the exercise performed and to evaluate the flight. Each trainee has their own database, which contains all the necessary information about the exercises already completed and the relevant assessment. Based on the evaluation of the completed exercises an overall assessment of the level of preparation achieved can be determined.

The main features of the application are:

- adding data for a new learner;
- removing or editing already existing learner data;
- selection of trainee;
- introduction of data, important in the formation of assessment of the completed exercise;
- analysis of the information recorded by the flight data recorder;
- assessment of the elements performed in the exercise;
- an electronic database of exercises already evaluated;
- calculating the overall assessment of the level of preparation achieved.

Advantages:

- use computerized systems for assessing pilot training;
- instructor staff is facilitated;
- make an objective assessment.

The application allows three choices to be made (Fig. 1):

- selection of a pilot;
- add/remove pilot;
- editing.

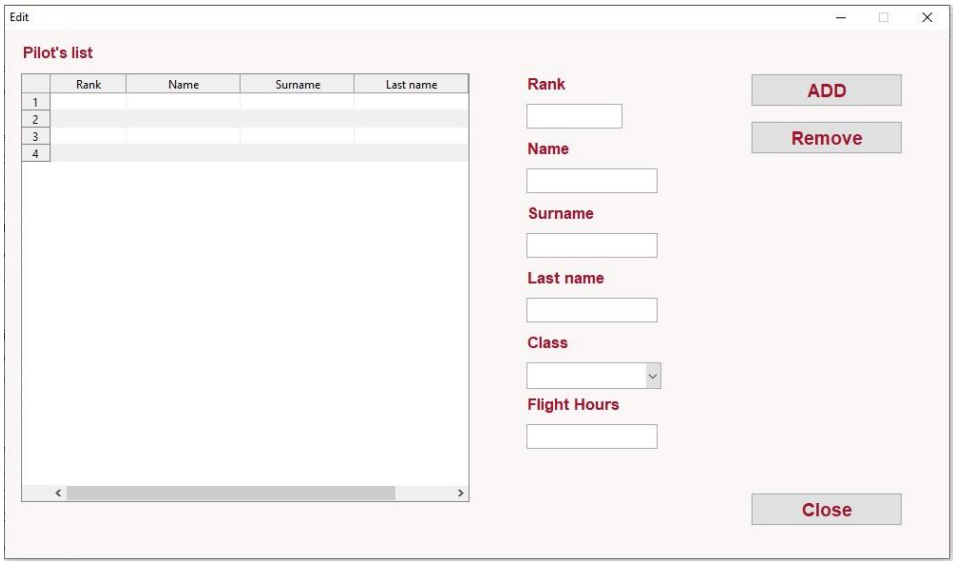

Fig. 1. Pilot's list

The choice of the trainee (pilot) to be assessed is related to the tasks they have already completed (Fig. 2). This information includes:

- exercise name and number and flight number;
- the type of aircraft on which the trainee flies;
- the flight height;
- the area of flight;
- type of flight;
- time of day;
- flight assessment.

The app allows you to add a flight to be evaluated, to remove incorrect information and to make an overall assessment of the level of preparation achieved.

All this information is printable.

Fig. 2. List of flight assessments

In order to evaluate the elements already selected, the entry from the flight data recorder must be added. This record can be taken in tabular form from the Flight Safety Office. Using this computer application, the recording is processed and presented graphically (Fig. 3). This allows the evaluator to see which the elements are and whether the safety measures are observed [1]. The evaluation of the elements is made by comparing the actual values of the flight parameters with those set by the already adopted evaluation standards (usually speed, load factor and altitude) [2].

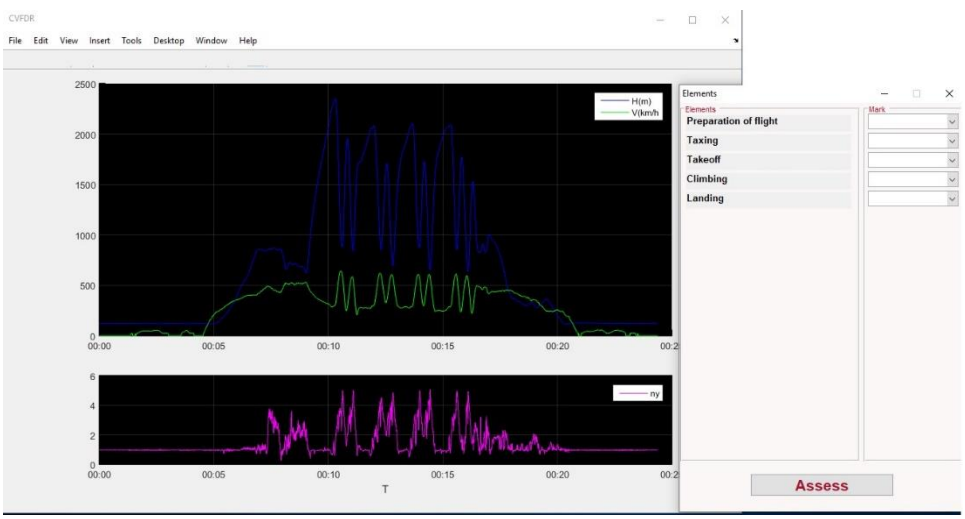

Fig. 3. CVFDR

Depending on the type of aircraft selected, the evaluator may see the relevant assessment standards.

The flight technique learning rate and the impact of pause are also important for the final assessment, so they can also be added.

When the flight assessment is made, all information is added and recorded in the database of the selected trainee.

For more accuracy during the analysis of the entry, the application allows the graphic to be zoomed in this part of the entry, where the element being evaluated is. Hereby the values of the recorded flight parameters can be determined more easily (Fig. 4).

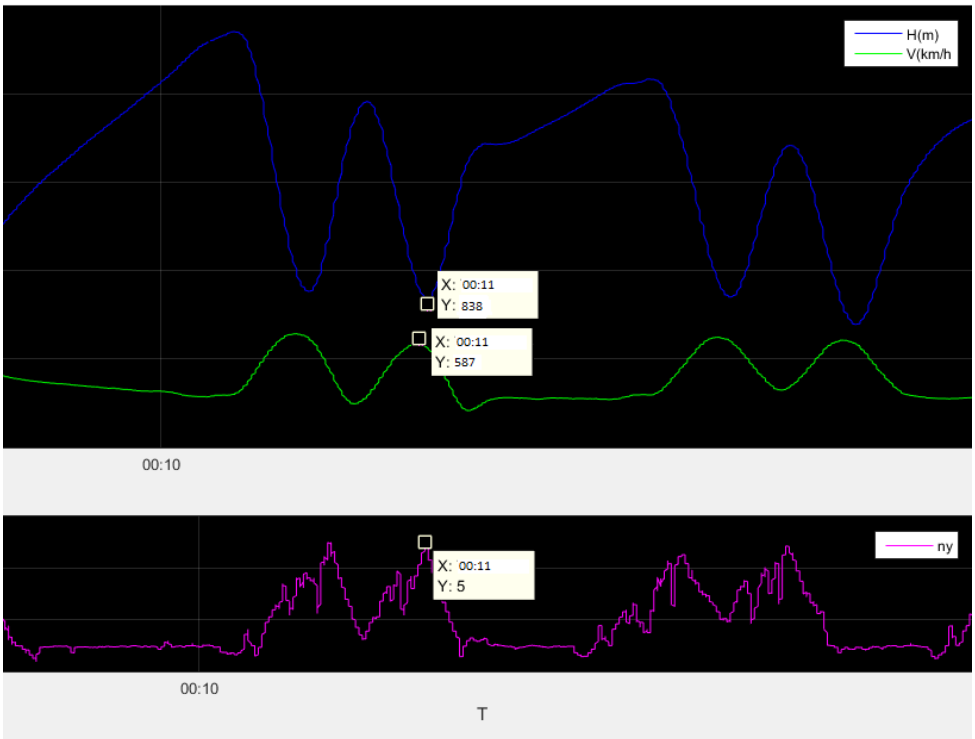

Fig. 4. Flight parameters

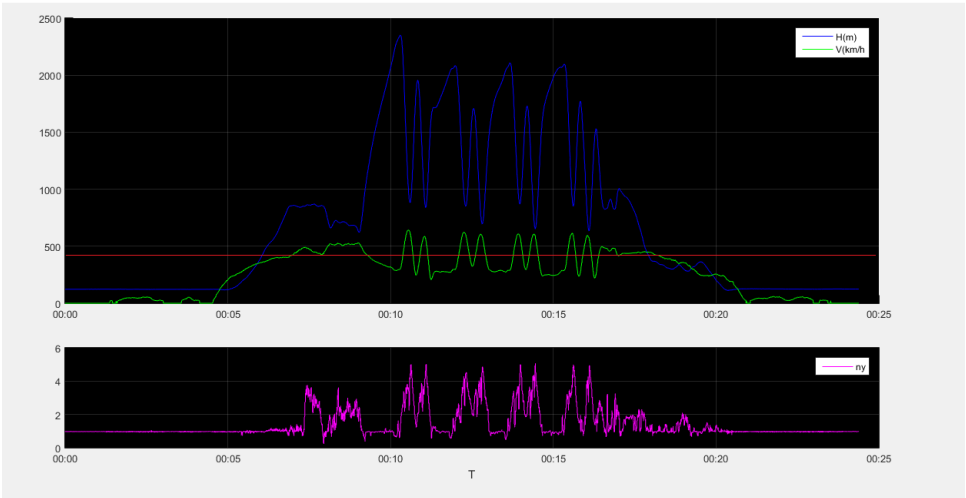

Fig. 5. Minimum safety height

When the area, the height and the type of flight are selected the minimum safety height is automatically determined – red line (Fig. 5). The minimum safety height is one of the important safety features. The minimum safety height can be different depending on the terrain and the pilot's skills. If the minimum safety height is violated, the instructor can see this on the entry, which is important in forming the flight assessment.

6. Conclusions

Quantitative evaluation of the piloting technique means the assessment of the pilot's actions in performing the flight elements in the different types of flight training. Unlike qualitative evaluation, in which the completed elements are determined and its main tasks is to determine the deviations and errors of the flight assignment, in the quantitative analysis, an assessment of the important elements of the type of preparation is made, and the main task is to determine their level. In the quantification of the piloting technique, each maneuver is evaluated by comparing the actual parameters for certain stages of the maneuver with recommended speeds, heights and load factor. The average value and the deviation are determined and the tolerances are compared.

References

1. Chikurtev, D., K. Yovchev, N. Chivarov, and I. Rangelov, Indoor Navigation Using Existing Infrastructure for Professional Service Robots, Advances in Intelligent Systems and Computing, 2019, 980, 231–239, ISBN: 978-303019647-9, ISSN: 2194-5357, DOI:10.1007/978-3-030-19648-6_27.

2. Chivarov, S, D. Chikurtev, K. Yovchev, and N. Chivarov, Multi-channel software infrastructure for remote control of service robots, 2019, Article number 8820362. ISBN: 978-172810521-5, DOI:10.1109/CoDIT.2019.8820362, 1283–1288.

КОЛИЧЕСТВЕНА ОЦЕНКА НА ТЕХНИКАТА НА ПИЛОТИРАНЕ ПО ЗАПИСИ ОТ РЕГИСТРАТОР НА ПОЛЕТНИ ДАННИ

А. Маринов, Г. Йорданов, М. Камбушев, С. Билидеров, К. Камбушев

Резюме

Оценяването е важна част от процеса на обучение на младия летателен състав, особено в случаите, когато от оценката зависи разпределението на обучаемите на самолет или вертолет. Оценяването на техниката на пилотиране в началния етап определя до каква степен обучаемите имат потенциал да възприемат, научат и осмислят новата за тях материя, и до каква степен успяват да приложат своите знания. Оценяването е пряко свързано с качеството на обучение, а оценката трябва да покаже на обучаемите пропуските, които допускат, а също и да ги стимулира да надграждат своите знания и умения. Обучаемите трябва да са добре запознати с методиката за оценяване и да разбират нейната цел, в противен случай, обучаемият остава с впечатлението, че получените оценки не са показател за техните знания и умения.

Bulgarian Academy of Sciences. Space Research and Technology Institute.
Aerospace Research in Bulgaria. 32, 2020, Sofia

DOI: https://doi.org/10.3897/arb.v32.e14

MODULE FOR WIRELESS COMMUNICATION IN AEROSPACE VEHICLES

Nikolay Gueorguiev[1], Aleksandar Kolarov[1], Ilian Iliev[2]

[1]Institute of metal science, equipment and technologies with Hidroaerodynamics centre "Acad. Angel Balevski"– Bulgarian Academy of Sciences
[2]Naval Academy "N. Vaptsarov", Varna, Bulgaria
e-mails: niki0611@abv.bg, aleksandar_kolarov@abv.bg, i.iliev@naval-acad.bg

Keywords: *Aerospace Vehicles, Wireless Communications, Composites, Sensors*

Abstract

The increase in air traffic and space flights, the rising cargo volumes and passenger numbers all set complex research and applied scientific tasks and therefore pose more complex requirements for obtaining up-to-date information on the system parameters and on the environment in which they function. After the advent of IoT platforms, their use in all areas of technology has been growing rapidly, as for instance in data collection and processing systems that are fully applicable to aviation needs. One of the major problems in the building of new systems or upgrading existing ones in line with current trends is the high cost of the innovations and the long time before their implementation. In line with the current trends in aviation, this paper proposes an approach for unified modules comprising a large set of possible sensors operating on a wireless standard for transmitting information and connected in a single and cost-effective network and with minimal time for construction, upgrading and renovation.

1. Introduction

There has been an exponential growth in the use of aeronautical and aerospace vehicles for various purposes. Also, a number of new types have come into existence, such as drones, unmanned aircraft, new classes of space rocket systems, and more.

Most devices related to the operation of aviation systems or their missions utilize multiple sensor-based, communications, executive and other types of means and it is often necessary to establish continuous or ad hoc information exchange between the ones located outside the skin of the aeronautic vehicle and those located inside [1–3]. In many cases, it is appropriate that the communication between the modules located on each side of the skin should be non-contact [4]. This will reduce the complexity of building a structure that requires resistance to

high mechanical accelerations and vibrations, as well as to sudden changes in ambient temperature.

Over the last few years, wireless sensor networks have focused professional interest towards the numerous theoretical and practical challenges associated with their application capabilities. Their wireless architecture enables easy measurement of physical parameters such as temperature, humidity, pressure, etc., as well as their integration into already existing measuring systems. Their flexibility and capabilities for mathematical analysis and processing of the data, as well as their easy programming, make it possible to build complete solutions for technological process monitoring [5].

Three basic technologies for wireless communications are available to date: radio frequency (RF) communication characterized by its high performance, optical transmission, which requires positioning on the line of sight, and the one most commonly used in modern underwater communications – acoustic (respectively hydroacoustic). In all these technologies, it is important to also consider the cost of bringing into production in relation to the target data bandwidth for a given frequency range. The wireless communication technologies suitable for use in aviation technology are the RF and optical ones. Nevertheless, the provision of a communication channel often requires engineering constraints that are extremely difficult to overcome [6, 7].

The article proposes an approach for providing wireless communication in aerospace vehicles based on the use of composite materials and of unified modules connected to a single network and operating on a wireless standard for transmitting information at a relatively low cost and requiring minimal time for building, upgrading and renovation.

The article proposes an approach for providing wireless communication in aerospace vehicles. The approach is based on the use of composite materials and of unified modules connected to a single network and operating on a wireless standard for transmitting information. It is charactersied by its relatively low cost and requires minimal time for building, upgrading and renovation.

2. Problem statement and solution

In the general case, the task of wireless communication comes down to the positioning on the skin of the aerospace vehicle of a device with good radio conductivity and/or optical transparency, and mounting on both of its sides of the transceivers of the wireless communication system. There are therefore two aspects to solving this problem:

- The first one involves the selection of a device with good radio conductivity to ensure contact between the on-skin and the under-skin wireless communication modules. The device should be able to withstand high mechanical loads and provide small radio signal attenuation.

- The second one involves means of reliable and stable wireless communication.

3. Results:

3.1. Device providing contact between the on-skin and the under-skin wireless communication modules

The contact device between the on-skin and the under-skin wireless communication modules is generally a multi component device consisting of a mechanical housing and a radio-transparent element. It is desirable that this device should also be provided with a window transparent to light, in this way enabling reduction of the energy consumption of the external sensor by activating the operation of the wireless communication system through a pair of light source and light receiver (LED). Magnetic impulse activation, for example with a reed relay, is also possible, though this method poses the risk of disrupting the performance of the electronic devices and of distortion of the radio signals.

The mechanical housing must be compatible in shape, construction and material with the mechanical structure of the aerospace vehicle and its manufacture should not generally constitute a serious engineering problem [8].

The main component of the composite device is the radio-transparent element, which, among other things, should be relatively light, inexpensive, easy to process, and must be able to withstand high mechanical loads.

It is known that the force that must be overcome when moving an object in the air is:

(1) $F = \frac{1}{2}.c_x.\rho\ .S\ .V^2$, where:

- ρ is the density of the air;
- S is the area of the transverse projection of the object (referent area);
- c_x is Drag coefficient;
- V is the velocity of the object relative to the air. The force of the air resistance depends on the square of the velocity and at a given constant high velocity can be reduced by varying within certain limits the cross-sectional area of the object.

Pressure (denoted by p) is a physical quantity characterizing the magnitude of the normal force component acting on a unit of area. Pressure is a scalar value. According to the definition in ISO / IEC 80000, pressure is the ratio of the force to the surface area:

(2) $p = \frac{F}{S}.$

Therefore, with some approximation, we can state that the pressure on the contact device between the on-skin and the under-skin wireless communication modules will be:

(3) $$P = \frac{1}{2} c_x \rho V^2.$$

The Drag coefficient values are shown in Table 1.

Table 1. Drag coefficient values

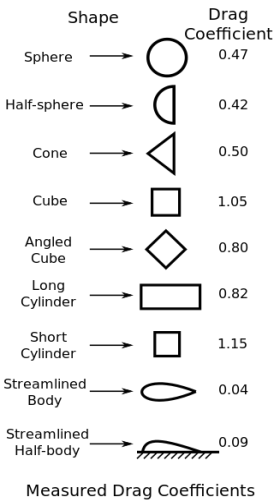

Calculations show that in extreme cases where the contact device is a long cylinder (for example, a flat porthole that can be approximated in this way), the speed of the spacecraft is in the range of 20 – 30 M (M ~ 300 m/s – first cosmic velocity at Mach number 27 is 8 km/s), assuming average air density of 1.5 kg/m³, the pressure on it reaches 26 MPa (~ 260 bar). At subsonic speeds the pressure reaches 0.4 bar and at speeds with Mach number below 5 it is up to 10 bar.

Our calculations allow the conclusion that for spacecraft from the moment of their launch until their orbit positioning it is appropriate that the contact device between the on-skin and the under-skin wireless communication modules should be provided with screens protecting them from the high dynamic external pressure values. For other aircraft this will not be necessary.

These requirements can be satisfied by a limited number of materials, mainly by composites. To this end, several types of composite materials have been developed at IMSETHC-BAS. They consist of different combinations of the following components:

- Fiberglass 300 gr/m², 500 gr/m² (Fig. 1);

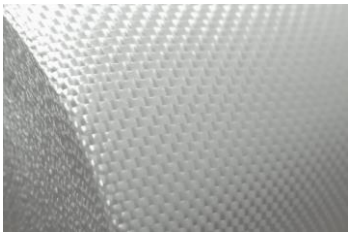

Fig. 1. Fiberglass

- Lantor Soric XF 3 mm (Fig. 2) – a special type of pressure-resistant core material (filler) designed specifically for vacuum infusion. Unlike traditional fillers such as Coremat, Soric is made of pressure-resistant cells that do not shrink in vacuum, thus preserving the structure and the thickness of the material;

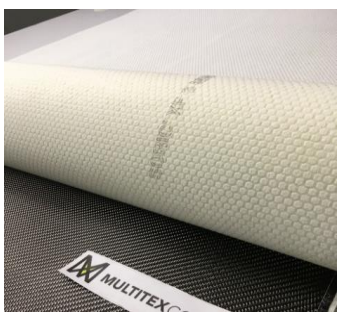

Fig. 2. Lantor Soric XF

- Aluminum honeycomb structure (Fig. 3), intended as a filler in the manufacture of composite panels and parts. Used properly, aluminum honeycomb can reduce weight and increase the rigidity of composite panels in a wide variety of applications;

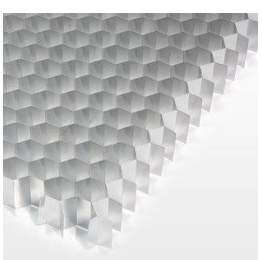

Fig. 3. Aluminum honeycomb

- Polyester resin MULTIPOL® TP200 – high quality polyester resin, thixotropic, pre-accelerated. It is very good for manual lamination or infusion. Hardener: MEKP Catalyst (from 1 to 3%) of BUTANOX®. Color: blue, transparent after application;
- Polyester isophthalic with neopentyl glycol gelcoat E-120. Composition: Styrene. Thixotropic unsaturated polyester resin designed to be sprayed onto the surface of the die as a protective layer against environmental influences. It gives the products resistance to impact, light, water and aging.

For the purpose of the research experiments, three types of composite material constructions have been developed at IMSETHC-BAS for contact devices between the on-skin and the under-skin wireless communication modules:

3.1.1. Composite plate designed to withstand pressures of up to 14 bars.
Composition:

– 4 layers of 3 mm thick fiberglass 500 gr/m²;
– 1 layer of 5 mm thick core material;

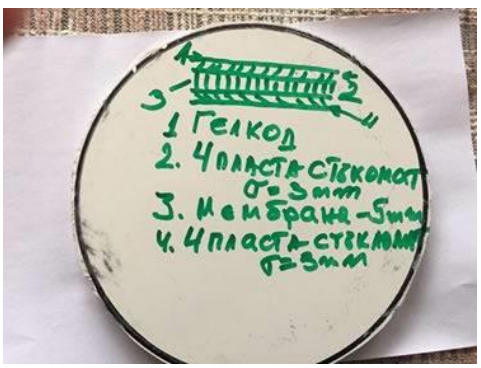

Fig. 4. Composite plate designed to withstand pressures of up to 14 bars

– 4 layers of 3 mm thick fiberglass 500 gr/m²;
– Polyester resin MULTIPOL® TP200;
– Polyester isophthalic gelcoat with neopentyl glycol E-120.
Total thickness: 12 mm.
Features – opaque to light, radio transparent, include for frequencies of up to 6 GHz.

3.1.2. Composite plate designed to withstand pressures of up to 10 bars.
Composition:

– 4 layers of 2 mm thick fiberglass 300 gr/m²;

– 1 layer of 5 mm thick core material;
– 4 layers of 2 mm thick fiberglass 300 gr/m²;
– Polyester resin MULTIPOL® TP200;
– Polyester isophthalic gelcoat with neopentyl glycol E-120.

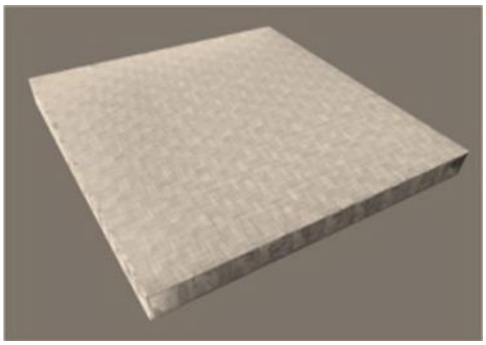

Fig. 5. Composite plate designed to withstand pressures of up to 10 bars

Total thickness: 10 mm.
Features – opaque to light, radio transparent, include for frequencies of up to 6 GHz.

3.1.3. Composite plate designed to withstand pressures of up to 10 bars.
Composition:

– 3 layers of 2.5 mm thick fiberglass 500 gr/m²;
– 1 layer of 5 mm thick Aluminum honeycomb;
– 3 layers of 2.5 mm thick fiberglass 500 gr/m²;
– Polyester resin MULTIPOL® TP200.

Total thickness: 10 mm.

Features – transparent to light, radio transparent, including for frequencies of up to 6 GHz.

Fig. 6 shows the experimental model for testing the functionality of the three types of composite material constructions for contact devices between the on-skin and the under-skin wireless communication modules.

Fig. 6. Experimental model for testing the functionality of the three types of composite material constructions

It consists of a metal cylindrical body (3) and a metal cylinder (2), mounted on which are respectively the elements of the on-skin and the under-skin modules for wireless communication.

The antennas of the transmitter and receiver module are connected by means of diaphragms (4, 5), in which circular plates of various radio conductive materials can be placed to analyze the communication efficiency.

3.2. Wireless communication device

Modern systems mainly use sensors producing digital output data, which also makes it easier to upgrade existing systems or to build new ones using wireless standards for data transmission. The requirements to be met by the channel used, taking into account the specificities of the particular application, are as follows [9]:

- provision of sufficient capacity to transmit sensor data without delay caused by the channel;
- validation of information transmitted by the sensor;
- guaranteeing uniqueness of the transmitted data in a multi-sensor mode of operation;
- channel capacity in working conditions;
- ensuring autonomy when using battery power supply.

In wireless data transmission, account must be taken of environmental features, i.e. the space distribution in the spacecraft/aircraft, which is a solid metal structure that would impede the passage of electromagnetic waves. This necessitates the availability of collector systems in single volumes. A single volume defines a space without partitions and whose linear dimensions do not exceed the maximum communication distance determined by the wireless protocol used [10].

Bluetooth is a wireless technology for short-distance data exchange from fixed or mobile objects, which is used for personal area networks (PANS). Bluetooth uses ultra high frequency UHF in the ISM frequency range from 2.4 to 2.485 GHz.

♦ Advantages:

1. Low power consumption.

2. Bluetooth can be integrated across devices, including portable devices and mobile phones.

3. Low cost – steadily decreasing price of the hardware module (single chip solution);

4. The distance between two devices can reach up to 60 m.

5. Well-designed structure.

6. Bluetooth uses 2.4 GHz bandwidth, data transfer speed can reach up to 1Mbps.

7. Supported by a free-membership consortium established in 1998, with more than 2,000 members, including IBM, Intel, Nokia, Erricson, Toshiba, 3COM, Lucent, Microsoft.

♦ Disadvantages: Its operating range is smaller compared to other wireless technologies.

The choice of Bluetooth Low Energy (BLE) is based on its being uniquely applicable for building wireless data transfer modules. The features provided in its specifications – authentication, encryption, and high-speed data transmission – fully meet channel requirements, while its low power consumption, depending on sensor consumption, ensures autonomy, for months, and at higher battery capacities, for years. This, combined with the small size, enables building self-unit networked modules that use a unified standard for data transmission. The fault clearing time is reduced since the module is usually replaced.

In aviation system automation, the wireless communication standard finds practical applicability mainly in the expansion of the capabilities of the sensor network and its rapid upgrade.

To optimize the data transmission channel, different types of sensors are used. The information collected via radio channel (Bluetooth standard) is transmitted to the data collection system. The proposed approach eliminates the need of a wired connection and allows the sensors to be repositioned when necessary.

Another advantage is the reduced time and human resources (no need for a skilled specialist to change the position of the sensors) necessary when changing the positioning of the sensors, nor does this require additional infrastructure.

In the proposed approach, the linear structure of the system is preserved, which, when using wireless communication channels, can be changed to star connection, as shown in Fig. 7.

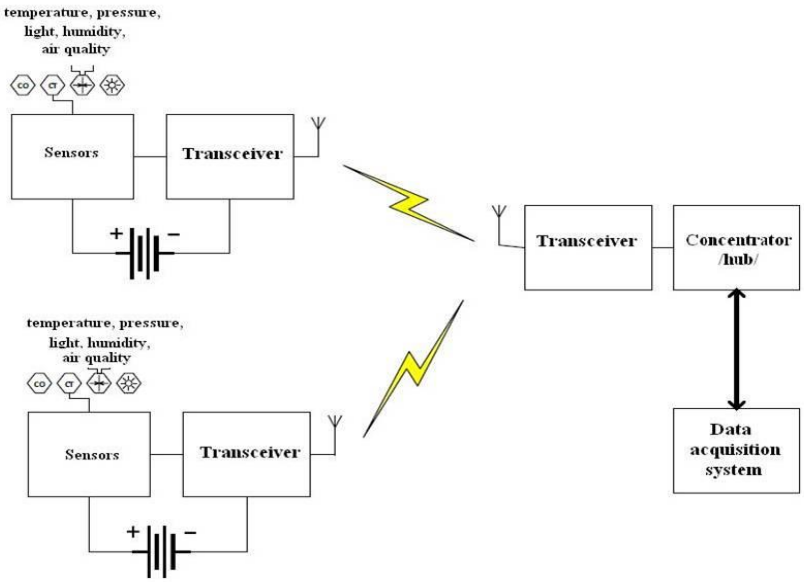

Fig. 7. Structure of the system is preserved, which, when using wireless communication channels

In the selected experimental model, all modules are of Arduino specifications, as shown in Fig. 8.

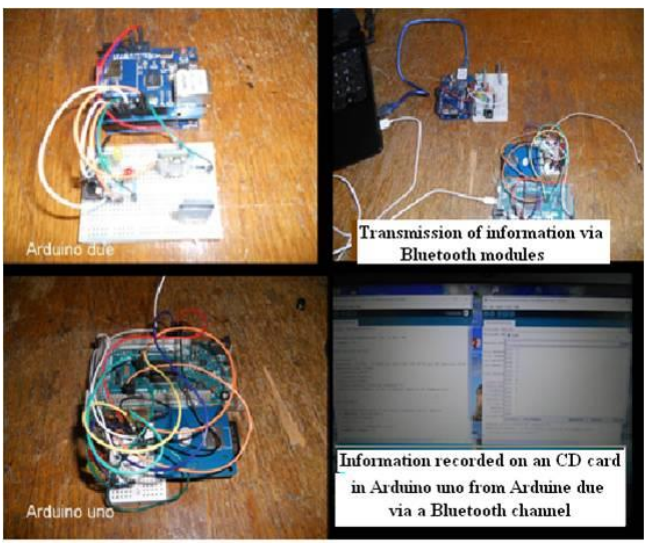

Fig. 8. Transmission of information via Bluetooth modules

The block diagram and data exchange principle of the test device are shown in Fig. 9.

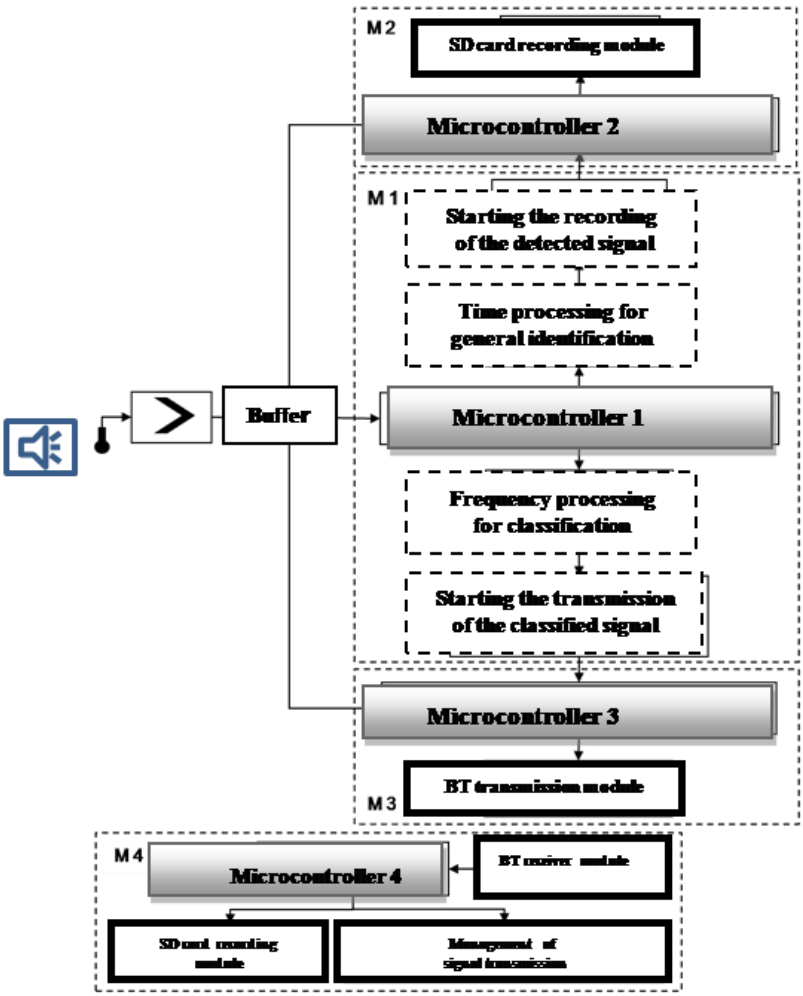

Fig. 9. Block diagram and data exchange principle of the test device

To analyze the capabilities of the Bluetooth communication standard, the sensor selected is an acoustic receiver, which allows qualitative and quantitative comparison (amplitude-frequency characteristics) of the input and output signals, in this case noise and speech. This is achieved by comparing the spectrograms of noise and noise + speech recorded on SD cards after the classification of speech signals (their separation from noise-only signals) and those of noise + speech after BLE communication.

3.3. Test results

The verification of the proposed technical solutions was carried out by two types of experiments: to determine the mechanical stability and to evaluate the possibility for wireless communication.

Fig. 6 shows the experimental set-up used to evaluate the resistance of the structure to mechanical stress. For this purpose, air was compressed in the metal cylinder (2) under controlled pressure and monitoring the condition of the plates made of composite materials according to item 3.1.1., 3.1.2., and 3.1.3. Deformation was taken as the percentage of the angle between the tangent to the most convex part of the plate (counting as its beginning the point where the plate is tightened to the periphery of the cylinder with a flange) and the normal to the plate. The test results are shown in Table 2.

Table 2. Tesr results

No	Composite according to the configuration in item	Deformation of 3% at pressure	Deformation of 5% at pressure	Destruction at pressure
1.	3.1.1.	11.8 bar	12,8 bar	15.6 bar
2.	3.1.2.	9.3 bar	10,1 bar	11.3 bar
3.	3.1.3.	8.9 bar	9,1 bar	10.8 bar

The results regarding the correspondence between the audio signal (speech) before and after its wireless transmission via Bluetooth communication through the plates made of the three composite materials are shown in Fig. 10.

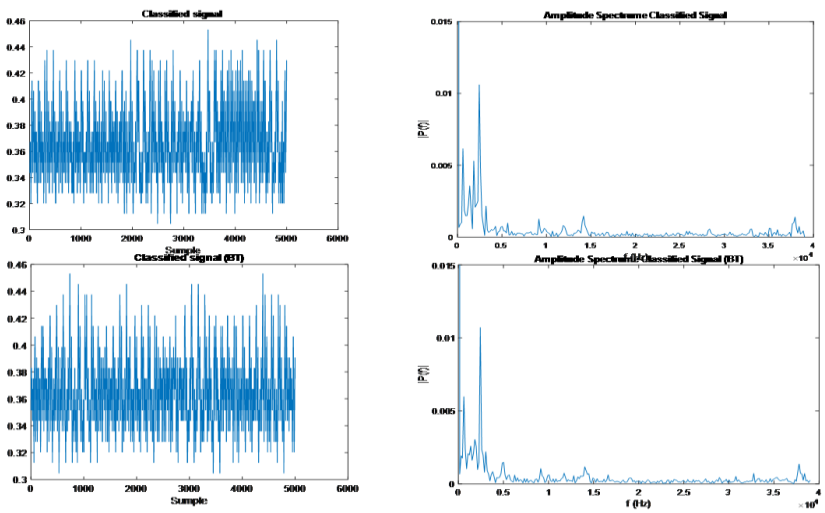

Fig. 10. Correspondence between audio signal (speech) before and after its wireless transmission

4. Conclusions

The results of the experiments using the model shown in Fig. 4 for testing the strength properties of the proposed composite plates and the Bluetooth-enabled wireless network for remote sensor data communication and transmission of the collected data to an aviation electronics server using Arduino designed and manufactured open source computer hardware and open source software and microcontroller kits for building digital devices, taking into account the technical, functional and financial requirements, allow the following conclusions to be drawn:

4.1. For spacecraft from the moment of their launch until their orbit positioning it is appropriate that the contact devices between the on-skin and the under-skin wireless communication modules should be provided with screens protecting them from the high dynamic external pressure values. For other aircraft this will not be necessary.

4.2. The proposed composite materials fully meet the requirements for providing wireless communication with on-skin sensors in aerospace vehicles;

4.3. It is advisable to activate the operation of the wireless communication system on a signal, and the easiest and cheapest way is with a pair of light source and light receiver (LED). This requires that the composite material should be transparent, i.e. most suitable is the composite of configuration 3.1.3.;

4.4. The use of wireless communication standards in the construction of sensor networks provides flexibility in their implementation and reduces the time consumption. Another benefit of BLE sensor modules is the possibility to use small-size batteries;

4.5. The construction of sensor concentrators/hubs enables the provision of information on the parameters at different points, thus ensuring the correct operation of the automated systems. It also allows a completely new approach in their implementation. In practice, it is possible for each system to be given individual configurations and to upgrade the sensors used;

4.6. The disadvantages of the presented approach include in the first place the limits on the distances imposed by the Bluetooth standard, though this will be partially overcome in its upcoming fifth version. Another shortcoming is the impossibility to position sensor modules behind metal partitions, which requires placing additional concentrators and the use of “windows” made of radio-transparent materials.

5. Acknowledgements

The results of the present study were achieved in implementation of administrative contract No KP-06-RUSSIA /23 dated September 28, 2019 for financing research project “Study of amplitude and frequency characteristics of seismic signals received from surface sources.” Financial support for the project came from the Bulgarian National Science Fund as a result of the 2018 bilateral cooperation competition Bulgaria - Russia 2018–2019.

The results can also be used in the implementation of Work Package 2 “Intelligent Security Systems” of Project BG05M2OP001-1.002-0006 – Creation and Development of a Centre of Competence “Quantum Communication, Intelligent Security Systems and Risk Management” (Quasar), funded by the European Regional Development Fund through the Operational Programme “Science and education for smart growth 2014–2020”.

References

1. Genov, B., D. Nedelchev, M. Mihovski, and Y. Mirchev. Comprehensive approach for service life assessment of solid-propellant rocket motors, NDT Days, 2019, II, 4, 467–475. ISSN: 2603-4018 (print), 2603-4646.
2. Petkov, S., P. Petkov, G. Nikolov, and A. Tumbarska. Mathematical model of the management of high-energy detonation processes through an energy generator (screen). European Journal of Engineering Research and Science, 2018, 3, 5, 65–70. EUROPA Publishing, ISSN 2506-8016, DOI:10.240818/ejers.
3. Petkov, S., Nikolova, V., Petkov, P., and Sv. Yaneva. Main directions for the Development of Protection Equipment of Dynamic Type Using Electrical Energy. Published in European journal of Engineering Research and Science, 2018, 3, 5, 55–59. EUROPA Publishing, ISSN 2506-8016, DOI: 10.24018/ejers.2018.3.5.730.
4. Kalpakchiev, S. and Y. Boichev. Instruments for reduction of the influence of an improvised explosive device for the protection of humans and material property in the area of airport and transport terminals. Project HOME/2010/CIPS/AG/019, 2013.
5. Bugaev, A. S., V. M. Agafonov, A. N. Antonov, K. S. Belotelov, P. V. Dudkin, E. V. Egorov, I. V. Egorov, T. V. Krishtop, A. V. Neeshpapa, V. G. Popov, A. S. Shabalina, S. S. Vergeles, V. V. Uskov, D. L. Zaytsev, D.A. Zhevnenko, S.N. Zhabin, and V. G. Krishtop, “Molecular electronic transducers for measuring instruments”, Journal of Communications Technology and Electronics (Radiotekhnika i Elektronika), 2018, 63, 12.
6. Martínez, C., Eras, L., and Domínguez, F. The Smart Doorbell: Aproof-of-concept Implementation of a Bluetooth Mesh Network. In: Proceedings of the 3rd 2018 IEEE Third Ecuador Technical Chapters Meeting, Cuenca, Ecuador, 15–19 October 2018.
7. Nilsson, M. and Deknache, H. Investigation of Bluetooth Mesh and Long Range for IoT Wearables; Malmö Universitet/Teknik och Samhälle: Malmö, Sweden, 2018.

8. Sarnchez-Soto, M., P. Pagers, T. Lacorte, K. Bricen, and F. Carrasco. Curing FTIR study and mechanical characterization of glass bead filled trifunctional epoxy composites. Composites Science and Technology, 2007, 67, 1974–85.
9. Boichev, Y. and N. Dyulgerov. The effect of superplasticity and its use in the manufacture of products in special production, 6th national conference with international participation „Metal Science'2017", Bulgarian Academy of Sciences, 2017, 285–288. ISSN 1313-8308.
10. Iliev, Il. and A. Kolarov. Study of Microprocessor System for Detection of Self Noise of an Underwater Object in Real-Time, Scientific journal "Acoustics", 2019, XXI, 21, 33–38. ISSN 1312-4897.

КОМПОЗИТЕН МОДУЛ ЗА БЕЗЖИЧНА КОМУНИКАЦИЯ В АВИОКОСМИЧЕСКИТЕ СРЕДСТВА

Н. Георгиев, А. Коларов, И. Илиев

Резюме

Увеличаването на въздушният трафик, в това число и на космическите полети, количествата пренасяни товари и пътници, както и поставените за решаване сложни научни и научно-приложни задачи, повишават изискванията за получаване на постоянна актуална информация за параметрите на системите и заобикалящата ги среда. С навлизането на платформите за IoT се наблюдава тендеция за използването им във всички сфери на технологиите, като системи за сбор и обработка на информация, което е в пълна сила и за нуждите на въздухоплаването. Един от основните проблеми на изграждането на нови системи или надграждане на съществуващи, събразени със съвременните тенденции, е високата себестойност и големият период за реализация на настоящите решения. Предлаганият подход на унифицирани модули с голям набор от възможни сензори, работещи по безжичен стандарт за предаване на информацията свързани в единна мрежа с относително ниска себестойност и минимално време за изграждане, надграждане и обновяване, дава възможност за отговаряне на тенденциите в сферата на въздухоплаването.

Bulgarian Academy of Sciences. Space Research and Technology Institute.
Aerospace Research in Bulgaria. 32, 2020, Sofia

DOI: https://doi.org/10.3897/arb.v32.e15

INFLUENCE OF LONG-TERM STAY OF ELEMENTS OF CAPILLARY INTAKE DEVICES IN LIQUID PROPELLANT COMPONENTS ON THEIR PARAMETERS

Oleksandr Minai, Oleg Ivanov, Ihor Siedykh

Design Office "YUZHNOYE", Dnepr, Ukraine
e-mail: info@yuzhnoye.com

Keywords: *Capillary Intake Devices; Mesh Phase Separators; Capillary Holding Capacity, Corrosion Rate*

Abstract

In this paper, we consider the results of a long-term study of the effect of prolonged stay (more than 30 years) of elements of capillary intake devices - mesh phase separators in the liquid propellant components (and under vapors) on the change in their working parameters (characteristics). In the process of research, the following types of work were carried out: extracting mesh phase separators from the propellant tanks of the missile stages to be detected after they were neutralized; analyzing the chemical composition of the substances located on the grids of mesh phase separators; determining the capillary holding capacity of the mesh, measuring the geometric dimensions of the mesh by the optical method; and performing metallographic studies of the mesh patterns.

As a result, the authors determined the decrease in the capillary holding capacity of the screen of mesh phase separators for 31 years of their stay in the liquid propellant components and under their vapor. The analysis of the main factors was made that influenced the change in the design parameters of the capillary intake device: uniform corrosion damage and local changes in the microstructure of the structural material of the meshes, as well as a change in the value of the contact angle of the propellant with the mesh material.

Introduction

Progress in space exploration is largely going along the path of creating and launching new spacecraft, as well as expanding the existing (International Space Station) and creating (in the future) a new space infrastructure for their maintenance and operation. The increase in the scale of space activity and its ever-increasing commercial orientation put forward special requirements for spacecraft, which determine the development process in this area. This is the possibility of reusable use and long-term operation of spacecraft [1].

The development of reusable spacecraft landing on Earth or transporting goods in space with a launch from low Earth orbit presents new requirements for all nodes and units, including mesh (capillary) phase separators, as the main functional

elements of capillary intake devices included in the system for ensuring the continuity of the supply of propellant components at the entrance to liquid rocket propulsion systems [2, 3].

At the same time, the following questions are becoming urgent: studies of near and far space, the study and development of planets and bodies of the solar system (moon, Mars, the sun, planetary satellites, asteroids, etc.). This will require the creation of [4–7]:

- research and observation satellites;
- space tugs of reusable use;
- space shuttles for the delivery of people and goods with the ability to land on the planet and return to the orbital station;
- long-running infrastructure facilities: space and orbital stations of various kinds, equipped with docking facilities, tugboats, tankers, propellant depots and personnel modules.

The creation, operation and maintenance of the above objects entails the need for permanent storage at orbital stations of various technical fluids transported from the Earth, including high-boiling liquid propellant components: an oxidizing agent - dinitrogen tetroxide N_2O_4 (AT) and combustible - unsymmetrical dimethylhydrazine $(CH_3)_2N_2H_2$ (UDMH), followed by filling them with orbit spacecraft. At present, these propellant components are widely used in rocket technology, in particular, in Proton, Cyclone, Titan, Arian rocket launchers, liquid ICBMs, in propulsion systems of manned ships, satellites, orbital and interplanetary space stations.

Obviously, their refueling and operation will occur under microgravity conditions. Therefore, it is advisable that the propellant tanks of space stations and spacecraft be equipped with capillary intake devices. Capillary intake devices and their elements will have to be able to work with large numbers of “filling-emptying” cycles (100 or more) and with a long active period of work in space (more than 15 years) [1].

Thus, at the present stage of development of space programs, the following requirements will be imposed on storage systems and liquid withdrawal in general and on capillary intake devices, as their integral part [1]:

- the possibility of reusable use;
- long period of operation;
- performance in aggressive environments.

At the same time, the operation of functional elements of systems (including mesh phase separators of capillary intake devices), when all of the above requirements are implemented, should take place without significantly reducing their operating parameters (characteristics) throughout the entire period of operation [1].

In this article, the authors present the results of many years of research on the effect of long-term storage (more than 30 years) of net phase separators in

components and under pairs of liquid propellant components (AT and UDMH) on the change in their operating parameters (characteristics).

Object of research and parameters studied

In this work, the object of research was the main functional element of the capillary intake device, which ensures the multiple launch of the propulsion system of the spacecraft under zero gravity conditions and the reduction of undeveloped residues of propellant components, the principle of which is based on the capillary forces of the surface interaction - mesh phase separator [8–10].

The mesh phase separator under study was made of steel mesh No. 008 (steel grade AISI 321), which is a twill weave fabric with square cells, having the following characteristics according to the technical specifications [11]:

- wire diameter 55^{+4}_{-3} microns;
- nominal cell size in the light of 80 microns;
- permissible deviations of the arithmetic mean cell size ± 13%;
- permissible deviation of the size of an individual cell + 75%;
- allowable deviation of the size of especially large cells 50–70%;
- the permissible number of especially large cells is not more than 9%, on a grid with an area of 1 m^2.

A schematic representation of a twill weave of wire cloth with square cells is shown in Fig. 1.

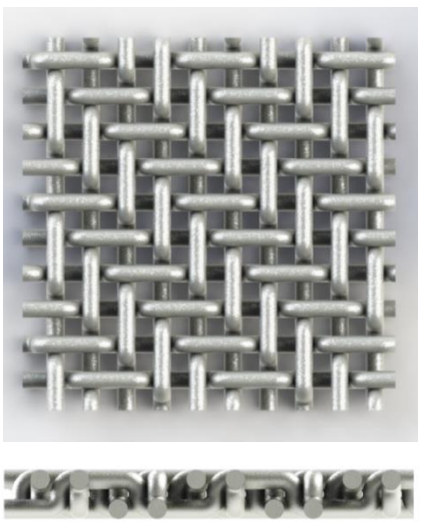

Fig. 1. Schematic representation of a twill weave of wire mesh with square cells

Since the principle of operation of the mesh phase separator is based on capillary forces acting in the grid cells at the gas-liquid phase boundary, the main parameter of its operability is capillary holding capacity.

Capillary holding capacity is the ability to prevent the penetration of free vapor-gas inclusions through a mesh phase separator under external power influences on propellant components. This parameter depends on the cell size, surface purity and wire material, type and temperature of the propellant components [1, 12–13].

The value of the Capillary holding capacity of the mesh phase separator is determined by the formula [12–15]:

$$\Delta H = \frac{k \cdot \sigma}{\rho \cdot g \cdot b} \cdot \cos\theta$$

where k is a coefficient that take into account the geometry of the mesh cell; σ is the coefficient of surface tension of the propellant components; ρ is the density of the propellant components; g is the longitechnical specificationdinal acceleration; b is the mesh cell size; θ is the contact angle between the propellant and the grid material, which is assumed to be equal to zero under nominal conditions for the propellant under consideration.

In spacecraft that have been in a charged state for a long time (15 years or more) under the influence of aggressive propellant components (AT and UDMH), the operational parameters of the mesh phase separators of capillary sampling devices can change.

The reasons for the change in the design parameters of the mesh phase separators of capillary sampling devices include the formation of films, gels, precipitation grids on the surface of the wire as a result of corrosion processes, with prolonged exposure to aggressive propellant (AT and UDMH) on the construction materials of meshes, which, in addition to measuring the change in the geometric dimensions of the wire and mesh cells can affect the value of the contact angle and lead to a decrease in the capillary holding capacity.

Since there was no experimental determination of the change in the contact angle, it was not possible to theoretically evaluate the influence of this factor on the capillary properties of fine-meshed meshes.

Based on the foregoing, in order to determine the effect of a long stay of elements of capillary intake devices in the components of liquid propellant components on their parameters, we studied the changes in the capillary holding capacity of the mesh phase separators of the screen meshes of the propellant components that were in the liquid phase (AT and UDMH) and under them in vapors for a) 15 years, b) 17 years and 6 months, c) 20 years, d) 20 years and 10 months, e) 23 years and f) 31 years, being in the propellant systems of refueling and ampouled space stages of rocket.

The work was carried out in stages in the period from 1997 to 2016.

According to the adopted test program, the work was performed in the following order:

1) removing the mesh phase separator from the propellant tanks of the vehicles being and analysing the chemical composition of substances located on the screen of the mesh phase separator;

3) determining the capillary holding capacity of the mesh phase separator;

4) measuring the geometric dimensions of the screen of the mesh phase separator with an optical method;

5) doing metallographic studies of screen mesh patterns of the phase separator.

Moreover, in addition to the detectable mesh phase separators, the work in items 3) and 4) was first carried out on new meshes No. 008 in order to obtain reference data for the existing test conditions, experimental designs, and working fluids.

1.1 Analysis of the chemical composition of substances located on the screen of mesh phase separators after its removing from the propellant tanks

After neutralization, the propellant tanks were opened and the mesh phase separator was dismantled.

Three samples of mesh No. 008, located in different parts of the tank, both in the liquid phase of the propellant components and under its vapor, were extracted from each propellant tank.

The following methods were used to determine the composition of substances found on the networks of phase-separated meshes: X-ray fluorescence, X-ray structural, atomic absorption, potentiometric, IR Fourier spectroscopy and chromatography-mass spectrometry.

Thus, the studies showed that the composition of cations on mesh of oxidizer and fuel tanks is almost the same. The detected metal cations correspond to the elements that make up the alloy of aluminum and steel - the main structural materials of the defective fuel system. However, due to the small amount of the substance on the mesh in contact with UDMH, it was not possible to establish its composition by the methods listed above.

1.2 Determination of capillary holding capacity of mesh phase separators

Tests of the mesh phase separator were carried out in a pilot plant. The experimental device is shown in Fig. 2.

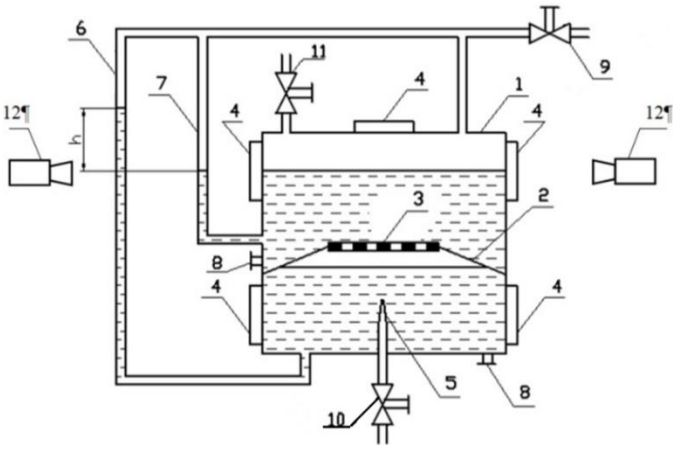

Fig. 2. Scheme of the experimental device for determining the capillary holding capacity of the mesh phase separators

In Fig. 2 is shown: 1 – cylindrical container; 2 – a partition; 3 – CPS; 4 – porthole; 5 – fitting with a calibrated nozzle; 6, 7 – piezometers; 8 – filling and drain fitting; 9 – valve for the removal of vapor of the working fluid; 10 – valve dosed gas supply; 11 – valve boost the upper compartment; 12 – video cameras.

In Fig. 3, as an example, photographs of a single breakthrough of gas bubbles and a mass breakthrough in whole groups of cells are presented.

To obtain the reference data, control samples of mesh phase separators using standard technology from the same mesh roll were prepared. Tests of the reference mesh phase separators were carried out according to the same procedure.

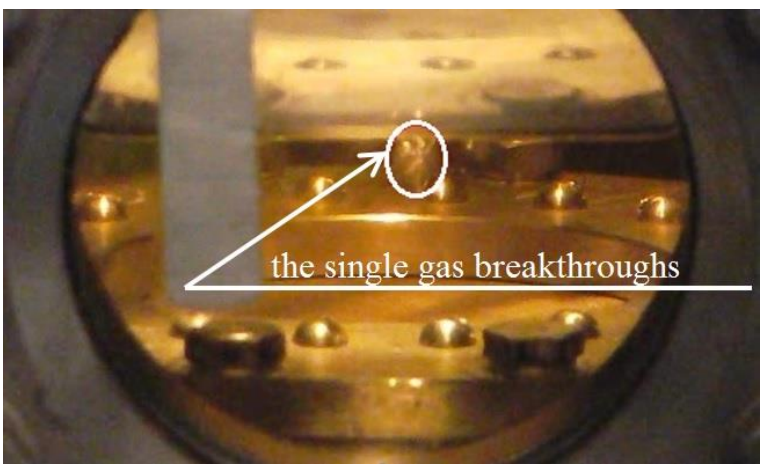

A

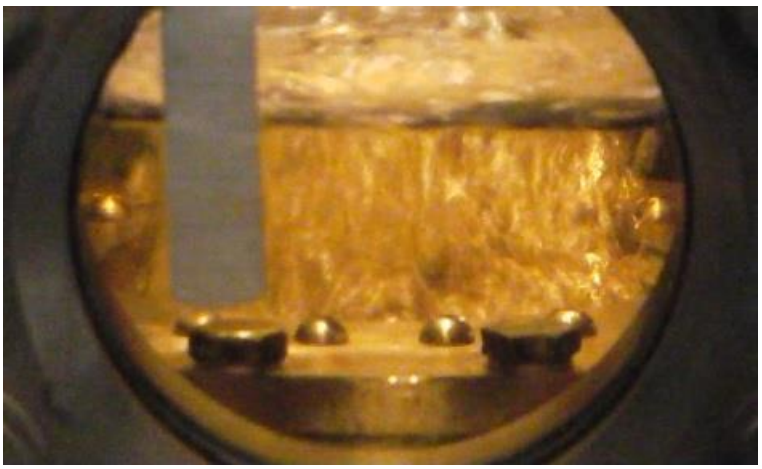

B

Fig. 3. Photographs of the single breakthrough of gas bubbles (A) and the mass breakthrough over whole groups of cells (B)

More than 56 samples of meshes (including reference ones) that were in the liquid phase of the propellant components and under their vapor for a period of a) 15 years, b) 17 years and 6 months, c) 20 years, g were tested. d) 20 years and 10 months, e) 23 years and f) 31 years, as part of the propellant systems of refueling and amplified space rocket stages.

AT and UDMH were used as working fluids, which are identical to those normally supplied to rocket propellant systems.

The tests were carried out in the temperatures range:

– plus 1 – plus 18 ºC – for AT;
– plus 1 – plus 16 ºC – for UDMH.

In total, it was carried out:

– 364 tests to determine the capillary holding capacity of mesh phase separators at AT;
– 337 tests to determine the capillary holding capacity of mesh phase separators at UDMH.

The array of experimental data obtained as a result of the tests was approximated by linear dependence by the least squares method.

Fig. 4 summarizes the test results to determine the capillary holding capacity of the mesh phase separators, mesh samples after 15–31 years of their presence in the highly toxic and aggressive components of liquid rocket propellant and under their vapors – AT (A) and UDMH (B) depending on temperature.

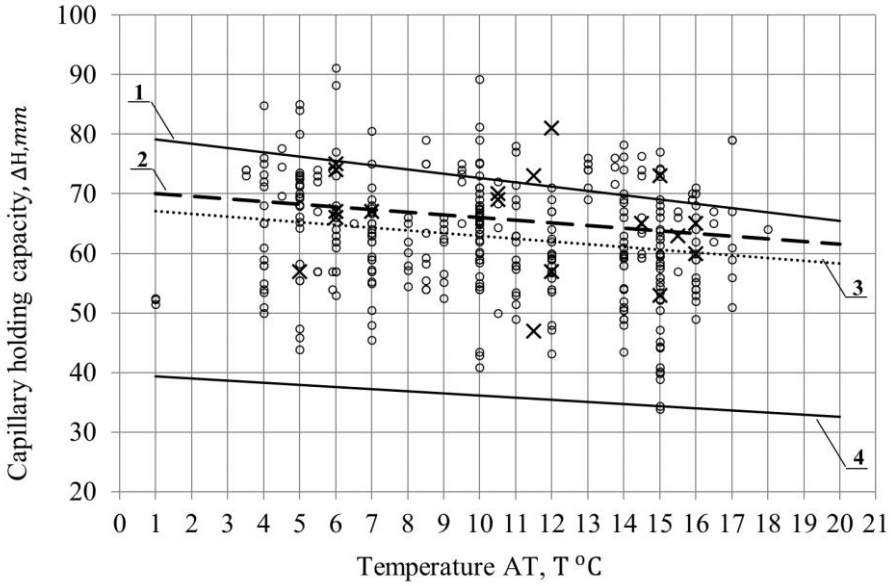

A

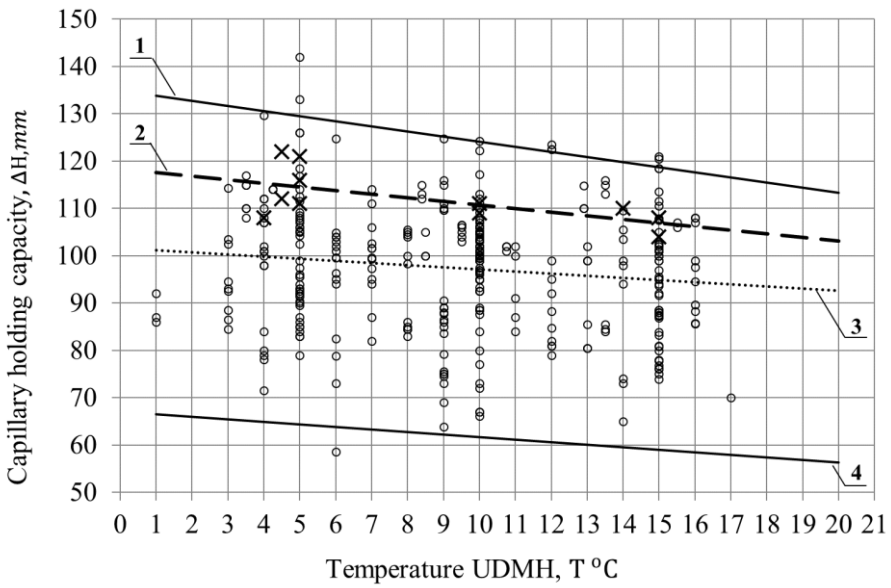

B

Fig. 4. Dependence of the capillary holding capacity of the samples of the mesh phase separator at temperature: A – for AT; B – for UDMH

In Fig. 4 shows: 1 – the upper limit of capillary holding capacity, calculated in accordance with the data on the permissible deviations of the geometric

parameters of the mesh No. 008; 2 – approximation of the test results to determine the capillary holding capacity of the reference mesh patterns; 3 – approximation of the test results to determine the capillary holding capacity of the mesh phase separator after a long stay in the fuel components; 4 – the lower boundary of the capillary holding capacity, calculated in accordance with the data on the permissible deviations of the geometric parameters of mesh No. 008; × – the values of the experimental determination of the capillary holding capacity of the reference mesh samples; o – the values of the experimental determination of the capillary holding capacity of the mesh phase separator after a long stay in the propellant components.

1.3 Optical method for measuring the geometric dimensions of mesh phase separators

To draw conclusions about the presence and magnitude of corrosion of the wires of the mesh phase separator, their initial geometric parameters (dimensions) must be known. For this, the dismantled mesh phase separators and reference mesh samples No. 008 were investigated by the optical method.

Measurements were made uniformly over the screen area in several zones not lying along the same wires. In each zone, in two perpendicular directions, "wire-cell-wire ..." measurements were performed in succession, 10 pieces of each element.

The main geometric parameters of the dismantled mesh phase separators and reference mesh samples are shown in Fig. 5.

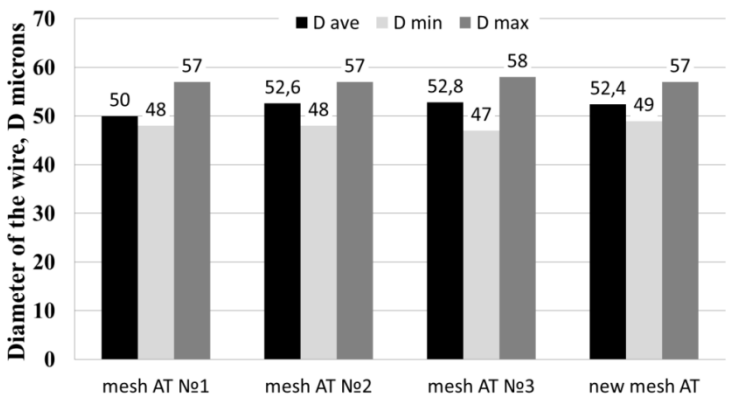

A

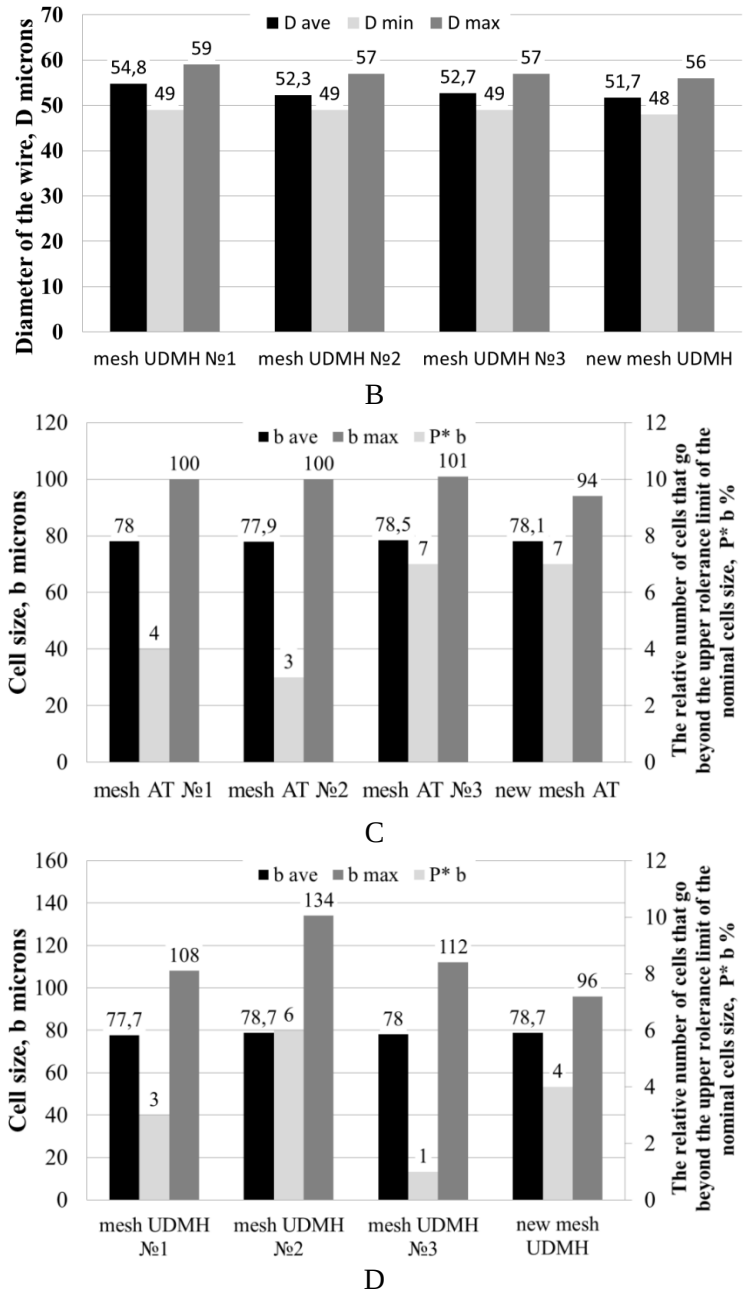

Fig. 5. The main geometric parameters of the dismantled mesh phase separators and reference mesh patterns: A - the basic geometric parameters of the wire mesh AT; B - the basic geometric parameters of the wire mesh UDMH; C - the basic geometric parameters of the cells of the grids of the AT; D - the basic geometric parameters of the mesh cells UDMH

In Fig. 5 shows: D ave. – the arithmetic mean of the diameter of the wire; D min – the smallest value of the diameter of the wire; D max – the largest value of the diameter of the wire; b ave. – the arithmetic mean value of the cell size; b max – maximum cell size; P*b – the relative number of cells that go beyond the upper tolerance limit of the nominal cell size.

From the graphs shown in Fig. 5 (C, D), it can be seen that the cell sizes of all mesh phase separators correspond to technical specification.

1.4 Metallographic studies of mesh phase separator

The purpose of the metallographic study was to determine the state of the screen of the mesh phase separators after prolonged exposure to propellant components.

For a metallographic study, samples (fragments) were cut out of the working part of the screen of mesh phase separators for the preparation of microsections, the studies of which were carried out using a metallographic optical microscope, which allows direct visual observation and photographing with an increase of 50 to 1000 times. The study revealed the presence of corrosion lesions and changes in the microstructure of materials in the samples.

Fig. 6 presents, as an example, the photographs of non-etched macro sections and the micro-structure of steel, indicating the absence of corrosion damage and changes in the microstructure of the structural materials of the mesh after a long stay in the propellant components – AT and UDMH.

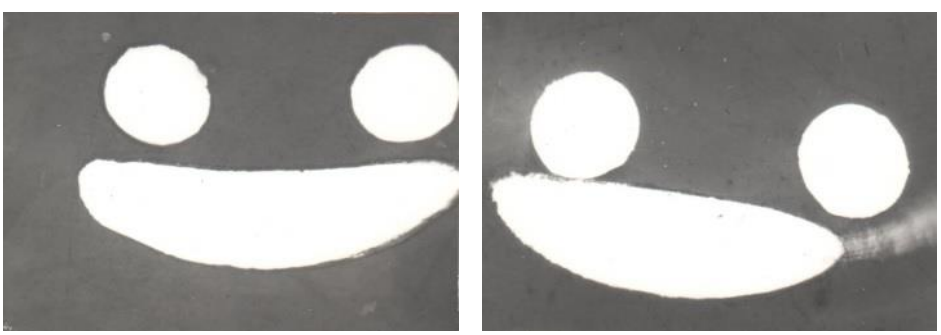

A B

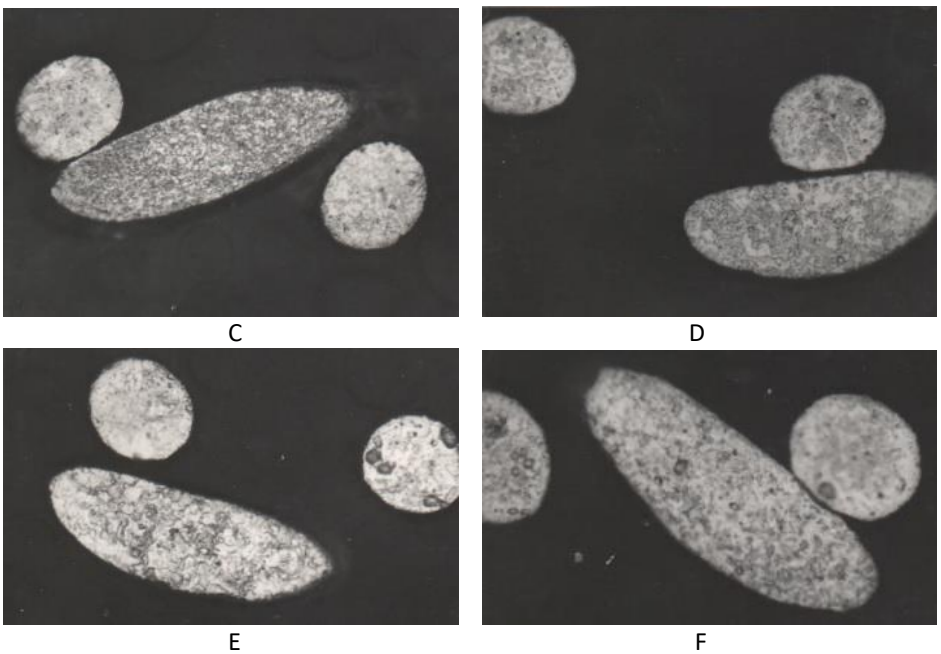

Fig. 6. Photographs of non-etched micro-sections and micro-structure of steel: A – non-etched micro-section of a mesh from the AT propellant tank; B – non-etched micro-section of a mesh from the UDMH propellant tank; C – microstructure of a mesh from the AT No. 1; D – microstructure of a mash from the UDMH No. 1; E – microstructure of a mesh from the AT No. 1; F – microstructure of a mesh from the UDMH No. 1

2. Analysis of the research results

The main factor determining the change in the design parameters of capillary intake devices after a long stay of its structural elements in the liquid propellant components (AT and UDMH) and under their vapors is a change in the characteristics of the capillary holding capacity of the mesh phase separators compared to reference patterns of meshes.

Capillary holding capacity, in turn, depends on the following factors (see formula):

a) physico-chemical properties of the propellant used;

b) propellant temperature;

c) geometric dimensions of the mesh (wire diameter and mesh cell sizes);

d) contact angle of the propellant with the mesh material.

Moreover, the parameters a), b), c) and d) are mutually dependent on each other and have a complex effect on capillary holding capacity.

Based on the obtained experimental data (see Fig. 5 (A, B)), a linear regression of changes in the approximate values of the parameters of capillary

holding capacity for 31 years of the stay of the elements of capillary intake devices in liquid propellant components (AT and UDMH) and under vapors with superimposed regression of the change in the parameters of capillary holding capacity under the condition of speed corrosion of stainless steel – $1 \cdot 10^{-4}$ mm/year was constructed, which is shown in Fig. 7 (A, B).

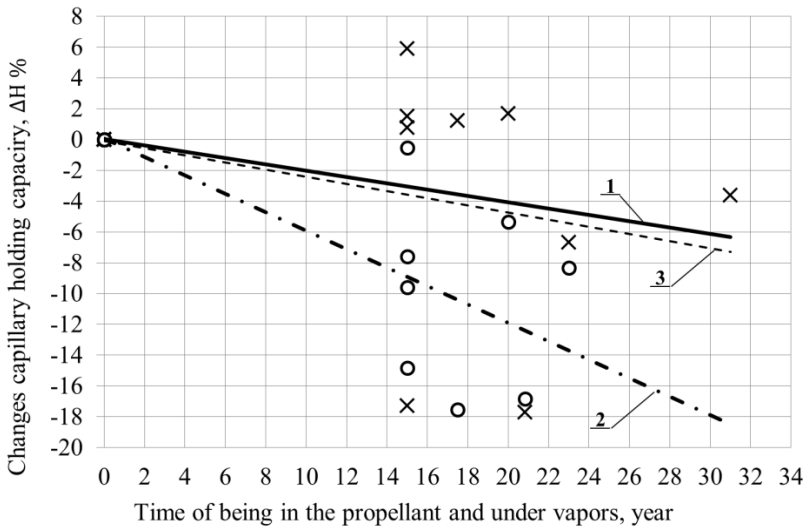

Fig. 7. Linear regression graph of changes in the approximated values of the parameters of capillary holding capacity over the 31 years of the stay of elements of capillary intake devices in liquid propellant components and under its vapors with superimposed regression of changes in the parameters of capillary holding capacity properties under the condition of steel corrosion rate - $1 \cdot 10^{-4}$ mm/year

In Fig. 7 shows: 1 – the curve of changes in the parameters of capillary holding capacity for the screen of the mesh phase separator located in the AT, approximated by the results of experimental data; 2 – the curve of changes in the parameters of capillary holding capacity for the screen of the mesh phase separator located in the UDMH, approximated by the results of experimental data; 3 – the curve constructed on the basis of the corrosion rate of stainless steel – $1 \cdot 10^{-4}$ mm/year; experimental values of arithmetic mean values of capillary holding capacity: × – AT, o – UDMH.

As can be seen from Fig. 7 for 31 years of being in the propellant components and under their vapors, the average approximated value of the capillary holding capacity for the screen of the mesh phase separator located in the AT has decreased by ~ 6.3% with respect to the reference mesh, and for those in UDMH – by ~ 18.5%.

The results of chemical analysis of samples of propellant components (AT and UDMH) discharged from propellant systems after long-term operation showed

that they practically did not change their indicators compared to the initial values given in the standards.

Therefore, the influence of changes in the physico-chemical properties of the fuel used on the capillary holding capacity can be neglected.

The effect of temperature was taken into account by using temperature-averaged values of capillary holding capacity.

Deposits found on meshes from a propellant tank of an oxidizer (AT) during defect detection hydrated nitrates of metal, are mainly aluminum and iron. Also, in the composition of the deposits, there are oxides, metal chlorides and water in small quantities. The formation of deposits occurred during technological operations (draining of propellant components, neutralization, opening of propellant tanks during fault detection) and cannot fully be a consequence of corrosion changes in the microstructure of the structural materials of the mesh phase separator due to its long stay in the AT.

Inspection of the screen of mesh phase separators from UDMH propellant tanks showed that the surface of the samples did not change compared to the initial one, there was neither darkening of the surface, nor the presence of deposits, or deposits.

Metallographic studies of samples of reticulated mesh phase separator that have been in the AT for a long time and in UDMH showed that the structural material of the presented samples of mesh of local corrosion lesions (intergranular, pitting, contact, crevice corrosion, cracks) was not detected.

Thus, one of the main factors affecting the change in the parameters of capillary holding capacity can be considered the change in the geometric dimensions of the mesh (excluding mechanical damage to the main structural material of the mesh), due to uniform corrosion.

Available domestic and foreign data on the rate of uniform corrosion for stainless steel indicate [16–18]:

- corrosion rate in AT at 50 °C $\leq 1 \cdot 10^{-4}$ mm/year;
- corrosion rate in UDMH at 50 °C $\leq 1 \cdot 10^{-4}$ mm/year.

It should be noted that for AT, the given values of the corrosion rate are an upper estimate, since they do not take into account the influence of super-blow gases and storage temperature regimes of charged and amplified upper stages of spacecraft.

So, nitrogen, which is the boost gas in this case, reduces the corrosion rate by 8 times in comparison with atmospheric air. And the corrosion of steel stored in non-leaking AT residues if nitrogen is used as boost gas is 10 times lower than when the air is used.

For the screen of mesh phase separators located in the AT and UDMH, the capillary holding capacity parameters decreased by ~ 7.2% over a period of 31 years, which would correspond to a decrease in the nominal wire diameter (55 microns) at 6.2 microns. This indicator is close to the values of the minimum diameters of wire meshes measured by the optical method (see Fig. 5 (A, B)).

For the screen of mesh phase separators located in the AT, the change in the parameters of capillary holding capacity over a period of 31 years does not contradict theoretical calculations about the corrosion rate of stainless steel in the liquid phase of AT and under its vapors. Over the course of 31 years, due to a corrosive change in the geometric dimensions of the mesh cells, the capillary holding capacity of the mesh phase separators has decreased by ~ 7.2%, while according to experimental data, the capillary holding capacity has decreased by ~ 6.3%.

For the screen of mesh phase separators found in UDMH, the change in the parameters of capillary holding capacity over a period of 31 years significantly exceeds the possible change in the value of capillary holding capacity due to corrosion ~ 18.5% against ~ 7.2%.

This may indicate that the main change in the parameters of capillary holding capacity occurs due to a change in the contact angle (θ).

Based on the assumption that the value of the contact angle (θ) is not equal to zero, using formula and the experimentally obtained value of the change in capillary holding capacity which is equal ~ 18.5% of the value for the reference mesh, we define the arithmetic mean value of θ in the 31 year, and it will be ~ 28.6º [1, 12, 13, 19, 20].

The reasons for the proposed change in the contact angle require additional study and analysis, as well as the reasons for the capillary holding capacity to exceed the upper tolerance limit calculated in accordance with the data on the allowable deviations of the geometric parameters of mesh No. 008 in accordance with the technical conditions (see Fig. 4 (A), curve 1), both for mesh phase separators that have been in the liquid phase of AT and under vapors for a long time, and for reference meshes, since it cannot be fully explained by grid cells impurity. An increase in the parameters of capillary holding capacity is not unambiguously a positive factor and should be considered within the framework of the operation of the entire pneumohydraulic system of the stage, since it can lead to an increase in the resistance of the mesh phase separator.

Conclusions

The results of a long-term study of the effect of a long stay (more than 30 years) of elements of capillary intake devices – mesh phase separators in the components (and under their vapor) of liquid propellant components (AT and UDMH) on the change in their operating parameters (characteristics), detail that:

- for the 31-year stay in the liquid propellant components and under its vapors, the average approximated value of the main parameter that determines the operability of capillary intake devices – the capillary holding capacity of the mesh phase separators for the mesh located in the AT decreased by ~ 6.3%, with respect to the reference mesh, and for those in UDMH – by ~ 18.5%;

- the most likely reason for the decrease in capillary holding capacity for the mesh phase separators located in the AT is the uniform corrosion of the structural materials of the mesh because its value is close to theoretical, which is ~ 7.2% for 31 years;

- for the mesh phase separators found in UDMH, the decrease in capillary holding capacity over a period of 31 years is significantly higher than expected as a result of uniform corrosion (~ 18.5%, against ~ 7.2%), which may be due to an increase in the arithmetic mean of the contact angle (θ) from zero to a value of ~ 28.6º. The reasons for the change in the contact angle require further study and analysis.

Based on the fact that when designing a continuity system, the parameters of the mesh phase separators are determined with a safety factor of 2, the results of studies of samples of the mesh phase separator indicate that during their long stay in liquid propellant components (AT and UDMH) and under their vapors for 31 years, a decrease in the parameters of capillary holding capacity by ~ 6.3% (for AT) and by ~ 18.5% (for UDMH) does not violate the design parameters of the mesh phase separators of capillary filters molecular devices.

The research results indicate that steel mesh No. 008 used as mesh phase separators fully meets the requirements for liquid storage and selection systems and for capillary intake devices, as their integral part at the present stage of development space exploration programs, namely:

- reusable features;
- long period of operation;
- operability in aggressive environments.

The use of steel mesh No. 008 in the functional elements of spacecraft flight continuity systems (using AT and UDMH as propellant) and space station propellant storage systems will definitely not lead to a critical decrease in their design parameters over a period of 31 years operation.

References

1. Bagrov, V. V., Kurpatenok, A. V., and Poljaev V. M. Capillary systems for selecting liquid from spacecraft tanks, UNPC «JeNERGOMASh» Publ., 1997, 328. (in Russian)
2. Siedykh, I. V. and Smolenskij, D. Je., Experimental confirmation of the operability of a capillary intake device in the separation of the spacecraft. Mechanics gyroscopic systems, 2017, 33, 105–14. DOI:10.20535/0203-3771332017119618. (in Russian)
3. Siedykh, I. V., Smolenskij, D. Je., Nazarenko, D. S., Experimental confirmation of the operability of a capillary intake device (mesh separator) during a program turn, Visn. Dnipr. un-tu. Raketno-kosmichna tehnika. 2018, 21, 26, 112–19. (in Russian)
4. Snead, J. M., Hellman, B. H., Near-future reusable space logistics vehicles, In: 43rd Propulsion Conference & Exhibit, 2007 AIAA/ASME/SAE/ASEE, 2007, 1–20. DOI:10.2514/6.2007-5847.

5. Bienhoff, D., The future of commercial space transportation, 2019, https://www.thespacereview.com/article/3776/1.
6. Kornuta, D., Abbud-Madrid A., Atkinson J., et al. Commercial lunar propellant architectechnical specificationre. A collaborative stechnical specificationdy of lunar propellant production, 2019, 188. DOI:10.1016/j.reach.2019.100026.
7. Abrego, A., Bair, C., Hink, A., et al. Project Hyreus. Mars sample retechnical specificationrn mission utilizing in sitechnical specification propellant production Washington Univ.; Dept. of Aeronautics and Astronautics, NASA-CR-197189, 1993, 383.
8. Walter, T., Philipp, B., Jaekle, D., and Netter, G. The Evolutionary forces and the design and development of propellant management devices for space flight in europe and the united states, In conference: Space Propulsion, 2016, 25.
9. Walter, T. and Jaekle, D., Review and history of ATK space systems surface tension PMD tanks, In conference: Space Propulsion, 2018, 24.
10. Hartwig, J. W., A detailed historical review of propellant management devices for low gravity propellant acquisition, Cleveland, GRC-E-DAA-TN32675, 2016, 25.
11. Woven with square micron mesh. Technical specification., OJSC LEPSE, 1999, 2. (in Russian)
12. Shevchenko, B. A. Estimated and experimental method for the development of means for collecting fuel components from tanks of aircraft with a liquid rocket engine, Dnepropetrovsk, KB «Juzhnoe» Publ., 1990, 209. (in Russian)
13. Chelomey, V. N. et al. Pneumohydraulic systems of propulsion system with liquid rocket engines, Moscow, Mashinostroenie Publ., 1978, 240. (in Russian)
14. Hartwig, J. W. Liquid acquisition devices for advanced in space cryogenic propulsion systems, Elsevier Inc., 2015, 488.
15. Fouad, A. On the pressure drop of fluids through woven screenmeshes, Chemical engineering science, 2019, 207, 464–78. DOI:10.1016/j.ces.2019.06.046
16. Uney, P. E. and Fester, D. A. Material compatibility with space storable propellants, California, Prepared for Jet Propulsion Laboratory California Institechnical specificationte of Technology, 1972.
17. Torrance, P. R., Lyndon, B. Point model for the formation of metal nitrate in nitrogen tetroxide oxidizer, Houston, NASA-TP-3107, 1991.
18. Michael, F.A., Norman, L., Simon, A., Dove, Wood. Corrosion of T1-6A1-4V alloy and 304L stainless steel in liquid nitrogen oxides, Journal of Propulsion and Power, 1996, 12, 1. DOI:10.2514/3.23989.
19. Fester, D. A., Villars, A. S., Uney, P.E., Surface tension propellant acquisition system technology for Space Shattle reaction control tank, In: 11th AIAA and SAE Propulsion conference, 1974, 8.
20. Hartwig, J. W. and Kamotani, Ya., The static bubble point pressure model for cryogenic screen channel liquid acquisition devices, International Journal of Heat and Mass Transfer, 2016, 101, 502–16. DOI:10.1016/j.ijheatmasstransfer.2016.05.024

ИССЛЕДОВАНИЕ ВЛИЯНИЯ ДЛИТЕЛЬНОГО ПРЕБЫВАНИЯ ЕЛЕМЕНТОВ КАПИЛЯРНЫХ ЗАБОРНЫХ УСТРОЙСТВ В КОМПОНЕНТАХ ЖИДКИХ РАКЕТНЫХ ТОПЛИВ НА ИХ ПАРАМЕТРЫ

А. Н. Минай, О. М. Иванов, И. В. Седых

В настоящей работе рассмотрены результаты многолетнего исследования влияния длительного пребывания (более 30 лет) элементов капиллярных заборных устройств – капиллярных фазоразделителей в компонентах (и под парами) жидкого ракетного топлива (N_2O_4 и $(CH_3)_2N_2H_2$)) на изменение их рабочих параметров (характеристик). В процессе исследований проведены работы по извлечению капиллярных фазоразделителей из топливных баков дефектируемых ступеней ракет после их нейтрализации, анализу химического состава веществ. находящихся на сетках капиллярных фазоразделителей, определению капиллярной удерживающей способности сеток, замеру геометрических размеров сеток оптическим методом и проведению металлографических исследований образцов сеток.

В результате проведенных работ авторами определена величина снижения капиллярной удерживающей способности сеток капиллярных фазоразделителей за 31 год их пребывания в компонентах жидкого ракетного топлива и под их парами, проведен анализ основных факторов, повлиявших на изменение проектных параметров капиллярного заборного устройства: равномерных коррозионных поражений и локальных изменений микроструктуры конструкционного материала сеток, а так же изменению значения краевого угла контакта топлива с материалом сеток.

Bulgarian Academy of Sciences. Space Research and Technology Institute.
Aerospace Research in Bulgaria. 32, 2020, Sofia

DOI: https://doi.org/10.3897/arb.v32.e16

APPLICATION OF CRYOTECHNOLOGY IN THE CREATION OF SPACE FOODS FOR CREWS WORKING IN EXTREME CONDITIONS

Peter Getsov[1], Tsvetan Tsvetkov[1], Georgi Sotirov[1], Iliana Nacheva[2], Zoya Hubenova[1], Maria Doneva[2], Petia Metodieva[2]

[1]Space Research and Technology Institute – Bulgarian Academy of Sciences
[2]Institute of Cryobiology and Food Technology
e-mail: getsovp@space.bas.bg; director@ikht.bg

Keywords: *Space Foods, Cryobiology, Lyophilisation.*

Abstract

The article presents the achievements in the field of cryobiology and is related to the work for ESA project. Space food is a variety of food products specially formulated and processed for space flight use. Food should meet specific requirements to ensure balanced nutrition for those working in extreme conditions while being easily and safely stored, prepared and consumed in low gravity environments. It is reviewed domestic and foreign market for space foods and defined requirements to astronauts; for other users: military; extreme professions; extreme sports, for hospitals and children gardens. There are summarizes the nutritional requirements for all mentioned above group users of space foods. There is shown Bulgarian experience in research and development of space foods and comparison of the Bulgarian Space Menu.

Introduction

The intake of food is one of the most important physiological factors which is of decisive importance in sustaining the work capacity, adaptive powers and health condition of the astronauts during long space flights. The dominant negative factors encountered in the extraordinary labour and living conditions in space are weightlessness, high pressure, high radioactivity, peculiar microclimate, and great nervous and psychological stress, limited scope of movement, noise and vibrations, among others. The qualitative and quantitative sufficiency of the food is of crucial importance in helping astronauts cope with the negative processes underway in the organism under the influence of the adverse factors typical of long space flights.

Space food is a variety of food products specially formulated and processed for space flight use. Food should meet specific requirements to ensure balanced nutrition for those working in extreme conditions while being easily and safely stored, prepared and consumed in low gravity environments. Despite the

wide variety of food and beverages consumed by astronauts, it is very important that they are provided with a nutritional formula that provides all the necessary vitamins and nutrients and guarantees the working capacity and nervous psychological resistance of the crews [1–4].

The different forms in which food is provided include the following [5, 6]:

1. *Rehydratable* – both commercial and internally processed freeze - dried foods are included in the NASA food provisions and then rehydrated during the mission using the potable water supply. Rehydratable foods are typically side dishes, such as spicy green beans and cornbread dressing, or cereals. ESA rehydratable products include soups, shrimp cocktail and scrambled eggs fall into this category. Ambient and hot water are available to the crew for rehydration of these items.

2. *Thermostabilized* – this process, also known as the retort process, heats food to a temperature that renders it free of pathogens, spoilage microorganisms, and enzyme activity. NASA thermostabilized products include pouched soups, sides, desserts, puddings, and entrees. ESA thermostabilized products include beef with mushrooms, ravioli and tuna in this way.

3. *Natural form* – natural form foods are commercially available, shelf stable foods. The moisture of the foods may range from low moisture (such as almonds and peanuts) to intermediate moisture (such as brownies and dried fruit), but all have reduced water activity, thus inhibiting microbial growth. These foods help to round out the menu by providing very familiar menu options, additional menu variety, and foods requiring no preparation time.

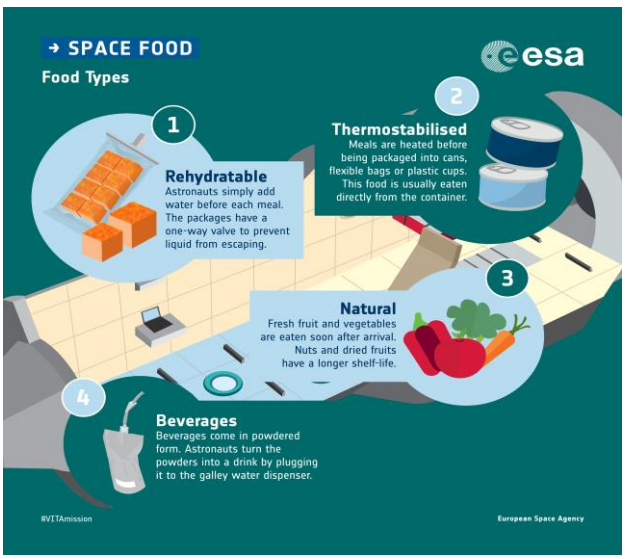

4. *Beverages* – the beverages currently used on the International Space Station (ISS) are either freeze-dried beverage mixes (such as coffee or tea) or flavoured drinks (such as lemonade or orange drink). The drink mixes are weighed and then vacuum sealed inside a beverage pouch. In the case of coffee or tea, sugar or powdered cream can be added to the pouch before sealing. Empty beverage pouches are also provided for drinking water [7, 8].

5. *Extended shelf life bread products* – items, such as scones, waffles, tortillas, and dinner rolls, can be formulated and packaged to give them a shelf life of up to 18 months. Like the natural form foods, breads add to menu variety and address crewmembers' desire for familiarity.

6. *Fresh food* – foods such as fresh fruits and vegetables, which have a short shelf life, are provided on a limited basis, more for psychological support than as a means to meet dietary requirements.

7. *Irradiated* – irradiation is not typically used to process foods to commercial sterility. However, NASA has received special dispensation from the Food and Drug Administration (FDA) to prepare 9 irradiated meat items to commercial sterility (FDA 2009).

Space foods Bulgaria

The Institute of Cryobiology and Food Technologies and the Space Research and Technologies Institute in Sofia are pioneered biotechnologies for the production of space foods, offering a comprehensive menu known as the **Bulgarian Space Menu (BSM)** to the joint Soviet-Bulgarian space flights, within the framework of the *Shipka* project. As a result, the Republic of Bulgaria became the third country in the world, alongside Russia and the USA, to produce space foods [9, 10].

Bulgaria has experience and traditions in the development of freeze-dried foods and beverages designed for space crews and people's contingents working in extreme conditions.

Lyophilisation is a process of separation of moisture from fresh produce by vacuum and low temperatures, allowing virtually completely (to 95%) to be stored in these nutrients, vitamins, trace elements, even the original form natural flavour, taste and colour. Preserved by Lyophilisation product excludes the use of flavourings, colourings or preservatives. One of the most important advantages of this method is the small deformation of the initial product, which allows avoiding its destruction and restoring the original structure of freeze-dried products in cellular hydration. For long-term, safe and proper storage of food and organic foods that method is highly reliable and highly efficient. The high quality, convenience of storage and transportation leads to a widespread industrial development of the sublimation drying of food products. Major manufacturers of such foods are the United States, England, Canada, Denmark, France, China and

others. The production list of most businesses includes fruit, vegetables, seafood, meat, poultry, eggs, mushrooms, tea, dairy products and ready-made culinary products. Over the last decade, cryobiotechnology enters more extensively in the manufacture of innovative products for the pharmaceutical, health, environment and other specific activities.

The BSM consists of 27 types of lyophilized foods based on meat, meat and vegetables and fruit and milk mixes; soups, main meals, desserts, Bulgarian yoghurt and fruit in the shape of quick meal and food pills. The pills are suitable for daily nutritional rations with a minimized mass of 300–500 g and a volume adapted to long space flights (Appendix1).

The BSM complies with modern nutritional requirements, with respect to composition and energy value, under extreme conditions during long space flights. The daily space food allowance of lyophilized foods has an energy value of 12 819 kJ /3 050–3 150 kcal/ and features the following chemical composition: proteins 135 g, fats 110 g, carbohydrates 380 g. The lyophilized space rations are rich in vitamins such as (3-carotene, A, the B complex, D, P, PP, C and others, mineral salts such as Na – 4.5g, K – 3.0 g, Ca – 0.8g, Mg – 0.4g, Fe – 0.05 g, P – 1.7g, organic acids, flavins, pectin substances, live lactic acid bacteria which play the role of detoxicants and regulators of the digestive tract.

The BSM is intended for a diet of four meals a day - two snacks, lunch and supper, with an interval between the meals of between three to five hours. Consumption of the lyophilized space foods is prescribed after rehydration, at temperatures between 27 to 65 °C /except the fruit/, depending on the type of foodstuff. The durability of the space foods extends to five years and they do not contain artificial preservatives.

The BSM is characterized by the delectable traditional flavour of Bulgarian cuisine, a high content of extracts, excellent organoleptic qualities assigned foods used in space conditions where sensory response is considerably subdued because of the change in the physiological activity of the sense of taste. The strong mix of flavour and taste of Bulgarian space foods contributes to the high rate of acceptance, good digestibility and favourable physiological impact on metabolism, adaptability, immune resistance and the work capacity of astronauts. At the same time, the Bulgarian space menu ensures a maximized diet free of dullness, providing for diversity in the daily menu of the astronauts in the course of protracted space flights.

The domestic and foreign market for space foods includes:

- Astronauts;
- Teams such as military, civil defence, firefighters, high rescuers, crew and others;
- Restorative infant feeding problems, mothers, students and athletes and other International market;

- Specialized hospitals to treat patients in the stages of medical evacuation, meals to troops operating in extreme terms.

- Extreme sports – mounting climbers, caving people and etc.

In addition to the above potential users of the innovative product markets are possible for crews working in conditions of prolonged space flight for the personnel of nuclear submarines, paratroopers, Special Forces, commandos and others.

Space Food's Requirements to Astronauts

Astronauts need the same number of calories during a spaceflight as they need on Earth. Fat, protein and carbohydrate provide energy to keep up their activities on the Space Station. Energy intake can differ for each person. The World Health Organization estimates energy requirements and issues recommendations based on a formula [11].

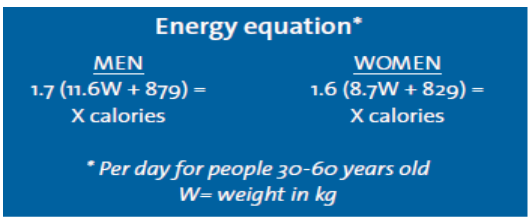

•*A 80 kg man needs about 3000 calories a day*
•*A 60 kg woman needs about 2100 calories a day*

Current ISS crew members receive about 1.8 kg of food plus packaging per person per day. Part of this food is thermostabilized, because the thermostabilized food is still generally preferred in taste tests to freeze dried items by crew members. Since the ISS utilizes solar panels for a power source and not fuel cells that produce water as a by-product, there is no mass advantage to using freeze-dried foods. Water is now transported to the ISS for rehydration. Furthermore, contributing to the mass increase is an increase in the required caloric delivery. The required calories as stated in the mission guidelines are based on the actual caloric needs of the crewmember, which are based on body weight and height. The result is an average caloric requirement of 3 000 kcal (12 550 kJ) as opposed to the 2 500 kcal (10 460 kJ) provided to the Apollo crew. In light of these mass challenges, NASA is considering various avenues of food mass reduction while still providing the crew with adequate calories and an acceptable diet [1].

Without adequate nutrition, human performance and sustainment are endangered. Adequate nutrition has 2 components – required nutrients and supplied energy in the form of calories. Distinct health issues stem from inadequate calories and from inadequate micronutrient intake. It is important that the crewmembers are provided with the required level of nutrition throughout their missions to prevent disease.

Table 1. Summarizes the nutritional requirements for long-duration missions

Nutrients	Daily dietary intake	Nutrients	Daily dietary intake
Protein	• 0.8 g/kg and	Thiamin	Women: 1.1 mg
	• ≤35% of the total daily energy intake and		Men: 1.2 mg
	• 2 of 3 of the amount in the form of animal protein and 1 of 3 in the form of vegetable protein	Riboflavin	1.3 mg
		Folate	400 μg
		Niacin	16 mg niacin equivalent
		Biotin	30 μg
		Pantothenic acid	30 mg
PGCarbohydrate	50% to 55% of the total daily energy intake	Calcium	1200 to 2000 mg
		Phosphorus	• 700 mg and
Fat	25% to 35% of the total daily energy intake		•·≤1.5 × calcium intake
		Magnesium	• Women: 320 mg
Ω - 6 fatty acids	14 g		• Men: 420 mg and
Ω - 3 fatty acids	1.1 to 1.6 g		• ≤350 mg from supplements only
Saturated fat	<7% of total calories	Fluoride	1 500 to 2 300 mg
Trans fatty acids	<1% of total calories	Potassium	4.7 g
Cholesterol	<300 mg/d	Iron	8 to 10 mg
Fiber	10 to 14 g/4187 kJ	Copper	0.5 to 9 mg
Fluid	• 1 to 1.5 mL/4187 kJ and	Manganese	• Women: 1.8 mg
			• Men: 2.3 mg
	• ≥ 2 000 mL	Fluoride	• Women: 3 mg
Vitamin A	700 to 900 μg		• Men: 4 mg
Vitamin D	25 μg	Zinc	11 mg
Vitamin K	Women: 90 μg		
	Men: 120 μg	Selenium	55 to 400 μg
Vitamin E	15 mg		
Vitamin C	90 mg	Iodine	150 μg
Vitamin B12	2.4 μg		
Vitamin B6	1.7 mg	Chromium	35 μg

The ability of the food system to meet the nutritional requirements can be determined only when the nutritional profile of the entire space food system is known for the time at which the food is consumed.

During the development of an extra-terrestrial food system, mission resources, including mass, volume, power, crew time, and waste disposal capacity,

must be considered. Misuse of these resources could limit mission success. Consistently, the balance of resources with other necessary mission factors-food quality or crew hygiene – is at the forefront of planning and design. The conundrum of long exploratory missions is that these missions are both resource constrained and of long duration, requiring strict adherence to nutritional guidelines. Even though food and resource utilization may be at odds, both are vital to mission success. In short, the food must provide the nutrients to sustain crew health and performance, must be acceptable throughout the course of the mission, must be safe even after cooking and processing, and must be formulated and packaged in such a way that the mass and volume are not restrictive to mission viability.

Bulgarian potential customers except astronauts are Ministry of Defence, State Agency "Civil protection", Emergency Services, and other Specialized Hospitals.

Space Foods Requirements for other users

Foods Requirements for Military

The exact determination of the energy requirements of the military personnel is linked with the implementation of scientifically grounded approaches for calculation of the total energy requirement. Each vital, work or daily human activity is connected with consumption of energy, which is supplied by the organism by means of dissolving the received nutrient substances [12–14].

The average daily energy requirement of female and male servicemen with the same functional duties and analogical physical activities is shown at Table 2.

Table 2. Average daily energy requirement of female and male servicemen with the same functional duties and analogical physical activities

Physical activities	Duration of the research in days	Gender	Examined persons	Average daily energy requirement kcal/daily	Average daily energy requirement for 1 kg of the body weight kg.kcal-1.daily-1
Continued work during the training of Norwegian rangers	7	M	6	6 678	93.5
		F	4	5 597	95.7
Field training with intense physical loads	2.25	M	29	6 129	83.0
		F	20	4 727	82.0
Physical training	14	M	20	4 048	56.1
		F	10	2 378	41.1
Administrative activities	11	M	1	2332	38.7

Foods Requirements for sailors and submariners

Nutritional requirements of Navy Personnel are different from those of ground forces due to logistic constraints posed when being away from sea-coast.

Energy expenditure at ships was in the range of 2 449–4 907 kcal/day with a mean of 3 313 + 578 kcal/day, while in the case of submariners, it was 3 168 + 282 (2 606–3 907) kcal/day.

Energy intake in the case of sailors and submariners was not different either at hoer establishment and/or at ship/submarines. Energy intake was found to be 3518 + 286 kcal/day. The energy contribution from carbohydrates, fats and proteins was 59.9 per cent, 27.8 per cent, and 12.3 per cent, respectively (Table 3) [15].

Table 3. Nutrient intake of sailors and submariners

Nutrients	Intake
Energy (kcal)	3518 ± 286
Protein (g)	108 ± 25
Total Fat (g)	109 ± 24
Visible Fat (g)	68 ± 10
CHO (g)	527 ± 51
Vitamin A (µg)	625 ±102
Vitamin C (mg)	58 ± 22
Thiamin (mg)	1.7 ± 0.15
Riboflavin (mg)	1.6 ± 0.3
Niacin (mg)	33 ± 3.7
Iron (mg)	38.0 ± 6.6
Calcium (mg)	1410 ± 156
Phosphorus (mg)	1534 ± 125
Sodium (mg)	7000 ± 330
Potassium (mg)	2856 ± 135
Zinc (mg)	16.2 ± 1.30
Copper (mg)	2.80 ± 0.50
Energy contribution	
Carbohydrates per cent	59.9
Protein (per cent)	12.3
Fat (per cent)	27.8

Energy requirements for military personnel in extreme conditions

Energy requirements in hot climate. In areas of hot climate, a person is in a state of permanent heat pressure, especially during the summer months. When the temperature of the habitat is equal to or higher than the average temperature of the body surface, evaporation of sweat is the only way to maintain the body's thermal equilibrium. Calculations show that in similar conditions for the discharge of every 4.2 MJ (1 000 kcal) of metabolic heat from the body surface and upper respiratory tract, at least 1 725 g of moisture should evaporate. This moisture comes mainly through the sweat glands, which are able to secrete 10–12 and even up to 15 litters of sweat per day under heat stress conditions [16].

With many days of loss of large amounts of sweat (over 4–5 litters), the deficiency of mineral salts, especially potassium, and vitamins can be significant, which necessitates the correction of dietary rations to prevent salt depletion and devitaminization.

Energy requirement under hot climatic conditions

The analysis of the available literature imposes the conclusion, that generally the high temperature of the environment influences insignificantly on the daily energy requirements of the military personnel. A study, carried out in the desert shows, that the artillery units consume averagely 4 108 kcal/daily under average daily air temperature of 20.6 °C. Similar total energy requirements (3 941 kcal/daily) are observed for the infantry units in Israel, where the temperatures vary from 23 up to 31 °C. The Royal Australian Air Forces in North Australia consume about 3 702 kcal/daily, at temperatures varying from 24 to 33 °C, and the reformed tasks are linked with guard and transport support of an airport [17].

The comparison between the energy requirements of the artillery, of the infantry and of the ground units from the Air Forces show, that the general energy requirements are similar to the values, observed under cooler conditions (4 099 kcal/daily for training at the permanent dislocation station, 3 346 kcal/daily and 3 568 kcal/daily for everyday activities of the supporting units).

One of the reasons for that, roots in the fact, that the servicemen perform their obligations more efficient in hot, dry and clear days. The energy requirements are connected mainly with the sort and the duration of the activities, which are being performed, not with the hot meteorological conditions.

Energy requirements in winter and under cold climatic conditions

Hoyt and team consider that the general energy requirement of the military personnel increases in winter and under cold climatic conditions. In the examination of the American marines in cold weather (under temperatures of the

environment from –10 up to 5 °C), average energy requirements of 5 398 kcal/daily are observed [18]. The general energy requirements had been around 4 156 kcal/daily in warm weather (under temperatures of the environment from 9 up to 31 °C) for the same course at the same place, under analogical general physical and mental pressure.

Energy requirements in the highlands

It is recommended to provide personnel operating in the mountains with a diet containing up to 4 500 kcal (about 17 MJ). With regard to the qualitative composition, then, given the difficulties of metabolizing fat and partially proteins, they provide an increase in the carbohydrate quota, and preference is given not to one of them, but to their mixtures.

The servicemen from the American Army, located in Potosi, Bolivia at 3 500–4 050 m altitude, have had an average daily energy requirement of 3 535 kcal, 10 days long, during the construction of the infrastructure [94]. These values are a little bit higher than the general energy requirements of 3 463 kcal/daily for servicemen from the engineering units, performing similar activity at a sea area.

Requirements for extreme professions

Civil protection crews. On-board emergency packages

Designed to provide rescue professional emergency services, professional emergency rescue units for civil defence, emergency situations and disaster relief when on board a ship in an emergency. The diet is a set of canned and concentrated foods per person per day and consumed with the permission of the ship's commander in case of accidents (Table 4).

Table 4. The Following Products are Included in the Food Ration

Products	Weight(g)
Bread (biscuits) army of wheat flour 1 grade	150
Canned meat-cereal and meat-vegetable	500
Food concentrates briquetted, not requiring cooking	120
Or Food concentrates briquetted for instant cooking	120
Condensed whole milk with sugar	90
Or chocolate paste	50
Or dry milk	70
Or dry milk drink	70
Sugar	15
Lollipop	20

Products	Weight(g)
Or sugar	40
Or fruit stick	50
Or fruit jam	60
Instant coffee	2
Black tea	2
Multivitamins, coated tablets	2
Plastic spoon, (pcs).	1
Can opener, (pcs)	1
Drinking water, canned , (ml)	125

Food And Energy Value of Food Ration – proteins 83 g; fats 92 g; carbohydrates 348 g, Energy Value – 2 552 kcal.

Requirements for fire brigade crews

This study piloted the use of an electronic activity monitor (MTI AM 7164-1.2) as a tool for estimating activity (EE(ACT), kcal day^{-1}) and total (EE(TOT) kcal day^{-1}) energy expenditure in wildland fire fighters during extended periods of wildland fire suppression. Ten Hot Shot fire fighters (9 men, 1 woman) volunteered to wear a MTI monitor during every work shift for 21 consecutive days. Summarizing whole-body motion data each 1 min, the raw activity data (counts min^{-1}) were transformed into units of kcal min^{-1} using a custom computer program with standard conversion equations. EE(TOT) averaged (Mean ± SD) 4 768 ± 478 kcal day^{-1}, while EE(ACT) averaged 2 585 ± 406 kcal day^{-1}, neither of which differed significantly (P = 0.198 and 0.268, respectively) from literature values reported for Hot Shots using the doubly labelled water technique. These data suggest that the electronic activity monitor provided reasonable estimates of EE in wildland fire fighters. This study should be verified, however, with a more complete validation methodology to ensure these findings [19].

Requirements for extreme sports

Caving peoples

The impact of caving activity on body composition and hydration were assessed through bioelectrical impedance, and nutritional habits of cavers surveyed. During cave activity, measured total energy expenditure (TEE) was in the range 225 ± 287 kcal/h for women-men (MET = 4.1), respectively; subjects had an energy intake from food in the range 1 000 ± 1 200 kcal, thus inadequate to restore lost calories.

Comparison of dietary intake and energy expenditure (TEE) in a normal day versus the full cave day and cave activity per se, offers interesting cues (Table 5).

Table 5. Anthropometric measurements, physiological variables, and dietary intake

	Men		Women	
	Mean	SD	Mean	SD
Height (m)	1.7	0.1	1.6	0.1
Weight (kg)	73.2	11.7	55.4	6.0
BMI	24.7	3.0	21.8	2.1
TEE (kcal/24h), normal day	3487.9	528.2	2367.3	316.6
TEE (kcal/24h), cave day	5128.5	862.5	3980.9	441.1
TEE (kcal/h), cave activity	287.5	48.5	225.4	27.9
MET's, cave activity	4.1	0.7	4.1	0.5
Intake (kcal/24 h), normal day	2640.7	673.5	1858.1	324.3
Intake (kcal/24 h), cave day	3393.7	1530.3	2672.9	732.3
Intake (kcal/10 h), cave activity	1186.8	473.4	1008.2	513.2

BMI, body mass index; MET, metabolic equivalent of task; TEE, total energy expenditure; SD, standard deviation.

Requirements for children gardens and hospitals

The physiological norms of nutrition of the population

Lyophilized space foods can also be used to feed the population based on physiological nutrition norms.

Energy needs are defined as mean energy needs expressed in MJ and kcal per day for population groups age-differentiated by reference height and weight estimated for different levels of physical activity and representing the average daily requirement over a period of at least one week.

The application of the physiological norms of nutrition aims at meeting the physiological needs, achieving normal growth and development and creating prerequisites for long-term good health of the population [20].

Table 6. Average energy needs for boys and girls from 1 to 19 years of ageby age groups

Age (years)	Boys		Girls	
	MJ/daily	кcal/daily	MJ/daily	кcal/daily
1 – <3	4.36	1 040	4.09	980
3 – <5	5.66	1 350	5.26	1 260
5 – <7	6.80	1 630	6.32	1 510

Age (years)	Boys		Girls	
	MJ/daily	κcal/daily	MJ/daily	κcal/daily
7 – <10	7.55	1 800	7.07	1 690
10 – <14	9.92	2 370	9.35	2 230
14 – <19	13.12	3 130	10.35	2 470

Table 7. Average adult energy needs

Age (years)	Body weight (κg)	Height (cm)	Low active lifestyle MJ (κcal)/daily	Moderately active lifestyle MJ (κcal)/daily	Active lifestyle MJ (κcal)/daily	A very active lifestyle MJ (κcal)/daily
	Men					
19 – <30	70	178	9.81 (2 344)	11.21 (2 679)	12.61 (3 013)	14.0 (3 348)
30 – <60	72	176	9.56 (2 286)	10.93 (2 612)	12.29 (2 939)	13.66 (3 265)
60 – <75	79	173	8.66 (2 070)	9.90 (2 365)	11.13 (2 661)	
75 +	68	171	8.47 (2 024)	9.68 (2 314)		
	Wimen					
19 – <30	56	164	7.65 (1 828)	8.74 (2 089)	9.83 (2 350)	10.93 (2 612)
30 – <60	60	164	7.63 (1 823)	8.72 (2 083)	9.80 (2 343)	10.89 (2 604)
60 – <75	60	160	6.99 (1 672)	7.99 (1 911)	8.99 (2 150)	
75 +	55	158	6.70 (1 600)	7.65 (1 829)		
	Pregnancy and nursing**					
Pregna-ncy	Trimester		I	+ 0.29 (+ 70)		
				+ 1.09 II (+ 260)		
			III	+ 2.09 (+ 500)		
Nursing	Month		0 – 6	+ 2.09 (+ 500)		

The main customers of lyophilised products are mountaineers and athletes who need long-term shelf-life foods. And when they have gone through this

freezing and drying, they last up to 5 years and more. Recently, consumers of this recipe are also vegetarians.

The Bulgarian Space Menu was highly praised and appreciated by the members of the Himalayan expeditions, the Transatlantic Women's Regatta, the two expeditions to the Antarctic and on many other occasions.

Conclusion

Taking into account the most common requirements, our potential customers and our long-standing experience in developing freeze-dried foods at this stage, we are continuing to study the trends in space-based food development.

The aim of the ESA project is the development and implementation of technology for astronauts and various contingents of people working in extreme conditions. This project will definitely contribute to the development of science and practice in the particular scientific field. Products developed under this project will contribute to improving the efficiency of contingent working in extreme conditions. At the same time the results of the experiments will serve as the basis for new theoretical and experimental research in cryobiology and contribute to its development.

Acknowledgements

We hereby would like to thank to the ESA for supporting generously ESA project titled “Development and application of technology for production of space food’s modules for crews working in extreme conditions”.

References

1. Billock, J. The Dark Side of the Spoon: What Astronauts Eat in Space. Serious Eats. Serious Eats, 18 June 2015. (Accessed on 19 January 2016).
2. “Meals Ready to Eat: Expedition 44 Crew Members Sample Leafy Greens Grown on Space Station.” NASA. NASA, 7 August 2015. (Accessed on 5 February 2016).
3. Zwart, S., Kloeris, V., Perchonok, M., Braby, L., and Smith, S. M. Assessment of Nutrient Stability in Foods from the Space Food System after Long-Duration Spaceflight on the ISS. Journal of Food Science, 2009, 74, 209–17.
4. Benson, C. D. and W. D. Compton. Living and Working in Space: A History of Skylab. NASA publication SP-4208.
5. Cooper, M., Gr. Douglas, and M. Perchonok, Developing the NASA Food System for Long -Duration Missions, March 2011 Journal of Food Science 76, 2, R40-8, DOI:10.1111/j.1750-3841.2010.01982.x.
6. SPACE FOOD, Astronaut nutrition, ESA production, 2017, hsocom@esa.int
7. Casaburri, A., Gardner, C. A. Space Food and Nutrition. Educator’s Guide. NASA. Washington, D.C. 1999.
8. Evans, J. Space Farming. C&I Agriculture, 2015, 10, 20–23.

9. Doneva, M., l. Nacheva, P, Metodieva, Application of cryobiotechnologies for development of lyophilized polyenzyme complexes, Bulgarian Journal of Agricultural Science, 2014, 20, 6, 1401–05.
10. Vassilev, V., Space Sector Activities in Bulgaria, Natal, Brazil, 2018, www.castra.org
11. "Food for Space Flight" NASA. URL: http://spaceflight.nasa.gov/shuttle/reference/factsheets/food.html.
12. Nichev, N. Energy requirement of the military personnel. International Conference "Knowledge-Based Organization". 2018, XXIV, 2, 338–344, DOI:10.1515/kbo-2018-0112.
13. Tharion, W. J. et al. Energy requirements of military personnel. Appetite, 2005, 44, 47–65.
14. Hoyt, R. W., Jones, T. E., Stein, T. P., McAninch, G. W., Lieberman, H. R., Askew, E. W., and Cymerman, A. Doubly labelled water measurement of human energy expenditure during strenuous exercise. Journal of Applied Physiology, 1991, 71, 16–22.
15. Singh, V. K., A., A. Dutta, V. Shukla, P. Vats, and S. N. Singh. Energy Expenditure and Nutritional Status of Sailors and Submarine Crew of the Indian Navy. Defence Science Journal, 2011, 61, 6, 540–544, DOI:10.14429/dsj.61.930.
16. Lane, H. W., Bourland, C., Barrett, A., Heer, M., and Smith, S. M. The Role of Nutritional Research in the Success of Human Space Flight. Advances in Nutrition, 2013, 4, 521–23.
17. McPhee, I. J, and Charles, J. Human health and performance risks of space exploration missions: evidence reviewed by the NASA Human Research Program (PDF). Johnson Space Center, Houston: National Aeronautics and Space Administration, Lyndon B. Johnson Space Center, 4–5. ISBN 978-0160846342.
18. Estimating energy expenditure in wild land fire fighters using a physical activity monitor. URL:https://www.ncbi.nlm.nih.gov/pubmed/12236649.
19. Antoni, G, E. Marini, N. Curreli , V. Tuveri, O. Comandini, S. Cabras, S. Gabba, C. Madeddu, A. Crisafulli, and A. C. Rinaldi. Energy expenditure in caving. PLOS ONE, 2017, DOI:10.1371/journal.pone.0170853.
20. BG Ministry Health Care -ORDINANCE No. 1 of 22 January 2018 about the physiological norms of nutrition of the population. http://www.mh.government.bg/media/filer_public/2018/02/13/naredba1-22-01-2018-fiziologicni-normi-hranene-naselenie.pdf.

ПРИЛОЖЕНИЕ НА КРИОТЕХНОЛОГИЯТА ПРИ СЪЗДАВАНЕ НА КОСМИЧЕСКИ ХРАНИ ЗА ЕКИПАЖИ, РАБОТЕЩИ В ЕКСТРЕМНИ УСЛОВИЯ

П. Гецов, Ц. Цветков, Г. Сотиров, И. Начева, З. Хубенова, М. Донева, П. Методиева

Резюме

Статията представя постиженията в областта на криобиологията и е свързана с работата на авторите по проект с ЕКА. Космическата храна е разнообразие от хранителни продукти, специално създадени и обработени за използване в космически полети. Тази храна трябва да отговаря на редица специфични изисквания, за да може да осигури балансирано хранене за работещите в екстремни условия, като същевременно лесно и безопасно се съхранява, приготвя и консумира в среда с ниска гравитация. Направен е преглед на вътрешния и чуждестранен пазар на космически храни. Определени са изискванията към астронавтите, както и за други потенциални потребители: военни; хора с екстремни професии; за екстремни спортове, за болници и детски градини. Дадени са обобщени хранителни изисквания за всички споменати по-горе групи потребители на космически храни. Показан е българският опит в изследването и разработването на космическите храни и създаденото българско космическо меню.

Bulgarian Academy of Sciences. Space Research and Technology Institute.
Aerospace Research in Bulgaria. 32, 2020, Sofia

DOI: https://doi.org/10.3897/arb.v32.e17

ZEOLITES APPLICATION IN TERRESTRIAL AND SPACE INDUSTRY – A REVIEW

Adelina Miteva[1], Valeria Stoyanova[2]

[1]Space Research and Technology Institute, Bulgarian Academy of Sciences
[2]Institute of Physical Chemistry, Bulgarian Academy of Sciences
e-mails: ad.miteva@gmail.com, valeria@ipc.bas.bg

Keywords: *Zeolite Synthesis; Catalysis, Adsorption and Ion Exchange; Space Applications; Fuel; Water and Gas Purification*

Abstract

This brief overview presents an attempt to systematize some of the available historical and recent data on the impact of zeolite science and engineering on the progress of various areas of Earth and Space development. The basic structural and chemical properties of natural and synthetic zeolites are presented. Valuable applications of the zeolites, such as catalysts, gas adsorbers and ion exchangers are also included. The most commonly used methods for the synthesis of zeolites from different materials are presented, as well as some Bulgarian developments for the reuse of waste materials to zeolites. The important role of zeolites as an indispensable material for improving the quality of soil, fuels, water, air, etc., required for the needs of orbiting space stations and spacecrafts has been confirmed by typical examples.

Aim and scope

The aim of this review is to briefly outline the application of zeolites in the vast field of aerospace engineering and the launch industry. Zeolitic materials are indirectly related to improving the quality of production of satellites, ground equipment, aviation and spacecraft flights, fuels, water and air purification in aircraft, as well as ensuring the safety of passengers and crew. Some of the general structural and chemical concepts are presented here, such as aerospace terms, catalysis, ion exchange and cracking, the main zeolite properties, materials, etc. Mentioned here are also some Bulgarian achievements.

Zeolites and their main properties

Zeolitites are a large group of crystalline minerals having microporous and regular structure [1, 2]. This definition usually refers to the natural zeolitic minerals, but it also refers to a synthetic crystalline substance with zeolitic properties, i.e. a material with a crystal structure formed by a three-dimensional

open framework of tetrahedra with inner channels and cavities providing the material with the capabilities of ion exchange and reversible dehydration. The main differences between natural and synthetic zeolites are the time scale in which they are produced, the amount of material that is produced and the quality of zeolites. The great advantage of natural zeolites is the volume and quantity that they can extract, unlike the relatively low volumes produced in the laboratory, but only the creating of synthetic zeolites can provide materials with certain desired properties tailored to the specific industrial needs. The number of naturally occurring zeolite types is about 40, and the artificially synthesized zeolites are almost 200 unique frameworks [2]. More information about both, natural and synthetic zeolites can be found in the International Zeolite Association (IZA) web pages such as, for instance: http://www.iza-structure.org/databases/.

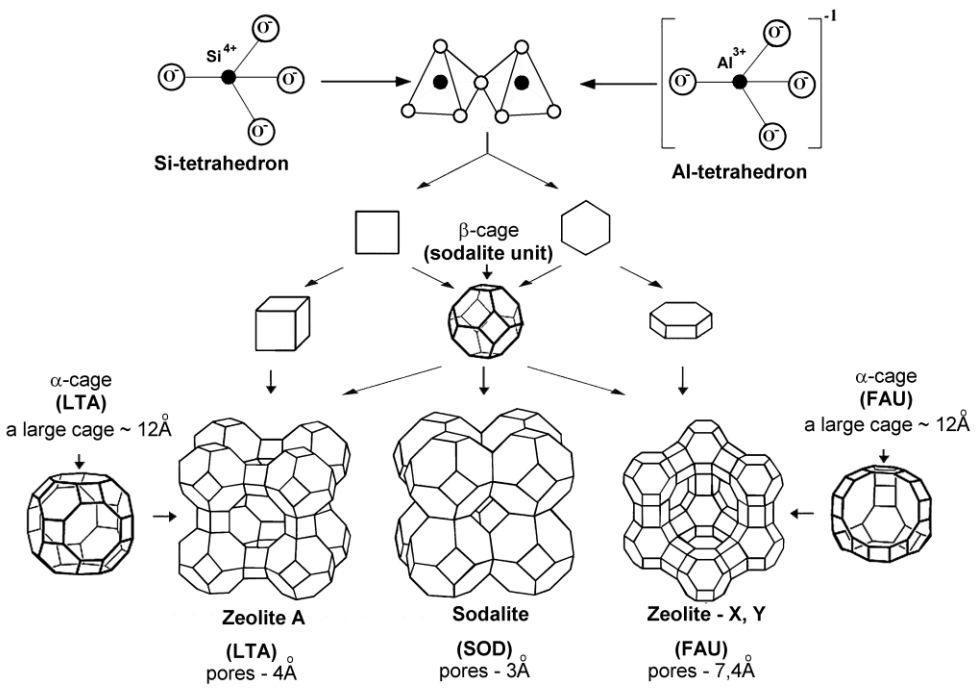

Fig. 1. Examples of building units and pore / cage sizes of three zeolite structures: zeolite A (LTA), sodalite (SOD), and faujazite (FAU) – zeolites X, Y

The composition of zeolites can be represented by the general formula $Mx/n[(AlO_2)x(SiO_2)y].zH_2O$, where n is the charge of the metal cation M, and the values of x, y and z depend on the type of zeolite. For example, the respective formula for zeolite NaA, also known as LTA (Linde Type A), is $Na_{12}[(AlO_2)_{12}(SiO_2)_{12}].27H_2O$, implying that zeolite LTA has 12 tetrahedra in

every cell unit, occupied by 12 Na atoms and 27 H_2O molecules. Zeolites X and Y belong to the group of faujasite (FAU), faujasite-Na, faujasite-Mg or faujasite-Ca, having the same basic formula*:* $(Na_2,Ca,Mg)_{3.5}[Al_7Si_{17}O_{48}].32(H_2O)$. The structures of these three types of zeolites are presented in Fig. 1.

Zeolitic materials are readily dehydrated and rehydrated, and can be used as cation exchangers (removal of metal cations from wastewaters, detergent ingredient), absorbers (for gases and liquids), molecular sieves (membranes, purificators), catalysts (petrochemistry, environmental issues, fine chemicals) etc. Due to these specific structural peculiarities, they are invaluable in chemical industry, and also in development of various traditional and modern fields, like green chemistry, hybrid materials, medicine, animal food, soil improvement, optical and electrical based applications, microsystems and nanotechnology, etc. The morphology and size of zeolite crystals could have also important impact on their applications. Besides, from a practical point of view, zeolites are environmental-friendly in technological processes.

Aerospace sector

The aerospace industry refers to Class 3530 of the United Nations' International Standard Industrial Classification (ISIC) which covers the manufacture of aircraft and spacecraft. This broad class comprises the manufacturing of both non-space items (passenger and military aeroplanes, helicopters, gliders, balloons, etc.) and space items (including spacecraft, spacecraft launch vehicles, satellites, planetary probes, orbital stations and shuttles). This also includes the manufacturing of their parts and accessories, used in civil or military applications, such as aircraft instrumentation, navigation and control systems, ignition parts and other electrical parts for internal combustion engines, space radio and telemetry systems, etc. [3, 4].

Scientific interest to zeolite growth in space

An important impetus for writing this review is the longstanding and growing interest in the topic of the zeolites and their current and future use not only on earth but also for the needs of the space industry.

Since the first flight of the Wright brothers in 1903, the humankind has come a long way, and in 2019 we have not only commercial aircraft for more than 850 passengers at once, but also a great variety of business and private aircrafts, such as airplanes, helicopters, drones, etc. Currently, we have more than 4800 satellites in orbit around the earth. In 2018 was tested the newest solar aircraft that stayed in flight for almost a month. One of the greatest achievements in engineering space industry is the International Space Station that is a low orbit space research center.

NASA's effort to stimulate commercial use of space, it is “to enlarge the technology base on which to build new commercial space industries and to help move emerging technologies from the laboratory to the marketplace with speed and efficiency” [4]. The Battelle center has sponsored experiments on eight Space Shuttle missions since 1990. The huge potential of the zeolites has aroused great interest among space competitors. Two NASA Space Commerce Centers (Battelle Advanced Materials Center, Columbus, Ohio, and Clarkson Center for Commercial Crystal Growth, Potsdam, New York) have merged their endeavours with a number of industrial and academic institutions, sending to fly 38 sample zeolite solutions in 1992 Shuttle mission. Results of that flight were applied to a zeolite growth experiment package flown aboard STS-57 in 1993. The clear conclusion was that zeolite crystals, which have wide and important significant commercial potential, can be grown larger and more efficient with fewer defects in orbit (Fig. 2).

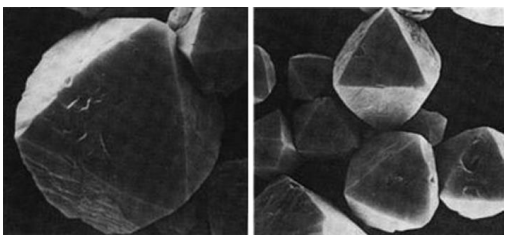

Fig. 2. Zeolite crystals, which have significant commercial potential, can be grown larger and with fewer defects in orbit. This photo compares orbit-grown (left) and Earth-grown zeolite crystals (right) [4].

Main zeolite applications

The three main applications of zeolites in the fields of catalysis, gas adsorption and ion exchange are schematically presented in Fig. 3 and are briefly described below [2]:

Catalysis**:** It is the most important application of zeolites in industry and benefits from a zeolite framework with well-defined pores and acidity. The largest application is the Fluid Catalytic Cracking (FCC) process, which is used for production of gasoline from heavy oil through cracking. Zeolite Y is the key component in the FCC catalysts, due to it pore size, and high activity provided by acid sites when is ion exchanged with rare earth or hydrogen cations. For example, ZSM-5 zeolite is used extensively as catalyst in the petrochemical industry.

Gas Separation**:** Adsorption is a common phenomenon in which a part of gas or liquid in contact with a solid is retained and concentrated at its surface. Zeolites are widely used in adsorption-related applications. Gas separation through adsorption may be achieved via the strength of adsorption (selective adsorption) or

rate of adsorption (molecular sieving by size and shape). Acid gases, such as HCl, SO_3, and NO_2 are strongly adsorbed on molecular sieves because of their polarity but are accompanied by degradation of the molecular sieve crystalline structure. Other gases, such as CO_2, SO_2 and H_2S are reversibly adsorbed. Examples of gas separation by selective adsorption using zeolites are the selective uptake of CO_2 over N_2 and separation of CO_2 from natural gas or synthesis gas. An example of gas separation by molecular sieving zeolites is the separation of xylene isomers.

Ion exchange**:** The ions held in channels and cavities of zeolites are exchangeable and zeolites can take up cations from mixtures with other cations. For instance, zeolite A is applied industrially as detergent builder to takes up Ca ions from water, and exchanges them with Na ions of the zeolite, which makes the water soft. The success of zeolite A as detergent is due to its high and fast calcium uptake, good dispersibility, low sedimentation tendency, low abrasiveness and high degree of whiteness. Zeolite crystals should have a small particle size (around 4 μm) and narrow particle size distribution.

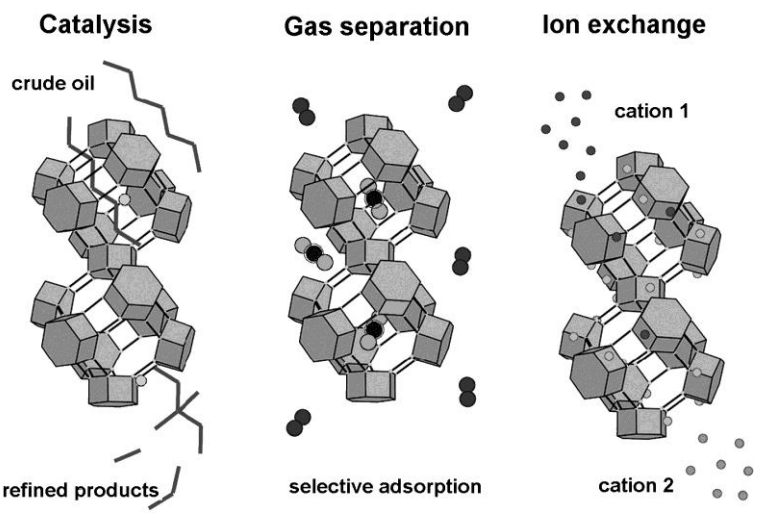

Fig. 3. Schematic illustration of the three main applications of zeolites: catalysis, gas adsorption and ion exchange [5]

Water and wastewater treatment

The most prominent features of zeolites include the exchange of undesirable cations and the absorption of inorganic and organic molecules of specific dimensions. Their values of high mechanical strength, chemical stability and abrasion make zeolites a special material for softening and purifying drinking and industrial waters, as well as many other applications [6]. The negative charges

act as a magnet to attract positively charged toxins, heavy metals and some radioactive elements. Due to their large surface area and porosity, zeolites are perfect catchers for bacteria.

As a rule, the greater the Al content corresponds to the higher cation exchange capacity of the zeolite. The negative charge at $[AlO_4]^-$ -tetrahedra is compensated by easy replaceable metal-cations such as Na^+ , K^+ , Ca^{2+} , Mg^{2+} , etc., that determine the ion-exchange ability of zeolites for effective removal of pollutants from contaminated waters. The most common cation in synthetic natural and natural zeolite structure is Na^+, which can be easily replaced from aqueous solution, e.g. by Sr^{2+} or Cs^+ ions.

Softening

Nowadays, most of the commercial washing powders contain zeolite, instead of harmful phosphates. Zeolites are widely used in industrial water softening systems and in domestic "on the tap" filters, since they could be easily regenerated. Zeolite NaA is nontoxic to fresh and marine waters, and is the first zeolite introduced as a water softener in laundry detergents in 1978. Similar behaviour has the zeolite NaP. Especially valuable appears to be the zeolite X, that due to its larger pore diameter of 0.74 nm has higher magnesium binding capacity compared to zeolites A and P [6]. It was successfully introduced into detergents market a dozen years ago. Synthetic zeolite 13X and the natural clinoptilolite have been also reported for use in detergent formulations. Experiments show that zeolite A and zeolite X were more effective in cleaning than clinoptilolite at low temperatures, while all these builders had the same effectiveness at high temperatures. Due to the advantageous builder properties of zeolites combined with their human and environmental safety, they have been included in an extensive range of detergent industry. In Europe, the USA, Japan and several regions of East Asia, zeolites have almost entirely replaced phosphates.

Ammonia removal

Ammonia in the environment originates from metabolic, agricultural and industrial processes and from water disinfection. Ammonia in water is an indicator of possible bacterial, sewage and animal waste pollution, and may have harmful effect on human and animal health. Natural clinoptilolite has higher selectivity for NH^{4+} ion than synthetic zeolites. Despite of their lower selectivity to ammonia ion, synthetic zeolites, namely types A, X and Y, have much higher ammonia exchange capacity than naturally occurring zeolites [6].

Heavy metals removal

Heavy metals, like Cd, Cr, Cu, Ni, Zn, Pb and Hg, are well known with their toxicity. Some of them tent to accumulate in living organisms, and may cause serious health effects, including reduced growth and development, cancer, organ damage, nervous system damage, and even death. Many natural and synthetic

zeolites have been widely explored for heavy metals immobilization form natural or industrial water. The number of the scientific articles devoted on this problem in the past ten years exceeds one hundred. Clinoptilolite, NaA, NaP, NaP1, NaX are among the most studied zeolites for adsorption of heavy metals (Pb^{2+}, Co^{2+}, Cu^{2+}, Zn^{2+}, Mn^{2+}, Fe^{3+}, Cd^{2+}, Ba^{2+}, As^{2+}, Cr^{3+}, Ni^{2+}, Hg^{2+}, Ag^{+} , etc.) from aqueous solutions. Generally, the synthetic zeolites have much better removal performance than natural ones. Heavy metals-loaded zeolite could be regenerated [6, 7].

Radioactive species removal

Various processes used in the nuclear fuel cycle and in the application of radionuclides in industry, medicine, and research generate low or intermediate level liquid wastes, containing radioactive isotopes (e.g. ^{137}Cs, ^{90}Sr, ^{60}Co, ^{45}Ca, ^{51}Cr, ^{111m}Cd, ^{110m}Ag). Adsorption of some radioactive elements (U^{6+}, Th^{4-}, I^{+}, Mo^{2+}, La^{3+}, Nd^{3+}, Sm^{3+}, Ag^{+}, Cs^{+}, Co^{2+}, Sr^{2+}, Cd^{2+}) on some natural (clinoptilolite, mesolite, analsite, etc.) and synthetic (NaA, NaX, NaY, ZSM5, etc.) zeolites are presented in [6]. Some of the main advantages of using zeolites for nuclear wastewater [7] are their resistance to degradation in the presence of ionizing radiation, their low solubility and that they can be used for long term storage of long-lived radioisotopes in stainless steel containers. The “saturated” zeolites can be also transformed into concrete, glass, or ceramic bodies, and stored indefinitely.

Sea water desalination

The reverse osmosis membrane materials for desalination have been recently reviewed as appropriate method for water desalination. According to this mechanism, MFI zeolite, which has an effective nanopore diameter of 0.51 nm, appears suitable for separating the smaller water molecules (0.26 nm) from larger ions like Na^{+} and Cl^{-} having hydrated sizes of 0.72 and 0.66 nm, respectively [6]. Hydroxysodalite and NaA zeolites (pore diameters 0.4 nm and 0.8 nm, respectively) are tested using an experimental pervaporation setup. The polymer-zeolite NaA nanocomposite membranes and those with added NaX nano-zeolite, being developed recently, appear to be particularly promising for ion removal from aqueous solutions.

Petroleum industry and fuels

Catalytic cracking

Catalytic cracking is the breaking of large molecules into smaller ones at elevated temperatures via the use of a catalyst (see Fig. 4). As discussed in the previous subsection, molecules will crack when subjected to severe thermal conditions without a catalyst. However, the presence of a catalyst allows for a more controlled reaction. Fluid Catalytic Cracking (FCC) is the most widely used process for the large-scale production of gasoline with high octane number [5].

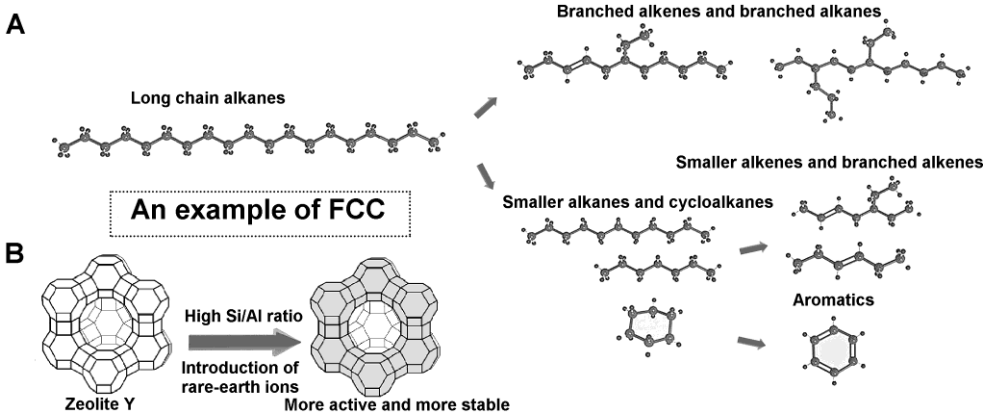

Fig. 4. Fluid catalytic cracking (FCC). A) An example of FCC. B) Schematic of development strategies for zeolite Y for FCC catalysis.

The remarkable properties of zeolites allow the development of cleaner and more efficient processes for the production of fuels and chemicals. Because zeolites are highly porous and possess adjustable acidity, they are commonly used as absorbents, as molecular sieves for separating mixtures by selective absorption, as well as catalysts in petroleum processing.

Synthetic zeolite Y, as well as other mesoporous materials (e.g. MCM-41), are long ago used as catalysts in the petrochemical industry, for instance in fluid catalytic cracking and hydrocracking. Various different solid acidic catalysts have been studied and tested for catalytic cracking, but zeolites are the best performing ones. The Y zeolite is the main zeolitic component of the FCC process, which can be incorporated in industrial catalysts in various forms: Recently, ZSM-5 zeolite is used as a co-component to increase the yield of light olefins which are produced as secondary products. The typical reaction temperature for catalytic cracking ranges from 450 to 560 °C. Examples of the various applications of zeolites and zeotypes in the catalytic conversion of oil and gas are given in the review paper of Vogt et.al. [8]. Some refinery applications are presented briefly, such as fluid catalytic cracking and hydrocracking, and also a wide variety of important petrochemical processes. Discussed are also effects of zeolite–binder interactions in commercial catalysts, where the zeolite is only part of the system.

With the right catalyst in hand, engineers may be able to steer the cracking process along a reaction path that increases cooling and generates better fuel products or ones less prone to coking. Catalysis specialists from University of Virginia have studied zeolite Y and its effect on the pyrolysis of JP-10 juel. Because of its compositional simplicity, JP-10 (exo-tetrahydrodicyclopentadiene) is often used in combustion research. Zeolite Y is a porous aluminosilicate catalyst used commercially for petroleum cracking. In the absence of the catalyst, thermal

cracking converted JP-10 to numerous products, the predominant ones being cyclopentadiene and cyclopentene. In the presence of the catalyst, however, the fuel reacted to form naphthalene and substituted indenes. The catalyst also slightly decreased JP-10's endothermic cooling capacity and lowered the cracking temperature by 210 °C. In effect, the catalyst protects the fuel by preventing it from reaching the temperature at which hard-to-control thermal reactions take off [9].

Scientists at Tianjin University also studied the effect of zeolites on JP-10 cracking using an acidic aluminosilicate catalyst HZSM-5. They succeeded to grow nanosheets of HZSM-5 with Si/Al values of 25 (ZNS-25) and thicknesses of about 2.0 nm. The catalytic cracking of JP-10 over ZNS-25 gave a better conversion than that obtained over a conventional bulk HZSM-5 catalyst, and the deactivation rate was relatively low. The nanosheets were more active at converting JP-10 than the respective bulk zeolites with the higher aluminium content. The explanation is that nanostructuring shortens the length of the zeolite channels and exposes more surface area for cracking. Shortening the zeolite channels enhances diffusion of reactants and products, especially the size of JP-10. And increasing the aluminium content increases the number of catalytically active acidic sites, which in the case of the nanosheets are located on the surface where they are exposed and accessible to reactants.

Gas separation, molecular sieves and adsorption

The most important property of zeolites is their internal porosity which derives from their dehydrated crystalline structure. With very active zeolites, the external surface area constitutes less than one percent of the total area available for adsorption. These materials have a great deal of internal volume available for adsorption which is only accessible by a network of channels or apertures (see Fig.1). Molecules small enough to enter the channels can access the internal volume where the crystal adsorption sites are located. Zeolites have the potential of providing precise and specific separation of gases, including the removal of H_2O, CO_2 and SO_2 from low-grade natural gas streams. Other separations include noble gases, N_2, O_2, freon and formaldehyde.

The first comprehensive published review of the design and performance of advanced oxygen systems was written in 1996 by members of the USAF Armstrong Laboratory and of the RAF School of Aviation Medicine. The evolution of on-board oxygen generating systems and the first generation of oxygen concentrators working by using molecular sieve adsorption technology are described. Such systems have been in use in the US Navy, the US Air Force and the Royal Air Force for over 20 years. They are mounted on high-performance combat aircraft and will continue to be used in the future. In 1998, the results of an American experiment were published in which 5A zeolite was used to remove CO_2 at the International Space Station. The device, known as the "four-bed molecular sieve" or 4BMS, was intended to eliminate through adsorption the excess CO_2

exhaled by the crew and on-board animals. The packed bed was filled with solid sorbent media (5A zeolite) to scrub CO_2 from the air blown through it. The CO_2-saturated bed was regenerated several times a day in a programmed cycle. During the regeneration cycle, the process air stream was diverted to a second (and previously regenerating). The concentrated CO_2 was removed from the bed using heat and vacuum [10].

An important aspect of air revitalization for life support in spacecraft is the removal of CO_2 from cabin air. Several types of CO_2 removal systems are in use in spacecraft life support. These systems rely on various removal techniques that employ different architectures and media for scrubbing CO_2, such as permeable membranes, liquid amine, adsorbents, and absorbents. Sorbent systems have been used since the first manned missions. The current state of key technology is the existing International Space Station (ISS) Carbon Dioxide Removal Assembly (CDRA), a system that selectively removes carbon dioxide from the cabin atmosphere. The CDRA system was launched aboard UF-2 in 2001 and resides in the U.S. Destiny Laboratory module. During the past four years, the CDRA system has operated with varying degrees of success. There have been several approaches to troubleshooting the CDRA system aimed at developing work-around solutions that would minimize the impact on astronaut time required to implement interim solutions. The CDRA is a critical piece of life support equipment in the air revitalization system of the ISS, and is demonstrated technology that may ultimately prove well-suited for use in lunar or Mars base, and Mars transit life support applications [11].

Another modern zeolite system has been described recently, in which the removal of carbon dioxide from space cabin air is under strict control. The system is integrated into a closed air regeneration cycle aboard spacecraft. The continuous operation of a double-adsorbent regeneration system with CO_2-dependable productivity is maintained through programmable setting of adsorption (desorption) semicycle time. The automatically changing system productivity ensures continuous intake of concentrated CO_2. Control of the adsorption-desorption process is based on calculation of the differential adsorption (desorption) heat from gradient of adsorbent and test inert substance temperatures. The adaptive algorithm of digital control is implemented through the standard spacecraft interface with the board computer system and programmable microprocessor-based controllers [12].

Coating technology

A molecular absorber is also based on absorption property of the highly porous materials which have large specific surface area. Currently, NASA Goddard Space Flight Center has developed a sprayable coatings technology with broad application by using of zeolites, named a Molecular Adsorber Coating (MAC). The coating is comprised of highly porous zeolitic materials that help capture outgassed

molecular contaminants on spaceflight applications. The adsorptive capabilities of the zeolite coating can alleviate molecular contamination concerns on or near sensitive surfaces and instruments within a spacecraft. The preliminary tests of NASA's MAC technology are discussed for use on future missions to Mars. The study involves evaluating the coating's molecular adsorption properties in simulated test conditions, which include the vacuum environment of space and the Martian atmosphere [13].

Electrically based applications

Electrically conducting zeolite-like frameworks are not typical electronic materials, but may offer new avenues in energy applications. Because of their superior catalytic, adsorption, and separation capabilities, zeolites can be used as cell component materials (such as electrodes and membranes). For instance, CeO_2-decorated ZSM-5 zeolitic nanocatalysts could be used to make CeO_2/ZSM-5-modified glassy-carbon electrodes for electrochemical oxidation of methanol.

Silver–zeolite composites are interesting materials with unique optical properties. Zeolites assist Ag in naturally emitting light, which could lead to new lighting technologies—supplementing or replacing fluorescent lights or LEDs. At present, the controlled synthesis of Ag–zeolite composites with responsive optical properties remains a challenge. Recently was reported the synthesis and characterization of novel LTA(Li)–Ag zeolites which display better luminescence performance, compared to LTA(Na)–Ag samples. Yellow (19% water content), green (17–2% water content) and blue (less than 1% water content) emitters were observed in LTA(Li)–Ag zeolite composites with the same composition (low silver loadings) but different hydration levels. This shows the great potential that this new type of luminescent Ag-zeolite might have as blue emitting materials and as luminescence-based humidity sensors at macro and micro scale [14].

Soil improvement

The main problem in space is the limitation of life support resources. The CO_2 removal from breading air in space and recycling of wastewater are two important areas of application for zeolites. Particularly promising application is the use of zeolites loaded with several substances as planting substrates and artificial soil in extra-terrestrial station to grow plants, which convert CO_2 back to O, remove excess environmental humidity and turn wastewater into drinking water.

Bulgaria is the third country in the world, after the USA and Russia, with a space greenhouse. In 1995 during the Zeolite Meeting' 95 in Sofia was presented the report "Zeolite Gardens in Space", devoted to the use of natural zeolites in space applications and occurrence in extra-terrestrial environments. These studies were initiated in the period 1950–1980 by the US Air Force and Russian scientists. In 1984, a Russian-Bulgarian group created the first space greenhouse named

SVET. The first experiment was realized in 1990 after the equipment was installed to the MIR Orbital Station and the first fresh vegetables (radishes and Chinese cabbage) were produced in space. Result of next experiments was the growth of wheat and beans, rich in proteins. The Balkanite substrate, made from the natural zeolite clinoptilolite, extracted in the Kardzhali region, with added mineral salts, was used as the nutrient medium for growing the plants. Zeolites mixed with Mars soil could solve the problems of Mars soil bioremediation and even with formation of the atmosphere [15].

Zeolite synthesis from natural and industrial products

Natural zeolites and synthetic zeolites from natural materials

Among the most common natural zeolites are clinoptilolite, analcime, chabazite, fauhazite, ferrierite, kaolin and mordenite. Their cations are mainly alkaline (Na and K) and alkaline earth (Ca and Mg) metals. Due to their high content of Si and Al, clays are often used and different zeolites (A, X, Y, P, etc.) have been synthesized [6].

Rice husk zeolites

Alkali activation of Bulgarian rice husk or rice husk ash, as sources of SiO_2, and almost pure Al from aluminum cans resulted in zeolites Sodalite, A, X, P and Y. Pure highly crystalline and completely white zeolite NaA was successfully synthesized from untreated rice husk by means of new economical and technologically feasible procedures, avoiding the rice husk burning [16].

Synthetic zeolites from coal fly ash

Coal fly ash is the most abundant coal combustion by-product, partly used in concrete and cement manufacturing. Most of this waste is disposed in open landfills, creating serious problems with air and water pollution. The fly ash contains a significant amount of crystalline and amorphous aluminosilicates which makes him a suitable material for the synthesis of zeolites. More than 15 types of zeolites (e.g. NaA, NaX, NaY, NaP1, Sodalite, K-chabazite, Linde F, etc.) could be synthesized, and the type and yield of the zeolite obtained are strongly influenced by the chemical and mineralogical composition of the fly ash used.

Fly ashes from Bulgarian TPPs (“Maritza East 2 and 3”, “Varna”, “Bobovdol”, “AES Galabovo”, “Republika” and “Rousse East”), burning local and foreign coals, have been hydrothermally activated [7, 17–19]. At higher temperatures and different alkali concentrations the ashes were transformed into different zeolitic materials, containing zeolite Linde F, blend of zeolites A and P, or Hydroxy Sodalite [17]. The obtained synthetic zeolites of type Hydroxy Sodalite were applied as ion-exchangers in systems of nuclear safety for trapping radioactive ^{137}Cs and ^{90}Sr [7]. The highly-porous zeolite Na-X from fly ash of TPP “Maritza East” has been studied as high capacity inexpensive adsorbent of CO_2

with application in gas separation systems [18]. Cobalt-modified zeolites showed high activity in degradation of different VOCs (acetone, n-hexane, toluene and 1,2 dichlorobenzene). It is promising candidate for development of a dual catalytic/adsorption system for VOCs and CO_2 elimination [19].

Slag zeolites

The waste slag from the Bulgarian TPP "Sviloza" was alkali treated at room temperature for more than a year. The zeolited product contains zeolites X and Linde F. It was tested as absorbent of a textile dye from aqueous suspensions. Due to its better developed active specific surface, the dye was almost completely absorbed for much shorter times than the untreated slag [20].

Conclusion

Undoubtedly, the zeolites are a necessary and obligatory element of present and future terrestrial and space engineering. Due to their unique properties, zeolites have a great potential as effective sorbent materials for a large number of water treatment applications, such as water softening (for boilers and drinking), ammonia removal (from municipal sewage, animal farms, additives to feed, fertilizer factory wastewaters, fish breeding ponds, swimming pools), removal of heavy metals (from natural waters, acid mine drainages, industrial wastewater), phosphates removal, removal of dissolved organic compounds and dyes, oil spillages treatment, soil conditioning agents, separation of solid impurities, radioactive wastewater purification, seawater desalination, and many others.

Synthetic zeolites obtained by reprocessing of industrial and municipal wastes have huge potential as a cost-effective, environmental-friendly solution that can improve the efficiency of waste water treatment. Their low price and the additional ecological benefit (reduced mining and solid wastes disposal) increase their popularity and inspire growing interest among researchers and manufacturers worldwide.

Many more challenges remain for the future, which require the development of brand new zeolitic materials that are suitable for a huge variety of practical needs and specifications of aerospace engineering. For many decades, NASA and its international partners have been at the forefront of Mars exploration through a series of missions. Advances in space exploration and space travels need new type zeolites. Aerospace engineering is one of the most important branches of engineering and will help humankind to dominate the skies and all the space above. Aerospace engineering with the help of novel technologies will help us not just to conquer the sky, but to reach the stars, and the zeolites will be an invaluable and indispensable tool in this mission.

References

1. Coronas, J. Present and future synthesis challenges for zeolites, Chemical Engineering Journal, 2010, 156, 236–42. doi:10.1016/j.cej.2009.11.006.
2. Van Bekkum, H., E. M. Flanigen, P. A. Jacobs, and J. C. Jansen. Introduction to zeolite science and practice. Amsterdam, Elsevier, 2001, p. 1061. ISBN: 0-444-82421-9.
3. Mardirossian, G. Fundamentals of remote aerospace technology, Chapter 3 and 4 (Book in Bulgarian). NBU, Sofia, 2015. ISBN: 978-954-535-882-1.
4. Haggerty, J. J. Spinoff'93, Chapter: Commercial use of space. Washington, NASA, 1993, p. 144. ISBN: 0-16-042100-04.
   URL: https://spinoff.nasa.gov/back_issues_archives/1993.pdf
5. Sadeghbeigi, R. Fluid Catalytic Cracking Handbook, Butterworth-Heinemann, 2020, p. 386. ISBN: 9780128126639.
6. Shoumkova, A. Zeolites for water and wastewater treatment: An overview. Special Issue of the Research Bulletin of the Australian Institute of High Energetic Materials on the Global Fresh Water Shortage, 2011, ISBN: 978-0-9806811-1-6.
7. Zgureva, D., and S. Boycheva, Synthetic zeolitic ion-exchangers from coal ash for decontamination of nuclear wastewaters, BgNS Transactions-, 2015, 20, 2, 132–36. http://bgns-transactions.org/Journals/20-2/vol.20-2_11.pdf.
8. Vogt, E. T. C., G. T. Whiting, A. D. Chowdhury, and B. M. Weckhuysen. Zeolites and zeotypes for oil and gas conversion. In Advances in Catalysis, Chapter 2, 2015, 58, 143–314. ISBN 978-0-12-802126-2, ISSN 0360-0564.
9. Huang, B., U. Shrestha, R.t J. Davis, and H. K. Chelliah, Endothermic pyrolysis of JP-10 with and without zeolite catalyst for hypersonic applications. AIAA Journal, 2018, 56, 4, 1616–26. DOI: 10.2514/1.J056432.
10. Mulloth, L. M., and J. E. Finn. Carbon dioxide adsorption on a 5A zeolite designed for CO2 removal in spacecraft cabins, NASA, California. 94035-1000, 1998. https://ntrs.nasa.gov/search.jsp?R=19980237902.
11. Jiao, Z., L. Jiang, J. Sun, et al. Outgassing environment of spacecraft: an overview, IOP Conf. Series: Materials Science and Engineering, 2019, 611, 012071, doi:10.1088/1757-899X/611/1/012071.
12. Chekov, Iu. F. Life support of the Mars exploration crew. Control of a zeolite system for carbon dioxide removal from space cabin air within a closed air regeneration cycle. (Article in Russian). Aviakosmicheskaia i ekologicheskaia meditsina (Aerospace and environmental medicine), 2009, 43, 2, 37–45.
13. Abraham, N. S., and D. E. Jallice. Preliminary testing of NASA's molecular adsorber coating technology for future missions to Mars. In: Proceedings of the SPIE. Soares, C. E., E. M. Wooldridge, and B. A. Matheson (Eds.). San Diego, SPIE. 2018, 10748, 41–46. doi:10.1117/12.2320400.
14. Coutino-Gonzalez, E., W. Baekelant, D. Grandjean, and J. Hofkens. Thermally activated silver-zeolite composites with responsive photoluminescence properties. Journal of Materials Chemistry C, 2015, 3, 11857–67. doi: 10.1039/C5TC02723C.
15. Ivanova, T., I. Stoyanov, G. Stoilov, P. Kostov, and S. Sapunova. Zeolite gardens in space. In: Natural zeolites. Sofia'95. Proceedings of the Sofia zeolite meeting'95. Kirov, L. Filizova, and O. Petrov (Eds.), Sofia, 1997, 3–10. PENSOFT, ISBN 954-6-42-0158, 978-9-54-6420152.

16. Shoumkova, A. and V. Stoyanova, SEM-EDX and XRD characterization of zeolite NaA, synthesized from rice husk and aluminium scrap by different procedures for preparation of the initial hydrogel. Journal of Porous Materials, 2013, 20, 249–55. doi:10.1007/s10934-012-9594-x.
17. Shoumkova, A. and V. Stoyanova, Zeolites formation by hydrothermal alkali activation of coal fly ash from thermal power station "Maritsa 3", Bulgaria, Fuel 2013, 103, 533–41. doi:10.1016/j.fuel.2012.07.076.
18. Kalvachev, Yu., D. Zgureva, S. Boycheva, B. Barbov, and N. Petrova. Synthesis of carbon dioxide adsorbents by zeolitization of fly ash. Journal of Thermal Analysis and Calorimetry, 2015, 124, 1, 101–06. doi:10.1007/s10973-015-5148-1.
19. Popova, M., S. Boycheva, H. Lazarova et al. VOC oxidation and CO2 adsorption on dual adsorption/catalytic system based on fly ash zeolites. Catalysis Today, 2019, doi:10.1016/j.cattod.2019.06.070. (in press)
20. Pascova, R., V. B. Stoyanova, and A. S. Shoumkova, Room temperature zeolitization of boiler slag from a Bulgarian thermal power-plant. Journal of the Serbian Chemical Society, 2017, 82, 2, 227–40, doi:10.2298/JSC160807091P.

ПРИЛОЖЕНИЕ НА ЗЕОЛИТИТЕ В НАЗЕМНАТА И КОСМИЧЕСКА ИНДУСТРИЯ – ОБЗОР

А. Митева, В. Стоянова

Резюме

Този кратък преглед е опит за систематизиране на някои от наличните исторически и по-нови данни данни за влиянието на зеолитната наука и техника върху прогреса на различни области от развитието на Земята и Космоса. Представени са основните структурни и химични свойства на природните и синтетичните зеолити. Включени са също така ценни приложения на зеолитите като катализатори, газови адсорбатори и йонообменници. Представени са най-често използваните методи за синтез на зеолити от различни материали, както и някои български разработки за рециклиране на отпадъци до зеолити. Важната роля на зеолитите като незаменим материал за подобряване качеството на почви, горива, води, въздух и т.н., необходими за нуждите на орбиталните космически станции и космическите кораби, е потвърдена с типични примери.

Bulgarian Academy of Sciences. Space Research and Technology Institute.
Aerospace Research in Bulgaria. 32, 2020, Sofia

DOI: https://doi.org/10.3897/arb.v32.e18

A REVIEW OF EARTH OBSERVATION RESOURCES FOR SECONDARY SCHOOL EDUCATION – PART 1

Lachezar Filchev[1], Ioannis Manakos[2], Rainer Reuter[3], Garo Mardirossian[1], Tsveta Srebrova[1], Lubomira Kraleva[1], Dimitar Dimitrov[4], Kalliroi Marini[2], Andreas Rienow[5]

[1]Space Research and Technology Institute – Bulgarian Academy of Sciences, Department of Remote Sensing and GIS, Sofia, Bulgaria;
e-mail: lachezarhf@space.bas.bg, G.Mardirossian@space.bas.bg, lkraleva@eeobss.space, Tsveta_Srebrova@space.bas.bg
[2]Information Technologies Institute of the Centre for Research and Technology Hellas (CERTH-ITI), Thessaloniki, Greece; e-mail: imanakos@iti.gr, marini@iti.gr
[3]Carl von Ossietzky Universität Oldenburg, Germany, Germany;
e-mail: rainer.reuter@uni-oldenburg.de
[4]National Institute in Geophysics, Geodesy and Geography at the Bulgarian Academy of Sciences (NIGGG-BAS), Sofia, Bulgaria; e-mail: clgdimi@abv.bg
[5]Ruhr-University, Bochum, Germany; e-mail: andreas.rienow@ruhr-uni-bochum.de

Keywords: *Secondary School, Science Education, Earth Observation Education, STEM, EO, MOODLE.*

Abstract

This article provides an overview of worldwide web and e-Learning resources for Earth Observation (EO) education for secondary schools. The main EO education initiatives supported by international, EU and national organizations. The article elaborates on future prospects of EO education in the education system its relevance for the society and its connection with STEM subjects.

Introduction

As space and remote sensing (RS) technologies develop and free spaceborne data abundance and availability becomes a fact, methods and approaches for information generation take advantage of the enhanced data quality offered and remote sensing applications gain value tackling societal needs and supporting economy. Spaceborne RS owes its origins to space exploration and military applications. It was used initially to serve strategic purposes for planetary research and wide covering earth exploration. The ending of the Cold War and the development of telecommunications shifted the emphasis from maintaining a strategic advantage to economic growth and environmental awareness.

In the 21st century the geospatial revolution generated a plethora of geospatial data. The need of standardization and homogenization has emerged to cope with credibility and user confidence issues. Addressing these on an international level was issued a draft K-12 strategy for earth observation (EO) education by CEOS [1]. On an EU level with the INSPIRE Directive, the European Commission set forth the goals of integration of geospatial data in the eGovernment. The initial operations of Copernicus services (formerly the GMES programme) have pushed developments forward both for data users and the governments to utilise and exploit the unprecedented availability of satellite data and products on an operational basis. The Copernicus programme is expected to boost up European economy, which is still recovering from the World economic crisis and now entering a new unprecedented COVID-19 crisis. It will create a new entrepreneurship opportunities in the space sector. Parallel to these scientific and technological developments the society shall be able to keep pace in understanding and adopting the latest products and make benefit from its investment in Earth Observation (EO). In this context, data and products must be provided in a comprehensible, easy to follow and accessible way. Users having the skills, knowledge and understanding may then use and incorporate them in existing production working chains or find new added value use cases. Users not having these skills shall at the same time understand what this information thesaurus brings along to embrace emerging changes, approve the work of the specialists and give their consent to support the EO investment in the future; thus, setting the foundation for a sustainable chain of services and products. In order to come up to this result fundamentals and understanding of EO must be integrated in an efficient manner within multiple disciplines or even stand-alone ones when necessary, in the already overloaded school training programmes. In this context citizens will be up-to-date with new data sources, remaining receptive to adopt spaceborne products and services, and understand the processing techniques and communication mechanisms that are relevant to their individual needs.

The wide variety of EO satellites, data sets (satellite and airborne), and application areas relevant to STEM subjects, has been reflected in the course of the years in the diversity of existing training initiatives and resources regarding secondary school education in EO. On a national level, the most structured approach towards mapping sciences and EO data use has the USA, which has carried out several studies on different aspects of this type of education. In 1981, the first comprehensive overview of the remote sensing education in USA was published in IJRS [2]. From this study it becomes clear that mapping sciences have been catalogued into a *Mapping Sciences Education Data Base*, which was to become operational and published on an annual basis as *'Directory of Courses and Programs in the Mapping Sciences'.* The authors of this work also emphasized on the standardization of RS education, which is at present also a hot topic in Europe. Although not yet implemented in the secondary-schools, it is a first attempt

towards a systematic view on geospatial sciences and education. On a European level, the first attempt to review RS education as a whole was performed in the 80s of the 20th century [3]. It is acknowledged hat France has played a pioneering role in promoting remote sensing at the level of secondary schools. In France, the introduction of remote sensing to modernise teaching in primary and secondary schools has become official government policy. In the mid of 1980s, an Institute, the *Groupement pour le Developpement de la Teledetection Aerospatiale*, regularly organized courses for school teachers [4]. In June 1986, EARSeL in co-operation with the Council of Europe, ESA and the Commission of the European Communities (CEC), organized an European Workshop to assess the current situation of remote sensing education and training in Europe and recommended further action (Council of Europe, 1989) [5]. But, the first more comprehensive outlook on RS education on an international level came only in the beginning of 1990s with the ISPRS Commission VI Symposium *Modern Trends of Education and Remote Sensing* held between 13 and 16 September 1990 on Rhodes Island, Greece. One of the Commission VI goals is targeted to the school education: '(3) compilation of ideal syllabi and course layouts for undergraduate education on remote sensing and GIS' [6]. However, at that stage there were still no discussions or papers dealing with the RS education in schools. At a dedicated workshop in 1992, RS was put for the first time on the round table discussions as part of the National Curriculum for Science of UK [7]. In this article, the teachers' perspective from career development point of view was studied for the first time [8]. At the Frascati's EO Education Workshop (2014) [9] a number of barriers to effective EO education at different levels were identified. Among these were: (i) the difficulties in identifying and accessing data suitable for education at different levels, (ii) the relative lack of clear and intuitive example data and case studies suitable for learning about different applications or relevant to specific geographical regions, and (iii) the fragmentation of European education resources which leaves newcomers to the arena of EO education overwhelmed by the task of finding resources that suit their own needs. During the LeanrnEO! Workshop in Frascati was recognising the importance of embracing EO education; the European Space Agency (ESA) has taken the initiative to develop a Roadmap for EO Education. It keeps up with the structure established by the LearnEO! *Roadmap for EO education in Europe* (2015) [10].

The aim of the present review is to provide an overview of the available international, regional and national education resources in EO for secondary schools, to identify subjects which are not yet well represented in the curricula but would benefit from using remote sensing in the classroom, and to address several didactic aspects which could help establishing Earth Observation in school. In first part of this work the authors have selected and presented in an alphabetical order the institutions providing the resources – web-resources and e-learning, EU funded

projects. In the follow-up of this work we will present the national and international projects, outreach activities, and FOSS software tools for education.

Data and methods

Besides other resources the review integrates material presented at the Frascati EO Education Workshop 2014 [11] with other information obtained in the ESA LearnEO! Project, and ESA EO Open Science 2016. It is also based on experience obtained in the project *Science Education through Earth Observation for High Schools* (SEOS)[1] supported in the 6th FP-EU, FIS, and from the ongoing EO4GEO project (ERASMUS+). The authors from the EEOBSS project team also made use of their own experience when introducing Earth Observation into the curriculum of Bulgarian high schools in 2016–2019.

Earth observation resources for secondary school education

The main review items are presented in an alphabetical order of the material producer/provider in order to not give priority of a specific resource, rather to list it as is. Thus, it is expected that this will allow the reader to have a more objective view on the state-of-the-art. In this article, the EO education is organized in the following categories: 1) web-resources and e-learning, 2) initiatives supported by national funding bodies and international organizations, 3) outreach activities, 4) citizen science, and 5) software and tools. The last three cathegories will be covered in the second part of the review.

Web-Resources and E-Learning

Carleton University

The University of Carleton has developed the Earth Exploration Toolbook (EET, URL: http://serc.carleton.edu/eet/index.html). It is developed by teams of scientists and educators; the EET is a collection of online Earth system science activities. Each activity or chapter introduces one or more scientific data sets and analyses tools that enable users to explore some aspect of the Earth system. The chapters are written for the teacher, generally at the secondary and college level. However, the chapters can be used by other educators, students, citizens, and policy makers to guide their own learning, adapt to their own purposes, and enable them to answer their own Earth system science questions based on scientific data.

[1]http://www.seos-project.eu

ESA

A dedicated website for *EO Education and Training activities* is published on ESA's EO portal [12]. This provides a comprehensive overview and easy access to all ESA programmes in EO education, training and capacity building. A section on primary and secondary level EO education includes descriptions and links to online tools, teacher training courses and material that can be ordered from the ESA education office. Another section includes summaries of EO training courses at University level with links to their respective webpages with access to presentations and ESA / Third Party Mission (TPM) data used for exercises. Similar material is available for advanced training at post-graduate level.

The *ESA Eduspace* multi-lingual website [13] is dedicated to secondary education. The aim of Eduspace is to provide attractive image data, information and tools suitable for teaching and learning a variety of topics in Geography, Physics, Environmental Science and related subjects, according to the curriculum of each country. The main value of Eduspace lies in the practical nature of its e-learning content. The website not only explains the theory and applications of EO in terms suitable for a secondary school audience, but also provides case studies that demonstrate practical examples of how EO data is used. Each case study presents the student with a real world problem, which one needs to address through hands-on processing of EO data using software designed for use in schools.

The *Eduspace Image Catalogue* [14] provides Eduspace users with a multi-mission catalogue of EO data over Europe. This offers teachers and students carefully selected example data for use in Eduspace case studies and allows them to adapt (personalise) the case studies with EO data from their specific region of interest. The *Interactive Meteosat on-line application* – a new online tool that shows satellite data combined with student measurements has been developed as an Eduspace module along with a case study on the interpretation of Meteosat images.

LearnEO! is an ESA project with partners such as the National Oceanography Centre (NOC), CLS, GEO-K, and UNESCO (Bilko) [15]. The project offers a holistic framework for EO education with lessons on different EO applications (200 data sets with description). The project is using the UNESCO Bilko software as a main application for the trainings. It also has a resource library with extra information and tools (hands-on materials, quizzes) and offers a support for lesson writers and lesson users.

In the field of e-learning, ESA has also developed *"Earth from Space: The living beauty"* [16] – the first electronic book showcasing EO applications, developed for Apple's iPad and available through iTunes. The 105 page book takes the reader on a scientific voyage that shows how some of the latest technology has changed the way we view the Earth. There are five chapters: Solid Earth, Oceans, Cryosphere, Atmosphere and Land, showing the most impressive results of ESA's EO missions. Electronic books on individual missions are also being developed.

In 2010, ESA jointly with Geospace GmbH issued a "*School Atlas: Geography from Space*" edited by Beckel, L. The Atlas presents a new way and outlook towards European EO education. It bridges the gap between the EO science and secondary school education through a tailored product built mainly on EO data. With this new approach the Atlas achieves one major goal – to prove that EO data and products can be used for virtually all class activities in Geography. The Atlas is available in German and English both in digital form and in print [17].

ESA Massive Online Open Courses (MOOC) has been specifically designed to overcome perceived 'barriers' to the use of EO by non-technical users. The *Monitoring Climate Change from Space* [18] MOOC, started in June 2015, provides basic information about the use of EO data to monitor and study climate variability and change. The course explores and addresses some of the problems related to the take-up and usage of EO data and demonstrates the benefits of using EO data in scenario planning. It encourages wider use of EO data by providing practical, real-world examples of how EO data are used to monitor and adapt to climate change, increase resilience to climate-related hazards, and provide decision support for sustainable development and resource management planning. In September 2016, ESA has started a new MOOC with topic *Earth Observation from Space: the Optical View* [19]. This free online course provides an introduction to optical Earth observation - monitoring our planet from satellites, using photography, imaging in various wavelengths, LIDAR and other optical sensing technologies. The SAR-edu [20] team is developed its own MOOC which was released in 2017, and provides the 'Radar View' on EO from space. The web-platform for MOOCs FutureLearn is the home of these MOOCs. However, the necessity to develop and host in one place as well as new and updated policy of ESA has led to the development of EO College where the first MOOC Echoes in Space: Introduction to Radar Remote Sensing is hosted [21].

Every summer, ESA's Education Office welcomes about 40 secondary school teachers from across Europe to ESA's European Space Research and Technology Centre (ESTEC) in the Netherlands for the *ESA Summer Workshop* [22]. In the course of over four days teachers participate in a variety of workshops that show how space can be used as a context for teaching different school subjects.

The *ESA Teacher's Pack "Watching Over the Earth"* includes a selection of Remote Sensing/EO topics and is targeted to lower secondary level students (age 11–14). The pack is available in several languages (English, French, German, Spanish, Italian and Dutch) in hard copy, and may also be downloaded from a dedicated ESA website [23].

Copernicus (European Commission)

The EC and Copernicus programme published its first Copernicus MOOC in the beginning of 2020 as an effort to make the Copernicus data and its services accessible to everyone [24]. The MOOC consists of three chapters: "Chapter 1: Understanding Copernicus data and services", "Chapter 2: Learning from success stories", and "Chapter 3: Do It Yourself!".

NASA

NASA has its own education programme and website – *NASA for Educators* [25]**,** which offers free resources in STEM subjects from K-4 until 9–12 (secondary school education) and higher and informal education. Some of the education resources are well suited both for the STEM subjects taught in class and for EO data applications. One of the most exciting initiatives of NASA is KidSAT/EarthKAM student remote sensing programme [26]. Within this programme the students developed a camera system for the Space Shuttle, while at a later stage the EarthKAM continued onboard the International Space Station (ISS). The students have been developing a series of image acquisition requests based on approved science proposals that have been combined into a set of instrument commands that are uplinked to the ISS. In this context, a brand new programme is Expedition Earth and Beyond (EEAB). This programme is designed to motivate the students to gain interest in Science, Math, Engineering, and Technology (STEM) related subjects [27].

The goal of the NASA *Applied Remote SEnsing Training (ARSET)* [28] is to increase the utility of NASA earth science and model data for policy makers, regulatory agencies, and other applied science professionals in the areas of Health and Air Quality, Wildfires, Water Resources, Eco Forecasting, and Disaster Management. As such, the training is highly specialized but some parts of it could be used also for education purposes in secondary schools. For instance, the topics are matching some of the Geography lessons in class and could serve as a supplementary material for extracurricular activities. The two primary activities of this project are webinars and in-person courses. There is also a recently added section for workshops. The user could also suggest a course, if it is not present on ARSET but is a topic of common interest.

European Spatial Data Research (EuroSDR)

European Spatial Data Research (EuroSDR) holds distance e-learning courses on EO and geo-information topics [29]. These courses can be followed over the Internet, allowing participants to update their knowledge with minimum disruption. Each course requires about thirty hours of online study and is completed in two weeks. However, these courses are not suited to secondary school students, but they could be used for capacity building of geography teachers.

University of Heidelberg

The Research Group for Earth Observation at the Heidelberg University of Education has developed two learning modules for secondary school education in web-based learning environment [30]. First, BLIF ("Blickpunkt Fernerkundung") or *Satellite Image Learning Center (SILC)* [31] which provides online software to analyse remote sensing data independently and to answer first problem oriented geographical questions. Ten game-based learning modules allow students to test their existing knowledge of satellite images and pick up new information. The games are organised into easy and difficult ones. Second, "geo:spektiv" (www.geospektiv.de) which provides specific online learning modules (based on BLIF) to work on spatially and environmentally relevant questions. Both platforms have been developed to get secondary school pupils in touch with remote sensing data and to use satellite imagery in applied geographic tasks.

Initiatives supported by national funding bodies and international organizations

Challenger Center

The Challenger Center is an international organization dedicated to bring all students dynamic educational experiences and help inspiring future generations of STEM-conscious leaders. The Center organizes various training activities through online lessons and resources which partially cover the EO topics [32]. The lessons are interactive and engaging which help build motivation.

CReSIS Middle School Program

The Center of Excellence in Remote Sensing Education and Research (CERSER) continuously strives to provide education and research opportunities on ice sheet, coastal, ocean, and marine science. One of those continued an outreach effort is the *Center for Remote Sensing of Ice Sheets (CReSIS) Middle School Program*. Sponsored by the National Science Foundation (NSF) CReSIS Middle School Program offers hands on experience for middle school students. CERSER and NSF offer students the opportunity to study and learn about remote sensing and its vital role in today's society as it relates to climate change and real world problems. The CReSIS Middle School Program is an annual two-week effort that offers middle school students experience with remote sensing and its applications. Specifically, participants received training with GPS where the students learned the tools, mechanisms, and applications of a Garmin 60 GPS. As a part of the program the students were required to complete a fieldwork assignment, where several longitude and latitude points were given throughout campus [33].

EARSeL

The European Association of Remote Sensing Laboratories (EARSeL) organises a *Special Interest Group on Education and Training* [34] which holds Workshops and sessions at its annual Symposia for educational experts and secondary school teachers. These typically last 1–2 days, often associated with conferences or exhibitions of interest, and are supported by ESA.

EUROGEO

The principal goals of the European Association of Geographers (EUROGEO) are to advance the status of geography by: organizing events and activities for members, producing publications for members, supporting geographers in their jobs and careers, identifying and promoting good practice, lobbying at European and national level, giving advice on geography, making recommendations to decision makers. During the past few years, two projects implemented by EUROGEO have targeted the geography and GeoICT to transfer innovation to meet changing labour market needs and improve the quality of geo-education. These projects are intended mainly for university and vocational training level: *GeoSkills Plus* [35] and *YouthMetre* [36]. The latter one provides useful statistics for the education of the youngsters on a country level within EU27.

European Geosciences Union (EGU)

The European Geosciences Union (EGU) Committee on Education has organised *Geosciences Information for Teachers (GIFT) Workshops* since 2003. These 2.5-day teacher-training workshops are held in conjunction with EGU's annual General Assembly and typically host about 80 teachers. Their main objective is to spread first-hand scientific information to science teachers in primary and secondary schools, thereby shortening significantly the time between discovery and text-book. Teachers are provided with material that can be used directly in the classroom and many of the lectures from the GIFT workshops are freely available as videos on YouTube™ or EGU TV [37].

Global Learning and Observations to Benefit the Environment (GLOBE)

The *GLOBE programme* (http://www.globe.gov) is one of the few international programmes (the programme is sponsored by NASA, NSF and supported by NOAA and U.S. Department of State) offering free education resources, tools and training to students and teachers in STEM subjects. The network consists of GLOBE students, teachers and scientists. The activities are various starting from the annual GLOBE conference, virtual workshops, and various dedicated data-collection campaigns. The programme has its own highly-structured approach towards data collection following specific protocols since 1995

[38]. The field data collected by various schools is accessible through a visualization tool [39]. Although the data collected by schools is field data, many students and their teachers choose to work with NASA satellite data and products for their projects showing a synergistic approach towards field and satellite measurements [40–42]. One of the field campaigns co-developed with NASA scientists in 2016 was for field data collection to validate the SMAP mission [43].

Joint Information Systems Committee (JISC)

The Joint Information Systems Committee (JISC) funded *Landmap* service which ran from 2001 to July 2014 and collected, modified and hosted a large amount of EO data for the majority of the UK, including imagery from ERS, ENVISAT, ALOS, high-resolution Digital Elevation Models (DEMs) and Digital Terrain Models (DTMs) and aerial photography dating back to 1930. After removal of JISC funding in 2013, the *Landmap* service is no longer operational, with the data now held at the NEODC [44].

"Remote Sensing Environmental Applications" - a Greek test course

The structure of the educational material of the "Remote Sensing Environmental Applications" test course developed for Greek schools is presented through a MOODLE platform. The educational e-material is designed for an e-learning course in the field of remote sensing and environmental applications. The e-material is written in Greek language and it is addressed to students in the first year of Lyceums. The e-material is used in the terms of the "Project" course [45].

UNESCO

UNESCO and its network of *Space for Heritage* partners use results of various space projects to develop educational packages and to organize exhibitions for the general public. These bring space science and technology closer to society [46]. The UNESCO's *Bilko* project [47] provides software, example data and tutorials for teaching marine and coastal applications of remote sensing.

University of New Hampshire

The University of New Hampshire has developed its *GLOBE Carbon Cycle* project (supported by NASA and NSF) [48]. The project is focused on bringing into the classroom the cutting edge research and research techniques in the field of terrestrial ecosystem carbon cycling. Students can collect data about their school field site through existing GLOBE protocols of phenology, land cover and soils as well as with protocols focused on biomass and carbon stocks in vegetation.

EU funded projects

Digital-earth Center of Excellence for the Geographical Education

The Greek digital-earth Center of Excellence for the Geographical Education was found in 08 June 2012 after the approval of the evaluation committee of the digital-earth.eu Centre of Excellence of the European Program Digital-earth (Comenius Network project). The Center has registered offices in the Faculty of Primary Education in the Aristotle University of Thessaloniki. An annex of the Center is operating in the Department of Geography of the University of Aegean in the island of Lesvos. The staff is composed by primary and secondary school teachers, PhD Students, postgraduate students, and students of the Faculty of Primary Education of the Aristotle University of Thessaloniki or the Department of Geography of the University of Aegean or other Greek Universities. The Center is expected to become an area of communication with teachers who work in schools abroad and it will support them in their work. There have already been initial agreements for future cooperation between the Centre for Research and Technology Hellas/Information Technologies Institute (ITI-CERTH) and EARSeL Education Department [49].

Science Education through Earth Observation for High Schools (SEOS)

The Science Education through Earth Observation for High Schools (SEOS) web-site [50–51] provides teaching modules that use remote sensing to support the science education curricula in high schools throughout Europe and beyond, with emphasis on Geography, Biology, Physics, Mathematics and Environmental Sciences [52]. Coordinated by the University of Oldenburg, Germany, 16 internet-based eLearning tutorials were developed on selected topics and tested in co-operation with European partner schools. These are available from the project web-site in different languages.

SAR-EDU

SAR-EDU [53] is a joint education initiative for Radar Remote Sensing, conducted and coordinated by the Friedrich-Schiller University Jena and the German Aerospace Centre (DLR) [54]. The project goal is to provide knowledge about the basics, methods and applications of Radar Remote Sensing to users and scientists.

FIS – Remote Sensing in School Lessons

Working with remote sensing data is postulated in the school curricula of several states in Germany. Moreover, the application of aerial, satellite, or even ISS imagery can be seen in the light of problem-based learning (pbl) fostering

competences and practice skills. These were and still are the main goals of the scientific projects "Remote Sensing in School Lessons" (FIS-I: 50EE0615, 2006–2009; FIS-II: 50EE0932, 2009–2015; FIS-III: 50EE1703, 2017–2019) funded by the German Aerospace Centre (DLR) and the Federal Ministry for Economic Affairs and Energy (BMWi). The project is carried out at the Universities of Bonn and Bochum. FIS established a close collaboration with several schools in Germany and has widened the reach through advanced teacher trainings all over Germany. Based on the elaborated and evaluated FIS-concept, a comprehensive, well-structured learning portal on remote sensing has been published comprising more than 30 digital learning units for 5 STEM subjects dealing with satellite data of ESA, DLR, and NASA missions (English: www.fis.uni-bonn.de/en). For FIS-I, a concept to demonstrate the value of remote sensing as a key technology within the scope of their standard education was developed. Since remote sensing is more than the simple visual interpretation of satellite imagery, this concept includes computer-based remote sensing methods [55]. The main task of FIS-II was to develop a comprehensive, well-structured learning portal to teach about remote sensing based on this concept. The learning portal was successfully implemented and can be accessed at www.fis.uni-bonn.de since 2012. It grants pupils and teachers alike a structured introduction into the topic by providing them with digital and interactive learning modules about all the important aspects of remote sensing [56]. Currently, Sentinel data and data of Copernicus contributing missions are integrated in existing modules. FIS-III also aims at the development of Massive Open Online Courses (MOOCs) in order to combine topics dealing with the sustainability of the coupled human-environmental systems. Additionally, augmented reality applications are tested for mobile learning as a possibility to overcome the technical limitations in German schools by mobile learning and the pupils' smartphones [57].

Columbus Eye and KEPLER ISS

In the project Columbus Eye – Live Imagery from the ISS in Schools (funded by DLR and BMWi, 50JR1307, 2013–2017), which was started in 2013 in Bonn and is now carried out in Bochum, the combination of research in microgravity and earth observation is integrated into education – which is unique in Germany. The project's initializer was the Blue Dot mission by astronaut Alexander Gerst and the NASA "High Definition Earth Viewing" (HDEV) experiment that begun around the same time. The astronaut and geophysicist's perspective became accessible to the pupils through Columbus Eye. HDEV consists of four commercial off-the-shelf (COTS) cameras mounted onto the Columbus External Payload Adapter (CEPA) of the ESA Columbus Laboratory. The main purposes of the HDEV experiment are to test the robotic installation of external payloads and to examine the suitability of COTS HD cameras for

upcoming space missions to the Moon and Mars [58]. Columbus Eye acts as the exclusive European partner of the HDEV experiment. The project is in charge of filing and publishing the HDEV data in a web portal and, thus, making the data accessible to the public [59]. A concept for the pupils to perform complex image processing in an intuitive way was developed and implemented. Pupils and teachers have access to interactive learning modules about earth observation data from the ISS and its uses at http://columbuseye.uni-bonn.de/english [60]. Materials for M-learning and the realization of augmented reality applications are currently being developed in KEPLER ISS (50JR1701, 2017-2019). The project succeeds Columbus Eye and exploits not only HDEV videos but also other remote sensing instruments onboard the ISS. In 2018, KEPLER ISS will accompany the ESA space travel mission "horizons" where Alexander Gerst fly for a second time to the ISS in order to manage the astronaut staff as first German commander. Here, KEPLER ISS will carry out a national school competition called "self-eSTEAM". It bridges the gap between space-related science, humanities, and the application of digital media. Finally, the project will use Moon and Mars digital elevation models implemented in virtual reality applications for pupils [61]. Learning materials of the mentioned projects aim at autonomous identification, handling and solving of problems by the pupils. The pupils' active participation in the lessons causes a shift from being taught to learning themselves: The teacher's role changes from presenter of knowledge to guide for autonomous learning, turning their main tasks toward giving directions and providing help for the learning process. Accompanying the Blue Dot mission, the DLR Space Administration held the "Beschützer der Erde" ("Earth Guardian") national school competition. Former and current members of the FIS and Columbus Eye projects produced scripts for Alexander Gerst to perform in videos as well as teaching materials used in the contest. So far, more than 5,000 pupils and 500 teachers were approached directly through 36 school events and 41 "teaching-the-teacher" workshops dealing with interactive STEM education based on satellite imagery and ISS footage. This included teachers at both elementary and the high school level. Downloads of the projects' over 53 classroom resources (digital teaching units, learning tools, experiments, augmented reality apps) in German and English language reach a number of ~1,500 per month.

Discussions and conclusions

Some of the most pronounced key issues yet to become perspectives are addressed here in short:

Lack of access to data and information suitable for non-experts

The problem is very much pronounced for non-scientific audiences with interest in EO education who do not usually have access to archives designed for

professional audiences. The lack of the necessary technical skills and the motivation to invest a large amount of effort required to identify and select relevant examples adds up to the barriers for employing EO education in schools on European level as in Bulgarian secondary schools. ESA and others have a number of initiatives to remedy this, with libraries that provide inspiring and often spectacular examples of EO images. As suggested in the EO Roadmap, to give students the opportunity to develop an intuitive understanding of EO, it is essential to give students and teachers easy access to relevant EO data instantly but on their own terms, both in school-based education and informal learning.

This is already done through ESA Academia (mostly European states), and GLOBE programmes (USA STEM programme with an international impact); although much effort is needed for a global impact. Teachers themselves do not have the time to be self-taught as it was noted in the EO Roadmap, requiring tailored teacher guidelines for EO education, which is the approach of EEOBSS.

Lack of relevant examples and case studies

This issue is to be addressed by revising the worksheets from different projects so as to make national case studies which will support the national STEM education strongly. If such examples are not present, they should be built from scratch based on best use-cases from the science or business practice which shall be adapted.

Fragmentation of EO education resources and initiatives

For a newcomer to EO, an impressive and wide array of information, websites and education related tools is available, which creates an information barrier where to start from and what is most important. The present article aims at addressing this issue by mapping the available resources to make an informed decision. More sustained efforts are provided, for example by the ESA portal for education and training [62] which provides access to resources for schools in EduSpace, as well as information about training courses and other resources provided by ESA for professional users.

Acknowledgements

The work is part of a Project task within EEOBSS (ESA-PECS for Bulgaria), Contract No. 4000117592. The views expressed herein do not in any way reflect the official position of the European Space Agency.

References

1. Hausamann, D. Practical EO Education for Students and Teachers, CEOS WG-D, draft strategy for K-12 education, 2014.

2. Jensen, J. R., and R. E. Dahlberg, Status and content of remote sensing education in the United States. International Journal of Remote Sensing, 1983, 4(2), 235–45. doi:10.1080/01431168308948543
3. Bullard, R. ~K. (). European remote sensing: future needs in education. In N. Longdon & O. Melita (Eds.), European Remote Sensing Opportunities: Systems, Sensors and Applications, 1985, 233, 151.
4. Voûte, C. Europe's role in remote sensing education and training, Journees internationales sur la Formation des Utilisateurs de Teledetection (Toulouse: Groupement pour le Developpement de la Teledetection Aerospatiale (GDTA). 1985, 169–84.
5. Voûte, C. The status of remote sensing education and training in 1990. Int. J. of Remote Sensing, 1992, 13(6–7), 1365–74. doi:10.1080/01431169208904197
6. Commission VI: Economic, Professional and educational aspects of photogrammetry and remote sensing. ISPRS Journal of Photogrammetry and Remote Sensing, 1993, 48(2), 43–45. doi:10.1016/0924-2716(93)90047-Q
7. Gilbert, J. K. Risk-taking and teachers' professional development: The case of satellite remote sensing in science education. Research in Science Education, 1992, 22(1), 157–62. doi:10.1007/BF02356891
8. Session 5. Cost/benefit aspects of remote sensing education. Short contributions. Int. J. of Rem. Sens., 1994, 15(15), 3101–09. doi:10.1080/01431169408954310
9. ESA: ESA Earth Observation Education and Training, Activities & Achievements 2010–2013, 2014.
10. LearnEO! D170 – Roadmap for EO Education. V.1.2. May 2015. URL: http://www.learn-eo.org/roadmap.pdf
11. EO Education and Training. https://earth.esa.int/web/guest/eo-education-and-training
12. ESA Eduspace. URL: http://www.esa.int/SPECIALS/Eduspace_EN
13. EARTH ONLINE. Earth Observation information discovery platform. URL: https://earth.esa.int/eogateway/
14. Earth Observation information discovery platformл https://earth.esa.int/eogateway/
15. LearnEO. URL: http://www.learn-eo.org/
16. ESA's first iBook. URL: www.esa.int/Highlights/ESA_s_first_iBook
17. ESA School Atlas. http://www.esa.int/Education/ESA_School_Atlas
18. Climate from Space MOOC. https://www.futurelearn.com/courses/climate-from-space
19. Optical Earth Observation. https://www.futurelearn.com/courses/optical-earth-observation
20. SAR-EDU. URL: https://saredu.dlr.de/
21. Echoes in Space. Introduction. URL: https://eo-college.org/courses/echoes-in-space/
22. Annual ESA Summer Teacher Workshop. URL: www.esa.int/Education/ Teachers_Corner/Annual_ESA_Summer_Teacher_Workshop
23. ESA Teacher's Pack. URL: www.esa.int/Education/Teacher_s_pack
24. Copernicus MOOC. URL: https://mooc.copernicus.eu/
25. STEM on station. URL: http://www.nasa.gov/audience/foreducators/stem_on_station/ index.html
26. Mah, G. R. Follow-Ons to the KidSAT/EarthKAM student remote sensing program. In M. ~S. El-Genk (Ed.), AIP Conference Proceedings, 2000, 504, 534–39. AIP. doi:10.1063/1.1302534

27. Expedition Earth and Beyond (EEAB). URL: https://ares.jsc.nasa.gov/interaction/eeab/
28. ARSET. NASA. URL: http://arset.gsfc.nasa.gov/
29. EUSDR. URL: http://www.eurosdr.net/education/current
30. BLIF. URL: https://www.rgeo.de/en/p/blif/
31. SILC. URL: http://rgeo.de/SILC/
32. STEM resources. Challenger. https://www.challenger.org/stem-resources/
33. Hayden, L. B., D. Johnson, and J. Baltrop. "Remote Sensing Training for Middle School through the Center of Excellence in Remote Sensing Education." In AGU Fall Meeting Abstracts, vol. 1, p. 1050. 2012.
34. EARSeL SIG 'Education and Training'. http://www.earsel.org/SIG/ET/index.php (last date visited 18 March 2017)
35. ADAM. URL: http://www.adam-europe.eu/adam/project/view.htm?prj=10734
36. Youth Development Index (YDI). URL: http://youthmetre.eu/youthmetre/
37. EGU. Outreach. URL: www.egu.eu/outreach/egu-tv
38. GLOBE protocols. URL: http://www.globe.gov/get-trained/protocol-etraining
39. GLOBE data. URL: http://www.globe.gov/globe-data
40. GLOBE International Virtual Science Fair, 2016. URL: http://www.globe.gov/news-events/globe-events/virtual-conferences/2016-international-virtual-science-fair/instructions
41. GLOBE International Virtual Science Fair, 2016. Reports. URL: http://www.globe.gov/news-events/globe-events/virtual-conferences/2016-international-virtual-science-fair/virtual-science-fair-reports
42. Becker, M. L., Congalton, R. G., Budd, R., & Fried, A. (1998). A GLOBE Collaboration to Develop Land Cover Data Collection and Analysis Protocols. Journal of Science Education and Technology, 7(1), 85–96. doi:10.1023/A:1022540300914
43. SMAP. GLOBE. URL: https://www.globe.gov/web/smap/overview/how-to-participate
44. Landmap Project. URL: http://catalogue.ceda.ac.uk/uuid/ 7f1280cf215da6f8001eae5c2f019fe8
45. Nikitopoulou, T., and A. Retalis. Development of an educational e-material on remote sensing environmental applications: a case study for schools. Proc. SPIE 8795, 1st International Conference on Remote Sensing and Geoinformation of the Environment (RSCy2013), 879503 (August 5, 2013); doi:10.1117/12.2028125.
46. Education and Outreach. UNESCO. www.unesco.org/new/en/natural-sciences/science-technology/space-activities/space-for-heritage/education-and-outreach
47. BILKO. URL: http://www.bilko.org
48. Global Carbon Cycle. URL: http://globecarboncycle.unh.edu/index.shtml
49. Digital Earth. URL: http://www.digital-earth.edu.gr/index.php/en/info
50. Reuter, R. SEOS – EARSeL's project on science education through earth observation for high schools. AMBIÊNCIA, 2012, 8(4), 583–90; URL: http://revistas.unicentro.br/index.php/ambiencia/article/view/1861
51. SEOS. URL: http://www.seos-project.eu/home.html
52. http://revistas.unicentro.br/index.php/ambiencia/article/view/1861
53. Eckardt, R., N. Richter, S. Auer, M. Eineder, A. Roth, I. Hajnsek, D. Walter et al. SAR-EDU-An education initiative for applied Synthetic Aperture Radar remote sensing. In: EGU General Assembly Conference Abstracts, 2013, 15, 2459.

54. SAR-EDU. URL: https://saredu.dlr.de/
55. Voß, K., Goetzke, R., Thierfeldt, F. and Menz, G. Integrating Applied Remote Sensing Methodology in Secondary Education. Proc. IGARSS 2007 Barcelona, Spain. 2007, 2167–69.
56. Goetzke, R., Hodam, H., Rienow, A. and K. Voß. Teaching Materials, Encyclopedeia, Easy-to-Use Image Processing – The FIS Learning Portal on Remote Sensing. EARSeL eProceedings, 2013, 12, 2, 164–73.
57. Lindner, C., Hodam, H., Ortwein, A., Selg, F., Schultz, J. & Rienow, A. (2018): Sentinel-Daten für digitale und interaktive Anwendungen im Schulunterricht. 38. Wissenschaftlich-Technische Jahrestagung der DGPF und PFGK18 Tagung in München – Publikationen der DGPF, 2018, Band 27, 117–28.
58. Rienow, A., Hodam, H., Menz, G., Weppler, J. and S. Runco. Columbus Eye – High Definition Earth Viewing from the ISS in Secondary Schools. 65th International Astronautical Congress 2014, 29 September-03 October 2014 in Toronto, Canada.
59. Schultz, J., Ortwein, A. and A. Rienow. Technical Note: Using ISS Videos in Earth Observation – Implementations for Science and Education. European Journal of Remote Sensing, 2018, 51(1), 28–32.
60. Rienow, A., Graw, V., Heinemann, S., Schultz, J., Selg, F., and G. Menz. Inspecting the Blue Dot: Goals, Methods, and Developments of the Project ‚Columbus Eye'. In: ESA Living Planet Symposium 2016, 9-13 May Prague 2016.
61. Lindner, C., Hodam, H., Ortwein, A., Schultz, J., Selg, F., Rienow, A. & Jürgens C. Towards a New Horizon in Planetary Observation in Education. In: Proc. of 2nd Symposium on Space Educational Activities, April 11-13, 2018, Budapest, Hungary.
62. EO Education and Training. https://earth.esa.int/web/guest/eo-education-and-training

ОБЗОР НА РЕСУРСИТЕ ПО НАБЛЮДЕНИЕ НА ЗЕМЯТА ЗА СРЕДНОТО ОБРАЗОВАНИЕ – ЧАСТ 1

Л. Филчев, Й. Манакос, Р. Ройтер, Г. Мардиросян, Ц. Среброва, Л. Кралева, Д. Димитров, К. Марини, А. Рийнов

Резюме

Тази статия предоставя преглед на световните интернет ресурси и ресурсите за електронно обучение по наблюдение на Земята (ЕО) за средните училища. Накратко се преглеждат основните образователни инициативи и проекти за ЕО, подкрепени от международни, европейски и национални организации. В статията се разглеждат проблемите и перспективи на ЕО образованието в образователната система, неговото значение за обществото и връзката му със STEM предметите.

DOI: https://doi.org/10.3897/arb.v32.e19

A NEW EDITION OF A BOOK ABOUT THE NATURAL HAZARDS, THEIR PREVENTION AND PROTECTION

Millions of victims, much more injured and homeless, great amount of losses and heavy destructions – these are only part of the negative consequences due to the different natural hazards all over the world. Even today – at the beginning of 21 century the humanity still pays the great price to the terrible effects of the natural hazards. There are no places on the Earth, where natural hazards do not disturb the almost everyday life of the humanity.

Almost everywhere in the world the victims and damages strongly depend of the quality of constructions and the ability of the population to combat the disasters. The effectiveness of the emergency planning and execution, the fast and well organized reaction to the negative effects of the disaster are among other important factors influencing the mitigation to the different hazards. The 21st century started with a lot of very heavy natural hazards – earthquakes (Japan, 2011, Sumatra, 2004 both with magnitudes larger then 9), tsunamis (2004, 2011 both with heights over going 20–30 meters – victims between 20–30 000 to 200 000–300 000, Palu and Krakatau events in 2018 – more then 10 000 deaths, coronavirus pandemic events, huge forest fires in Australia, California, Spain, etc.).

That's why the new edition of the book "Natural hazards and ecological catastrophes – study, prevention, protection" is extremely useful and knowledgeable. The author – Prof. Garo Mardirossian from the Space Research and Technology Institute of the Bulgarian Academy of Sciences (SRTI-BAS) is well known author with his publications on the natural hazards, risk perception and risk management as he is working hard on the problems of the natural hazards and their effects to the population. This is his 3rd edition of his famous book of these topics. All editions have been accepted gratefully by the audience.

In this there are some general topics on the natural hazards, their generation and propagation as well as the physical properties as a base of their abilities to produce negative effects. Many terms like risk, vulnerability, multi risk and preliminary assessment of the consequences and damages are among the initial

items developed at the book. Separately a lot of space is targeted to the ecological catastrophes, man-made wars and their consequences and the geophysical weapons. Step by step the study goes deeper discovering the nature and effects of such events as earthquakes, landslides, cyclones, volcanic eruptions, tsunamis, avalanches, floods, forest fires, thunderstorms, tornadoes, etc. A lot of data about the observed cases, statistics about the victims and the damages, the most extreme cases etc. are under the focus of the author. Special attention is paid to the natural hazards at the territory of Bulgaria. Under discussion are the main parameters generating the negative effects to the population and the infrastructure. Special attention is paid to the prevention and the protection as well to the individual and societal directions. Very useful is the presentation of the abilities of the aerospace technologies about such investigations and observations and their high effectiveness. Completely new chapter is targeted to the aerospace technologies used to the natural disasters identification, development and on Earth effects. Thus supporting the idea that such methodologies could be very effective and useful tool against the natural hazards the book provides a lot of improvements in that direction.

The book is presented well to the readers and illustrated with many schemes, figures and photos. It could be useful to many different specialists – scientists and researchers in the fields of geophysics and ecology, geography and meteorology, etc. as well as to the decision-makers and Civil defence authorities, engineers and land planers, etc. and about the students and pupils from the schools and universities.

The book contains 372 pages, 56 figures, 20 tables, etc. Useful annexes contain the measuring scales about the different natural hazards.

That's why due to its actual content and usefulness and because such books are rare not only for us but also in the world practice, the appearance of the book – by Prof. Mardirossian is a huge event among the scientific community.

Prof. Boyko Ranguelov

Mardirossian, G. Prirodni bedstvija i ekologichni katastrofi – izuchavane, prevencija, zashtita. Izdatelstvo na BAN „Prof. Marin Drinov", Sofija, 2020, 372 p. ISBN 978-619-245-013-7 (in Bulgarian)

PROF. ROUMEN NEDKOV
(1956 – 2020)

Prof. Dr. Eng. Roumen Donchev Nedkov, our dear colleague, friend, leader, teacher and scientist, dedicated to research, and training of young scientists, passed away on November 28, 2020.

Prof. Nedkov graduated in 1980 in St. Petersburg, Russia, as a Dipl. Engineer in "TV Systems Qualimetri, Video Recording and Image Processing". In 1981 he started working at Bulgarian Air Force Academy "G. Benkovski". In 1989, at the Technical University, Sofia, he graduated as a Ph.D., with a thesis "A Study of the possibilities for automated digital signal processing in aircraft systems". Without a break, since 1987, his scientific space-research career at the Bulgarian Academy of Sciences started in the Space Research Institute (SRI) and reached the professor academic title in the later renamed Space Research and Technology Institute (SRTI). He was also a part-time associate professor and a professor at Sofia University "St. Kliment Ohridski", Faculty of Biology (2006–2018). He was the founder and head of the Aerospace Information Department (2006–2020), a Deputy Director (2010-2018) and a Director (2018-2020), a member of the Scientific Council of SRTI-BAS and of the Council of the Educational Centre at BAS. He was a member of Editorial Board of "Aerospace Research in Bulgaria".

Prof. Nedkov is the author of a number of patents and a lot of scientific articles and reports published in renowned journals and collections of prestigious scientific forums. His works in the field of Remote Sensing of the Earth and the planets are valued by the scientific community.

His activity on various programs, contracts and projects for realization of scientific applied developments is significant. He actively participated in:

The program of the 2nd Bulgarian Cosmonaut - the "Shipka" project (1988);

The development of the Video Spectrometric Complex VSK "FREGAT" (1989) - the international project "Phobos" as part of the study of the Planet Mars;

Projects for regular monitoring studies of the pollution of a number of cities and territories of Bulgaria as part of National and Regional programs and projects with the European Academy of Sciences (ESA).

Prof. Roumen Nedkov was fully devoted to the development and strengthening of the SRTI-BAS by constantly supporting its scientists from all departments and research fields for the successful continuation of the fundamental and applied space research.

ASSOC. PROF. DOYNO PETKOV
(1947 – 2020)

Assoc. Prof. Dr. Eng. Doyno Ivanov Petkov suddenly passed away on November 28, 2020. We lost a SCIENTIST and a dear colleague, friend, mentor.

His whole life was devoted to the science. In 1971 Doyno Petkov graduated as a Dipl. Engineer in "Electronics and Information Technologies" at the Technical University, Sofia. In 1993, at the Technical University, Sofia, he graduated as a Ph.D. with a thesis "Application of the principles of self-organization in remote sensing systems". In 1971 he started working at the Central Institute of Computer Science where he designed and implemented minicomputers and software operating systems. In 1976 he was invited to join the Central Laboratory for Space Research at the Bulgarian Academy of Sciences (BAS). As a member of the smart engineers' young team he was heading a couple of scientific projects in the field of the creating Multi-channel spectral image acquisition and processing Systems for Remote Sensing of the Earth and Planets. His theoretical and practical knowledge, creative scientific spirit, and management abilities were constantly of great importance for the development and implementation of computer systems for remote sensing spectrometric and radiometric systems. Some of them are: * The Spectrometric systems "SPECTRUM" aboard the 'Salyut' and 'MIR' space stations, part of the Scientific Programs of the two Bulgarian Cosmonauts; * The Satellite spectrometric system for remote sensing, part of Bulgarian National Space Program "BULGARIA-1300-II" focused on the remote sensing of the Earth; * The Video-spectrometric and navigational complex VSK "FREGAT" aboard the interplanetary space station "PHOBOS" for exploring Mars and its satellite Phobos.

As a head of the Department "Science" at the Bulgarian Ministry of Education and Science he developed regulations and laws in the field of science for Universities, BAS and other national scientific organizations. There as a Director he was responsible for the projects: "Creation of the National Academic Internet Network"; "Science Park Network" ('Phare' Program) and "Identification of sources for research funding" (World Bank).

Assoc. Prof. Petkov was a long-term Head of Departments "Methods for Remote Sensing of the Earth and Planets" and "Remote Sensing Systems", Deputy Director of 'Solar-Terrestrial Influences Laboratory' and later the 'Space Research and Technology Institute' (SRTI). He was the National Contact Person for the 'Space' theme as part of the EU's 7th and Horizon 2020 Framework Programmes for Research & Innovation. He was a participant in the negotiating delegation for accepting Bulgaria as a member of the European Space Agency.

Doyno mastered the words' sense, his wisdom was of great support for many of us, his dedication to science is a life-standard for some of us. With an experience as a visionary, coupled with the understanding of academic ethics as a norm for the progress of the scientific teams, Doyno's moral served as a drive for the strengthening the SRTI-BAS. His friends will sadly miss him.